Dark Screening of the Cosmic Microwave Background with Hidden-Sector Particles and New Dynamical Observables in First Order Phase Transitions

by

Dalila Maria Pîrvu

A thesis
presented to the University of Waterloo
in fulfillment of the
thesis requirement for the degree of
Doctor of Philosophy
in
Physics

Waterloo, Ontario, Canada, 2024

Examining Committee Membership

The following served on the Examining Committee for this thesis. The decision of the Examining Committee is by majority vote.

External Examiner:	Mustafa A. Amin Associate Professor, Physics & Astronomy, Rice University
Supervisor(s):	Matthew C. Johnson Adjunct Faculty, Physics & Astronomy, University of Waterloo Assistant Professor, Physics & Astronomy, York University Associate Faculty, Perimeter Institute for Theoretical Physics Luis Lehner Adjunct Faculty, Physics & Astronomy, University of Waterloo Faculty, Perimeter Institute for Theoretical Physics
Internal Member:	Robert B. Mann Professor, Physics & Astronomy, University of Waterloo
Internal-External Member:	Florian Girelli Associate Professor, Applied Mathematics, University of Waterloo
Other Member(s):	Asimina Arvanitaki Adjunct Faculty, Physics & Astronomy, University of Waterloo Faculty, Perimeter Institute for Theoretical Physics

Author's Declaration

This thesis consists of material all of which I authored or co-authored: see Statement of Contributions included in the thesis. This is a true copy of the thesis, including any required final revisions, as accepted by my examiners.

I understand that my thesis may be made electronically available to the public.

Statement of Contributions

This thesis is based on research papers which I co-authored and made significant scientific contributions to, as well as material from textbooks and other public sources.

Chapter 2 covers work from [1] written with J. Braden and M. C. Johnson.

Chapter 3 covers work from [2] written with M. C. Johnson and S. Sibiryakov.

Chapter 4 covers work from [3] written with J. Huang and M. C. Johnson.

Chapter 5 covers work from [4] written with C. Mondino, M. C. Johnson and J. Huang.

Abstract

This thesis focuses on two research directions within the field of Cosmology. It comprises the main results of my work as a PhD student. Part I introduces new observables of false vacuum decay derived from real-time numerical simulations. Part II describes a new method to search for hidden-sector particles using information from Cosmic Microwave Background (CMB) and Large Scale Structure (LSS) data.

The first part studies metastable 'false' vacuum decay in relativistic first order phase transitions. It is a phenomenon with broad implications for Cosmology and is ubiquitous in theories beyond the Standard Model. Describing the dynamics of a phase transition out of a false vacuum via the nucleation of bubbles is essential for understanding vacuum decay and the full spectrum of observables. We study vacuum decay by numerically evolving stochastic ensembles of field theories in 1+1 dimensions from an initially metastable state. First, we demonstrate that bubble nucleation sites cluster by measuring correlation functions in simulations. Next, we show that bubbles form with a Gaussian spread of center-of-mass velocities for a field with an initial thermal spectrum. Finally, we show that nucleation events are preceded by oscillons - long-lived, time-dependent, pseudo-stable field configurations. We provide theoretical tools to model and generalize our findings.

In the second part, we introduce a new type of secondary CMB anisotropy: the patchy screening induced by resonant conversion of CMB photons into dark-sector massive scalar (axions) and vector (dark photons) bosons as they cross non-linear LSS. In two of the simplest low-energy extensions to the SM, CMB photons can resonantly convert into either dark photons or axions when their local plasma frequency matches the mass of the hidden sector particle. For the axion, the resonance also requires the presence of an ambient magnetic field. After the epoch of reionization, resonant conversion occurs in dark matter halos if the hidden-sector particles have masses in the range $10^{-13}\ \mathrm{eV} \lesssim m_{\mathrm{A}'} \lesssim 10^{-11}\ \mathrm{eV}$. This phenomenon leads to new CMB anisotropies correlated with LSS, which we refer to as dark screening, in analogy with anisotropies from Thomson screening. Each process has a unique frequency dependence, distinguishing both from the blackbody CMB. In this thesis, we use a halo model-based approach to predict the imprint of dark screening on the CMB temperature and polarization and their correlation with LSS. We then examine n-point correlation functions of the dark-screened CMB and correlation functions between CMB and LSS observables to project the sensitivity of future measurements to the dark photon and axion coupling parameters.

Acknowledgments

First and foremost, I thank my advisor and mentor, Matt Johnson. I am grateful for his time, lessons, and countless discussions, and most of all, for his ability to always remind me of the joy of doing research. His guidance and support have been invaluable, and I believe we made a great team.

I am also grateful to my collaborators at the Perimeter Institute and beyond: Junwu Huang, Cristina Mondino, Sergey Sibiryakov, Andrey Shkerin, Jonathan Braden, Alex Jenkins, Andrew Pontzen, Hiranya Peiris, Ian Moss and others. I feel fortunate to have worked with and learned from such great physicists, and I look up to each of them.

To my friends, you have made this experience a deeply rewarding one, also from a personal side. Your companionship, shared joy, and unwavering support have been a constant source of strength and inspiration throughout the last four years.

I thank the examining committee for their interest in my work and for granting me this degree. Defending this thesis before them was a memorable and joyful experience.

Throughout my time as a graduate student at the Perimeter Institute and the University of Waterloo, I connected with many remarkable individuals, including research and administrative staff and visitors. I consider myself extremely fortunate to have been a part of the outstanding scientific environment here.

On the technical side, this thesis owes much to the following computational resources: in Part I, numerical simulations of a relativistic scalar field were performed using a modified version of J. Braden's *1d-scalar* code [5]; throughout Part II, numerical halo-model computations have been performed using a modified version of *hmvec* [6] by M. Madhavacheril; in the modelling and data analysis I made hefty use of NumPy [7] and SciPy [8] Python libraries, as well as Mathematica [9]. All numerical work in this thesis was performed on the Symmetry HPC at the Perimeter Institute.

Finally, my deepest gratitude goes to my parents, Lucia and Marian, and my sister Irina. They have remained my constant and unconditional support throughout my academic pursuit. This thesis is dedicated to them.

Table of Contents

List of Figures

List of Tables

Chapter 1

Introduction

Cosmology is the branch of science dedicated to understanding the evolution and structure of our Universe. Over the last century, this field has experienced remarkable growth thanks to advancements in observational technologies. The discovery of the Cosmic Microwave Background (CMB) radiation has revolutionized the field and led to the establishment of the Standard Model in Cosmology known as Lambda Cold Dark Matter (ΛCDM). In its standard form, ΛCDM is a seven-parameter theoretical model that has provided a consistent explanation for various observational data, including the statistical properties of the CMB and distribution of galaxies on large scales, as well as the Universe's expansion history. The values of these parameters have been measured to sub-percent level precision by instruments such as the Planck satellite [10]. At the same time, on a different front and guided by laboratory experiments searching for fundamental particles and their interactions, the Standard Model of Particle Physics (SM) was developed. Experiments have been testing the SM and ΛCDM predictions for decades and, combined, provide a robust description of physics on all scales.

Today, Cosmology and Particle Physics are becoming increasingly intertwined, as theoretical and experimental progress in one area can inform and guide efforts in the other. For example, ΛCDM provides concrete evidence that the SM is incomplete: cold dark matter and dark energy, essential in ΛCDM, do not fall under the SM framework. Furthermore, there are indications that ΛCDM itself is inconsistent with some experimental observations [11, 12, 13]. In time, as more precise measurements will be made available, the SM and ΛCDM will be under increasing pressure. In order to continue to provide a comprehensive description of our observable Universe, they will need to be modified or extended.

The collection of all phenomena and theories that do not lie under the standard framework is termed physics Beyond the Standard Model (BSM) of Cosmology and Particle Physics. The theoretical modelling of new BSM observables within the context of an extended framework is essential, as it can both facilitate the interpretation of upcoming data and help identify promising experimental directions to follow in the future.

In this Thesis, we investigate two topics within BSM physics. In the first part, we focus on bubble nucleation in relativistic first-order phase transitions – a process termed false vacuum decay. We propose the first new observables of the phenomenon of bubble nucleation introduced in decades. In the second half, we introduce a new type of CMB secondary anisotropy sourced by two compelling candidates for particle species BSM – dark photons and axions. We demonstrate that using available cosmological data from the Planck satellite [14], we can place the strongest bounds to date on the coupling between the SM photon and the dark photon for a mass range $10^{-11} - 10^{13}$ eV, stronger by two orders of magnitude compared to the current best constraints [15]. We further show that using upcoming CMB data, our method is sensitive to an additional order of magnitude for the dark photon coupling, and for the axion, the sensitivity is one order of magnitude above the current best constraints [16]. We elaborate in the following.

In first-order phase transitions, vacuum decay from a metastable configuration of a quantum field theory (QFT) occurs via the formation of bubbles containing a lower energy state. Benchmark analytical methods, namely Euclidean instanton techniques, cannot be used to describe the real-time dynamics of the field during the phase transition. Instead, they provide a framework for computing the decay rate of the false vacuum and general properties of the critical solution, which is the most probable bubble to form from quantum [17, 18] or finite temperature [19, 20] fluctuations. In our work, we employed a real-time stochastic description introduced in [21] to study the formation and evolution of bubbles.

First, we show that bubble nucleation sites cluster and measure the associated two-point function. We argue that bubbles form from peaks in the field, which act as seeds for nucleation. Since peaks in the background field cluster, bubble nucleation events inherit this property, in the same way that galaxies act as tracers for the underlying dark matter density field [22]. We also explore the case of a real scalar field with an initial Bose-Einstein distribution of fluctuations and identify additional observables. We demonstrate that bubbles nucleate with a distribution of center-of-mass velocities that has a spread proportional to the temperature of the false vacuum. Next, we show that the peaks from which bubbles form are oscillons. These are long-lived, oscillatory, pseudo-stable field configurations and can be understood as an intermediate state between the freely propagating field degree of freedom and the emergent bubble [23, 24, 25]. Their role in vacuum decay has previ-

ously been hypothesized in [26, 27, 28, 29, 30]. All of these observables are fundamentally inaccessible via Euclidean instanton methods.

To obtain these new observables, we employ real-time lattice simulations. These enable the dynamical exploration of the bubble nucleation process, albeit under a set of assumptions which are different from those of instanton theory (see e.g. [21, 31, 32, 33, 34, 35, 36, 37] for discussions). We see these new results as a first step towards bridging the gap between field theoretical methods and observation. Furthermore, we find good agreement between the simulation results and the instanton theory established theoretical predictions. This validation motivates their use to extract additional observables, as we do in this Thesis. The main focus of the work presented in Part I is to introduce new observables of bubble nucleation that can only be accessed through a real-time approach. We model the new observables using thermodynamic and statistical arguments and find good agreement with simulation measurements.

There have been a variety of recent efforts to perform laboratory-based simulations of false vacuum decay at low temperature using cold atom systems [38, 39, 40, 41, 42, 43, 44, 45, 46, 47, 48, 49, 50], quantum annealers [51], spin chains [52, 53], and (for the related Schwinger process) quantum computers [54, 55]. Notably, a realization of vacuum decay using cold atoms was performed in [50], with further results expected in the near future [43]. Therefore, our new predictions can be tested in practice within the next few years. These will provide the first tests of our assumptions related to real-time simulations and potentially the first measurements for the observables which we introduce in this Thesis. If confirmed, we will have introduced a new picture of the dynamics of vacuum decay that can be applied to modelling phase transitions in the early Universe and whose effects on cosmological observables could be targets for future cosmological surveys. Some examples of possible cosmological observables from vacuum decay have been discussed in works such as [56, 57, 58].

On the topic of dark matter phenomenology for Cosmology, we show that hidden sector particles can induce new spectral distortions and anisotropies in the CMB. We modelled the interaction of CMB photons with light vector bosons (dark photons) via a kinetic mixing term and their resonant conversion into scalar bosons (axions) in the presence of an ambient magnetic field. In both cases, the conversion happens in astrophysical environments where the dispersion relation of the CMB photon (plasma frequency) is naturally scanned, causing it to acquire an effective mass. These processes act as a screen for CMB radiation, leading to frequency-dependent anisotropies in temperature and polarization. The screening traces the distribution of matter across the sky, and the signal morphology depends on the properties of the hidden particle, such as its mass. Notably, both processes carry unique frequency scalings that distinguish each individually from the blackbody.

The mass range accessible via this method is beyond the scope of laboratory experimentation, so this method opens the exploration of a new region in the parameter space for BSM. Using a halo model approach [59, 60], we construct two- and three-point correlation functions of the dark-screened CMB, as well as correlation functions between CMB and LSS observables and demonstrate that existing CMB data can improve upon current constraints on the kinetic mixing parameter of the dark photon coupling by two orders of magnitude, and up to three orders of magnitude for future surveys. In the case of the axion, we show that an analysis using Planck data and a galaxy catalog would be sensitive to couplings comparable to the most sensitive existing astrophysical axion searches. Additionally, we show that future CMB data could improve the sensitivity by an additional order of magnitude. This framework can be readily extended to include other tracers of LSS besides galaxy surveys, which would further increase the range of masses that can be probed. It can also be extended to search for other couplings to hidden-sector candidates.

The remainder of Chapter 1 reviews theoretical knowledge and background assumed throughout the main Chapters. A brief review of Cosmology is covered in 1.1. Section 1.2 reviews the motivation to study vacuum decay for Cosmology and includes a summary of basic concepts in instanton theory applied to vacuum transitions.

1.1 Cosmology Review

In this section, we summarize a list of general concepts in Cosmology that relate to the material presented in the main Chapters of this Thesis. First, we introduce the language and equations needed to talk quantitatively about the physics of an expanding Universe. Then, we outline the main events in the thermal history, highlighting the role of phase transitions in producing the particle content observed today. Next, we introduce the inhomogeneities that lead to the formation of Large Scale Structure (LSS) and CMB anisotropies. We use linear perturbation theory to explain why their statistics can be understood in terms of growing density fluctuations in an expanding background. Finally, we motivate the search for two of the most promising hidden particle candidates: the dark photon and the axion.

The upcoming review combines topics from several textbooks and lecture notes on modern Cosmology, including [61, 62, 63, 64, 65, 66, 67], as well as various papers and review articles which are highlighted throughout the text, where relevant.

Conventions

For all cosmological quantities, the subscript 0 is used to label their present value, e.g. H_0 is the value of the Hubble parameter today. Unless stated otherwise, we work in natural units where $\hbar = c = k_B = 1$. We use the $(-,+,+,+)$ signature for the metric. Greek indices (e.g. μ, ν) refer to 4-dimensional spacetime quantities. The spatial dimension of variables is usually clarified in the text. However, bold text notation is used when a vector quantity is highlighted. For example, in integrals, the infinitesimal volume element states the variable dimension, as does the superscript in Dirac delta functions – e.g. $\mathrm{d}^n k$ is an n-vector and $\delta^n(k)$ an n-dimensional distribution – but when denoting a vector product, we usually use vector boldface notation – e.g. for two momenta we use $\mathbf{q}_1 \cdot \mathbf{q}_2$. Unit vectors are denoted with a hat, e.g. $\hat{n}$.

The convention used for Fourier transforms is the following:

$$\varphi(\boldsymbol{k}) = \int \mathrm{d}^3\chi e^{-i\boldsymbol{k}\cdot\boldsymbol{\chi}}\varphi(\boldsymbol{\chi}), \quad \varphi(\boldsymbol{\chi}) = \int \frac{\mathrm{d}^3 k}{(2\pi)^3} e^{i\boldsymbol{k}\cdot\boldsymbol{\chi}}\varphi(k), \tag{1.1}$$

and for multipole expansions, we write

$$\varphi(\hat{n}) = \sum_{\ell=0}^{\infty}\sum_{m=-\ell}^{m=\ell} \varphi_{\ell m} Y_{lm}(\hat{n}), \quad \varphi_{\ell m} = \int \mathrm{d}^2\hat{n}\, Y^*_{\ell m}(\hat{n})\varphi(\hat{n}), \tag{1.2}$$

where the $Y_{\ell m}$ are the spherical harmonic functions, which are normalized as follows:

$$\int \mathrm{d}^2\hat{n}\, Y_{\ell m}(\hat{n}) Y^*_{\ell' m'}(\hat{n}) = \delta_{\ell\ell'}\delta_{mm'}. \tag{1.3}$$

The '$*$' superscript refers to complex conjugation.

1.1.1 Background Cosmology

The Universe is expanding. On average, it is spatially homogeneous and isotropic. These are strong constraints that define the symmetry properties of the spacetime geometry. To first order, this is given by the Friedmann–Lemaître-Robertson–Walker (FLRW) metric:

$$\mathrm{d}s^2 = -\mathrm{d}t^2 + a(t)^2 \mathrm{d}S_3^2 = a(\eta)^2\left(-\mathrm{d}\eta^2 + \mathrm{d}S_3^3\right), \tag{1.4}$$

where $\eta = \int \mathrm{d}t/a(t)$ is the conformal time, $a(t)$ is the scale factor and $\mathrm{d}S_3^2$ is the spatial volume element. Depending on the geometry, in the most general case, it is:

$$\mathrm{d}S_3^2 = \frac{\mathrm{d}\chi^2}{1 - \kappa\frac{\chi^2}{\chi_*^2}} + \chi^2 \mathrm{d}\Omega^2, \tag{1.5}$$

where the curvature κ can take values $\kappa \in \{-1, 0, +1\}$ corresponding to a closed (spherical), flat, and open (hyperbolic) Universe, respectively. The parameter χ_* is an arbitrary curvature radius and $\mathrm{d}\Omega^2 = \mathrm{d}\theta^2 + \sin\theta^2 \mathrm{d}\phi$ represents the volume element on the 2-sphere.

Most of the information we receive from space travels towards us in the form of light, which follows null geodesics defined by the condition that $\mathrm{d}s^2 = 0$. As with any other length scale, the wavelength of light increases along with the scale factor. This phenomenon is called gravitational redshift. Formally, redshift is defined as the fractional change in wavelength of a photon emitted by a distant source. In terms of the scale factor, this is given by

$$z = \frac{1}{a(t)} - 1, \quad 0 < a \leq 1, \tag{1.6}$$

where by convention the redshift today is $z_0 = 0$ corresponding to $a_0 = 1$. The proper distance is the physical distance between any two points at a fixed moment in time, and we denote it by r:

$$r = a(z) \int \mathrm{d}\chi' = \frac{\chi(z)}{1+z}, \tag{1.7}$$

where z is the redshift calculated at the source. Finally, the comoving distance χ to an object at redshift z is the length of the path travelled by a photon along a null ray:

$$\chi = \int_0^{\chi} \mathrm{d}\chi' = \int_t^{t_0} \frac{\mathrm{d}t}{a} = \int_a^1 \frac{\mathrm{d}a}{a^2 H} = \int_0^z \frac{\mathrm{d}z}{H}. \tag{1.8}$$

The scale factor always increases with redshift in an expanding Universe like ours. Along with the scale factor, they have a one-to-one relationship with time and are often used as a proxy for the time parameter.

Notice that the comoving distance is constant with the expansion, while the physical distance r increases monotonically. This is the Hubble flow. In the comoving coordinate system defined by (1.4), all matter is on average at rest.

Our goal is to understand how matter evolves in the FLRW spacetime. To do so, we now introduce some concepts from General Relativity. We can define the metric tensor $g_{\mu\nu}$ in relation to the infinitesimal FLRW interval as:

$$\mathrm{d}s^2 = g_{\mu\nu} \mathrm{d}x^\mu \mathrm{d}x^\nu, \tag{1.9}$$

where $x^\mu = (x^0, x^i) \equiv (t, \chi, \theta, \phi)$ are event coordinates, the 0 superscript denotes the time index and i the spatial index $i = 1, 2, 3$. Usually, when we refer to spatial 3-vectors, we use bold vector notation $x^i \equiv \mathbf{x}$.

The differential equations which relate $g_{\mu\nu}$ to the matter distribution are the Einstein equations

$$R_{\mu\nu} - \frac{1}{2} g_{\mu\nu} R = 8\pi G T_{\mu\nu}, \tag{1.10}$$

where $R_{\mu\nu}$ is the Ricci tensor and R the Ricci scalar, related to the metric and its first two derivatives. G is Newton's gravitational constant. The quantity $T_{\mu\nu}$ is the stress-energy tensor, which measures the relevant properties of matter, such as energy, momentum, or shear density. For Cosmology, matter is usually modelled as an ideal fluid, defined by an isotropic pressure $p(x^\mu)$ and a rest-frame mass per unit volume $\rho(x^\mu)$. The equation relating a fluid's energy density and pressure is called its equation of state e.g. $p(x^\mu) = w\rho(x^\mu)$, where w is a constant. The stress-energy tensor of an ideal fluid has the following definition:

$$T^{\mu\nu} = (\rho + p)\, u^\mu u^\nu + p g^{\mu\nu}, \tag{1.11}$$

where u^μ is its four-velocity. Measured by a comoving observer such that $u^\mu = (1, 0, 0, 0)$, the stress tensor reduces to $T^\mu_\nu = \mathrm{diag}\,(-\rho, p, p, p)$.

In general, one can start from the Einstein field equations (1.10), apply the FLRW metric from (1.4) and enforce an equation of state in (1.11) to arrive at a set of equations of motion relating the scale factor $a(t)$ with the energy density ρ. It is then possible to choose some initial conditions and solve for the dynamics of the relativistic fluid in the smooth expanding background. For example, for the ideal fluid which has $w = p/\rho$, the Einstein equations simplify to the Friedmann equations:

$$\begin{aligned} H^2 + \frac{\kappa}{a^2} &= \frac{8\pi G}{3}\rho, \\ \frac{\ddot{a}}{a} &= -\frac{4\pi G}{3}(\rho + 3p), \end{aligned} \tag{1.12}$$

where $H(t) \equiv \frac{\mathrm{d}a}{\mathrm{d}t}\frac{1}{a}$ is the Hubble parameter. The first equation above comes from the $\mu = 0, \nu = 0$ component of the Einstein equations, while the second one can be derived from the trace.

In GR, the stress-energy tensor is covariantly conserved $\nabla_\mu T^{\mu\nu} = 0$. Imposing the FLRW metric yields the continuity equation:

$$\dot{\rho} = -3H(\rho + p), \tag{1.13}$$

which describes the time evolution of density and pressure.

Some of the most important examples of perfect fluids are listed in Table 1.1, along with their equation of state and relationship between energy density and expansion parameter $a(t)$. These are dust (non-relativistic pressureless matter where $p^2 \ll m^2$), radiation

(derived by treating relativistic matter with $p^2 \gg m^2$ as a quantum photon gas), and dark energy (negative pressure). If the spacetime has intrinsic curvature $\kappa \neq 0$, this also has an associated energy density, which grows linearly in time.

Component	w	$\rho(a)$	$a(t)$
Dust	0	a^{-3}	$t^{2/3}$
Radiation	$1/3$	a^{-4}	$t^{1/2}$
Dark Energy	-1	a^0	e^{Ht}
Curvature	$-1/3$	a^{-2}	t

Table 1.1: Perfect Fluids in Cosmology.

Cosmological data is consistent with a flat FLRW model in which the energy density is divided between dark energy, radiation and dust. Schematically, the total stress-energy tensor in our Universe can be written as:

$$T^{\mu\nu} = T^{\mu\nu}_{\text{radiation}} + T^{\mu\nu}_{\text{matter}} + T^{\mu\nu}_{\text{dark energy}}. \tag{1.14}$$

From now on, we will use the short-hand notation where 'm' stands for dust, 'r' for radiation, and 'Λ' for dark energy. Each component individually satisfies the continuity equation (1.13). The total energy density at a particular time is given by:

$$\rho = \rho_{\text{r}} + \rho_{\text{m}} + \rho_{\Lambda}. \tag{1.15}$$

The scaling of each component with the expansion parameter a is listed in Table 1.1. Depending on the value of a, the relative importance of each term changes. In the beginning, where $a \to 0$, radiation dominated the energy density of the Universe. As a increases, the magnitudes of the first and second terms become comparable. When the second term dominates, we say that the Universe is in a period of matter domination, where in the absence of radiation pressure and under the action of gravity, the expansion slows down. Today, we live in an epoch where matter and dark energy take up a similar fraction of the total energy density while radiation is strongly suppressed. In the future, the dynamics will be dominated by Λ, and the Universe will undergo accelerated expansion because of its negative pressure, behaving as if it were empty of matter particles.

To paint a quantitative picture of this story, it is useful to introduce the critical density

$$\rho_c(t) = \frac{3H(t)^2}{8\pi G} \tag{1.16}$$

as the total density of the Universe at a given time t such that the total curvature is flat: $\kappa = 0$. A density parameter is then defined by $\Omega \equiv \rho/\rho_c$ and we measure the relative importance of each term compared to the total as a function of these time-dependent dimensionless quantities:

$$\Omega = \sum_i \Omega_i = \sum_i \frac{\rho_i}{\rho_c} = \Omega_m + \Omega_r + \Omega_\Lambda. \tag{1.17}$$

The Universe may have an intrinsic spacetime curvature $\kappa \neq 0$. The associated density parameter is then added as an offset from unity: $\Omega_\kappa = \Omega - 1$. Modern instruments have measured the present values of these parameters to sub-percent level accuracy [10]. Their values are listed in Table 1.2. Given these numbers, it is possible to calculate several notable times in expansion history. For example, the scale factor at which the density of matter and radiation are equal, a_{mr}, and when the density of matter and Λ are equal, $a_{m\Lambda}$:

$$a_{mr} = \frac{\Omega_r}{\Omega_m}, \quad a_{m\Lambda} = \left(\frac{\Omega_m}{\Omega_\Lambda}\right)^{1/3}. \tag{1.18}$$

Other important redshifts are the listed in Table 1.3. We expand on the significance of each era before the end of this Chapter.

We can also write the first Friedmann equation in terms of the current energy density of all the main components present in our Universe:

$$\frac{H^2}{H_0^2} = \frac{\Omega_r}{a^4} + \frac{\Omega_b + \Omega_c}{a^3} + \frac{\Omega_k}{a^2} + \Omega_\Lambda, \tag{1.19}$$

Integrating this equation over the scale factor, we can calculate that the total age of the Universe is $t_{\text{age}} = 13.78$ Gyr.

total matter density	$\Omega_m = \Omega_c + \Omega_b = 0.315$
dark matter density	$\Omega_c = 0.264$
baryonic matter density	$\Omega_b = 0.0493$
dark energy density	$\Omega_\Lambda = 0.685$
total radiation density	$\Omega_r = 9.17 \times 10^{-5}$
dark energy equation of state	$\lvert w_\Lambda + 1\rvert < 0.03$
spatial curvature	$\lvert\Omega_\kappa\rvert < 0.0037$
Hubble constant	$H_0 = 67.4$ km s^{-1}Mpc^{-1}

Table 1.2: Measured FLRW parameters based on the *Planck* 2018 best-fit Cosmology [10].

Event	Redshift z
Matter-radiation equality	3400
Recombination	$1100 - 6000$
Last scattering surface	1100
Dark Ages	$20 - 1100$
Reionization	$6 - 20$
First galaxies	$8 - 12$
Typical galaxy surveys	$0.5 - 2$
Matter-dark energy equality	0.4

Table 1.3: Chronology of the Universe since matter domination.

1.1.2 Thermal History

Under the FLRW cosmological model and given state-of-the-art observation, our Universe started from a flat, homogeneous, isotropic geometry and a hot, radiation-dominated state. We think of this state as one where all particles in the Standard Model are in thermal equilibrium. Inflation is the current best candidate for the process by which the Universe arrived at this state. This topic is presented in a later section.

When particles exchange energy and momentum efficiently for a long enough time, the system is said to be in equilibrium and has reached a state of maximum entropy. Statistical mechanics arguments can be used to show that for a particle species with mass m and temperature T, the distribution function, i.e. the number density in phase space, is given by

$$f(q) = \frac{1}{e^{E(q)/T} \pm 1}, \tag{1.20}$$

where the '+' sign is satisfied by fermions and '−' by bosons, and we omitted the chemical potential. The distributions in each case are called Fermi-Dirac and Bose-Einstein, respectively. Particle species that are in equilibrium share the same temperature. We refer to the radiation fluid that dominates the energy density in this epoch as the primordial plasma. Particles and anti-particles are free and exchange energy continuously in the form of photons. Current LHC experiments can reach energies of order several TeV $= 10^{12}$ eV, momentarily reproducing the conditions of this era. So far, these are the largest scales we can probe on Earth.

Because the plasma temperature at this time is well above any mass scale $T \gg m_{\rm SM}$. In such a system, the entropy per comoving volume is conserved. It can be shown that this implies $T \propto a^{-1}$. Every time a particle species falls out of equilibrium, i.e. the temperature

falls below its mass scale, the associated entropy is redistributed among the degrees of freedom still coupled to the plasma, causing T to decrease slightly less slowly than a^{-1}.

Schematically, the reactions that occur at this time are $b + \bar{b} \leftrightarrow 2\gamma$. For example, if $T \gg m_b$, the respective particle species b is relativistic with $E \propto q$, and particle-antiparticle pairs are created from the vacuum. The number density is similar to massless photons, i.e. $n \propto T^3$. As the Universe expands and cools, the temperature reaches the mass scale $T \sim m_b$ and the '$\leftarrow$' process becomes inefficient: $b\bar{b}$ pairs only annihilate and are no longer produced. For non-relativistic particles, $E \gg m$, and if the temperature continues to drop $T \ll m$, the number density distribution becomes exponentially (or Boltzmann) suppressed, i.e. $f \to e^{-m/T}$. One by one, in inverse order of mass, particles are said to decouple from the heat bath, and their number density freezes out. An initial imbalance in the number of matter particles versus anti-matter prevents complete mutual annihilation. The extent of the observed imbalance can not be sourced within the SM. However, mechanisms such as phase transitions could explain it.

The electroweak phase transition occurs once the temperature reaches the energy scale of the Higgs mass $m_H \approx 125$ GeV. The Higgs mechanism reorganizes the degrees of freedom of the existing bosons, endowing SM particles with their masses. Until this point, the temperature is still large enough that quarks escape confinement. This remains true until the QCD phase transition, at $T \approx 150$ MeV when quarks condense into bound hadrons: three-quark baryons such as protons and neutrons and unstable two-quark mesons. Electron and positrons continue to remain in thermal equilibrium $e^- + e^+ \leftrightarrow 2\gamma$ until $m_{e^-} \approx 0.5$ MeV $\ll 150$ MeV. They are the last matter species to decouple. Their annihilation process produces additional photons, which heat the Universe by a fraction. This is the final photon-producing process, so their number density is conserved from here onward.

Around 3 minutes after the Big Bang, the Universe is still mostly homogeneous, well into radiation domination. All neutrons are either bound into atomic nuclei or have decayed into protons to form the light elements: Hydrogen, Helium and traces of others such as Lithium. The fraction of neutrons captured in each element depends on the ratios between photons and baryons and of protons to neutrons at the time and on details of nuclear stability and binding energies. All of these are well studied: nuclear physics provides a detailed picture of the matter content at that time based on the observed abundances of elements.

The next step is recombination. Absent of positrons and with the temperatures low enough that the photon bath no longer ionizes atoms, electrons become trapped inside neutral atoms via $p + e^- \to H + \gamma$ as similar reactions. Decoupling soon follows, where the photons finally fall out of equilibrium with the electrons. The Universe has grown large

Event	age t	temperature T
Planck scale	10^{-44} s	10^{28} eV
Inflation	?	?
GUT transition	10^{-36}	10^{15} eV
Baryogenesis	?	?
EW phase transition	10^{-11} s	10^{11} eV
QCD phase transition	10^{-5} s	150 MeV
Electron-positron annihilation	6 s	500 keV
NucleosynThesis	3 min	100 keV
Recombination	$260 - 380$ kyr	$0.26 - 0.33$ eV
Decoupling	380 kyr	$0.23 - 0.28$ eV
Reionization	$100 - 400$ Myr	$2.6 - 7.0$ meV
Present	13.8 Gyr	$\bar{T}_{\rm CMB} = 0.24$ meV

Table 1.4: Key events in the thermal history, together with a rough estimate for the age of the Universe at that time and associated energy scales [65].

enough that the photon mean free path reaches the Hubble size. The Universe becomes transparent as photons are free to propagate on cosmic distances. They contain much information about the state of the Universe at that time from the properties that were imprinted on them via scattering off the final electron around a redshift of $z = 1100$. We refer to the surface we 'see' when we detect these photons today as the surface of last scattering. This is the cosmic microwave background.

Since decoupling, the Universe has stayed neutral until the formation of the first stars in a process called reionization. Since then, photons have been produced in nuclear processes with large enough energies to re-ionize atoms. The characteristic timescale of reionization defines another cosmological parameter called the average optical depth. Its current best-fit value is $\bar{\tau}^{\rm Th} = 0.054$, provided by the *Planck* satellite. This places the reionization redshift around $z \approx 7.7$, much later than photon decoupling. The value of $bar\tau^{\rm Th}$ implies that roughly 5% of the measured CMB photons have re-scattered since reionization. They hold information about the distribution and properties of matter in the recent Universe. The remaining 95% is a direct snapshot of the surface of last scattering.

We list the events defining the thermal history of the Universe Table 1.4. The corresponding energy scales and the approximate time they took place are also shown.

1.1.3 Inhomogeneities

The Universe, however, is not entirely homogeneous. On small scales, perturbations exist in every density distribution we observe. For example, perturbations in the matter density field are apparent in the distribution of galaxies. We also measure anisotropies in the relic radiation field from the surface of the last scattering – the CMB.

Focusing on the cold dark matter (CDM) density field, we define the local perturbations $\delta\rho(\mathbf{r}, t)$ around a smooth time-dependent background $\bar{\rho}(t)$ in terms of the density contrast:

$$\delta(\mathbf{r}, t) \equiv \frac{\delta\rho(\mathbf{r}, t)}{\bar{\rho}(t)} = \frac{\rho(\mathbf{r}, t) - \bar{\rho}(t)}{\bar{\rho}(t)}. \tag{1.21}$$

We can model analytically the dynamics of inhomogeneities using perturbation theory, valid as long as $\delta(\mathbf{r}, t) \ll 1$. Once this approximation breaks, nonlinear effects, such as gravitational collapse, become important. In practice, CMB temperature fluctuations are of order $\delta T/T \approx 10^{-5}$, which is well within this margin. However, for the observed matter distribution, on small scales, the fluctuations can be of order the mean density: $\delta(\mathbf{r}, t) \sim \mathcal{O}(1)$. Perturbation theory is therefore only valid on scales of order ~ 10 Mpc and above.

Statistical Description of Random Fields

Before moving on to perturbation theory, we summarize some important concepts and properties of density contrast fields. Statistically, they are characterized by the collection of all n-point functions, where $n \geq 1$. These capture all relevant information and general features of the distributions and represent the main observables in any experiment.

In real space, and suppressing the time-dependence, the correlation functions are denoted by:

$$\langle \delta(\mathbf{r}_1) \cdots \delta(\mathbf{r}_n) \rangle \equiv \xi_n(\mathbf{r}_1, \cdots, \mathbf{r}_n). \tag{1.22}$$

If all position vectors $\mathbf{r}_i$ are equal, the correlation functions describe the moments of the distribution. Given the definition of δ, its first moment is zero. The second moment defines the power spectrum:

$$P(k) = \int \mathrm{d}^3 r e^{i\mathbf{k}\cdot\mathbf{r}} \xi(r) = 4\pi \int \mathrm{d}r r^2 \frac{\sin kr}{kr} \xi(r), \tag{1.23}$$

where here rotational invariance, or the fact that $\xi(\mathbf{r} \equiv |\mathbf{r}_1 - \mathbf{r}_2|) = \langle \delta(\mathbf{r}_1)\, \delta(\mathbf{r}_2) \rangle$, are consequences of isotropy. Working in Fourier space simplifies the structure of all correlation

functions. Since δ is real, $\delta(-\mathbf{k}) = \delta^*(\mathbf{k})$ and we can write the two-point function in k-space as:

$$\left\langle \tilde{\delta}(\mathbf{k})\tilde{\delta}^*\left(\mathbf{k}'\right)\right\rangle = (2\pi)^3\delta^3\left(\mathbf{k}-\mathbf{k}'\right)P(k). \tag{1.24}$$

The simplification comes from the n-dimensional Dirac delta function, δ^n, which expresses that the different wavenumbers k are uncorrelated in this expression. It is useful to define the dimensionless contribution per logarithmic integral to the mean-square fluctuations:

$$\Delta^2(k) = k^3P(k)/\left(2\pi^2\right). \tag{1.25}$$

This quantity measures the variance of density fluctuations on length scales $\chi \sim 2\pi/k$. The Fourier transform of the three-point correlation function of density perturbations is called the bispectrum. For real fields, this is:

$$\left\langle \tilde{\delta}(\mathbf{k})\tilde{\delta}\left(\mathbf{k}'\right)\tilde{\delta}\left(\mathbf{k}''\right)\right\rangle = (2\pi)^3\delta^3\left(\mathbf{k}+\mathbf{k}'+\mathbf{k}''\right)B\left(\mathbf{k},\mathbf{k}',\mathbf{k}''\right). \tag{1.26}$$

Higher-order functions are constructed similarly.

The second-order moments and the mean describe a Gaussian distribution entirely because all higher moments are zero. Since linear theory does not mix the evolution of different modes, if a distribution started as Gaussian, it remains so at a later time, although the power spectrum can change. However, higher-order functions become relevant if the initial conditions are non-Gaussian or the evolution is nonlinear.

Growth of Matter Perturbations

The following summarises the main ideas behind the perturbation theory applied to the CDM density contrast. The first step is to consider linear corrections to the flat FLRW metric:

$$g_{\mu\nu}(x,t) = g_{\mu\nu}^{FRW} + \delta g_{\mu\nu}. \tag{1.27}$$

As a four-dimensional symmetric tensor, the metric perturbation $\delta g_{\mu\nu}$ has 10 degrees of freedom. Four of these are fixed by the choice of gauge, leaving six dynamical variables. Two more are vector quantities, which decay over time and do not affect the distribution of matter. Two more are tensor degrees of freedom, representing transverse and traceless gravitational waves, which we do not discuss besides mentioning that they couple to the spatial part of the metric as $h_{ij}\mathrm{d}x^i\mathrm{d}x^j$. The remaining degrees of freedom are scalars and couple directly to the density perturbations.

The preferred gauge for studying the formation of LSS and CMB anisotropies is the Newtonian gauge. Here, the metric takes the following form, with Φ and Ψ representing scalar perturbations:

$$\mathrm{d}s^2 = -(1+2\Phi)\mathrm{d}t^2 + a^2(t)(1+2\Psi)\delta_{ij}\mathrm{d}x^i\mathrm{d}x^j, \tag{1.28}$$

The free parameter Φ is identified with the Newtonian gravitational potential.

The matter sector receives linear corrections as well. Recall that the ideal fluid is described to zeroth order by constant density $\bar{\rho}$, pressure $\bar{p}$ and four-velocity $u^\mu = (1,0,0,0)$. In an expanding Universe, first-order corrections are added as

$$\rho = \bar{\rho}(1+\delta), \quad p = \bar{p} + \delta p, \quad u^\mu = \left(1-\Phi, u^i\right), \tag{1.29}$$

where δ is the density contrast, δp are pressure fluctuations and $u^i \equiv \mathbf{u}$ fluctuations in the spatial comoving velocity. Meanwhile, the first-order correction to the stress-energy tensor is:

$$\delta T^\mu{}_\nu = (\delta\rho + \delta p)\bar{u}^\mu\bar{u}_\nu + (\bar{\rho}+\bar{p})\left(\delta u^\mu \bar{u}_\nu + \bar{u}^\mu \delta u_\nu\right) - \delta p\, \delta^\mu_\nu. \tag{1.30}$$

In the absence of anisotropic stress, i.e. all off-diagonal terms are zero as is the case for an ideal fluid, we can replace $\Psi = -\Phi$ in the metric.

Similarly to how the Friedmann and continuity equations were derived, it is possible to use the perturbed metric and conservation of the perturbed stress-energy tensor to derive the linearized equations of motion for any ideal fluid, order by order. The perturbed Friedmann equations will relate the density perturbation to the expansion. Furthermore, since the stress-energy tensor is conserved independently for each component, they give a set of coupled differential equations for their co-evolution. In general, one can simplify equations by considering only contributions from a single component, which dominates the energy density at that time. In particular, to describe both the linear growth of perturbations leading to the formation of structure and the CMB, we need to consider the matter-driven expansion of the background metric, as both processes occur during matter domination.

There is one complication. Non-relativistic matter comprises baryonic and cold dark matter, so we write $\Omega_m \equiv \Omega_b + \Omega_c$. This distinction is important for the following discussion, as CDM only reacts to fluctuations in the gravitational potential Φ, while baryonic matter also interacts additionally with electromagnetically. Qualitatively, the baryonic component δ_b couples to δ_r to form the coupled photon-baryon fluid. The corresponding equation of state is $w \approx 1/3$ and evolves effectively as relativistic matter until recombination at redshift $z \approx 1100$, well into matter-domination.

We now specialize to the case of non-relativistic matter in the Newtonian limit where coordinates can be chosen such that locally, the fluid velocities are small (pressureless dust $\delta p \ll \delta, w = 0$) and the spacetime metric is locally flat. This case is of interest for understanding the formation and evolution of LSS. As mentioned above, it is a story about CDM, and we ignore baryonic effects. From the 0-component of the Einstein equations, we obtain the Poisson equation:

$$\nabla^2 \Phi = 4\pi G\, a^2 \bar{\rho}\, \delta, \tag{1.31}$$

which states that the density perturbations source a gravitational potential (equivalently spacetime curvature fluctuations) and vice-versa. The i-component gives the Euler equation for fluid dynamics, and from conservation of $\delta T^{\mu\nu}$ for δ, we get the continuity equation. In the linear regime where $\delta \ll 1$, these may be combined to yield the following equation:

$$\frac{\partial^2 \delta}{\partial t^2} + 2H \frac{\partial \delta}{\partial t} - 4\pi G\, \bar{\rho}\, \delta = 0. \tag{1.32}$$

Schematically, this reads:

$$\ddot{\delta} + (\text{Pressure} - \text{Gravity})\, \delta = 0. \tag{1.33}$$

During the matter-domination $H \propto 2/3\, t$. Using also that for the background $4\pi G \bar{\rho} = \frac{3}{2} H^2$, we simplify the equation above to $\ddot{\delta} + \frac{4}{3t}\dot{\delta} - \frac{2}{3t^2}\delta = 0$. It has two independent solutions, corresponding to modes that grow or decay with time. Parametrizing as $\delta \propto t^p$, these are:

$$\delta \propto \begin{cases} t^{-1} \propto a^{-3/2}, \\ t^{2/3} \propto a. \end{cases} \tag{1.34}$$

Only the growing mode solution is relevant and says that dark matter fluctuations grow as the scale factor during matter domination. The potential Φ is constant during matter domination. We can plug this solution into the Fourier transform of the Poisson equation, making the substitutions $\nabla^2 \to k^2$, $\Phi \to \tilde{\Phi}_k$ and $\delta \to \tilde{\delta}_k$. The density contrast takes the following form:

$$\tilde{\delta}_k(a) \propto \frac{a\, k^2\, \tilde{\Phi}_k}{H(a)^2}. \tag{1.35}$$

This scaling will be relevant later.

It can be shown that during a radiation-dominated era, the conservation of energy and momentum produce similar equations of motion for the density contrast. However, the gravitational potential is coupled to radiation and matter fields here. The solution

for the δ_r fluctuations oscillates on small scales, and the time-averaged density contrast is vanishingly small. In practice, it means that the time-averaged solution for $\tilde{\Phi}_k$ is only sourced by matter perturbations and the growing mode scales as

$$\tilde{\delta}_k(a) \propto \ln(ak)\,. \tag{1.36}$$

Finally, for matter fluctuations evolving in a dark energy-dominated era, the expansion is fast enough to suppress matter fluctuations. Dark energy does not cluster, so its density contrast is zero. Without perturbations, the equation of motion for δ is just $\ddot{\delta} + 2H\dot{\delta} \approx 0$, where $H \approx$ constant. This equation has no growing solutions.

Doing this kind of analysis much more carefully, it can be shown that the growing mode solutions for the density contrast at late times can be written in the following form:

$$\tilde{\delta}_k(a) = \tilde{\delta}_k^{(0)}\, D(a)\, T(k), \tag{1.37}$$

where $\tilde{\delta}_k^{(0)}$ represents the primordial perturbations (also known as the initial conditions), $T(k,a)$ is a transfer function and $D(a)$ the growth factor. Both quantities are described below. Notice that under linear theory, different modes do not couple.

The transfer function is usually defined for the gravitational potential Ψ; however, we illustrate its purpose using the CDM density contrast we have been discussing so far. For adiabatic perturbations, such as cold dark matter and scalar metric perturbations, the transfer function in (1.37) is normalized as $T(k=0) = 1$. Therefore, it becomes a measure of how the primordial fluctuations $\tilde{\delta}_k^{(0)}$ have changed until a standardized late time. As mentioned, departures are expected because the density contrast is subject to different equations of motion depending on when a particular mode first started interacting with the gravitational potential and the other fluids. The transfer function depends primarily on how the scale k compares to the comoving Hubble size $\mathcal{H}^{-1}$ at the time of matter-radiation equality. For example, a currently large-k mode entered the horizon early during radiation domination and is subject to different evolution compared to small-k perturbations, which only become relevant during matter domination. Interactions with other species, such as dark energy or neutrinos, also affect the form of $T(k)$. Therefore, the transfer function can be used as a probe for physics on all scales.

The growth factor $D(a)$ from (1.37) is a universal proportionality factor for all modes relevant to structure formation. It describes the late-time evolution of the linear matter perturbations. It is only a function of Cosmology and has the following definition:

$$D(a) \propto \frac{H(a)}{H_0} \int_0^a da' \left[\frac{H_0}{a' H(a')}\right]^3, \tag{1.38}$$

It formalizes the qualitative discussion above on how the perturbations grow with the scale factor in the linear regime, but taking into account the full matter content, as illustrated in the Friedmann equation (1.19) with values from Table 1.2.

To summarize, equation (1.37) says that to linear order, we can use the transfer function to modify the primordial perturbations according to the sum of all interactions until late time, while the growth factor describes how cosmological evolution has driven each mode since.

Of course, it is possible to repeat the exercise and find a similar parametrization for radiation fluctuations or any other component. To make contact with observation for the matter distribution and the CMB, it is necessary to evolve the complete system of coupled partial differential equations, considering relativistic effects and allowing for spatially varying density perturbations and interactions between sectors in thermal equilibrium at various times. The latter is done by using a perturbed version of the Boltzmann equation. The full machinery of perturbation theory is well developed at this point [68], and in practice, so-called cosmological Boltzmann codes such as CAMB [69] or CLASS [70] are used to obtain numerical solutions. Confronting the output of these codes with experimental data has allowed us to build the precise present-day picture of our cosmological model.

For a multi-component Universe, if the matter density contrast has some spatial distribution at time t, and this is the same as the perturbation field of another component at a slightly different time $t + \delta t(\mathbf{r})$, it is said that the perturbations are adiabatic. The Poisson equation (1.31) illustrates this idea for matter density and curvature perturbations. It seems to be the case that all perturbations in the Universe are adiabatic [71]. Furthermore, on large scales, the linear matter power spectrum and the CMB are consistent with Gaussian initial conditions [72, 73]. This means that statistically, inhomogeneities in the cold dark matter distribution on large scales today are correlated with the anisotropies in the CMB, formed 13.7 billion years ago, and both of their power spectra are related to a primordial random Gaussian field.

Linear Matter Power Spectrum

The matter power spectrum describes the matter density contrast as a function of scale k. It is one of the most important tools in Cosmology, and the fact that various observational methods agree on the inferred shape and features in the power spectrum is an achievement of the ΛCDM model [74].

It is defined as the square of the density perturbation $\tilde{\delta}_k(a)$ defined in (1.37). We can

write it as:

$$\Delta^2(k,z) = \delta_H^2 \left(\frac{k}{H_0}\right)^{3+n} T^2(k,z) D^2(z), \tag{1.39}$$

where δ_H is a normalization factor equal to the amplitude of matter perturbations on the scale of the Hubble parameter today. n represents the initial power spectrum index. A perfectly scale-invariant initial power spectrum has $n = 1$, while n less than one is said to be red-tilted, and n slightly above 1 is blue-tilted.

We showed in (1.35) that the amplitude scales as $\delta_k \propto k^2$ for modes that become relevant during matter domination. Therefore, the power spectrum on those scales grows as follows:

$$k^3 P(k) \propto \delta_k^2, \tag{1.40}$$

which implies that

$$P(k) \propto k. \tag{1.41}$$

Similarly, if perturbations grow as $\delta_k \propto \ln k$ during radiation domination, the modes which were relevant at that time scale as

$$P(k) \propto k^{-3} \ln k^2. \tag{1.42}$$

Indeed, the linear matter power spectrum asymptotes to $P(k) \sim k^1$ for k small, and $P(k) \sim k^{-3} \ln k^2$ for large k, as predicted. The turning point where the two regimes meet corresponds roughly to the matter-radiation equality scale, $1/k_{\rm eq} \approx 100$Mpc. This is the size of the comoving Hubble horizon at $z_{\rm eq}$. Large scales with $k < k_{\rm eq}$ correspond to fluctuations that entered the horizon after $z_{\rm eq}$ during matter domination, while small scales $k > k_{\rm eq}$ correspond to modes which crossed during radiation domination. In Fig. 1.1, we show the linear and nonlinear matter power spectra corresponding to the best-fit Planck 2018 cosmological parameters [10]. The data was produced using CAMB [69].

There are many additional features in the matter power spectrum, all of which hold information about the dynamics that took place on different scales. For example, the modes that crossed the horizon before recombination show an oscillatory pattern. This is produced by baryon-photon sound waves known as the baryon-acoustic oscillations (BAO). They measure the characteristic scale of propagation of fluctuations in the baryon-photon fluid until decoupling. The BAO scale corresponds today to 100 Mpc and provides a standard ruler to measure cosmological parameters, and is also a dominant feature in the CMB.

Structures grow according to linear theory on large scales where the gravitational potential competes with the cosmic expansion, i.e. $k < k_{\rm eq}$. The power spectrum on these scales

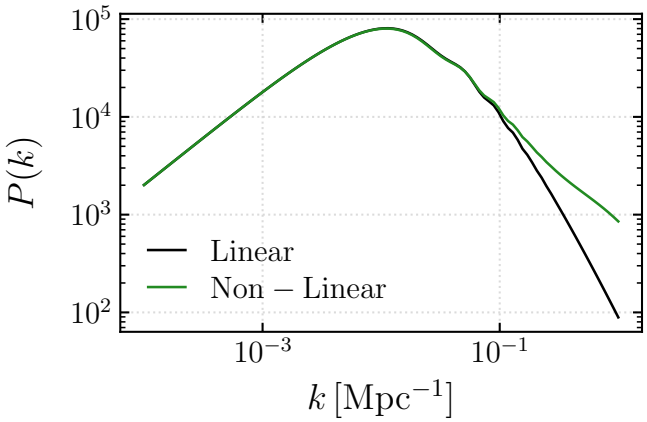

Figure 1.1: The matter power spectrum today. Modes k that crossed the horizon after matter-radiation equality follow $P(k) \propto k$. The modes which crossed before follow $P(k) \propto k^{-3} \ln k^2$. The peak corresponds to the scale at matter-radiation equality $k_{\mathrm{eq}} \approx 10^{-2}\mathrm{Mpc}^{-1}$. Also shown for comparison is the nonlinear matter power spectrum, calculated with CAMB [69]. Large scales agree with the linear approximation, but on small scales additional power is due to nonlinear collapse.

provides an important constraint on the non-Gaussianity present in the initial conditions. In the opposite limit, where gravitational collapse is strongly nonlinear, interactions introduce higher-order correlations in the matter distribution, and the linear approximation fails to reproduce the measured values. A comparison between the numerically obtained linear and nonlinear matter power spectra is shown in Fig. 1.1.

For completeness, we mention that perturbation theory can still be used to model the primordial contributions to higher-order functions of the matter distribution, such as the bispectrum, but only when including second-order corrections. To lowest order in perturbation theory, it is scale-free and time-independent. Schematically, it scales as the square of the power spectrum: $\mathcal{B}(k, k', k'') = \sum_{\mathrm{cyc}} f(k, k') P(k) P(k')$, where f depends weakly on Ω_m.

Large Scale Structure

The spherical collapse model was proposed as a simple framework to explain the formation of nonlinear structures on scales below k_{eq}. In this model, a region of space with an initially small but uniform density profile $\delta \ll 1$ within a finite region of space collapses under its

self-gravity in the presence of an expanding FLRW background. The differential equation governing the evolution of the perturbation is [60, 59]

$$\ddot{\delta} + 2H\dot{\delta} - \frac{4}{3}\frac{\dot{\delta}^2}{1+\delta} = \frac{3}{2}\Omega_{\rm m}(a)H^2\delta(1+\delta), \tag{1.43}$$

which linearized gives exactly the equation of motion for the matter density contrast during matter domination. A typical solution to the equation above initially grows until it reaches a maximum amplitude, then collapses to an infinite-density singularity. The turn-around value is independent of the mass inside the region but is a function of Cosmology. In our Universe, it is given by $\delta_c(z) \approx 1.68/D(z)$ and represents the critical overdensity at redshift z. If the density within a finite region is above this threshold, it will collapse despite the expansion. However, angular momentum prevents the formation of a singularity, and instead, the collapsed structure reaches a steady state where its kinetic and gravitational potential energies are equal. This equilibrium configuration represents a virialized spherical structure, termed a halo, with a finite radius – the virial radius. The overdensity at the boundary can be shown to be ≈ 178 times greater than the background $\bar{\rho}$. By convention, the boundary is sometimes defined at $200\bar{\rho}$, slightly below the virial radius scale. It is important to recognize that realistic collapse processes often deviate from spherical symmetry, and the estimation of the virial density is somewhat arbitrary. Nonetheless, this is a useful model in practice.

The spherical collapse model is the basis and precursor of a more sophisticated framework called the halo model [60, 59]. It is a statistical approach to model nonlinear structure formation and demonstrates good agreement with numerical results derived from simulations. It characterizes the dark matter field as a collection of halos. Baryonic matter, organized in the form of galaxies, populates the density profile of each sphere according to a halo occupation distribution function (HOD). This approach allows us to construct n-point functions to characterize the galaxy and matter distributions as a function of only two parameters: the redshift and mass of each halo at virialization. Other properties – such as the halo mass function (their number density distribution), the amplitude of the density profile per halo, and bias relative to the background density field – are studied using analytical models and numerical simulations. Halo-based calculations accurately reproduce the power spectra, while uncertainties in higher-order correlations largely stem from assumptions such as the spherical collapse model or the substructure model.

Over the years, many statistical tools have been developed to link theory and observation in Cosmology. As an example, it is well known that a Gaussian random field can be characterized by the properties of its maxima (or other extrema) [22, 75]. In particular, these maxima – or peaks – tend to be spatially correlated. Since the dark matter field is

Gaussian, its maxima represent regions with greater matter density. Therefore, there is a higher chance of collapse within these regions. So, peaks in the density field are expected to coincide with locations of galaxies. Therefore, measuring the abundance and clustering of galaxies is a proxy for the statistical properties of the underlying dark matter field. This observation forms the starting point for the study described in Chapter 2.

1.1.4 Anisotropies

The CMB is characterized by the temperature and polarization fluctuations imprinted on the background photon distribution from the last scattering surface. Their distribution depends not just on coordinates $(t, \mathbf{x})$ and energy E, but also on the direction of propagation $\hat{\mathbf{q}}$, i.e. momentum. A photon travelling in direction $\hat{\mathbf{q}}$ is observed in direction $\hat{\mathbf{n}} = -\hat{\mathbf{q}}$. By integrating the geodesic equation of a primordial photon along a line of sight, we can relate the observed CMB temperature anisotropies to the fluctuations at recombination. In the synchronous gauge, the fractional temperature perturbation is given by [65]:

$$\frac{\delta T}{T}(t_*, \hat{\mathbf{n}}) \equiv \Theta\left(t_*, \hat{\mathbf{n}}\right) \propto \left(\frac{1}{4}\frac{\delta\rho_\gamma}{\rho_\gamma} + \Phi\right)_* - \left(\hat{\mathbf{n}} \cdot \mathbf{v}_{e^-}\right)_* + \int_{t_*} \mathrm{d}t \left(\dot{\Phi} + \dot{\Psi}\right), \tag{1.44}$$

where '$*$' subscript denotes the time of last scattering – although note that not all photons in the CMB frequency range and temperature were scattered into our line of sight at the time of decoupling. Hence, this equation receives additional terms in its most general form. The first term is a function of the radiation energy density $\rho_\gamma \sim T^4$ at the last scattering surface. It is proportional to a blackbody. The second term, Φ, arises from the gravitational redshift that the photons experience when climbing out of a potential well at that time. The combination $\left(\frac{1}{4}\delta_\gamma + \Psi\right)$ is called the Sachs-Wolfe (SW) term. The next term is the relative Doppler shift between the photon – or equivalently the observer – and a matter particle moving with velocity $\mathbf{v}_{e^-}$, i.e. the motion of the electrons at the surface of last-scattering. The last term is the integrated Sachs-Wolfe (ISW) effect. Considering only contributions up to the surface of the last scattering, the ISW is subdominant, and the SW and Doppler terms mostly determine the shape of the power spectrum. All three terms in (1.44) can be thought of as small perturbations, which is why the CMB temperature fluctuations are treated as a linearized functional of the initial density perturbations δ_γ. The full solution is obtained numerically from general relativity and the full perturbed Boltzmann equation.

As the CMB is a two-dimensional spherical surface, the mathematics simplifies not in Fourier space but in multipole space. Projecting the fluctuations into spherical harmonics,

we find:

$$\Theta\left(\chi,\hat{n}\right)=\sum_{\ell=0}^{\infty}\sum_{m=-\ell}^{+\ell}a_{\ell m}(\chi)Y_{\ell m}(\hat{n}),\quad a_{\ell m}=\int\mathrm{d}^2\hat{n}\,\Theta\left(\chi,\hat{n}\right)Y^*_{\ell m}(\hat{n}),\tag{1.45}$$

where we chose to parametrize as a function of comoving distance χ instead of conformal time to last scattering. Statistical isotropy implies that correlation functions on the sky are only a function of the angular separation $\hat{n}_1\cdot\hat{n}_2=\cos\theta$. Therefore, the power spectrum is

$$\langle\Theta(\hat{n}_1)\Theta(\hat{n}_2)\rangle=C(\theta),\tag{1.46}$$

or, in multipole space

$$\langle a_{\ell m}a^*_{\ell' m'}\rangle=C_\ell\,\delta_{\ell\ell'}\delta_{mm'},\tag{1.47}$$

where $\delta_{\ell\ell'}$ is the Kronecker delta function and C_ℓ is known as the angular power spectrum. The real and angular two-point functions are related by

$$C(\theta)=\sum_\ell\frac{2\ell+1}{4\pi}\,C_\ell\,\mathcal{P}_\ell(\cos\theta),\tag{1.48}$$

where $\mathcal{P}_\ell$ is a Legendre polynomial. The power spectrum is then again related to the initial conditions $\tilde{\delta}^{(0)}_k$ as

$$C_\ell=\int\mathrm{d}k\,T^2_\ell(k)|\tilde{\delta}^{(0)}_k|^2\equiv\int\mathrm{d}k\,T^2_\ell(k)P^{(0)}(k),\tag{1.49}$$

where the radiation transfer function captures both the evolution of the fluctuations in the primordial plasma and the projection of the anisotropies onto the sky.

The temperature auto-power spectrum produced using CAMB [69] is illustrated in Fig. 1.2 for the Planck 2018 best-fit Cosmology [10]. Below, we give qualitative explanations for the processes that give rise to the main features in the CMB angular power spectrum, relating to the master equation that determines its phenomenology (1.44).

The SW term represents the balance between the intrinsic temperature fluctuation at last scattering and gravitational redshift. Decoupling occurs during matter domination, where the potentials satisfy $\Phi=\Psi$ and are constant in time. According to the relativistic Poisson equation, we have $-\Phi\propto\delta_b,\delta_\gamma$ on large scales where SW dominates. This means over-densities where $\delta_\gamma>0$ correspond to under-densities in $\Phi<0$. Redshifting out of these potential wells leads to cold spots in the CMB map $\Theta<0$. Conversely, hot spots correspond to under-densities at last scattering.

Thomson scattering is the dominant scattering effect around the time and energy scale of decoupling. This is a fully elastic interaction between photons and free electrons in the

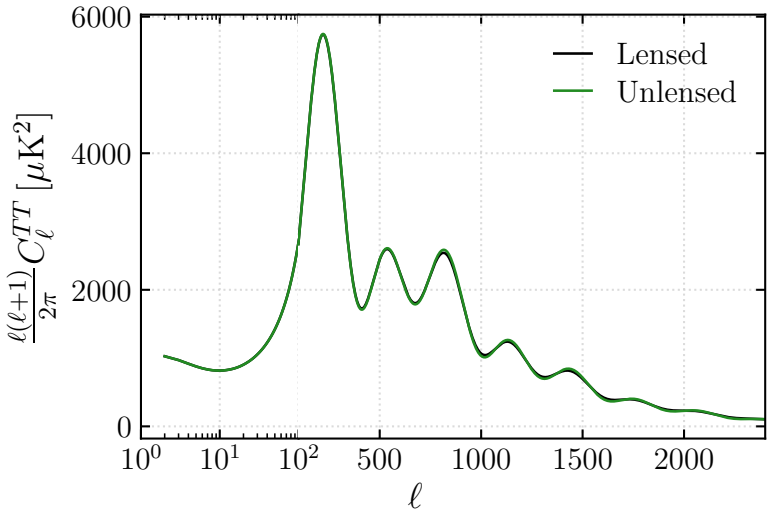

Figure 1.2: The CMB temperature angular power-spectrum obtained from CAMB [69]. The dominant features are the peaks sourced by acoustic oscillations. Due to Silk damping, these attenuate on small scales $\ell > 1000$. On the largest scales where $\ell < 30$, we see the Sachs-Wolfe plateau. We illustrate the lensed and unlensed spectra to showcase the magnitude of the effect on the primary CMB of an important source of secondary anisotropies.

plasma. It does not change the energy of photons, only their momentum, which leads to the Doppler distortion above. For an isotropic and initially unpolarized photon flux, the differential Thomson cross-section averaged over the outgoing polarization is proportional to the Thomson cross-section $\sigma_T \approx 6.65 \times 10^{-29}\,\mathrm{m}^2$ and depends on the inverse of the electron mass. Scattering with protons and neutrons can be ignored since $m_{e^-} \ll m_p$. The quantity $\Gamma \equiv a\bar{n}_{e^-}\sigma_T$ is the Thomson scattering interaction rate function of scale factor, where n_{e^-} is the number density of free electrons. Its inverse is proportional to the mean free path of CMB photons. Thomson scattering at the surface of last scattering also induces a small polarization in the CMB radiation field [76].

The ISW term models the redshift due to the time-varying gravitational potentials along the line-of-sight between emission and until observation. As mentioned, the two terms are equal and constant during matter domination, so the ISW term vanishes. During radiation domination, the oscillating radiation density induces a non-zero fluctuating potential. This is called the early ISW effect. At late times, once dark energy begins to dominate, it sources once again time-varying Φ and Ψ fields. This leads to the late ISW effect that adds power to the CMB spectrum on the largest scales.

The angular variations in the CMB power spectrum result from the dynamics of sound waves in the photon-baryon fluid. The sound horizon r^s is defined as the product between the speed of sound in the plasma and conformal time: $r^s \simeq c^s\eta$. Photon fluctuations in the early Universe remain constant until they cross the sound horizon, then oscillate in the plasma. These oscillations are captured in the CMB angular power spectrum at the last scattering, which fixes r^s_*. The positions of the peaks in the CMB spectrum depend on the projected size of the maxima in these oscillations, characterized by the harmonic series $k_n = n\pi/r^s_*$ with $n = 1, 2, \ldots$. Cosmological parameters control these scales. For example, the relative ratio between matter contents Ω_b and Ω_c can dampen or drive the oscillations, changing the relative peak amplitudes. Also, the curvature parameter Ω_κ influences the relationship between angular scale and distance between an observer and the surface of last scattering. Thus, the CMB has provided the most substantial proof for CDM – a component of matter that does not react electromagnetically — and that the Universe is flat. On scales larger than the first acoustic peak, the photon perturbations never entered their sound horizon and have remained constant. The CMB on these scales is a direct probe of the characteristics of the primordial power spectrum. We develop this in the next section.

The coupling strength between electrons and photons depends on the balance between the Thomson cross-section and the mean free path between electrons. At early times, when the separation between particles is small, photons scatter efficiently, and the photon baryon fluid is said to be in a tight coupling regime. Around the end of recombination, the

ionization fraction n_{e^-}/n_b drops, and the Thomson interaction rate Γ^{-1} is comparable to the electron mean free path. This effect dampens small-scale fluctuations, where $k \gtrsim 2\pi\Gamma_*$. For the modes in this regime, the transfer function receives an exponential suppression called Silk or diffusion damping.

As mentioned several times in this text, CMB phenomenology has provided a highly accurate probe of our cosmological model. In the paragraphs below, we summarize a few promising directions of interest for the future of CMB science.

The monopole or spectral distribution was measured by the FIRAS instrument on the COBE satellite [77] to follow a nearly perfect blackbody with a current temperature $\bar{T}_{\rm CMB} = 2.725$ K and a peak blackbody frequency of 160.4 GHz. The blackbody nature is explained by the fact that during most of their history before the last scattering, photons were in thermal equilibrium and obeyed Maxwell-Boltzmann statistics. Deviations from the blackbody are termed spectral distortions and are expected to occur in any process that changes the photon energy, e.g. inelastic scattering or interactions away from thermal equilibrium. These can be used as probes for the physics of recombination but also physics BSM [78, 79, 80] – for example as a probe of primordial non-Gaussianity, alternative models for dark matter, primordial black holes, and, as we discuss in Chapters 4 and 5, to search for hidden-sector particles.

The *primary* CMB anisotropies originate directly from the conditions present at the surface of last scattering. The sum of all fluctuations or modulations that appeared since the last scattering and are due to the intervening structure are called *secondary* anisotropies. A significant source of secondary anisotropies is the Sunyaev-Zel'dovich (SZ) effect due to the interaction of photons with free electrons since reionization. Another example is lensing, where gravitational potentials of collapsed LSS change the propagation direction of CMB photons. Both of these secondaries modify the CMB power spectrum in a deterministic way and are correlated with LSS. The changes on the CMB power spectrum caused by secondaries are typically orders of magnitude less than its peak amplitude. However, they can significantly modify the signal on small scales of order $\ell \gg 1000$ – as illustrated in Fig. 1.2. Improving precision on small scales is a central focus of future CMB experiments. These hold valuable information about the initial conditions and the formation and growth of structure [81, 82, 83, 84, 85, 86, 87, 88].

Polarization is generated through the anisotropic scattering of the radiation field. It is typically decomposed into zero curl (E-modes) and zero divergence (B-modes) components. The first category can be used as a probe for the distribution of charged electrons in the late Universe and for measuring the primordial scalar power spectrum. The second category is only produced by parity-violating processes. Scalar density fluctuations can not create such

modes; however, tensor metric fluctuations can. These can be sourced by astrophysics (e.g. gravitational lensing produces B-modes on small scales), or by primordial gravitational waves, which may generate B-modes on the largest scales. Studying the polarization background is another key focus of next-generation CMB experiments. Measuring B-modes is a primary goal, as they can reveal the energy scale of inflation and place significant constraints on the physics driving it [89, 71].

1.1.5 Inflation

Several open questions come from the cosmological picture we have derived so far:

- In the first part of this section, we explained that 13.8 billion years ago, the observed Universe started from a nearly flat, homogeneous, isotropic radiation-dominated state. How did this state originate?
- Inhomogeneities in both the matter and radiation distribution are adiabatic, meaning they are related to the same primordial perturbations. Indirect measurements are consistent with a Gaussian distribution and a nearly scale-invariant power spectrum, with a slight preference for long wavelength fluctuations, i.e. negative tilt. What sourced these specific initial conditions?
- Across the Hubble horizon, the CMB has the same blackbody temperature. An expansion history based on radiation and matter domination alone can not explain this. Given the measured cosmological parameters, the age of our Universe and the estimated age at decoupling imply that patches on the sky with angular size greater than 1° would have never been in causal contact. How did these regions thermalize?

Inflation is a simple mechanism developed to answer these questions [90, 91, 92, 93, 94, 95]. Through the years, it has suffered many iterations, and to date, it is the preferred paradigm that explains the origin of the hot Universe. In many models, it is realized through a phase transition – we come back to this point later when introducing vacuum decay. Although alternatives to it exist, they require additional assumptions and have yet to gain much momentum in comparison.

Inflation represents a period of exponential growth of the scale factor – similar to a dark energy-dominated era – that took place before the radiation-dominated epoch. In the simplest model, it is realized by a single scalar field – the inflaton – evolving in a non-linear potential. The inflaton lies initially in a metastable vacuum, where it exhibits fluctuations

associated with its zero-point energy. As it evolves in time, it rolls down a positive and nearly flat potential, slowly accelerating as potential energy is exchanged for kinetic. As it relaxes, the inflaton sources an energy-momentum tensor that drives a cosmic period of exponential expansion.

In the same way that $\rho_\Lambda \propto a^0$ dominates the energy density at late times, inflation quickly dilutes any other existing components besides the inflaton field. During this period, $H \approx$ constant, while the volume increases by a factor of $e^{H\delta t} \approx e^{100}$. The temperature decreases by the inverse amount. The exponential expansion ensures that the final state is virtually independent of the properties of the initial state while also preserving the fact that all particles currently within our comoving Hubble volume have been in causal contact.

The inflaton dynamics is fully determined by the shape of the potential it evolves under. In single field inflation, the inflaton only couples to Einstein gravity:

$$S = \int \mathrm{d}^4x\sqrt{-g}\left[\frac{M_{\mathrm{pl}}^2}{2}R - \frac{1}{2}g^{\mu\nu}\partial_\mu\varphi\partial_\nu\varphi - V(\varphi)\right], \tag{1.50}$$

where $g_{\mu\nu}$ is the metric, R the Ricci curvature and g is the metric determinant. The primordial state before inflation is unknown, but in general, it could not have been above the Planck scale, beyond which quantum gravity effects become important. The first term in the action above symbolizes the energy density associated with the spacetime curvature at the Planck scale.

Inflation ends naturally when the potential energy is below the kinetic energy, as the expansion time becomes longer than the oscillation period of the field around the minimum of the potential, i.e. $H^{-1} \gg m_\varphi^{-1}$, where the curvature of the potential gives the inflaton mass m_φ at a point. The equation of state evolves into that for pressureless matter. At this stage, the inflaton is coupled to the standard model particles. Reheating is the process by which the potential energy that is used to drive the expansion is converted into SM particles [96]. The inverse reaction is frozen out. The new, lighter particles reach thermal equilibrium to form the primordial plasma, and the radiation-dominated era begins.

Primordial Power Spectrum

We can write the inflaton field as the sum of a classical background and the vacuum fluctuations:

$$\varphi = \bar{\varphi} + \delta\varphi, \tag{1.51}$$

where φ is the inflaton field, $\bar{\varphi}$ stands for its mean (or classical expectation value) and $\delta\varphi$ represents the quantum fluctuations. For the free vacuum state, $\delta\varphi$ fluctuations are, by

definition, Gaussian and certainly in the perturbative regime. As the background expands, it can be shown that they evolve with an amplitude proportional to the Hubble parameter:

$$\langle \delta\tilde{\varphi}_k \delta\tilde{\varphi}_{k'} \rangle = (2\pi)^3 \delta^3 (\mathbf{k} + \mathbf{k}') \frac{H^2}{2k^3}, \tag{1.52}$$

where $H \approx$ constant during inflation. This means that the amplitude of the inflaton perturbations is the same on every scale. In a suitable choice of gauge, the scalar curvature fluctuations can be related to the fluctuations in the inflaton field to show that (1.52) produces a scale-invariant power spectrum [65].

The CMB constrains the primordial power spectrum for scalar metric fluctuations to be nearly scale-invariant, consistent with the above prediction. Such a power spectrum can be parametrized as:

$$P^{(0)}(k) \equiv A_s \left(\frac{k}{k_*} \right)^{n_s - 1}, \tag{1.53}$$

The parameters n_s and A_s are the scalar spectral index and the amplitude of scalar fluctuations when the pivot scale k_* is fixed. A similar expression can be derived for tensor fluctuations $\propto A_T \, (k/k_*)^{n_T}$ that are produced if the inflaton couples to tensor metric perturbations. The tensor-to-scalar ratio is defined as $r = A_T/A_s$ and, together with n_s and A_s, they represent standard cosmological parameters that describe the initial conditions. All of them are related to the shape of the inflaton potential $V(\varphi)$. The best constraints on their values come from *Planck* satellite data and are $n_s = 0.965$, $\ln(10^{10} A_s) = 3.047$ and $r < 0.11$ when $k_* = 0.002 \text{Mpc}^{-1}$ [10, 71]. The measured values of these parameters help to greatly constrain the enormous parameter space spanned by theories of inflation: from deformations of $V(\varphi)$ to introducing additional fields and interactions in the inflaton action.

1.1.6 The Hidden Sector

Searching for a comprehensive understanding of the evolution of the Universe and its fundamental constituents, the limitations of the SM have become increasingly apparent over the years. Although it successfully describes the known fundamental particles and their interactions, several key phenomena remain unexplained, such as the origin of the initial conditions, the nature of dark matter and dark energy, or the quantum origin of gravity. A wide range of solutions have been put forward to fill the gaps – an example of which is inflation. The 'hidden' or 'dark' sector is an umbrella term for the collection of hypothetical particles – such as inflaton candidates – and new gauge symmetries that arise

in these models. So far, direct experimental evidence for hidden particles remains elusive, meaning they interact weakly, if at all, with the known SM. Two compelling candidates of particles in the dark sector are the dark photon and the axion, which we describe below [97, 98, 99].

The Dark Photon

The dark photon is a hypothetical vector boson that arises in various extensions of the SM [99, 100, 101, 102, 103, 104]. We label the dark photon field by A'. It couples to the SM electric charge gauge group via a kinetic mixing term [105, 106]:

$$\mathcal{L} \supset -\frac{\varepsilon}{2} F_{\mu\nu} F'^{\mu\nu} - \frac{m_{\mathrm{A}'}^2}{2} \mathrm{A}'_{\mu} \mathrm{A}'^{\mu}, \tag{1.54}$$

where $F_{\mu\nu}$ and $F'^{\mu\nu}$ are the SM photon and dark photon field strength tensors, respectively. Dark photons may have a small, non-zero mass $m_{\mathrm{A}'}$, which sources the second term above. Both $m_{\mathrm{A}'}$ and the coupling constant ε are free parameters. In the BSM models that predict a kinetic mixing coupling, the dark photon is the main carrier of interactions among the dark sector states, i.e. it forms an independent U(1) gauge symmetry. The existence of a mass term would imply finite-range forces within the dark sector. For this reason, the dark photon is referred to as a mediator with the dark sector.

A substantial portion of the parameter space of the dark photon has been probed. In the massless case, collider physics and Big Bang Nucleosynthesis has placed important bounds on the massless photon [97, 107, 108]. In the massive case, for keV and higher masses, strong bounds come from supernovae [109], dark matter direct detection efforts, or collider and experimental constraints on lepton decays [110, 97]. However, a region in the parameter space is still largely unexplored, corresponding to scales that are only accessible through cosmological or astrophysical tests and ultra-light masses. An illustration of the parameter space for the dark photon is shown in Fig. 1.3a, with data from [16]. Past and ongoing efforts to probe ultra-light dark photons include tests of superradiance [111, 112, 113, 114, 115], cosmological evolution [116, 117, 118, 119] and stellar objects [120, 121, 122], as well as lab searches [123, 124, 125, 126, 127]. Chapter 4 offers a new method to search within this particular region.

The Axion

The axion is a pseudo-scalar (spin-0) boson, denoted by a. BSM models predict that below the scale of EW symmetry breaking, the axion couples to gauge fields and fermions ψ (both

leptons and hadrons). A typical Lagrangian reads [65]:

$$\mathcal{L} \supset g_{\mathrm{a}\gamma\gamma}\, \mathrm{a}\, F^{\mu\nu}\tilde{F}_{\mu\nu} + g_{\mathrm{a}\psi}\, \partial_\mu \mathrm{a}\, \bar{\psi}\gamma^\mu\gamma_5\psi + g_{\mathrm{a}GG}\, \mathrm{a}\, G_{\mu\nu}\tilde{G}^{\mu\nu}. \tag{1.55}$$

Each operator has dimension five. $F_{\mu\nu}$ and $G_{\mu\nu}$ represent the photon and gluon field tensors, while $\tilde{F}_{\mu\nu}$ and $\tilde{G}_{\mu\nu}$ are their duals. The form of this Lagrangian is tied to the resolution of the strong CP problem in QCD [128, 129, 130, 131]. This problem arises from the absence of observable violation of CP symmetry in QCD, which is not in line with theoretical expectations. Axions arise from a field that dynamically adjusts to cancel CP-violating contributions from QCD.

Axions can be produced in abundance during phase transitions associated with GUTs [128, 129, 130, 131, 132, 99]. Similar to the Higgs field, they are created by spontaneously breaking additional global symmetries. String theory also predicts the existence of ultra-light ALP's, spanning a wide range of masses down to the Hubble scale [99]. In this context, axion fields arise from the topological complexity of multi-dimensional manifolds. The compactification of the extra dimensions leads to effective potentials for the scalar degrees of freedom – axions – that can also drive an inflationary period. Axion phenomenology is characterized by derivative couplings, such as the one with fermions in (1.55). They can have small non-zero mass terms m_{a}. If the requirement to solve the strong CP problem is waived, one can drop the gluon coupling $g_{\mathrm{a}GG}$ in the Lagrangian and describe an axion-like particle (ALP). Misalignment [133, 98, 134] is the proposed mechanism for axion particle production: random quantum fluctuations in the axion field $\delta\varphi^a(x^\mu)$ settle at different amplitudes away from the global potential minimum at the end of inflation. As the Universe expands and cools, the 'misaligned' fields oscillate and produce axion dark matter particles. Their abundance depends on the initial misalignment angle and the energy scale of inflation. In many allowed ALP models, axions can make up all of dark matter [135].

Upcoming astrophysical experiments aim to explore the vast parameter space for axions and ALP's [136, 16]. Depending on their specific mass range, ultra-light ALPs are expected to manifest observable effects in different astrophysical phenomena [99]. An illustration of the available parameters space and typical constraints for each decade in mass is shown in Fig. 1.3b. For instance, axions with masses below 10^{-33}eV would act as the cosmological constant. Axions with masses between 10^{-33}eV to 10^{-28}eV could induce a constant rotation of the CMB (CMB) polarization called birefringence, while those within the range 10^{-28}eV to 10^{-18}eV could produce features in the matter power spectrum, observable through galaxy surveys and are termed 'fuzzy dark matter'. Axions in the mass range 10^{-22}eV to 10^{-10}eV can cause superradiance, which affects the dynamics and gravitational wave emission of rapidly rotating astrophysical black holes [99]. Other astrophysical constraints on low mass axions arise from scenarios where axions sourced by stars [137]

or supernovae [138] are converted to photons in the galactic magnetic field or the inverse process where background astrophysical photons are converted in extragalactic magnetic fields [139]. We propose a new method to observe axions in the $10^{-13} - 10^{-11}$eV range using the CMB and distribution of LSS in Chapter 5.

1.2 Relativistic First-Order Phase Transitions

False vacuum decay occurs in field theories with an associated potential with two non-degenerate vacuum states. Given a large region of space localized around the false minimum, the system wants to minimize its energy and make the transition into the true vacuum. There are several ways it can do so. For example, the barrier can be overcome if an external input of energy is provided. Alternatively, the field can experience fluctuations that may trigger the decay themselves. Of interest are fluctuations at finite temperature or, in lack of a thermal bath, the fluctuations sourced by the quantum vacuum state. Eventually, locally, a finite region of the field will cross the potential barrier towards the true minimum. In order to compensate for the change in energy density, a boundary layer is created called the bubble wall. In time, bubbles materialize throughout the whole available space, and as they expand and collide, they undergo all kinds of dynamics dictated by the shape of the underlying potential. The phase transition ends when the state of the field across the entire volume is localized around the true vacuum.

Vacuum decay is an important phenomenon with a wide range of cosmic implications. In the context of inflation, false vacuum decay was the original mechanism by which inflation was proposed to end [90]. However, it was quickly realized [91] that the phase transition from an inflating false vacuum to a non-inflating true vacuum can not be complete unless the epoch of inflation is exceedingly short. Instead, inflation becomes eternal, only ending locally inside isolated clusters of true vacuum bubbles (for a review, see e.g. [140, 141]). In string theory, our observable Universe is thought to reside inside one such bubble. The rare collisions between bubbles could provide observable evidence for this scenario [142, 143, 144]. In the late Universe (e.g. after inflation), first-order phase transitions can occur in models of baryogenesis [145, 146], string theory [147, 148, 149], grand-unified theories [150, 151], supersymmetry [152, 153], and even dark energy [154, 155].

A subset of these phase transitions can produce stochastic gravitational waves (GW) observable by gravitational wave detectors; see e.g. [56] for a review. A first measurement of stochastic GW has been made recently using Pulsar Timing Arrays [57]. It is known that by-products of vacuum decay in early-Universe first-order phase transitions could source a primordial component of this signal. In the original idea, electroweak baryogenesis could

occur via a first-order phase transition, and primordial GW with measurable amplitude today could be produced [156, 157]. A stochastic GW background could be observable in the future with LISA [158].

Further motivation to study vacuum decay is given by evidence that the current Higgs vacuum could be metastable [159, 160, 161].

Vacuum decay is most frequently described in the literature using Euclidean instanton methods. It can occur at zero temperature via quantum tunneling [17, 18], at finite temperature due to thermal fluctuations [19, 20], or more generally from an excited state above the false vacuum [162]. First developed by Coleman, instanton methods have been the status quo for studies of vacuum decay ever since. In this framework, one obtains a semi-classical approximation for the decay rate by solving the field equations of motion in imaginary time and imposing $O(d+1)$ symmetry on the resulting solutions, which describe the bubble nucleation event. This symmetry assumption is invalidated in cosmologically relevant scenarios involving dynamical and inhomogeneous spacetimes.

Furthermore, to interpret the instanton in real time, additional assumptions are required. For example, the critical bubble is said to appear at some instant in time, out of the vacuum fluctuations via a tunneling event, and with a finite size. It is not possible to study the precursor of such an event in terms of real-time field dynamics. However, ultimately, it is precisely dynamical evolution that is required to connect with observables.

The Instanton Formalism

In particle physics, typical problems involve finding scattering cross-sections and transition amplitudes or calculating energy level shifts in an evolving classical background. These problems can be solved in QFT by applying perturbation theory. The result of a perturbative calculation is typically a power series in some small coupling parameter, such as a coupling constant g. On the other hand, non-perturbative effects typically look like $e^{-A/g}$, where A is a constant. Such terms are invisible in perturbation theory because the terms in the Taylor expansion of an exponential around $g = 0$ are zero. Instantons are examples of such solutions: they represent non-trivial saddle-point solutions to Euclidean path integrals with finite action. Methods to find the instanton solution are considered generalizations of the WKB approximation generalized to infinitely many degrees of freedom. Below, we illustrate the concepts and techniques used in these calculations by focusing on the pioneering paper by Coleman [163].

Consider a $1+1$-dimensional scalar field theory with Lagrangian density

$$\mathcal{L} = \frac{1}{2}\left(\partial_t \phi\right)^2 - \frac{1}{2}\left(\partial_x \phi\right)^2 - V(\phi). \tag{1.56}$$

In QFT, the vacuum state is defined as the state with the lowest energy, associated with the global minimum of a potential $V(\phi)$. We will be focused on potentials $V(\varphi)$ with a high-energy 'false' vacuum separated by a barrier from a low-energy 'true' vacuum. The form of the potential is otherwise arbitrary, although for specificity in this Thesis, we focus on a fiducial potential $V(\phi)$ with the form:

$$V(\phi) = V_0 \left[-\cos\left(\frac{\phi}{\phi_0}\right) + \frac{\lambda^2}{2}\sin^2\left(\frac{\phi}{\phi_0}\right)\right]. \tag{1.57}$$

This is shown in Fig 1.4. Note that in 1+1 dimensions, ϕ is dimensionless and $V(\phi)$ has mass dimension two. The parameter λ modulates the depth of the false-vacuum potential well such that if $\lambda > 1$, the potential has an infinite periodic sequence of false minima at $\phi_{\rm fv} = (2n+1)\pi\phi_0$, alternating with true minima at $\phi_{\rm tv} = 2n\pi\phi_0, n \in \mathbb{Z}$. The field is initialized around the false vacuum located at $\phi_{\rm fv} = \pi$ and can decay to the stable configuration on either side – $\phi_{\rm tv} = 0$ or 2π. In a classical theory, the false vacuum is stable. In a quantum theory, barrier penetration is allowed, making the local minimum unstable.

This form of the potential is motivated by proposals to simulate vacuum decay with cold atom experiments [164, 165, 39, 41, 38]. Our results are relevant to this program but can be generalized to any potential with multiple vacuum states.

The path integral describing the probability of the state initially in the false vacuum to transition into the true vacuum after a time t is given by:

$$\left\langle \phi_{\rm tv} \left| e^{iHt/\hbar} \right| \phi_{\rm fv} \right\rangle \approx \int_{\phi_{\rm fv}(0)}^{\phi_{\rm fv}(t)} \mathcal{D}\phi \; e^{iS[\phi]/\hbar}, \tag{1.58}$$

where the integrand $\mathcal{D}\phi$ is over all possible field configurations satisfying the boundary conditions. The propagator is highly oscillatory, which makes this problem seem intractable. The solution is analytic continuation into Euclidean space by converting to an imaginary time variable defined as $\tau = it$. The Euclidean action is given by

$$S_E[\phi] = \int \mathrm{d}\tau \, \mathrm{d}x \left[\frac{1}{2}\left(\partial_\tau \phi\right)^2 + \frac{1}{2}(\partial_x \phi)^2 + V(\phi)\right]. \tag{1.59}$$

The solution to the Euclidean equations of motion with the highest contribution to the path integral has been coined 'the bounce'. To calculate it, we take the saddle points solution

with maximal symmetry, known as the instanton. These are trajectories that satisfy the Euclidean equations of motion $(\partial_\tau^2 + \partial_x^2)\,\phi = -V'(\phi)$. It is assumed that contributions from fluctuations around the instanton are vanishingly small.

In order to describe the $O(2)$-dimensional solution, it is convenient to define the coordinate $\rho^2 = \tau^2 + x^2$. The equation of motion becomes

$$\frac{\mathrm{d}^2\phi}{\mathrm{d}\rho^2} + \frac{d-1}{\rho}\frac{\mathrm{d}\phi}{\mathrm{d}\rho} = V'(\phi), \tag{1.60}$$

where d is the number of spatial dimensions, here $d = 1$. The boundary condition $\lim_{\rho\to\infty}\phi(\rho) = \phi_{\mathrm{fv}}$ ensures that the end state is always the false vacuum. We also impose $\partial_\rho\phi \to 0$ to avoid a singularity when $\rho \to 0$. The equation (1.60) can be solved numerically. The solution describes a particle evolving in an inverted potential, which starts near the true vacuum, then rolls down against a time-dependent friction term and settles precisely at the false vacuum $\phi_{\mathrm{fv}} = \pi$. An illustration of the inverted potential is shown in Fig 1.5, along with example solutions for two choices of λ.

Reverting to real time, we can envision this solution as the spatial profile of a critical bubble at some initial time $t = 0$. The instanton is interpreted as the outcome of a tunneling event where a bubble with a finite radius has appeared on top of the background false vacuum field. Inside the bubble, the field is localized around $\phi_{\mathrm{tv}} = 2\pi$. The region where ϕ changes rapidly with increasing ρ, interpolating between the two states, is called the bubble wall. It can be seen from Fig 1.5 that a larger value of λ corresponds to a smaller difference between energy densities of the relative vacua, giving rise to a thinner wall.

Two forces are competing on the bubble boundary. On one hand, the energy density in the true vacuum exerts pressure on the wall proportional to the volume of the bubble. On the other hand, there is a pressure term pointing inwards due to the tension in the wall from the higher-energy false vacuum state. In order to prevent collapse, bubbles must materialize with a radius above some critical threshold, function of the shape of the potential. Starting from this configuration, the walls then expand with constant acceleration, converting the surplus energy of the false vacuum to drive the expansion.

Considering the path integral expression again, since the potential $V(\phi_{\mathrm{fv}})$ is not the global minimum, the true vacuum has an associated energy state below the zero-point eigenstate E_0 set by the false vacuum. In practice, the presence of such an eigenmode signals the instability of the solution towards growth (or shrinkage), as in the case of the critical bubble. In the instanton formulation, this determines an imaginary part to the

false vacuum energy E_0, and hence the existence of a decay width:

$$\Gamma = -2 \operatorname{Im} E_0. \tag{1.61}$$

To first order in $\hbar$, it can be shown that this is given by the expression

$$\Gamma/V \sim A\, e^{-B/\hbar}, \tag{1.62}$$

where $B \equiv S_E$ is the bounce action, and the proportionality factor A is calculated from fluctuations around the saddle-point solution. Translational invariance results in a state with zero eigenvalue termed the 'zero mode', which motivates adding the volume factor V. This is the decay rate of the false vacuum. Together with the bubble profile, they are the two main observables of instanton theory.

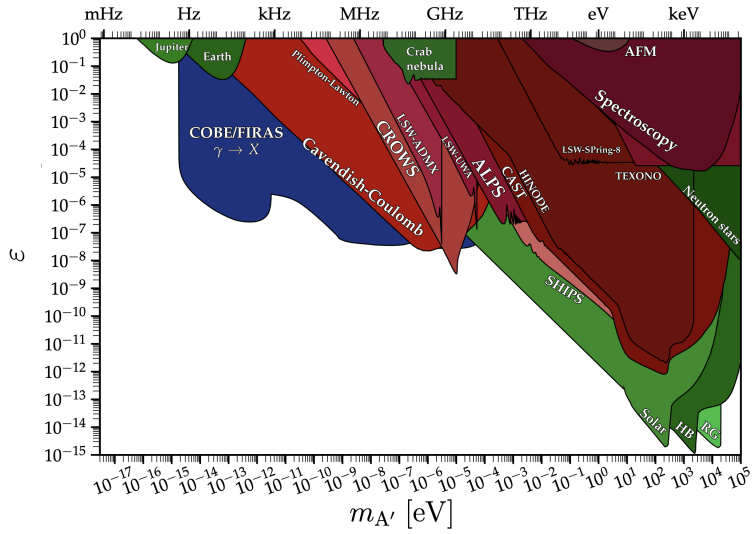

(a) Combined current limits on the coupling between light dark photons and SM photons, denoted by ε.

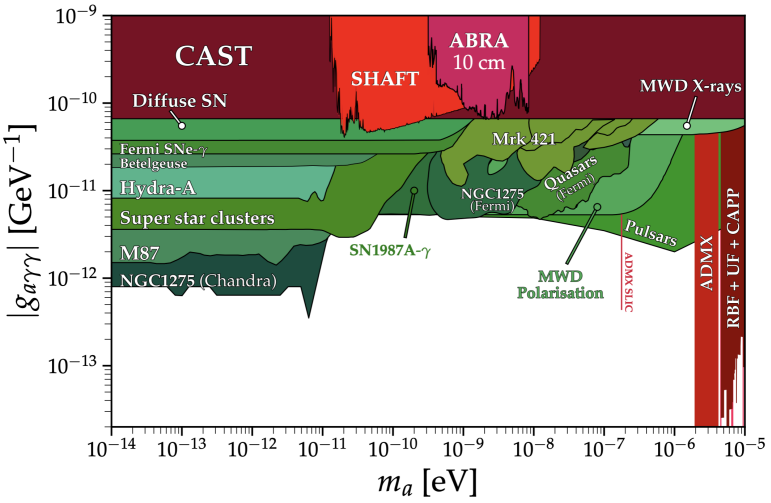

(b) Combined current limits on light axions coupling to SM photons, denoted by $g_{a\gamma\gamma}$.

Figure 1.3: We show a part of the parameter space of the processes highlighted in Section 1.1.6. The contours show the present bounds on the couplings between SM photons and hidden-sector candidates. Those shown in red come from laboratory probes, astrophysical bounds are shown in green, and blue depicts constraints from the CMB. Notice that within the mass ranges shown, much of the area is still unexplored (shown in white). Figures taken from [16].

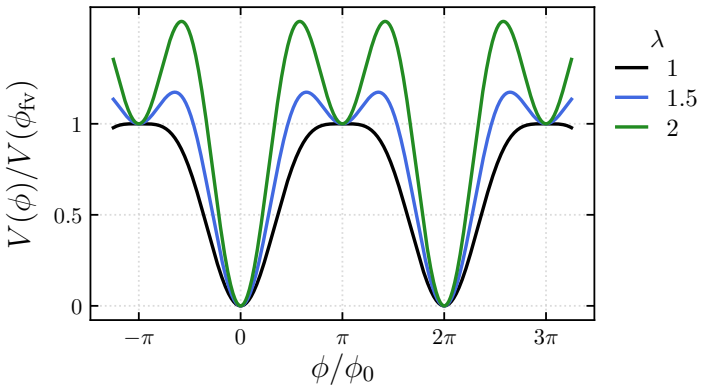

Figure 1.4: The potential $V(\phi)$ we chose to study vacuum decay throughout this Thesis. The parameter λ modulates the shape of the potential around the local minimum and the depth of the barrier. When the parameter $\lambda > 1$, the potential $V(\varphi)$ supports the formation of bubbles. It acquires an infinite sequence of local minima at $\varphi_{\rm fv} = (2n+1)\pi\varphi_0$ alternating with global minima at $\varphi_{\rm tv} = 2n\pi\varphi_0, n \in \mathbb{Z}$. If the field begins in the false vacuum, then through quantum mechanical or thermal effects, bubbles containing the true vacuum phase will form, expand, and coalesce - this is false vacuum decay.

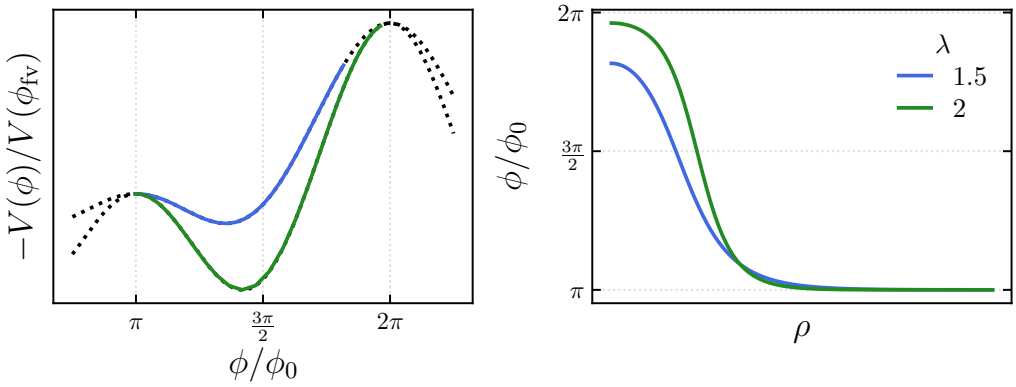

Figure 1.5: Left: The inverted potential which sources the equation of motion (1.60) for two values of coupling λ. The Euclidean solution describes a particle that starts at the false vacuum and then rolls towards the true vacuum against a time-dependent drag. On the right: The instanton solutions. Going back to real time, and setting the time coordinate to zero, this profile is interpreted as the spatial profile of a bubble which has just materialized out of the false vacuum.

Part I

New Dynamical Observables in First-Order Phase Transitions

Summary of Part I

In Chapter 2 we introduce the first new dynamical observable of vacuum decay: the presence of a two-point correlation function in the distribution of bubble nucleation sites – a measure of clustering. First, we set up the field theory of a scalar field in a Minkowski vacuum and explain how false vacuum decay arises from semi-classical evolution. Next, Gaussian peak theory is reviewed in one spatial dimension. Using empirical observations from our simulations, we then argue that bubbles form around peaks in the field and define the relevant estimator for the two-point function. We present our results and compare them with the free field theoretical prediction, showing qualitative agreement. We finish by discussing the implications of this result for bubble collisions and associated cosmological observables.

In Chapter 3 we turn to the case of a metastable scalar field at finite-temperature and introduce two additional new observables: the distribution centre-of-mass velocities in bubbles at nucleation and the oscillon precursor. First we give an overview of the Euclidean instanton description for vacuum decay at finite temperature, and the properties of the critical bubble solution. Next, we describe in detail the computational methods that were used to extract these observables. We discuss the role of fluctuations in thermalization and show how the theory parameters such as the effective temperature and field mass evolve in time around the false vacuum. We measure the decay rate and compare it to the predictions of the thermal Euclidean theory, finding good agreement. We also verify the consistency of several empirical measurements of the critical bubble energy with the theoretical prediction. Finally, we comment on the implication of these new observables for early universe scenarios.

Chapter 2

Bubble clustering in cosmological first-order phase transitions

2.1 Introduction

As explained in section 1.2, vacuum decay is most frequently described in the literature using Euclidean instanton methods. The framework treats this problem in analogy with quantum tunneling in non-relativistic quantum mechanics. Crucially, its predictions cannot be applied to configurations with more than one bubble. Therefore, while the instanton methods can be used to compute decay rates (i.e. the probability per unit 4-volume that a bubble will nucleate), one must assume that bubble nucleation events are independent in order to build a spacetime picture of the percolation of true vacuum bubbles. Testing this assumption is the primary goal of this Chapter. As we describe in more detail below, this assumption does not hold, but rather nucleation events are clustered in analogy with the clustering of rare peaks in Gaussian random fields.

Recently, a real-time semi-classical approach to vacuum decay was developed in [21]. In this approach, the dynamical phase space evolution of a quantum state initially in the false vacuum is modelled using the truncated Wigner approximation [166, 167]. One generates an ensemble of initial conditions of the field and its conjugate momentum, drawn from the ground state defined by the false vacuum minimum. These initial states are then evolved classically with the non-linear Hamiltonian using lattice simulations. The field configuration in each realization is sampled at late times; in some realizations, bubbles of the true vacuum form. This procedure yields a semi-classical approximation to the first-order phase transition dynamics leading to the decay of the false vacuum. Although both

the real-time semi-classical and instanton methods are semi-classical approximations it is still an open question precisely how these two approaches are related; see Refs. [21, 33, 34, 31] for some discussion. More details on the interpretation of real-time simulations, and a practical comparison with Euclidean methods is given in Appendix A.1.

In the limit where the nucleation rate is relatively slow (e.g. compared to the light crossing time of the lattice), in any given realization the field behaves like a free scalar (with mass determined by the curvature about the false vacuum minimum) for much of its evolution. Starting from vacuum initial conditions, if the field truly were just a free massive scalar, then on each timeslice we obtain a Gaussian random field. As described in Chapter 1, peaks in a Gaussian random field cluster, and the properties of this clustering encode the power spectrum of the underlying field. This is the basis of cosmological studies using galaxies as a tracer of the underlying large-scale distribution of dark matter. Returning to our simulations, over a decorrelation timescale of order the inverse mass, the configuration of the field randomizes yielding a new set of peaks. Eventually, a peak will be high enough to leave the basin of attraction of the false vacuum, and the non-linearities of the potential allow something interesting to happen: the formation of a bubble inside of which the field settles into the true vacuum. If this bubble is large enough, it will expand. Within this picture, bubbles nucleate from peaks in the vacuum fluctuations of the field, and since peaks are clustered, bubble nucleation events should be clustered as well. Put simply, it is easier to nucleate bubbles from a region of space where the field is closer to the true vacuum. This runs contrary to existing work on relativistic first-order phase transitions, which have implicitly assumed a distribution of bubbles statistically independent of position and time.

In this Chapter, we look more closely at the field region where the bubbles form and demonstrate that peaks of a critical spatial size and amplitude can act as seeds for bubble nucleation. Using the nucleation seed properties to identify bubble sites, we compute the two-point correlation function between nucleation sites over an ensemble of 1+1-dimensional lattice simulations. We compare the result to the spatial correlation function for peaks in a scalar field with mass set by the false vacuum curvature, finding qualitative agreement, and validating the description above.

There are a number of implications of a non-trivial two-point bubble correlation function:

- Just like galaxies provide a biased tracer of the underlying density field, bubble nucleation events provide a biased tracer of the underlying vacuum fluctuations. Just as a galaxy survey can be used to determine the statistics of the density field, the distribution of bubble nucleation events can be used to determine the statistics of

vacuum fluctuations. The bubble correlation function is sensitive to deviations from the vacuum state, and would yield a different result for e.g. a thermal or vacuum state. There are associated connections with quantum measurement which deserve further exploration.

- A number of analogue experimental systems that can be used as quantum simulators of false vacuum decay have been proposed [168, 164, 169]. The two-point bubble correlation function (or more generally, an n-point function) is an observable for these experiments, which could be used to confirm the validity of the semi-classical picture of vacuum decay and the properties of the initial state (as outlined in the point above).

- The frequency of collision between bubbles during eternal inflation and in post-inflation phase transitions is affected by the clustering of bubble nucleation sites. This has implications for programs to detect these effects in the CMB and spectrum of stochastic primordial gravitational waves.

The Chapter is organized as follows. In section 2.2 we set up our field theory and explain how false vacuum decay arises from semi-classical evolution. In section 2.3 we review Gaussian peak theory and discuss the general features of the two-point correlation function between peaks in one spatial dimension. In section 2.4 we argue that bubbles form around peaks in the field and use empirical observations from our simulations to define bubble nucleation sites. In section 2.5 we present our results and compare with the free field theoretical prediction. In section 2.6 we discuss the implications of this result for bubble collisions and associated cosmological observables, and conclude in section 2.7.

2.2 Real-time semi-classical formalism

We consider a scalar field theory in 1+1 dimensions with Lagrangian density and potential defined in the Introduction:

$$\mathcal{L} = \frac{1}{2}\dot{\phi}^2 - \frac{1}{2}\left(\partial_x \phi\right)^2 - V(\phi), \tag{2.1}$$

$$V(\phi) = V_0 \left[-\cos\left(\frac{\phi}{\phi_0}\right) + \frac{\lambda^2}{2}\sin^2\left(\frac{\phi}{\phi_0}\right)\right]. \tag{2.2}$$

In this Chapter, we focus on the regime where the decay rate of the false vacuum is relatively fast ($\lambda \sim 1$), so that we find a sufficient number of nucleation events to empirically compute

correlation functions. The parameter ϕ_0 scales the width of the potential, while V_0 scales its height. V_0/ϕ_0^2 sets the typical mass squared scales in the potential. To adjust the amplitude of quantum effects, it is therefore convenient to vary ϕ_0 while holding $V_0\phi_0^{-2}$ fixed. This adjusts the width of the false vacuum minima relative to the typical amplitude of quantum fluctuations, which can be alternatively be viewed as adjusting $\hbar \propto \phi_0^{-2}$.

We initialize an ensemble of simulations with the mean field in the false vacuum $\phi = \pi\phi_0$, with fluctuations consistent with the ground state of the quadratic approximation to the false vacuum potential minimum

$$\phi(x, t = 0) = \phi_{\rm fv} + \delta\phi(x), \quad \Pi(x, t = 0) = \dot{\phi}(x, t = 0) = \delta\Pi(x). \tag{2.3}$$

The fluctuations $\delta\phi(x)$ and $\delta\Pi(x)$ are drawn from the Wigner functional of the initial state, with each initial draw corresponding to a single member of the ensemble. Since we are interested in evolution from a false vacuum, we will approximate the initial Wigner functional as the vacuum associated with the quadratic expansion of the potential about the false vacuum. Investigating departures from this choice for the initial state is beyond the scope of this thesis.

The initial fluctuations $\delta\phi$ and $\delta\Pi$ are drawn as realizations of Gaussian random fields whose Fourier coefficients $\delta\tilde{\phi}_k$ and $\delta\tilde{\Pi}_k$ have covariance

$$\left\langle \delta\tilde{\phi}_k^* \delta\tilde{\phi}_{k'} \right\rangle = \frac{1}{2\omega_k}\delta(k - k'), \quad \left\langle \delta\tilde{\Pi}_k^* \delta\tilde{\Pi}_{k'} \right\rangle = \frac{\omega_k}{2}\delta(k - k'), \quad \left\langle \delta\tilde{\phi}_k \delta\tilde{\Pi}_{k'}^* \right\rangle = 0\,, \tag{2.4}$$

where $\omega_k^2 = k^2 + m^2$ and $m^2 = m_{eff}^2 = V''(\phi = \pi\phi_0) = V_0\phi_0^{-2}(\lambda^2 - 1)$. Here $\langle\cdot\rangle$ represents an ensemble average, and we have assumed unitary normalization for the Fourier transforms in the continuum.

Each realization is evolved using the classical Hamilton's equations:

$$\frac{{\rm d}\phi}{{\rm d}t} = \Pi, \quad \frac{{\rm d}\Pi}{{\rm d}t} = \nabla^2\phi - V'(\phi)\,. \tag{2.5}$$

At a later time, we make measurements on the evolved ensemble. This approach captures the dynamical evolution of the Wigner functional [170] to leading (nonperturbative) order in $\hbar$ of the form $e^{i/\hbar}$. Meanwhile, the leading perturbative quantum corrections are encoded in statistics of the initial fluctuations [21] (see also [171, 172]). In the cold atom community, this is known as the Truncated Wigner Approximation (see e.g. Ref. [173] for a review), while in cosmology it is known as the stochastic lattice approximation and is used extensively in preheating studies (see e.g. Ref. [174] for a review). For a free massive scalar, this procedure exactly describes the full quantum evolution for any initial state with

positive definite Wigner functional, such as the vacuum state. Including non-linearities in the potential, the story is more complicated. The classical non-linear time-evolution should capture all tree-level interactions between the Fourier modes. One complication arises from our need to initialize modes up to some cutoff $k_{\rm cut}$ as introduced below—the effective dynamics of the longest wavelength modes on the lattice are modified from what we would expect in the bare potential alone (i.e. renormalization effects will arise). Nevertheless, in scenarios with unentangled initial states where quantum dynamics give rise to many particle, effectively classical final states, we can expect this procedure faithfully tracks the dynamics. One such situation is the decay of the false vacuum, which will be our main focus.

In order to implement the above procedure numerically, we must work with dimensionless spacetime coordinates and field variables. As well, we must adapt the continuum prescription above to a discrete lattice of finite side length. It is convenient to introduce dimensionless variables

$$\bar{t} = \mu t \quad \bar{x} = \mu x \quad \bar{\phi} = \frac{\phi}{\phi_0}\,, \tag{2.6}$$

where μ is some inverse length scale, and ϕ_0 is as defined in the potential. We assume throughout that $\hbar = c = 1$, so that μ has units of mass and ϕ_0 has units of $(\text{mass})^{(d-1)/2}$, where d is the number of spatial dimensions. In these units, the dimensionless equations of motion are

$$\frac{\mathrm{d}\bar{\phi}}{\mathrm{d}\bar{t}} = \bar{\Pi} \tag{2.7}$$

$$\frac{\mathrm{d}\bar{\Pi}}{\mathrm{d}\bar{t}} = \bar{\nabla}^2\bar{\phi} - \frac{V_0}{\mu^2\phi_0^2}\left[\sin\left(\bar{\phi}\right) + \frac{\lambda^2}{2}\sin\left(2\bar{\phi}\right)\right]\,. \tag{2.8}$$

We initialize the fluctuations on our finite discrete lattice of side length L as

$$\delta\bar{\phi} \equiv \frac{\delta\phi}{\phi_0} = \frac{1}{\phi_0\sqrt{\mu L}}\sum_{j=1}^{n_{\rm cut}}\left[\frac{\hat{\alpha}_j}{\sqrt{2}}\sqrt{\frac{\mu^2}{V''(\phi_{\rm fv})+k_j^2}}e^{ik_jx} + \text{c.c.}\right]\,, \tag{2.9}$$

where $\hat{\alpha}_j$ is a realization of complex random deviate with variance $\left\langle|\hat{\alpha}_j|^2\right\rangle = 1$ and $k_j = \frac{2\pi}{L}j$. Here we have truncated the spectrum at wavenumber $k_{\rm cut} = \frac{2\pi}{L}n_{\rm cut}$. The initial realization of the momentum fluctuations is generated analogously

$$\delta\bar{\Pi} \equiv \frac{1}{\mu}\frac{\delta\dot{\phi}}{\phi_0} = \frac{1}{\phi_0\sqrt{\mu L}}\sum_{j=1}^{n_{\rm cut}}\left[\frac{\hat{\beta}_j}{\sqrt{2}}\sqrt{\frac{V''(\phi_{\rm fv})+k_j^2}{\mu^2}}e^{ik_jx} + \text{c.c.}\right]\,, \tag{2.10}$$

with $\hat{\beta}_j$ a realization of a unit variance complex random deviate that is uncorrelated with $\hat{\alpha}_j$. The temporal evolution is performed using a 10th order accurate Gauss-Legendre scheme [175, 176]. Spatial derivatives are computed by forward Fourier transforming, multiplying by the appropriate power of ik, then inverse Fourier transforming. We refer to this as a Fourier pseudospectral approximation, and as a consequence the simulations have periodic boundary conditions. We verified that the total field energy in the simulations is conserved to near machine-precision levels.

In the next section, we describe the picture expected for a free massive scalar, where the semi-classical approach described above is exact and we can compare numerical and analytical approaches. We then move on to a numerical study with the potential (2.1), where vacuum decay can occur.

2.3 Peak-peak correlation for a massive scalar

In this section we describe the expected peak-peak correlation function for vacuum fluctuations in a free massive scalar field, which provides a warm-up and a point of comparison for the analysis of the bubble correlation function. As described in the previous section, the initial condition is a spatially homogeneous Gaussian random field with spectrum given by (2.4). Evolving over a time of order m^{-1}, we obtain an uncorrelated Gaussian random field with the same power spectrum. Therefore, evolving an ensemble of simulations with vacuum initial conditions simply propagates the vacuum. In addition to the two-point statistics (i.e. power spectrum) of the field, we can compute the statistics of extremal points on a fixed time-slice. For the free field example, we focus on maxima (i.e. peaks). The statistics of peaks in a Gaussian random field are described in the classic paper [22]. In this section, we review the derivation of the peak number density and of the two-point peak correlation function in one dimension. A similar derivation can be found in [177]. We then validate our numerical code by comparing with this expectation and show good agreement.

2.3.1 Analytic derivation of the peak-peak correlation function

Full realizations of our approximate false vacuum initial state possess fluctuations on all possible spatial scales, although the use of a discrete lattice enforces a truncation of this spectrum above some wavenumber below the Nyquist frequency. However, we are primarily

interested in variations of the field over distances of order m^{-1}. Therefore, given a fine-grained realization of a Gaussian random field $\phi_{\rm fg}(x)$ (e.g. a realization of the field described in the previous section), it is natural to smooth it with a Gaussian kernel W of width R_0

$$\phi(x) \equiv \int \mathrm{d}x'\; W(x,x')\phi_{\rm fg}(x') = \int \mathrm{d}x'\; \frac{e^{-\frac{(x-x')^2}{2R_0^2}}}{\sqrt{2\pi}R_0}\phi_{\rm fg}(x')\,. \tag{2.11}$$

For the case of exploring peaks in the field, R_0 roughly corresponds to the width of peaks we are interested in. Although many filters are possible, we choose a Gaussian filter because of its conceptual simplicity both as a local Gaussian smoothing in real space and a Gaussian truncation of high frequency modes in Fourier space. We do not expect our qualitative conclusions to depend on this choice. In a given field realization, the peaks in the smoothed field are distributed as a random process throughout space. A first guess may be that the peak locations are independent of each other. However, this is not quite correct, and there are important correlations between the peak locations as we review below.

We model the number density of peaks in a single field realization as a sum of Dirac delta functions

$$\rho_{\rm pk}(x) = \sum_i \delta(x - x_{{\rm pk},i})\,, \tag{2.12}$$

where the $x_{{\rm pk},i}$ are the locations of peaks, labelled by the index i. We want to relate the statistics of $\rho_{\rm pk}$ (and $x_{\rm pk}$) to the underlying field $\phi(x)$. We denote the field, its gradient, and its curvature by $\phi(x)$, $\eta(x) = \phi'(x)$, and $\zeta(x) = \phi''(x)$, respectively. In the vicinity of a peak, we have $\phi(x) \approx \phi_{\rm pk} + \frac{1}{2}\zeta_{\rm pk}(x - x_{\rm pk})^2$ and $\eta(x) \approx \zeta_{\rm pk}(x - x_{\rm pk})$. Here we have indicated quantities evaluated at the location of the peak by $\cdot_{\rm pk}$. It follows that $\delta(x-x_{\rm pk}) = |\zeta(x_{\rm pk})|\delta(\eta(x))$. The number density of maxima of ϕ where $\eta(x) = 0$ and $\zeta(x) < 0$ becomes $\rho_{\rm pk}(x) = |\zeta(x)|\,\delta(\eta(x))$. Therefore, to understand the statistics of individual peaks, it is convenient to first reduce the infinite dimensional space of field configurations down to the three-dimensional space of $\mathbf{y} \equiv (\phi, \eta, \zeta) = (\phi(x), \eta(x), \zeta(x))$ evaluated at a single point. By translation invariance, the statistics of the random vector $\mathbf{y}$ over the ensemble of field configurations is independent of the choice of position x. Peaks are selected by imposing appropriate constraints on η and ζ. Similarly, peak-peak statistics can be tackled by considering the six dimensional random vector $\mathbf{y}_2 = (\phi(x), \eta(x), \zeta(x), \phi(x + r), \eta(x + r), \zeta(x + r))$, which depends only on the separation r.

The statistics of $\mathbf{y}$ and $\mathbf{y}_2$ are specified by various two-point correlation functions be-

tween the field and its derivatives. For future convenience, we therefore introduce

$$\sigma^2_{(m+n)/2}(r) = \left\langle \partial^{(m)}\phi(x)\, \partial^{(n)}\phi(x+r)\right\rangle = \begin{cases} \int_{-\infty}^{+\infty} \mathrm{d}k\, k^{m+n} P(k)\cos(kr), & \text{if } m+n \text{ even} \\ \int_{-\infty}^{+\infty} \mathrm{d}k\, k^{m+n} P(k)\sin(kr), & \text{otherwise}. \end{cases} \tag{2.13}$$

The case $r = 0$ is sufficient to specify the distribution of single peaks, while the $r \neq 0$ information is required to explore peak-peak correlations. Here $P(k)$ is the power spectrum of the smoothed field

$$P(k) = |W(k;R_0)|^2\, P_0(k), \qquad W(k;R_0) = e^{-(kR_0)^2/2}\,, \tag{2.14}$$

where $P_0(k)$ is the power spectrum of the unsmoothed field and $W(k;R_0)$ is the Fourier transform of our Gaussian kernel with size R_0. We will use the notation $\sigma^2_{(m+n)/2}(r)$ when $r \neq 0$, and $\sigma^2_{(m+n)/2}$ when $r = 0$.

A first quantity of interest is the ensemble average peak density with height above a given threshold ϕ_t

$$n_{\rm pk}(\phi_t) \equiv \langle \rho_{\rm pk}(x)\rangle = \langle |\zeta(x)|\, \delta(\eta(x))\rangle = \int_{\phi>\phi_t}\int_{\zeta<0} \mathcal{P}(\phi,\eta,\zeta;\mathcal{M})\Big|_{\eta=0} |\zeta|\, \mathrm{d}\zeta \mathrm{d}\phi, \tag{2.15}$$

where $\mathcal{P}(\phi,\eta,\zeta;\mathcal{M})\mathrm{d}\phi\mathrm{d}\eta\mathrm{d}\zeta$ is the joint probability distribution for the random variables $\vec{y} = (\phi,\eta,\zeta)$ evaluated at a single spatial position. The conditions $\eta = 0$ and $\zeta < 0$ select maxima of the field, but the statistics of maxima are no different than that of the minima. Finally, the number density depends on the peak amplitude threshold ϕ_t. Since we are ultimately interested in 'peaks' probing the nonlinear structure of our false vacuum potential (2.1), it is convenient to consider the rescaled threshold $\bar{\phi}_t = \phi_t/\phi_0$.

All that remains is to obtain the probability density $\mathcal{P}$. It is straightforward to see that (ϕ,η,ζ) are jointly Gaussian distributed

$$\mathcal{P}(\phi,\eta,\zeta;\mathcal{M})\mathrm{d}\phi\mathrm{d}\eta\mathrm{d}\zeta = \frac{e^{-\frac{1}{2}\mathbf{y}^{\rm T}\cdot\mathcal{M}^{-1}\cdot\mathbf{y}}}{\sqrt{(2\pi)^3\det\mathcal{M}}}\mathrm{d}\phi\mathrm{d}\eta\mathrm{d}\zeta\,. \tag{2.16}$$

The probability density is specified by the covariance matrix $\mathcal{M}$ with elements $m_{ab} \equiv \langle y_a y_b\rangle$, where $\mathbf{y} = (\phi,\eta,\zeta)$ as above. Using (2.13), we thus have

$$\mathcal{M} = \begin{pmatrix} \sigma_0^2 & 0 & -\sigma_1^2 \\ 0 & \sigma_1^2 & 0 \\ -\sigma_1^2 & 0 & \sigma_2^2 \end{pmatrix} \tag{2.17}$$

and (2.15) becomes

$$n_{\rm pk}\left(\bar{\phi}_t\right) = -\frac{1}{\sqrt{(2\pi)^3\sigma_1^2\left(\sigma_0^2\sigma_2^2-\sigma_1^4\right)}}\int_{\bar{\phi}_t\phi_0}^{+\infty}\int_{-\infty}^{0} e^{-\frac{1}{2}\mathbf{y}^T\cdot\mathcal{M}^{-1}\cdot\mathbf{y}|_{\eta=0}}\zeta {\rm d}\zeta {\rm d}\phi\,, \tag{2.18}$$

with

$$\mathbf{y}^{\rm T}\cdot\mathcal{M}^{-1}\cdot\mathbf{y}\Big|_{\eta=0} = \frac{\sigma_2^2\phi^2+2\sigma_1^2\phi\zeta+\sigma_0^2\zeta^2}{\sigma_0^2\sigma_2^2-\sigma_1^4}\,. \tag{2.19}$$

In the limit of high $\bar{\phi}_t \gg \sigma_0/\phi_0$, the dominant term in the exponent is $-\phi^2/\sigma_0^2$. We therefore see that the number density of peaks decreases as the threshold is increased.

Now we turn to the derivation of the peak-peak correlation function. It describes the clustering of peaks, which are a biased tracer of the underlying field. Excluding self-pairs, the two-point correlation function $\xi_{\rm pk}$ is defined in terms of the peak number density as

$$n_{\rm pk}^2(\bar{\phi}_t)\left(1+\xi_{\rm pk}(r)\right) = \langle\rho_{\rm pk}(x)\rho_{\rm pk}(x+r)\rangle\,, \tag{2.20}$$

which is the joint probability that peaks exist in two volume elements separated by a distance r divided by the square of the overall peak number density at fixed threshold $\bar{\phi}_t$. Denoting the properties of the peak at x and $x+r$ with the subscript $_1$ and $_2$, a point in configuration space is now specified by the six dimensional vector $\mathbf{y}_2 = (\phi_1,\eta_1,\zeta_1,\phi_2,\eta_2,\zeta_2)$. As in the case of the single peak parameter space, these variables are jointly Gaussian distributed. To investigate the correlation between pairs of maxima that both exceed the same threshold ϕ_t, we enforce $\{\phi_1>\phi_t,\eta_1=0,\zeta_1<0,\phi_2>\phi_t,\eta_2=0,\zeta_2<0\}$. Equation (2.20) can be rewritten as

$$1+\xi_{\rm pk}(r) = \frac{n_{\rm pk}(\bar{\phi}_t)^{-2}}{(2\pi)^3\sqrt{\det\mathcal{M}_{\rm pair}}}\iint_{\bar{\phi}_t\phi_0}^{\infty}\iint_{-\infty}^{0} e^{-\frac{1}{2}\mathbf{y}_2^{\rm T}\cdot\mathcal{M}_{\rm pair}^{-1}\cdot\mathbf{y}_2}\zeta_1\,\zeta_2\,{\rm d}\zeta_1{\rm d}\zeta_2{\rm d}\phi_1{\rm d}\phi_2. \tag{2.21}$$

Here, the correlation matrix for the pair of peaks is given by

$$\mathcal{M}_{\rm pair}(r) = \begin{pmatrix}\mathcal{M}_{11} & \mathcal{M}_{12}(r)\\ \mathcal{M}_{21}(r) & \mathcal{M}_{22}\end{pmatrix}, \tag{2.22}$$

$$\mathcal{M}_{11} = \mathcal{M}_{22} = \begin{pmatrix}\sigma_0^2 & 0 & -\sigma_1^2\\ 0 & \sigma_1^2 & 0\\ -\sigma_1^2 & 0 & \sigma_2^2\end{pmatrix}, \tag{2.23}$$

$$\mathcal{M}_{12}(r) = \mathcal{M}_{21}^*(r) = \begin{pmatrix}\sigma_0(r)^2 & -\sigma_{1/2}(r)^2 & -\sigma_1(r)^2\\ \sigma_{1/2}(r)^2 & \sigma_1(r)^2 & -\sigma_{3/2}(r)^2\\ -\sigma_1(r)^2 & \sigma_{3/2}(r)^2 & \sigma_2(r)^2\end{pmatrix}. \tag{2.24}$$

From this we obtain the exponent in (2.21) as

$$\begin{aligned}\mathbf{y}_2^{\mathrm{T}} \cdot \mathcal{M}^{-1} \cdot \mathbf{y}_2 = m_{11}^{-1}\left(\phi_1^2+\phi_2^2\right) + 2m_{14}^{-1}\phi_1\phi_2 + m_{33}^{-1}\left(\zeta_1^2+\zeta_2^2\right) \\ + 2m_{36}^{-1}\zeta_1\zeta_2 - 2m_{13}^{-1}\left(\phi_1\zeta_1+\phi_2\zeta_2\right) - 2m_{16}^{-1}\left(\phi_1\zeta_2+\phi_2\zeta_1\right)\,, \end{aligned} \tag{2.25}$$

where m_{ab}^{-1} be elements of the 6×6 matrix $\mathcal{M}_{\mathrm{pair}}^{-1}$. The matrix $\mathcal{M}_{\mathrm{pair}}^{-1}$ is singular at $r=0$, but well defined for r positive. For the scales below the smoothing scale R_0, $\xi_{\mathrm{pk}}(r\to0)=-1$. At small separations the dominant term in the exponent has prefactor $m_{11}^{-1}\sim r^{-2}$, so $\xi_{\mathrm{pk}}(r)$ picks up as e^{-c/r^2} for some constant c. For large separations the exponential inside the integral dominates and $\xi_{\mathrm{pk}}(r\gg R_0)$ plateaus around a constant value. In the limit of large $\bar{\phi}_t \gg \sigma_0/\phi_0$, the main contribution to ξ_{pk} at intermediate separations is from $n_{\mathrm{pk}}(\bar{\phi}_t)^{-2}$ which grows as $e^{2\bar{\phi}_t^2\phi_0^2}$. Therefore, peaks of greater height (i.e. increasingly rare) cluster more strongly than peaks of lower height. Examining the falloff of $\xi_{\mathrm{pk}}(r)$ in greater detail, the correlation length is of order a few times mR_0.

Note, equation (2.20) holds for the case with 3 spatial dimensions, and the scaling of the bias parameter with separation r is similar to the 1-dimensional case. It can be shown by working in analogy with the case presented here, using the generalized spectral moments, how it is still true that ξ_{pk} peaks around a few times mR_0. For numerical interests we restrain ourselves to the $1+1$-dimensional volume but the implications are valid in the $3+1$ case as well.

When we compare the prediction for the peak-peak correlation function of the formalism in the continuum limit with the results from simulations, we must use the discrete version of the field power spectrum. This is so that we obtain an analytic result that matches the implementation on the discrete lattice of the field. In practice this means replacing the integrals in (2.13) with a sum over all modes

$$\sigma^2_{(m+n)/2}(r_{ij}) = \begin{cases} \sum\limits_{\substack{l=-n_{\mathrm{cut}}\\ l\neq0}}^{n_{\mathrm{cut}}} k_l^{m+n}P(k_l)\cos\left(k_l r_{ij}\right), & \text{if } m+n \text{ even} \\ \sum\limits_{\substack{l=-n_{\mathrm{cut}}\\ l\neq0}}^{n_{\mathrm{cut}}} k_l^{m+n}P(k_l)\sin\left(k_l r_{ij}\right), & \text{otherwise}\,, \end{cases} \tag{2.26}$$

where we assume either that the spectral cut is below the Nyquist frequency, or else that we have an odd number of grid sites, so that the lower limit of the sum extends to $-n_{\mathrm{cut}}$.

2.3.2 Numerical peak-peak correlation function

We now wish to demonstrate that we can reproduce the peak-peak correlation function empirically using an ensemble of our lattice simulations. This is an important step to

confirm that our simulations accurately time-evolve the peak statistics, in preparation for studying the bubble-bubble correlation function. Since our initial conditions are Gaussian, and Gaussianity is maintained by linear field evolution, in this section we consider a free massive scalar field with potential

$$V(\phi) = \frac{1}{2}m^2(\phi - \phi_{\rm fv})^2 = \frac{1}{2}m^2\phi_0^2\left(\frac{\phi}{\phi_0} - \frac{\phi_{\rm fv}}{\phi_0}\right)^2 , \tag{2.27}$$

with initial conditions corresponding to Minkowski vacuum fluctuations with mass m. For convenience, and ease of comparison with later results, we choose a mass consistent with the second derivative of the bare potential (2.1) about the false vacuum, $m^2 = V_0\phi_0^{-2}(\lambda^2 - 1)$. The field and momentum are initialized as described in section 2.2. From (2.21), we see that the predicted peak-peak correlation is determined by the peak threshold ϕ_t, as well as a few lower order sinusoid weighted 'moments' of the field power spectrum. For our initial conditions, the moments are in turn specified by the field mass m and filter smoothing scale R_0 in the combination mR_0, and the field scale ϕ_0. A key quantity characterizing the rarity of the peaks is $\phi_t^2/\sigma_0^2 \propto \phi_0^2$.

Evolving the field, we obtain $\xi_{\rm pk}(r)$ on a single randomly selected timeslice in each simulation by detecting all peaks above a fixed threshold $\bar{\phi}_t$. We then compute the equal-time peak-peak correlation function using the estimator [178]:

$$1 + \xi_{\rm pk}(r) = \left\langle \frac{1}{K}\sum_{i=1}^{K}\frac{K_i(r)}{n_{pk}V_i} \right\rangle , \tag{2.28}$$

where $K_i(r)$ is the number of peaks inside a search volume $\Delta V_i = 2\Delta r\phi_0^{-1}\sqrt{V_0}$ at spatial separation within $\pm[r, r + \Delta r)\phi_0^{-1}\sqrt{V_0}$ from the reference peak i. The factor of 2 arises from the fact that we search for peaks both to the left and to the right of the reference peak i up to separations $L/2$. $n_{\rm pk}$ is the measured number density of peaks on the timeslice, and K the total number of peaks on that slice, for a given realization. In other words, the correlation function is the expected ratio of the number density of peaks a distance r from a randomly chosen peak to the mean number density. The $\langle\cdot\rangle$ denotes the ensemble average of the correlation function, which in this section we take to be $200,000$ simulations. The result for fixed mass and smoothing scale, but varying threshold, is shown in Fig. 2.1, where the smoothing scale is $mR_0 \sim 1/3$, and $k_{\rm cut}R_0 \sim 2$. Data is binned such that $\Delta r/R_0 \sim 0.2$. The lattice parameters are consistent with those described in detail in section 2.4 for the simulations including false vacuum decay. We compare the empirically measured correlation function to the analytic expectation from (2.21). The prediction and lattice simulation results agree up to a small sampling bias at higher thresholds arising

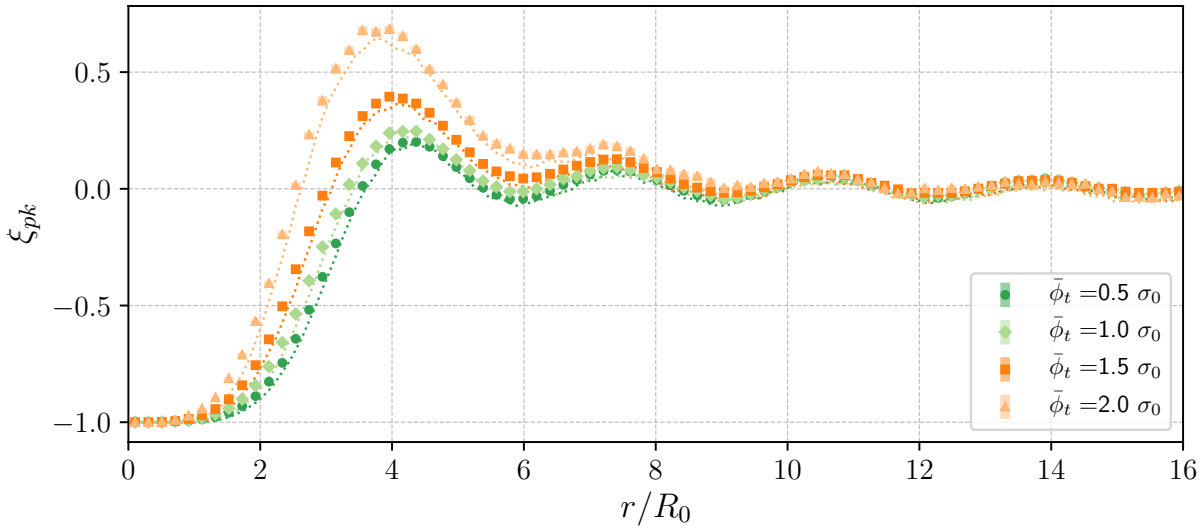

Figure 2.1: The equal-time peak-peak correlation function for four detection thresholds $\bar{\phi}_t$ computed analytically (dashed lines) and extracted from an ensemble of simulations (points). The agreement between analytic and numerical results serves as a validation exercise for the simulations. The thresholds are chosen in units of the field RMS σ_0. Larger values correspond to a larger peak amplitude in $\xi_{\rm pk}$ showing that the tallest peaks cluster more strongly. $\xi_{pk} = -1$ where the separation r is less than the smoothing scale R_0. It picks up exponentially to reach a maximum at separation $r \sim 4R_0$, the scale where peaks are the most frequent. This balances out at larger separations where $\xi_{pk} < 0$. Note that the lattice size is $r_{max}/R_0 \sim 415$. The small mis-match between the analytic curves and simulations arises due to a small bias in the estimator (2.28) from realizations with few peaks.

due to a large sample variance on the realization peak number density. We find that the distribution is independent of timeslice, confirming our expectation that time evolution merely propagates the vacuum statistics.

A few properties of the correlation function are noteworthy. First, it can be seen that the peak amplitude of the correlation function increases with threshold, holding to the expectation that rarer peaks cluster more strongly. The increasing noise and bias on the data points for higher thresholds in Fig. 2.1 is due to increasing sample variance (i.e. rarer

peaks). A consistency check on the estimator (2.28) is to ensure that

$$\int_{-L/2}^{L/2} \mathrm{d}r \;\; (1 + \xi_{pk}(r)) = 1 \,, \tag{2.29}$$

to good approximation. In other words, if peaks are correlated at short separation then to maintain the average number density throughout the volume they must be anti-correlated at large separation. We verify that this is indeed true for our ensemble of simulations, at all times.

Before moving on to discuss vacuum decay, let us consider the following thought experiment. Imagine that we had a physical system consisting of a scalar field in its vacuum state. Now suppose we could construct a 'peak detector' that was sensitive to peaks in the (spatially) smoothed vacuum fluctuations above some threshold $\bar{\phi}_t$, enabling one to replicate our numerics with an experimental protocol. For example, one could imagine that the value of ϕ controls the lifetime of some unstable particle such that when $\bar{\phi} > \bar{\phi}_t$ decay happens very quickly, but is shut off when $\bar{\phi} < \bar{\phi}_t$. Filling space with a dilute gas of such particles (with the inverse number density roughly corresponding to the smoothing scale), we could then detect the position of peaks by locating the origin of the detected decay products of the unstable particles. From this distribution of peak positions, we could compute the two point correlation function using the estimator (2.28). Finally, since the spatial dependence of the peak-peak correlation function is in one-to-one correspondence with the power spectrum of the vacuum fluctuations, it is possible to extract the statistics of the vacuum fluctuations underlying the peaks (at least in the infrared) [1]. As we will see in the next section, false vacuum decay appears to be analogous to this example.

2.4 False vacuum decay

We now move on to discuss vacuum decay in the potential (2.1). Our ultimate goal is to compute the two point correlation function between bubble nucleation sites as a function of both their spatial and temporal separations. The following two sections address this. In this section, we review the spacetime picture of false vacuum decay and construct an algorithm for identifying bubble nucleation sites. In the next section we will apply this formalism to bubble nucleations in our numerical simulations.

[1] The interaction with the unstable particle will alter the vacuum state of the massive scalar, so one must be a bit careful with this thought experiment to be precise about which state one is probing. Here, we assume it is the state defined by the non-interacting vacuum of the massive scalar.

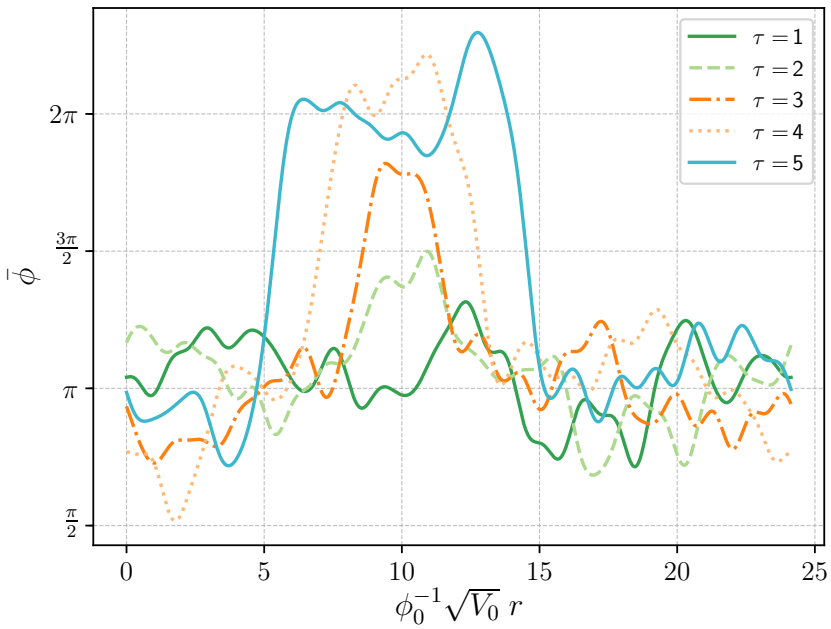

Figure 2.2: Stages in the evolution of a bubble, as snapshots of the smoothed field amplitude over a lattice region. The snapshots are spaced by equal-time intervals. One can follow time backwards and trace the bubble to the location of a peak rising gradually above the mean field.

We initialize an ensemble of simulations as described in section 2.2. The mean field is at the false vacuum minimum $\bar{\phi}_{\rm fv} = \pi$, and fluctuations about the false vacuum evolve non-linearly according to the equations of motion. Every once in a while, the non-linear evolution leads to large localized fluctuations in the field. Some of these fluctuations overcome the potential barrier, and from here the field may either bounce back or continue to roll down the potential into one of the true vacua, depending on the size of the spatial region where the fluctuation occurs. In the latter case, a bubble of true vacuum is formed, which subsequently expands. We confirm below that this is a reasonably good proxy for bubble formation. Each realization experiences a different number of decay events, and the full ensemble is used to extract statistics about the bubble formation process.

A series of timeslices around a typical nucleation event found in the simulations is shown in Fig. 2.2. Not every peak triggers a nucleation event; it must be of sufficient amplitude and width to do so. This led us to consider extrema in a smoothed field as a proxy for nucleation events. Since there are two true vacua at $\bar{\phi}_{\rm tv} = 0,\ 2\pi$, maxima about the false

vacuum decay to $\bar{\phi}_{\rm tv} = 2\pi$ while minima decay to $\bar{\phi}_{\rm tv} = 0$.

In order to remove the small scale noise while still resolving the structure of individual bubbles, we want to define our smoothing scale to be slightly smaller than the typical size of a bubble early in its time evolution. We empirically determine the typical bubble size by stacking bubbles from different simulations in our ensemble to find the mean bubble profile. An immediate challenge is that most bubbles are not formed at rest, and many have a centre-of-mass velocity that is highly relativistic. The shape of the bubble walls and the bubble size in the frame of reference of the simulation is distorted by relativistic length contraction. To obtain the average bubble, we have to bring the bubbles to rest before averaging. The detailed properties of the average bubble and the distribution of velocities are of general interest for understanding the properties of vacuum decay. A more comprehensive treatment of bubble nucleation velocities makes the topic of Chapter 3. Below we outline a simplified method to bring these bubbles into their rest frame. Our goal here is simply to motivate a smoothing scale. Note that although we define the smoothing scale by the size of the average bubble in its rest frame, relativistic bubbles which are length contracted can still be detected. We elaborate upon this below.

We prepare an ensemble of simulations with $\lambda = 1.5$ and $\phi_0 = 2.22$. We initialize the field fluctuations with this larger value of ϕ_0 (and hence lower amplitude) in order to decrease noise around the bubble walls. In turn, this lowers the decay rate, allowing us to more easily isolate individual bubbles. If we vary ϕ_0 while holding V_0/ϕ_0^2 fixed, the shape of the bubble is independent of ϕ_0 at tree level, allowing us to use the same average bubble size for all the simulations presented below. We initialize the field evolution using the same grid parameters as the non-linear simulations, which are defined below. Nucleation events are identified in the simulations where the field has transitioned to the true vacuum, and bubbles are extracted. These bubbles materialize with a spread of velocities ranging between zero and nearly the speed of light. In order to bring a bubble into its rest frame, we extract the velocity of the walls (which follow hyperbolic trajectories) from which we obtain the centre of mass velocity of the bubble $v_{\rm COM}$, and apply an inverse Lorentz boost in order to bring the bubble into its rest frame. We start by obtaining the $r_{\rm L}(t)$ and $r_{\rm R}(t)$ trajectories for the centres of the left- and right-travelling bubble walls respectively, on each timeslice, over the entire extent of the bubble, and most importantly around the moment of nucleation where the vertex is located. We proceed as follows:

1. We obtain $r_{\rm L/R}$ in each timeslice t as the best fit parameters of the field value $\bar{\phi}(t, r)$ to the expression $\pm\left(\tanh\frac{r-r_{\rm L}}{w_{\rm L}} + \tanh\frac{r_{\rm R}-r}{w_{\rm R}}\right)\frac{\bar{\phi}_{\rm fv}}{2} + \bar{\phi}_{\rm fv}$, where r is a coordinate that spans the lattice and $w_{\rm L/R}$ is a measure of the wall thickness. We impose that $w_{\rm L} = w_{\rm R}$ in the rest frame.

2. With the values $r_{\mathrm{L/R}}$ obtained this way, we fit each wall individually to a hyperbola $r_{\mathrm{L/R}}(t) = \pm\sqrt{a_1 + (t - a_2)^2} + a_3$ with free parameters $a_1, a_2, a_3 \in \mathbb{R}$ to get the full trajectory. The wall velocity is $v_{\mathrm{L/R}} = \dot{r}_{\mathrm{L/R}}(t)$.

3. Using relativistic velocity addition we obtain the centre of mass velocity for the entire bubble v_{COM}, and the instantaneous wall velocity $v_{\mathrm{wall}}(t)$ in the bubble's rest frame. The Lorentz boost factor is the value of $v_{\mathrm{wall}}(t)$ that minimizes the difference $|v_{\mathrm{COM}} - v_{\mathrm{wall}}(t)|$.

4. We apply a Lorentz boost transformation on the grid coordinates, deforming the bubble by interpolating it onto the new grid.

5. This process is iterated until the v_{COM} of the transformed bubble is below $0.1c$, with c the speed of light on the lattice. Due to computational limitations imposed by our interpolating scheme, the maximum boost factor on each iteration we apply is $v = 0.9c$.

Applying this procedure to our simulations, we obtained 15 stationary bubbles. Ten of these were found to have nucleated with relativistic velocities $v > 0.5c$, with 3 of these having $v > 0.9c$. The average bubble profile is shown in Fig. 2.3. We identify the time interval where the instantaneous wall velocity is $\leq 25\%$ of the speed of light. We extract the time-averaged field profile for the rest-frame average bubble over this interval. We then obtain the FWHM of this field profile and identify average bubble radius $\bar{R}$ with one half of this value. This procedure is pictured in Fig. 2.3 Once a bubble materializes in simulations in its own rest frame with the above width and height, it will continue to grow and expand relativistically until it stabilizes in amplitude around the true vacuum.

Having defined a smoothing scale to apply to the simulation data, we now define an algorithm for identifying the peaks in the field that correspond to nucleation sites for bubbles decaying to $\bar{\phi}_{\mathrm{tv}} = 2\pi$ as follows:

1. We smooth the field in each realization along the spatial axis on each timeslice. The smoothing is done with a Gaussian kernel of width R_0, as we do for the case of the free field (see (2.14)). We choose two smoothing scales for comparison: $R_0 = \bar{R}/4$ and $R_0 = \bar{R}/2$, where $\bar{R}$ is the average radius of bubbles. Fluctuations over significantly smaller spatial regions do not seed bubble nucleation events.

2. To eliminate bubbles nucleating directly from peaks in the initial conditions, we discard all events detected to occur for $t \leq 2m^{-1}$. For a free field, this is of order the

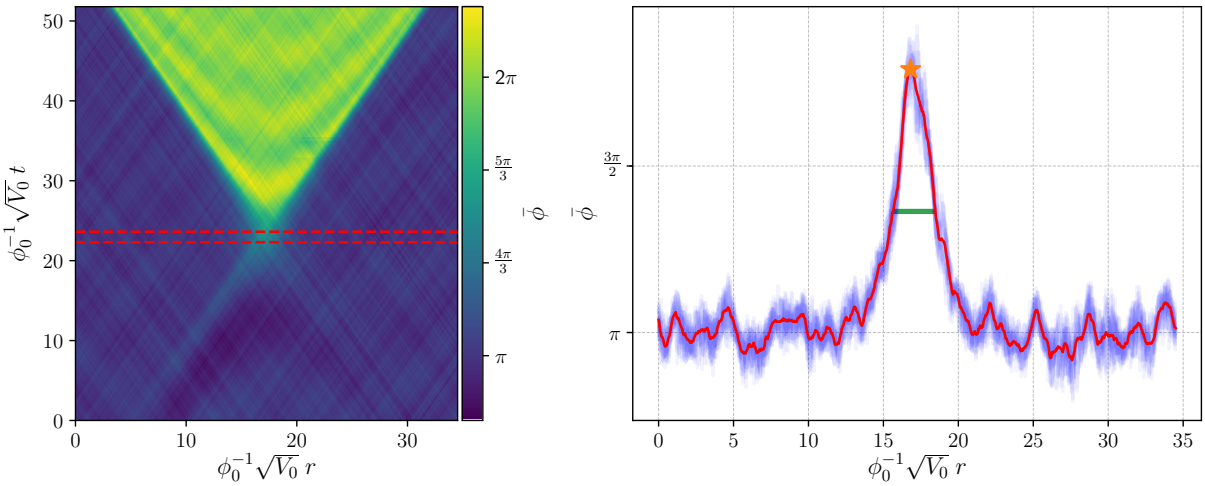

Figure 2.3: On the left we show the averaged bubble in its rest frame. We construct this by de-boosting 15 bubbles to their rest frame, translating the nucleation center to a specified location, and averaging. On the right we show in blue the field profile of the average bubble for all the timeslices highlighted between the red curves on the left. These correspond to the interval where the wall velocity is $\leq 25\%$ of the speed of light on the lattice. The red curve shows the time average of these profiles. The green line shows the FWHM of the red curve, relative to the maximum highlighted by the orange star. The average bubble radius $\bar{R}$ is taken to be a half FWHM.

decay time for peak-peak correlations. The remaining events occur from nonlinear processing encoded in the equations of motion.

3. Stepping through each subsequent timeslice, we locate extrema in the smoothed field that exceed a threshold $\bar{\phi} > \bar{\phi}_t$, $\bar{\phi}_t = \bar{\phi}_{\rm max} + \Delta|\bar{\phi}_{\rm max} - 2\pi|$, with $\bar{\phi}_{\rm max}$ the value of the field at the potential maximum to the right of the false vacuum, and $\Delta \in \{0.2, 0.25, 0.3\}$. These values for Δ are chosen as they give a $\bar{\phi}_t$ greater than the amplitude of the average bubble at nucleation. We compare three choices for threshold below, and confirm that our results are not highly sensitive to the value chosen over a significant range.

4. To confirm that a peak is indeed a nucleation event, we check the field evolution within the future light-cone of the detection site. In order for a detection site to be classified as a nucleation event, we require that the field within the future light cone both exceeds detection threshold over a period $\sim m^{-1}$ and remains within the true vacuum well. Specifically, if the field peak returns to the original false vacuum we consider that the bubble has dispersed. Alternatively, if the amplitude reaches a different false or true vacuum, we consider that the signal corresponds to a collision of the bubble wall with large fluctuations in the background field, or with another bubble. These cases are excluded by imposing amplitude cuts at $\bar{\phi}_t \leq \bar{\phi} \leq 2\pi$.

5. Once a nucleation event is located, we do not assign further nucleation events within its future light-cone or within the bounds of the bubble at subsequent times (the bubble associated to a nucleation event is defined as the field region where $\bar{\phi} > \bar{\phi}_t$). Imposing a maximal amplitude cutoff as described in the previous step is also useful way of discarding false signals that mimic a nucleation event around the bubble wall, which occur marginally outside of the future light-cone of the nucleation sites and would otherwise add noise to our data.

To identify nucleation events for bubbles decaying to $\bar{\phi}_{\rm tv} = 0$ we reflect the field around the original false vacuum $\bar{\phi} = \pi$ through the linear transform $\bar{\phi} \to 2\pi - \bar{\phi}$ and apply the detection algorithm to the transformed field.

We simulated ensembles of $30,000$ field evolutions for three choices of potential parameters: $\{\phi_0 = 1.35, \lambda = 1.5\}$, $\{\phi_0 = 1.27, \lambda = 1.5\}$, and $\{\phi_0 = 1.35, \lambda = 1.6\}$. These combinations produce field evolutions with sufficiently rapid nucleations to have multiple events within a single simulation. The physical size of the lattice is $\phi_0^{-1}\sqrt{V_0}L = 200\sqrt{2}$ with $V_0 = 0.008\ \phi_0^2\mu^2$, and $N = 8192$ lattice sites. The field spectrum is truncated at wavenumber index $n_{\rm cut} = 256$, corresponding to a wavenumber $k_{\rm cut} \approx 5.7\phi_0^{-1}\sqrt{V_0}$. The lattice spacing is $\mathrm{d}x = L/N$ and the discrete time step was $\mathrm{d}t = \mathrm{d}x\,/16$.

We checked that these parameters ensure a fully resolved vacuum state. To do this, we ran ensembles of 100 simulations initialized with a sequence of modes up to the $n_{\rm cut} = 256$ threshold used in our final results. First, we set $n_{\rm cut}$ to the Nyquist frequency $n_{\rm nyq} = N/2$, then we gradually changed N such that $n_{\rm nyq}$ increased each time by a factor of 2. At each resolution, the coordinates assigned to bubble nucleation events remained constant, proving that the modes not sampled (i.e. between $n_{\rm cut} = 256$ and $n_{\rm nyq}$) do not change the realizations significantly.

To measure the efficiency of our detection algorithm, we visually inspected 100 simulations for each combination of $\{\phi_0, \lambda\}$ and smoothing scale. We refer to a true positive event as one that has been confirmed as a true nucleation event by visual inspection; a false positive is an event that is detected but confirmed false by visual inspection. We define the efficiency as the ratio of true positive events to all positive (i.e. true positive and false positive) events. For $R_0 = \bar{R}/4$ we estimate the efficiency for all three thresholds at $> 95\%$ when $\lambda = 1.6$ and $> 93\%$ when $\lambda = 1.5$ by counting the fraction of false positive events out of the total. Fig. 2.4 shows three events which we labelled as false positives: the orange triangle at $\phi_0^{-1}\sqrt{V_0}\ t \approx 17$ is clearly within the wall of a bubble previously accounted for by the orange detector; meanwhile we considered the yellow circle and blue star at roughly $\phi_0^{-1}\sqrt{V_0}\ r \approx 110$ to correspond to background field fluctuations. Around 60% of false positive events are misattributions within the physical extent of bubble walls, while the remaining 40% of false positive assignments are represented by large amplitude vacuum fluctuations in the background field that eventually dissipate. Visual confirmation of results is subjective but gives a rough estimate for the error. According to our test, the total number of detected events differs by at most 4% between the three thresholds, and this difference is made up of mostly false positive events. Moreover, the largest threshold $\bar{\phi}_t$ gives up to twice as many false positives compared to the other two thresholds. The explanation for this difference is the following: since the bubble grows in amplitude with time, higher thresholds assign the events to later times than the lowest threshold and decrease the extent of the light-cone for the respective bubble, leading to erroneous detections at late times, i.e. the example of the orange triangle at $\phi_0^{-1}\sqrt{V_0}\ t \approx 17$ in Fig. 2.4. We do not have an estimate for the percentage of false negatives (i.e. nucleations that have not been detected). However, by visual inspection, false negative candidates appear only around nucleation sites already accounted for (e.g. two neighbouring peaks that merge during the bubble formation process can, in some cases, be detected as a single nucleation site, but sometimes as two). The number of bubble nucleation sites in such clusters is intrinsically ambiguous, and it depends on the details of how nucleation events are defined. The inclusion of such false negatives would make the correlation function computed in the next section larger at small separations. Moreover, since bubbles form with a range of

centre-of-mass velocities, their spatial coordinate also changes between different detection thresholds. Consequently, we discard as unphysical events that coincide exactly in (t, r) for all three thresholds, noting that on average only about 20% of these are indeed confirmed visually as nucleation sites for bubbles. We do not find a significant number of false negatives associated with bubbles that have large centre-of-mass velocities so long as they are not associated with clusters of nucleation events, implying that relativistic length contraction does not affect the ability of our algorithm to detect bubbles.

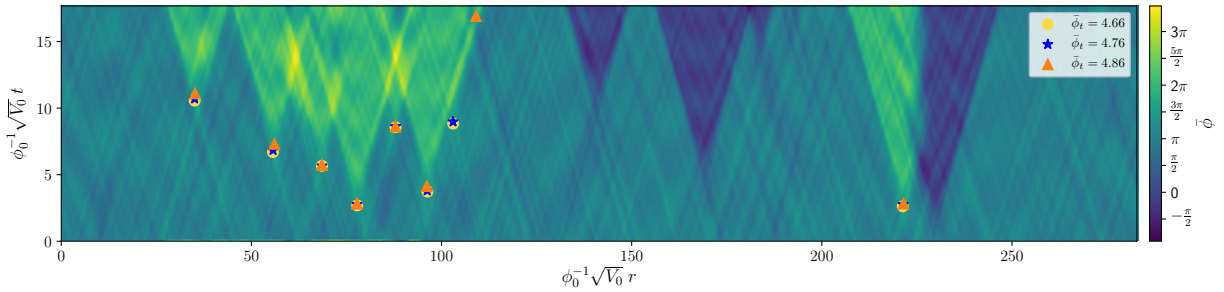

Figure 2.4: An example simulation with bubbles formed through both decay channels. We ran the detection algorithm to identify the nucleation sites of bubbles decaying to the true vacuum at $\bar{\phi}_{\rm tv} = 2\pi$. The detected nucleation events are shown for each threshold $\bar{\phi}_t$. The smoothing scale used here is $R_0 = \bar{R}/4$. We show two of the most common types of detection error. First, the orange triangle at $\phi_0^{-1}\sqrt{V_0}\, t \approx 17$ corresponding to the largest threshold is found around the edge of a bubble already accounted for, and second the background field fluctuations at $\phi_0^{-1}\sqrt{V_0}\, r \approx 110$ picked up by the two lowest thresholds.

2.5 Bubble-Bubble correlation function

In the previous section, we made a connection between extrema in fluctuations about the false vacuum and bubble nucleation events. In analogy with the free field case, where peaks are correlated, we might expect the same to be true for bubble nucleation events. Indeed, we now show that this is the case. This is the main result of this Chapter.

The bubble-bubble correlation function $\xi_{bb}(t, r)$ measures the probability in excess of random that a bubble is found a fixed distance in space and time away from another. Measuring this correlation function in our data is essentially a counting problem. The bubble-bubble correlation function is defined by looking at the distribution of bubble nucleation sites. The nucleation sites are defined as the coordinate pairs (t, r) where the field

amplitude satisfies the conditions we enumerated in the section above. We are asking what is the probability that if a bubble is nucleated at spacetime coordinates $(0,0)$, another bubble is created within $[t, t+\Delta t)\phi_0^{-1}\sqrt{V_0}$ and $\pm[r, r+\Delta r)\phi_0^{-1}\sqrt{V_0}$. By analogy with the equal-time two-point correlator, we estimate the bubble-bubble correlation function using

$$1 + \xi_{bb}(t,r) = \left\langle \frac{1}{B}\sum_{i=1}^{B} \frac{B_i(t,r)}{\rho V_i(t,r))} \right\rangle , \tag{2.30}$$

for a sample containing $B \in \mathbb{N}$ bubble nucleation sites. Here, $B_i(t,r)$ is the number of bubbles lying in a shell of fixed spacetime volume $V_i = 2\Delta t \Delta r\, \phi_0^{-2} V_0$ and minimal separation t and $\pm r$ in time and space, respectively, from the i^{th} bubble. We have defined the binning parameters $\Delta t = 16 n_t\, \mathrm{d}t$ and $\Delta r = n_r\, \mathrm{d}x$ and $n_t \in \mathbb{Z} \setminus \{0\}$ and $n_r \in \mathbb{N}, n_r \leq N/2$. ρ plays the role of the bubble number density for the respective sample. Averaged over all samples, we obtain our estimate for the correlation function.

We first compute the equal-time bubble correlator, given by equation (2.30) where $t = 0$ (defining 'equal-time' since the reference bubble is translated to $t = 0$). The number density of nucleation sites ρ is computed in each realization. Using an ensemble-average number density produces very similar results for the correlation function. Because the false vacuum has two decay channels, we can construct four different bubble-bubble correlation functions: ξ_{bb}^{--} is the correlator between two bubbles filled with $\bar{\phi} = 0$, ξ_{bb}^{++} is the correlator between two bubbles filled with $\bar{\phi} = 2\pi$, ξ_{bb}^{+-} is the correlator between one bubble filled with $\bar{\phi} = 0$ and one with $\bar{\phi} = 2\pi$, and ξ_{bb} is the correlator between all bubbles. Because the potential is symmetric about the false vacuum, we have $\xi_{bb}^{++} = \xi_{bb}^{--}$. We verify that this is true in our numerical results, providing one check against biases in our algorithm for locating nucleation events. The average number density of bubbles filled with either vacuum is equal across the ensemble, therefore ξ_{bb} is the correlation function of twice more frequent events than either ξ_{bb}^{++} or ξ_{bb}^{--}.

The result for the three distinct equal-time correlators is shown in Fig. 2.5 corresponding to the different choices of the threshold, as well as two smoothing scales, in the bubble finding algorithm. To estimate the errors, we break our ensemble of $30,000$ simulations into 30 ensembles of 1000 simulations each. We compute the peak-peak correlator in each sub-ensemble, and use the RMS of the sub-ensemble means in each radial bin as an estimate of the error. Most importantly, we see from $\xi_{bb}^{++}(t,r)$ that bubbles of the same type have a statistically significant and non-trivial positive correlation. Nucleation events are significantly correlated, and therefore cluster, over a distance of order a few times the initial size of bubbles when they nucleate, $\bar{R}$. Bubbles of opposite type have a negative correlation $\xi_{bb}^{+-}(t,r)$, which follows from the fact that finding a large peak and a large

trough near each other in the field is a rare event. The dependence of $\xi_{bb}^{++}(t,r)$ on the threshold chosen in the bubble finding algorithm is significant, but the qualitative features of the correlation function remain unaltered. The mismatch is a result of the different definitions for a nucleation site that each threshold implies. Some signals in the field are detected as bubbles for one choice of $\bar{\phi}_t$, but not for another. Moreover, different thresholds assign a different location for each bubble nucleation event (e.g. a larger choice of threshold implies a relatively later stage in the process of formation for a bubble). Therefore events corresponding to the same bubble might show up in different bins of ξ_{bb}, depending on $\bar{\phi}_t$. Note, however, that the correlation function peaks at roughly the same scale regardless of the choice of threshold. We also compare two choices of smoothing scale, equal to $\bar{R}/4$ (top panel of Fig. 2.5) and $\bar{R}/2$ (bottom panel of Fig. 2.5). As expected, for a larger smoothing scale, we lose the ability to resolve correlations at short distances. Smoothing is equivalent to coarse-graining the lattice, merging clusters into single, stand-alone bubbles. Nevertheless, there is still a significant correlation for identical bubbles, and a significant anti-correlation for non-identical bubbles.

In Fig. 2.6, we compare the bubble-bubble correlation function to the peak-peak correlation function obtained for a free massive scalar with mass set by the curvature about the false vacuum. We choose the lowest threshold imposed in the bubble finding algorithm, and compute the correlation function for three choices of potential parameters. The qualitative similarity between the bubble-bubble and peak-peak correlator is apparent (with an exclusion region, peak, and decay), and for this choice of threshold there is even reasonably good agreement in the amplitude.

There are, however, a few important differences. Increasing the threshold for the free field reduces the number density of peaks, thus increasing the amplitude of the correlation function. For a perfect bubble detection algorithm, there should be a critical value for the threshold beyond which the bubble finding algorithm will be insensitive to the threshold choice, at least until it approaches the true vacuum. This is because once the threshold is high enough for bubbles to form, increasing the threshold should only displace the nucleation event in space and time. However, as commented on above, the highest threshold has the largest false-positive rate. This systematic has the effect of suppressing the correlation function with increasing threshold. This is the reason we have chosen the lowest threshold, which has the lowest false-positive rate, and should more faithfully represent the true bubble-bubble correlator. Another difference is the change in amplitude of the correlation function for different potential choices. For peaks in the free field, larger values of ϕ_0 decrease the amplitude of vacuum fluctuations relative to the width of the false vacuum minimum, decreasing the number density of peaks exceeding our threshold and leading to stronger clustering (comparing the red and blue curves in Fig. 2.6). For bubbles,

the nucleation rate does decrease with increasing ϕ_0 as expected. However, the clustering of bubbles for the two different values of ϕ_0 we probed is unchanged, as we see when comparing the correlation functions for potentials with $\lambda = 1.5$ and $\phi_0 = 1.35$ vs $\phi_0 = 1.27$ in Fig. 2.6. The fractional increase in the peak correlation function is far larger than for the bubble correlation function. On the other hand, increasing λ at fixed ϕ_0 makes both peaks and bubbles more rare on the lattice (in fixed length units of $\phi_0^{-1}\sqrt{V_0}$), manifesting as a higher amplitude correlation function in both cases. Finally, the peak-peak correlator has a maximum closer to the filter width than the bubble-bubble correlator. This is due to the fact that bubbles are somewhat larger than the filter, and cannot cluster on scales smaller than their size (which is roughly 4 times the filter width).

In Fig. 2.7 we show the ensemble-averaged ξ_{bb}^{++} correlator in both space and time (2.30) for the three parameter choices for $\{\phi_0, \lambda\}$. The contours describe the increased (or decreased) probability for a bubble to nucleate at some point $\{t, r\}$ given a bubble whose nucleation centre is at $\{t = 0, r = 0\}$ In the standard picture of vacuum decay, the bubble at the origin would nucleate at $t = 0$ with a size of $r = \bar{R}$ and the wall would expand on the hyperbolic trajectory shown in Fig. 2.7. We also show the past-directed hyperboloid for reference. Note that the correlation function has no structure inside of the bubble wall hyperboloid, which is a good check on the bubble detection algorithm: nucleation events cannot happen inside of a bubble or in its causal past. Additionally, note that the correlator is time-symmetric, but it does not have a symmetry with respect to Lorentz boosts. Although the vacuum state is Lorentz invariant, a configuration with a bubble nucleation event is not. From the perspective of the peak-peak correlator in a Gaussian random field, we could understand the decay of the correlation function in time as being due to the finite lifetime of peaks. Therefore, clustering should occur in a concentrated region of both space and time. We now discuss the phenomenological consequences of a space-time bubble correlation function.

2.6 Phenomenological implications

In this section we briefly highlight the phenomenological implications of a non-trivial bubble-bubble correlation function. We can begin to understand these implications by considering Fig. 2.7. Given a bubble at some location in spacetime, there is an enhanced probability of another bubble nucleating nearby in space and time. This is in contrast to the typical assumption that bubble nucleation events occur with equal probability in any region of spacetime. Consider an observer at the origin of the central bubble in Fig. 2.7, which originates at $\{t = 0, r = 0\}$. If another bubble were to nucleate from the false vac-

uum region outside of the central bubble, and in the causal past of the observer at proper time τ (the spacetime volume in Fig. 2.7 between the hyperbola and the past light-cone), then they would have causal access to a bubble collision. The average number of collisions $N(\tau)$ is an integral of the nucleation rate $\langle\rho\rangle$ over the spacetime volume available to nucleate colliding bubbles. The existence of a non-trivial bubble correlation function can lead to an enhancement or suppression in the average number of collisions given by:

$$\frac{N(\tau)}{N_0(\tau)} = \frac{\int_{V_{cp}(\tau)} \mathrm{d}t\, \mathrm{d}r\, \langle\rho\rangle\, (1+\xi(t,r))}{\int_{V_{cp}(\tau)} \mathrm{d}t\, \mathrm{d}r\, \langle\rho\rangle} = \langle (1+\xi(t,r)) \rangle_{V_{cp}(\tau)}, \tag{2.31}$$

where $V_{cp}(\tau)$ denotes the spacetime volume that is both in the causal past of an observer at proper time τ and also outside of their bubble. In the second equality we have assumed that $\langle\rho\rangle$ is independent of space and time, in which case the enhancement or suppression in the number of observed collisions is simply the average of the correlation function over $V_{cp}(\tau)$. From the definition of the correlation function, if an observer had access to the entire volume of space and time then this volume average would be unity. Crucially, for an observer at fixed proper time, the result of evaluating (2.31) will be non-trivial. For the examples shown in Fig. 2.7, we expect an enhancement in the number of observed collisions that peaks at a time of order $\tau \sim \bar{R}$ (when the peak in the correlator is encompassed by $V_{cp}(\tau)$) and subsequently decays with τ as the volume average dilutes the region of significant correlation. We show this in Fig. 2.8 by numerically integrating the amplitude of ξ_{bb}^{++} for each of the cases shown in Fig. 2.7. The data used is the raw binned data for the correlation function smoothed with a 1+1-dimensional Gaussian filter of size $3 \times 16\, \mathrm{d}t\, \phi_0^{-1}\sqrt{V_0} \approx 0.105$ and $5 \times \mathrm{d}x\, \phi_0^{-1}\sqrt{V_0} \approx 0.175$ in the time and space dimensions, respectively.

There are two contexts where bubble-bubble correlations could have interesting phenomenological consequences. The first is percolating phase transitions that produce observable gravitational waves [179, 156, 180]. The gravitational wave spectrum peaks at a frequency set by the average size of bubbles at the time when percolation occurs [179, 156, 180, 181]. In previous literature, it was assumed that bubbles nucleate at random positions, in which case the average size of bubbles at the time of collision is simply the duration of the phase transition. In the presence of a bubble-bubble correlation function such as the one in Fig. 2.7, bubbles are likely to form significantly closer together than in the standard picture. Understanding the consequences in detail is beyond the scope of the present study, but we can speculate that there will be a secondary peak in the gravitational wave spectrum corresponding to the scale over which bubbles are correlated, namely their initial radius. There may also be implications for the angular power spectrum of the stochastic gravitational wave background [182]. The second scenario where

bubble-bubble correlations could be relevant is bubble collisions produced during eternal inflation [142, 143, 144]. In this case, the enhancement in the expected number of collisions due to the bubble-bubble correlator described above will enhance the probability of observing the signatures of collisions in the CMB [183]. Again, we defer a detailed investigation of the consequences of such an enhancement to future work.

2.7 Discussion

In this Chapter, we showed that, analogously to the process of biased galaxy formation, the nature of the fluctuations around the false vacuum state gives rise to clusters of bubble nucleation sites. To our knowledge this is the first time biasing has been investigated in the context of bubble formation in vacuum decay. We found that a significant correlation exists between the nucleation sites of thick-wall bubbles in a single scalar field theory. A finite correlation length between bubble nucleation sites implies a greater chance of collisions between bubbles nearby in space and time. We briefly speculated that this could lead to new features in the stochastic gravitational wave spectrum associated with first-order phase transitions in the early Universe, and could increase the probability of observing the collisions between bubbles in the scenario of eternal inflation.

There are several directions for future work. Extending the present study to more spatial dimensions and confirming that the bubble-bubble correlation function is qualitatively similar to that presented here is clearly an important first step. Moreover, we explained that the existence of the bias is a consequence of the statistical properties of the fluctuations, rather than of their origin. This means that our discussion could be generalized to the thermal case with similar conclusions to be drawn. We expect that the only difference would be in the absolute magnitude of the bias parameter, however the scaling between bubble size at nucleation (depending largely on the shape of the potential) and the amplitude of the correlation should continue to be present. Testing these observations will be the subject of future work. Furthermore, a detailed investigation of the impact of the bubble-bubble correlation function on the phenomenology of first-order phase transitions in the early Universe should be undertaken. This could lead to new targets for future gravitational wave observatories such as LISA. In another direction, the potential we studied is motivated by the program of simulating vacuum decay in cold atom systems. These systems should exhibit a bubble-bubble correlation function analogous to the one investigated here, and could constitute an important observable. Exploring how the bubble-bubble correlation function can be used to determine the vacuum statistics could also be useful in understanding the results of these experiments. More broadly, the bubble-bubble correla-

tion function is just one example of how the real-time simulations of vacuum decay might be used. The next Chapter explores another possible application.

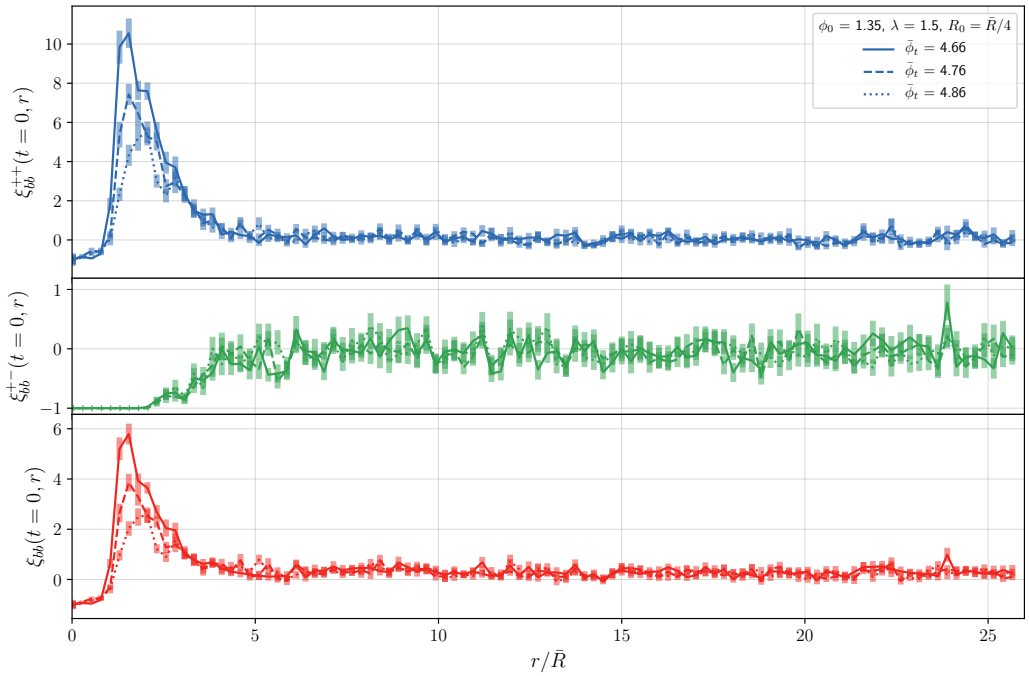

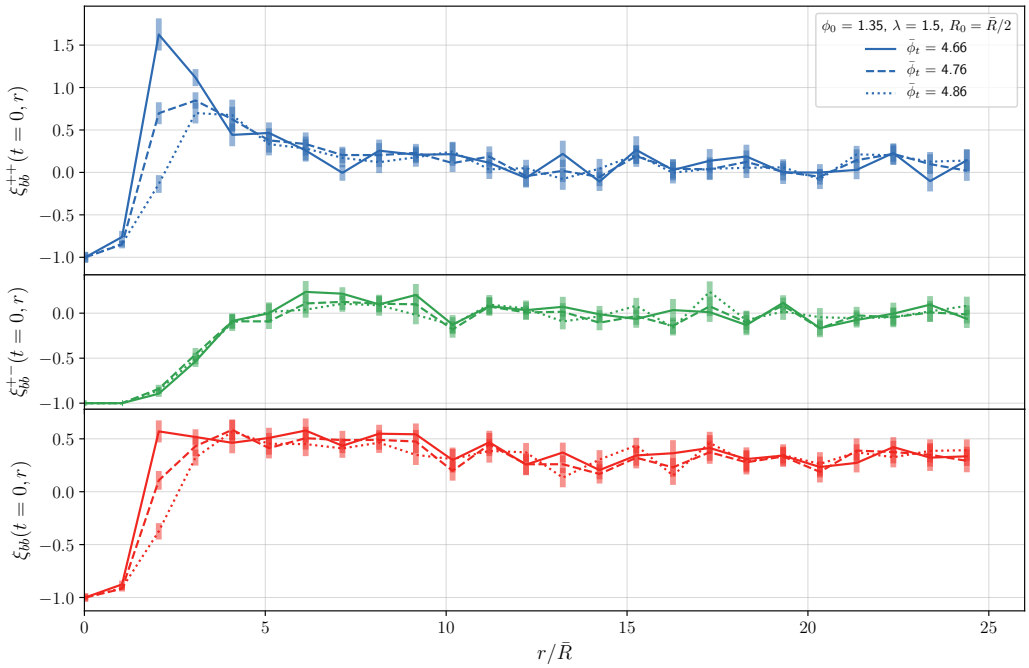

Figure 2.5: The image caption is on the next page.

Figure 2.5: The three types of bubble auto-correlation functions. In each panel, from top to bottom, these are the correlation between nucleation sites of like-bubbles, bubbles of opposite true vacua, and the total correlation function. We show them for the same choice of field parameters and threshold values $\{\phi_0, \lambda, \bar{\phi}_t\}$, but different smoothing filter widths: $R_0 = \bar{R}/4$ (top) and $R_0 = \bar{R}/2$ (bottom). Data is binned into volumes size $n_t = 3, n_r = 10$.

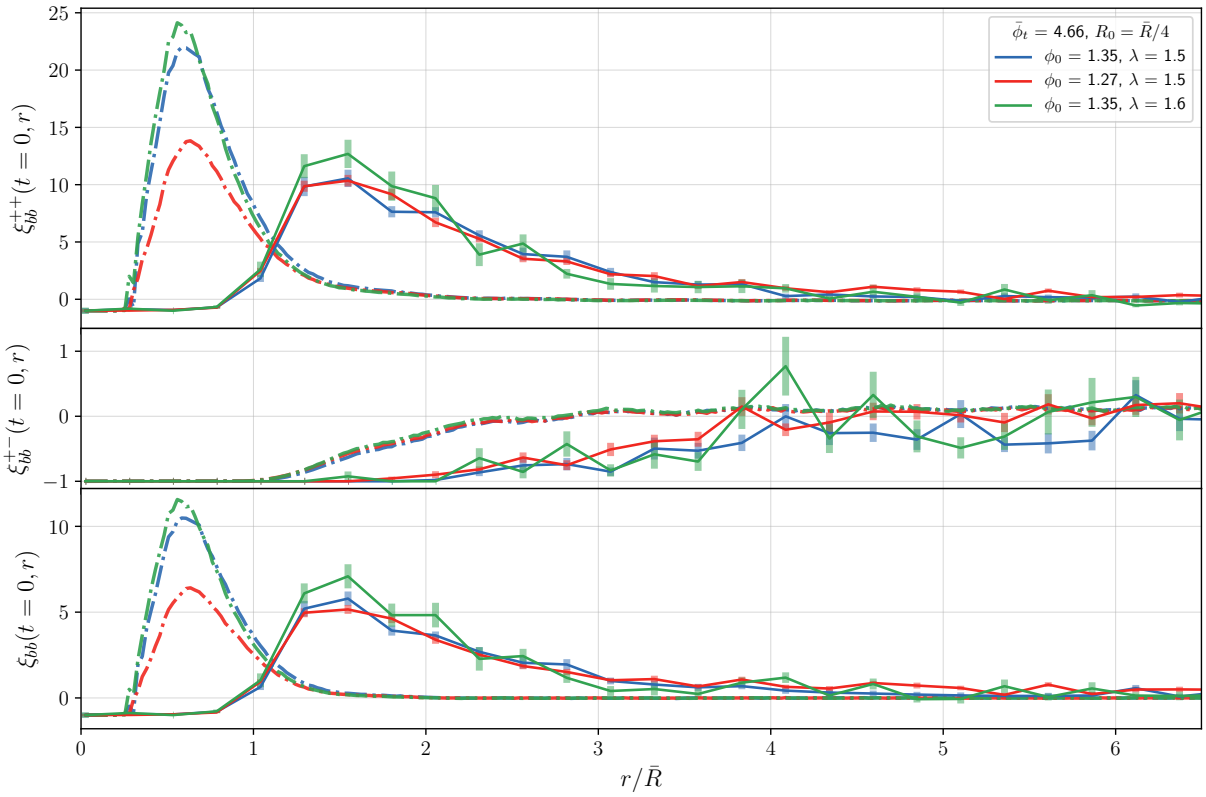

Figure 2.6: The bubble-bubble correlator $\xi_{bb}^{++}(t, r)$ (solid curves, with error bars) versus the peak-peak correlator $\xi_{pk}(r)$ (dotted curves, no error bars) for all three combinations of parameters $\{\phi_0, \lambda\}$ and fixed threshold $\bar{\phi}_t$ and smoothing scale $R_0 = \bar{R}/4$. The qualitative agreement between the curves is apparent except that the peak-peak correlator picks up amplitude at $r = R_0$, and the bubble-bubble correlator at $r = \bar{R}$, which is expected. The mixed two-point functions ξ_{bb}^{+-} and ξ_{pk}^{+-} show anti-correlation over scales up to the correlation length of their counterparts ξ_{bb}^{++} and ξ_{pk}^{++}. While the ξ_{pk} is sensitive to the size of the fluctuations at initialization ϕ_0, the ξ_{bb} only reacts noticeably to the λ parameter. Data is binned into boxes of size $n_t = 3$ and $n_r = 10$.

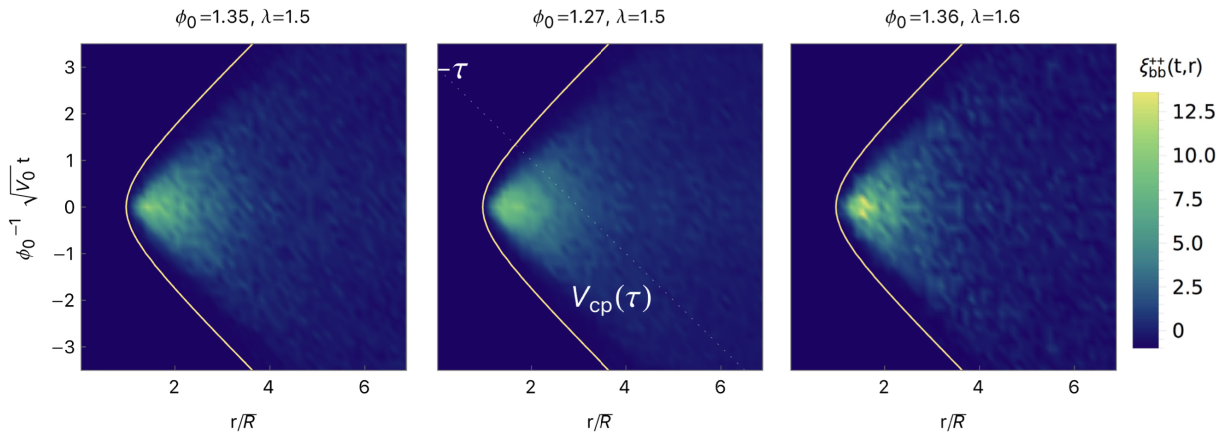

Figure 2.7: The 2-dimensional bubble-bubble correlator $\xi_{bb}^{++}(t, r)$ for all three combinations of parameters $\{\phi_0, \lambda\}$ and smoothing scale $R_0 = \bar{R}/4$. The correlation function implies clustering in both r and t directions. Data is binned into $n_t = 3$ and $n_r = 5$ intervals. Errors are not shown and symmetry is assumed for negative r. In each panel, we overplot the trajectory of the (time-symmetric) average bubble wall; a hyperbola with radius $\bar{R}$. In the centre panel, we depict the past light-cone of a hypothetical observer at the origin of coordinates. This observer will have causal access to bubbles that nucleate in the spacetime volume $V_{cp}(\tau)$ between the bubble wall and the past light-cone.

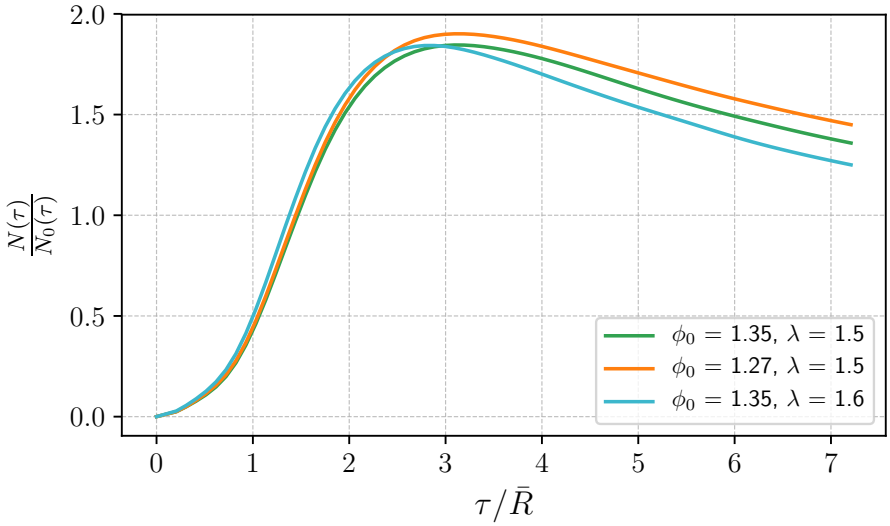

Figure 2.8: The fractional change in the number of observed collisions to the causal past of an observer situated at time τ at the centre of the reference bubble for the correlation functions in Fig. 2.7. The distribution peaks once the peak of the correlation function ξ_{bb}^{++} is entirely to the observer's past.

Chapter 3

Bubble velocities and oscillon precursors in first-order phase transitions

3.1 Introduction

In this Chapter we employ the classical stochastic description of vacuum decay on a single real scalar field with an initial Bose-Einstein distribution of fluctuations in 1+1 dimensions. We explore additional observable phenomena related to the dynamical process of bubble nucleation. We develop a set of algorithms to analyze in detail the properties of bubbles, before, during, and after nucleation. Our qualitative results are summarized in Fig. 3.1. Defining an empirical temperature for infrared modes on the lattice, the observed decay rate is consistent with the instanton prediction at this effective temperature. This is somewhat surprising as the input Bose-Einstein distribution is not the true thermal equilibrium state of the field, and thermalization is an extremely slow process in 1+1 dimensions. Nevertheless, we find throughout that the predictions of a thermal ensemble describe our empirical measurements well.

Studying individual nucleation events, we find that bubbles never form at rest. We measure the distribution of the bubble center-of-mass velocity, which has a variance determined by the effective temperature for infrared modes and the energy of the critical bubble. An accurate measurement of the center-of-mass velocity allows us to stack nucleation events in their rest frame to determine the critical bubble and its time evolution. The measured critical bubble is consistent with the thermal Euclidean instanton prediction. Focusing on the

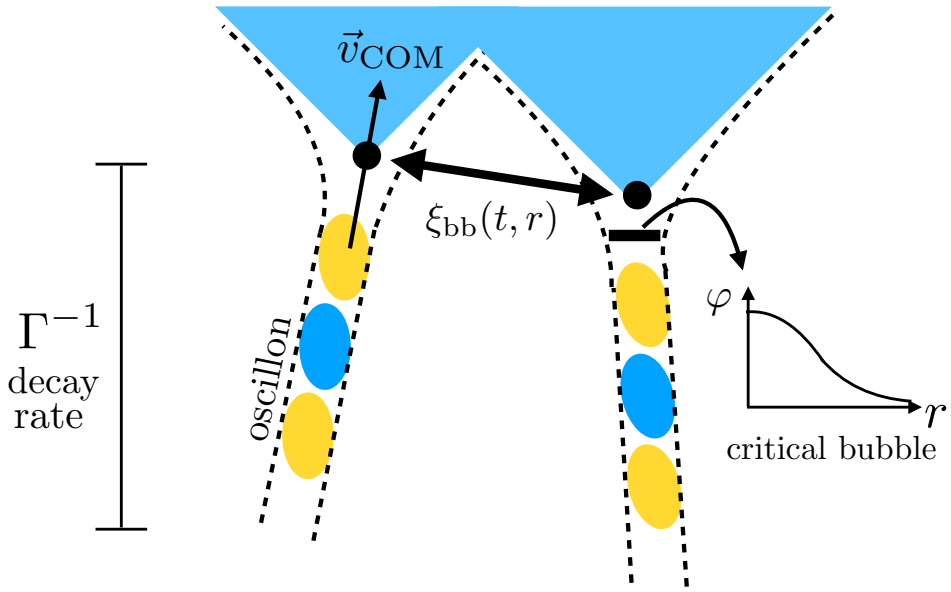

Figure 3.1: Observables in vacuum decay. The basic observables in vacuum decay are the decay rate Γ and the critical bubble profile $\varphi(r)$, which can both be predicted from the instanton techniques and measured from bubbles formed in real-time simulations. Observables beyond the decay rate include the bubble-bubble correlation function $\xi_{bb}(t,r)$ that was explored in Chapter 2, as well as the center-of-mass velocity $\vec{v}_{\rm COM}$ of nucleated bubbles and oscillon precursors that we investigate in this Chapter.

field configuration prior to nucleation, we confirm the prediction of Ref. [30] that the most likely formation channel for bubbles includes an oscillon precursor. Oscillons are long-lived time-dependent field configurations [23] arising in scalar field theories with anharmonic potentials (see e.g. [24, 25]), whose role in vacuum decay has been discussed previously in Refs. [26, 27, 28, 29, 30]. The existence of bubble precursors and a center-of-mass velocity distribution could only have been confirmed with real-time description of vacuum decay, and open the door to further investigations using similar techniques. Further, we speculate that these features of vacuum decay can have observable implications for early-Universe phenomenology.

Further details on the interpretation of decay and bubble nucleation in real-time simulations as well as possible experimental applications of our work are given in Appendix A.1. In particular, cold atom simulations of vacuum decay have recently been performed [50], with further results expected in the near future [43]. The detailed properties of vacuum

decay described above will be important observables for these experiments. Through comparing these observations with simulation and other real-time theoretical descriptions, we hope to learn a great deal about the fundamentals of vacuum decay.

The Chapter is organized as follows. In section 3.2 we give an overview of the Euclidean instanton description for vacuum decay at finite temperature, and the properties of the critical bubble solution. In section 3.3 we introduce our numerical tools. Section 3.4 introduces several new observables in false vacuum decay and describes in detail the computational methods that were used to extract them. We discuss the role of field fluctuations for thermalization in section 3.4.1 and measure the effective temperature and mass of the field about the false vacuum. We measure the decay rate from lattice simulations and compare it to the predictions of the thermal Euclidean theory in section 3.4.2. In section 3.4.3 we measure the distribution of the center-of-mass velocities of nucleated bubbles in ensembles of simulations. In section 3.4.4 we stack many nucleation events to determine the ensemble-averaged most likely bubble configuration directly from the simulations. In section 3.4.5 we show that bubble nucleation events are preceded by oscillons. In section 3.4.6 we verify the consistency of several measurements of the critical bubble energy. Finally, we comment on the implication of these new observables for early universe scenarios in section 3.5. We assume the units with $c = 1$ and work in the limit $\hbar \to 0$, unless stated otherwise.

3.2 Euclidean computation of the decay rate at finite temperature

We consider a scalar field theory in $1+1$-dimensions, defined by the same Lagrangian and potential:

$$\mathcal{L} = \frac{1}{2}\dot{\varphi}^2 - \frac{1}{2}\left(\partial_r \varphi\right)^2 - V(\varphi), \tag{3.1}$$

$$V(\varphi) = V_0 \left[-\cos\left(\frac{\varphi}{\varphi_0}\right) + \frac{\lambda^2}{2}\sin^2\left(\frac{\varphi}{\varphi_0}\right)\right]. \tag{3.2}$$

Fig. 3.2 illustrates the potential for the case where $\lambda = 1.5$, which is of relevance for the data analysis done in this Chapter.

In thermal equilibrium at some temperature T, the decay rate can be computed using Euclidean instanton techniques [19, 20]. The goal is to find saddle points of the Euclidean action (equivalently the partition function) corresponding to critical bubble solutions that interpolate between a false vacuum initial condition and a true vacuum final

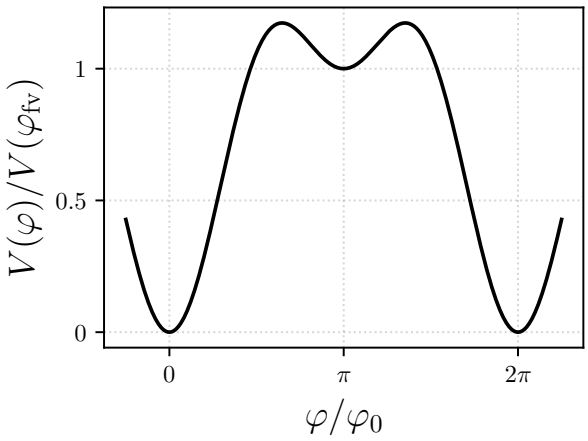

Figure 3.2: Choice of bare potential for the relativistic field φ that supports the formation of bubbles of true vacuum. It is given by (3.1) where $\lambda = 1.5$. The field starts off in the false vacuum centered at $\varphi_{\rm fv} = \pi\varphi_0$ and can decay to either $\varphi_{\rm tv} = 0$ or $\varphi_{\rm tv} = 2\pi\varphi_0$.

condition - a bubble. Beyond the temperature, the most important scale in the problem is the characteristic (Euclidean) size of the bubbles. This can generically be estimated as $r \sim 1/\sqrt{\partial_\varphi^2 V(\varphi_{\rm fv})} \equiv m^{-1}$ (it could be far larger in the thin-wall limit, but we do not consider such cases here). The statistical mechanics of the field at finite temperature can be described by a field theory in Euclidean space with a time variable that has period $\beta \equiv \hbar/T$. For $T \ll \hbar m$, the bubble is far smaller than the size of the time dimension, and the full (in our case 2 dimensional) Euclidean solution must be used - this is the solution appropriate to describe quantum mechanical formation of bubbles [18, 17]. In the opposite limit where $T \gg \hbar m$, the bubbles are far larger than the size of the time dimension, and the solutions are independent of Euclidean time.

The relevant saddle point solution $\varphi_{\rm crit}(r)$ (also known as the 'critical bubble') in the high-temperature limit is found by solving

$$\partial_r^2 \varphi_{\rm crit} = \partial_\varphi V(\varphi_{\rm crit}), \tag{3.3}$$

with the boundary conditions $\varphi(r \to \infty) = \varphi_{\rm fv}$ and $\partial_r \varphi(r \to 0) = 0$. We disregard thermal corrections to the potential which are small for the case of a single scalar field studied here. Note, however, that they may be important if the decaying field couples to other species. The prediction for the decay rate per unit time per unit volume in our 1+1 dimensional system is

$$\Gamma = AB^{1/2}e^{-B}, \tag{3.4}$$

where the critical bubble action (divided by $\hbar$) is given by

$$B = \frac{1}{T}\int \mathrm{d}r \left[\frac{1}{2}\left(\frac{\partial\varphi_{\rm crit}}{\partial r}\right)^2 + V(\varphi_{\rm crit})\right] = \frac{E_{\rm crit}}{T}. \tag{3.5}$$

In expression (3.4) the exponential term is the solution to the saddle point approximation to the path integral with one periodic dimension of size $\hbar/T$, while the factor A encompasses the effects of fluctuations around this solution. The factor of $B^{1/2}$ comes from integrating out the shift-symmetric degree of freedom. See e.g. [184, 185] for a review of thermal instanton theory.

The critical bubble $\varphi_{\rm crit}$ is also a static solution to the Lorentzian equation of motion

$$-\partial_t^2\varphi_{\rm crit} + \partial_r^2\varphi_{\rm crit} = \partial_\varphi V(\varphi_{\rm crit}). \tag{3.6}$$

It is unstable to either growth or collapse under small perturbations. For illustration, in Fig. 3.3 we show the time evolution of a slightly rescaled configuration $\varphi_{\rm crit}(r, t = 0)$ under the equations of motion (3.6). The field profile at $t = 0$ for the image on the left is the solution where the central value of the field in the bubble is $\varphi(r = 0) = 4.8238\varphi_0$. The stationary field profile remains nearly static for a finite amount of time, and then expands into the true vacuum. Once the bubble wall begins to expand, the surfaces of constant field follow timelike hyperboloids $\sqrt{r^2 - (t - t_0)^2} = \text{const}$, while the surfaces of constant field inside the bubble follow spacelike hyperboloids $\sqrt{(t - t_0)^2 - r^2} = \text{const}$. The spontaneous generation of hyperbolic symmetry in expanding thermal bubbles was studied in detail in Ref. [186], where it was shown to be a generic phenomenon. On the right, we change the central value of the field by one part in 10^4 choosing $\varphi(r = 0) = 4.8237\varphi_0$. This yields a solution that collapses, forming an oscillon. The collapse of subcritical bubbles into oscillons was first discussed in Ref. [27].

3.3 Lattice simulations

In this Chapter, we focus again on a single scalar field in 1+1 dimensions. We take initial conditions where the 'occupation number' in each Fourier mode is given by the Bose-Einstein distribution:[1]

$$n_k = \frac{1}{e^{\omega_k/T} - 1}, \quad \omega_k^2 = m^2 + k^2. \tag{3.7}$$

[1]This is a classical analog of the occupation number. It is related to the true occupation number $\hat{n}_k$ by $n_k = \hbar\hat{n}_k$. So, $\hat{n}_k$ diverges in the classical limit $\hbar \to 0$ with n_k fixed.

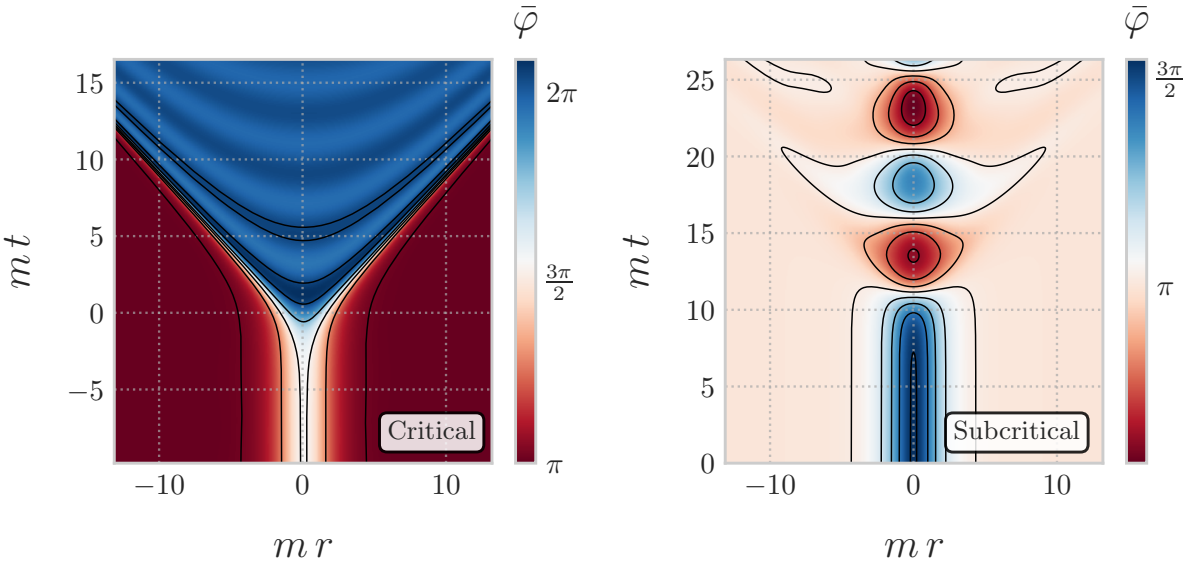

Figure 3.3: The time evolution of the critical bubble solution to (3.6). The critical bubble is in unstable equilibrium between expansion and collapse, and small changes to the initial condition determine the outcome. Here we show both outcomes, where the black contours denote constant field amplitude. Lengths and times are measured in terms of $m \equiv \sqrt{\partial_\varphi^2 V(\varphi_{\rm fv})}$; the normalized field is $\bar{\varphi} \equiv \varphi/\varphi_0$. The false vacuum is located at $\bar{\varphi} = \pi$; the true vacuum is located at $\bar{\varphi} = 2\pi$. *Left:* After loitering near the critical solution, the field evolves to the true vacuum inside an expanding bubble. The constant-field surfaces composing the expanding wall and the bubble interior asymptote to timelike and spacelike hyperboloids, respectively. *Right:* The field configuration is slightly subcritical (the central value of the field is altered by one part in 10^4 as compared with the left panel), so after a brief loitering period, it collapses into an oscillon - a long-lived compact oscillating field configuration.

Using the potential (3.1), we set the scalar field mass m^2 equal to the curvature around the false vacuum $m^2 = V''(\bar{\varphi}_{\rm fv})$. The field and conjugate momentum have the spectra:

$$\langle \delta\varphi_k^* \delta\varphi_{k'} \rangle = \frac{n_k}{\omega_k}\, \delta(k - k'), \quad \langle \delta\Pi_k^* \delta\Pi_{k'} \rangle = n_k \omega_k\, \delta(k - k'), \quad \langle \delta\varphi_k \delta\Pi_{k'}^* \rangle = 0. \tag{3.8}$$

Throughout this Chapter we will use the $\langle \cdot \rangle$ notation to denote an ensemble average unless otherwise stated. Initial configurations of the field and conjugate momentum are random draws from a multivariate Gaussian for each mode with covariance (3.8).

Let us make an important comment. The choice of the Bose-Einstein distribution for the initial conditions is convenient since it ensures approximate equipartition of energy among long modes relevant for bubble nucleation, while exponentially cutting off the power in the ultraviolet, thereby reducing the sensitivity to the lattice spacing. However, it *does not* represent an equilibrium thermal distribution of the classical field theory which we simulate. In a free theory, the equilibrium would correspond to the Rayleigh-Jeans spectrum which has a significant power in the ultraviolet and is numerically challenging. Presence of the field self-interaction further complicates the definition of the equilibrium state – in fact, makes it strictly speaking impossible for the dynamics around a *metastable* false vacuum.[2]

On the other hand, thermalization is extremely slow in $1+1$ dimensions [194]. This provides an opportunity of studying in real time false vacuum decay from non-equilibrium states – a process inaccessible with Euclidean methods (see [195] for the generalization of the instanton techniques for this case). The initial state with the spectrum (3.7) should be viewed as an example of such non-equilibrium configurations. Remarkably, we will see that nucleation of the true vacuum bubbles in this state still admits an approximate thermal description, albeit with an effective temperature $T_{\rm eff}$ different from the parameter T in the initial Bose-Einstein distribution (3.7). We give more details on the spectrum and its evolution below. We stress that our focus in this thesis is not on defining a precise physically motivated set of initial conditions, but rather the identification of new observables in vacuum decay beyond the decay rate. The quantitative predictions for observables in specific early-Universe or experimental scenarios can be obtained by extending our results to different choices for the initial state. The mean field and conjugate momentum at initialization are chosen precisely at the false vacuum, while fluctuations are sampled

[2]The Rayleigh-Jeans spectrum was adopted in the first numerical studies of non-perturbative processes in classical field theory in $1+1$ dimensions [187, 188, 189]. Other previous works [190, 191, 192, 193] either explicitly introduced a heat bath, a thermalization phase preceding a sudden change in the potential (a quench), or incorporated the effect of a heat bath into effective equations of motion. This introduces additional complexity and model assumptions that are avoided in our approach - we simply have an ensemble of closed systems with an initial spectrum of fluctuations.

stochastically in each realization around these values according to $\bar{\varphi}(r, t=0) = \pi + \delta\bar{\varphi}(r)$ and $\bar{\Pi}(r, t=0) = \delta\bar{\Pi}(r)$, where

$$\begin{aligned} \delta\bar{\varphi}(r) &= \frac{1}{\varphi_0}\frac{1}{\sqrt{L}}\sum_k \left[\frac{\hat{\alpha}_k}{\sqrt{\omega_k}}\frac{e^{ikr}}{\sqrt{e^{\omega_k/T}-1}} + \text{ c.c. }\right], \\ \delta\bar{\Pi}(r) &= \frac{1}{\varphi_0}\frac{1}{\sqrt{L}}\sum_k \left[\hat{\beta}_k\sqrt{\omega_k}\frac{e^{ikr}}{\sqrt{e^{\omega_k/T}-1}} + \text{ c.c. }\right]. \end{aligned} \tag{3.9}$$

The complex random deviates $\hat{\alpha}_k$ and $\hat{\beta}_k$ are drawn from a Gaussian distribution of unit variance. Each realization of the initial conditions is then evolved using equations of motion

$$\begin{aligned} \frac{\mathrm{d}\bar{\varphi}}{\mathrm{d}t} &= \bar{\Pi}, \\ \frac{\mathrm{d}\bar{\Pi}}{\mathrm{d}t} &= \nabla^2\bar{\varphi} - \frac{V_0}{\varphi_0^2}\left[\sin(\bar{\varphi}) + \frac{\lambda^2}{2}\sin(2\bar{\varphi})\right]. \end{aligned} \tag{3.10}$$

The parameter φ_0 controls the width of the potential, while V_0 controls its height. The potential and lattice parameters are fixed throughout this Chapter. The only parameter we vary across ensembles is T in the initial spectrum (3.7) which can take one of the following values: $T = \{0.9m, m, 1.1m, 1.2m\}$. The potential is defined by $\lambda = 1.5$ and $V_0/\varphi_0^2 = 0.008$, with $\varphi_0 = 2\pi/4.5$. The physical size of the lattice is $L = 50\sqrt{2}\varphi_0/\sqrt{V_0}$ and we sample $N = 1024$ points. This gives a lattice unit $\mathrm{d}r = L/N \approx 0.77$ and an IR scale $\mathrm{d}k = 2\pi/L \approx 7.95 \times 10^{-3}$. Wave-numbers k run from $k_{\mathrm{IR}} = \mathrm{d}k$ to $k_{\mathrm{UV}} = \mathrm{d}kN/2$. We perform a total of 4000 simulations at each value of T, and monitor the time evolution up to at most $5L$, i.e. five lattice crossing times, or until the field has completed the phase transition into the true vacuum. The discrete time step for the integration procedure is $\mathrm{d}t = \mathrm{d}r/16$. The speed of light is fixed in simulations to $c = \mathrm{d}r/\mathrm{d}t_{\mathrm{out}} = 1$, where $\mathrm{d}t_{\mathrm{out}} = 16\mathrm{d}t$ is the interval over which the data are output to produce spacetime diagrams such as e.g. Fig. 3.3. We typically express length and time scales as a function of the mass which is fixed to $m(\varphi) = V_0\varphi_0^{-2}\left(\lambda^2 - 1\right) = 0.1$ in the dimensionless code units. The critical bubble energy is $E_{\mathrm{crit}} \approx 0.33$ in the code units, or $E_{\mathrm{crit}} \approx 3.3m$. We also use the notation $\bar{\varphi} = \varphi/\varphi_0$, where $\bar{\varphi}$ is the normalized field amplitude. A summary of the most relevant parameters is given in Table 3.1. In the rest of this Chapter, all dimensionful quantities are plotted in terms of the bare mass scale m.

For future reference, we denote the expectation values for the variance of field and momentum fluctuations by $\sigma_\varphi^2 \equiv \langle\delta\varphi^2\rangle$ and $\sigma_\Pi^2 \equiv \langle\delta\Pi^2\rangle$, where the average is taken over many different realizations. At the initial moment of time we can write them in terms of

the Bose-Einstein distribution (3.7) as

$$\varphi_0^2\sigma_\varphi^2 = \frac{1}{L}\sum_k \frac{n_k}{\omega_k}, \quad \varphi_0^2\sigma_\Pi^2 = \frac{1}{L}\sum_k n_k\omega_k. \tag{3.11}$$

From low to high values of T, the ratio $\sigma_\varphi = \sigma_{\bar{\varphi}}/\varphi_0$ gives $\approx \{0.20, 0.22, 0.24, 0.26\}$, whereas $\sigma_\Pi = \sigma_{\bar{\Pi}}/\varphi_0 \approx \{0.028, 0.032, 0.036, 0.040\}$.

Parameter	Value in code units	Comparison with mass
Potential coupling λ	1.5	–
Potential barrier width φ_0	$2\pi/4.5$	–
Potential barrier height V_0	$0.008\varphi_0 \approx 0.011$	–
Bare field mass m	$\sqrt{V_0\varphi_0^{-2}\,(\lambda^2-1)} = 0.1$	m
Parameter in the initial spectrum T	$0.09, 0.1, 0.11, 0.12$	$0.9m, 1m, 1.1m, 1.2m$
Physical lattice size L	$50\sqrt{2}\varphi_0/\sqrt{V_0} \approx 791$	$80/m$
Lattice sample points N	1024	–
Maximum evolution time	$5L \approx 3953$	$400/m$
Lattice spacing $\mathrm{d}r$	$L/N \approx 0.77$	$0.08/m$
Integration time step $\mathrm{d}t$	$\mathrm{d}r/16 \approx 0.048$	$0.0005/m$
UV spectral cutoff $\mathrm{d}k$	$2\pi/L \approx 7.95\times10^{-3}$	$0.08m$
IR spectral cutoff k_{IR}	$\mathrm{d}kN/2 \approx 4.1$	$41m$
Critical bubble energy E_{crit}	≈ 0.33	$3.3m$

Table 3.1: List of relevant physical quantities used in this Chapter, together with their numerical values and comparison with the mass scale.

3.4 Observables in vacuum decay

In this section, we analyze the ensembles defined above to identify new classes of observables in vacuum decay. In the previous Chapter it was demonstrated that bubble nucleation centers cluster, and their two-point correlation function $\xi_{\mathrm{bb}}(t, r)$ was measured using simulations. Here, we demonstrate that a detailed study of nucleation events can reveal additional observables in vacuum decay. An overview is presented in Fig. 3.1. We expect the qualitative results to apply to a broad set of classical excited states about the false vacuum characterized by large occupation numbers and stochastic phases of the field modes.

We begin by examining the fluctuations about the false vacuum prior to bubble nucleation and measure the effective mass and temperature that the field fluctuations evolve under. Next we measure the decay rate observed in our ensemble of lattice simulations as a function of the effective temperature and find good agreement with the theoretical prediction of Euclidean instanton theory for finite temperature vacuum decay, as reviewed in section 3.2. Moving on to study individual nucleation events, a number of features are evident. First, we demonstrate that typical bubbles do not form at rest, but rather have a center-of-mass velocity distribution that agrees well with the hypothesis that boosted bubbles are Boltzmann suppressed. By stacking many nucleation events in their rest frame, we determine the critical bubble configuration on the lattice. This empirical profile closely matches the analytical critical bubble solution. Next, we observe that bubble nucleation is preceded by a long-lived oscillon precursor field configuration. Finally, we compare three different ways of determining the critical bubble energy: from the static solution of (3.3), from the stacked decaying numerical simulations, and from the bubble velocity distribution. We find them to be in good agreement. The analysis techniques we present can be used in future lattice simulations or experiments using analogue quantum simulators of vacuum decay.

3.4.1 Fluctuations around the false vacuum before decay

Beyond the formation of bubbles of the true vacuum, the non-linear nature of the potential coupled with the finite size of the system and finite lattice spacing have several important implications.

- The existence of field fluctuations around the minimum leads to a renormalization of the coupling constants m and λ for the effective potential seen by infrared modes on the lattice. These corrections depend on the field variance. These effects have been studied quantitatively in [32] for the potential we use here; for a detailed discussion of renormalization effects on thermal vacuum decay see e.g. [192, 193].

- Because the system is initially out of equilibrium, the statistics of the fluctuations about the false vacuum evolve in time. In particular, power is transferred from the IR to the UV. In principle, if the false vacuum were arbitrarily long-lived, the system could thermalize to a Rayleigh-Jeans spectrum with a new temperature.

- The effective couplings seen by IR modes on the lattice depend on the spectrum of fluctuations about the false vacuum. Since this spectrum is time-dependent, there

will be time evolution of the properties of the IR modes which participate in vacuum decay.

We choose the parameters of our simulations to mitigate the consequences of these effects. For the Bose-Einstein distribution with our choice of parameters, contributions to the field variance near the ultraviolet cutoff are small $\left\langle \delta\varphi^2_{k_{UV}} \right\rangle \to 0$. In this limit, the corrections to coupling constants in the potential depend only on the amplitude of long modes with $\omega \lesssim T$. We can then choose the values of T that are small enough such that corrections to the potential are small, but large enough to yield vacuum decay on a reasonable computational timescale. These choices also mitigate the second and third items above, since typical fluctuations do not experience the strong non-linearities away from the false vacuum and power that does 'cascade' to the UV does not contribute significantly to the field variance. Nonetheless, it is possible to extract empirically the effective mass and temperature of the IR fluctuations around the false vacuum. Since the critical bubble is itself made up of modes with wavenumber $k \sim R^{-1}_{\rm crit} \sim m\mathcal{O}(1)$, the occupation numbers of the long-wavelength modes and any changes from the initial theoretical spectrum will affect the observables of vacuum decay. We investigate these changes quantitatively in this section.

We begin by focusing on the members of our ensemble that do not decay. The initial conditions for these simulations are drawn from the Bose-Einstein distribution according to (3.8). Choosing the undecayed members of the ensemble yields an observable selection effect on the initial power spectrum in the infrared. In simulations where the initial power on scales relevant to the formation of the critical bubble $k < k_{\rm crit} \sim R^{-1}_{\rm crit}$ is larger than the average, the probability to form a bubble is enhanced. Therefore, the undecayed realizations have a deficit in initial power at low-k. Simulations where the phases and initial momentum cause a time-dependent loss of power at low-k are also members of the ensemble of undecayed solutions. The time-dependent loss of IR power in the field power spectrum with respect to the initial theoretical Bose-Einstein distribution is illustrated in Fig. 3.4. This is due to a combination of two main effects: the favoring of an initial deficit of power on scales relevant for bubble formation and a phenomenon we refer to as thermalization, where the IR power 'cascades' towards the ultraviolet over long time-scales as the closed system tends towards thermal equilibrium.

The fact that the high-k part of the power spectrum remains largely unperturbed implies that the time-dependent corrections to the couplings parameters experienced by UV modes is minimal over the timescales relevant here and that the far-UV tail of our field and its conjugate momentum remain exponentially suppressed. We conclude that UV effects associated with the finite lattice spacing are not important for the analysis below. On the other hand, the changes in the IR are visible in the power spectrum, as shown in

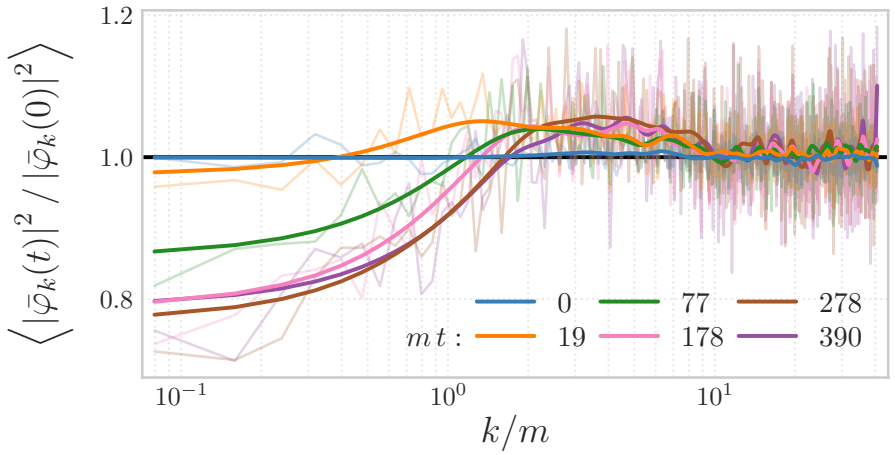

Figure 3.4: Ensemble averaged power spectrum at $T = 1.2m$ as a function of time, normalized with respect to the theoretical average power spectrum on the initial slice, n_k/ω_k as defined in (3.8). The faint lines show the true data, while the solid lines have been smoothed with a Gaussian kernel of width $0.48/m$ to visualize the shape of the spectrum. The ensemble average is performed over the realizations that have not decayed by the time t. Since the number of surviving simulations decreases as a function of time, the statistical fluctuations on the average spectrum increase at late times. Barring this effect, there is no significant change in the UV end of the power spectrum. In the IR however, the spectral amplitude oscillates over very long timescales. In the process, the power from the largest scales $k \leq m$ migrates slowly towards the UV. This is evidence that thermalization is an extremely slow process of transferring power from the IR towards the UV, as more and more modes interact to reach a local thermal equilibrium. During this process the effective temperature is determined by the power spectral amplitude on those scales which are in thermal equilibrium.

Fig. 3.4 and Fig. 3.5. This observation signals that the effective mass and temperature controlling the power on large scales are running.

It is possible to measure the mass from the numerical dispersion relation using the power spectral density $\left\langle |\delta\varphi(\omega,k)|^2 \right\rangle$ as was done in [32]. Here we use an alternative approach and measure the ratio between the conjugate momentum and field power spectra:

$$\omega_k^2(t) = \left\langle \frac{|\delta\Pi_k(t)|^2}{|\delta\varphi_k(t)|^2} \right\rangle = m_{\rm eff}^2(t) + k^2, \tag{3.12}$$

where we explicitly indicate the t-dependence to stress that the power spectra and coupling constants, in particular the effective mass and temperature, are dynamical quantities. In Fig. 3.5 we show the late-time ensemble averaged power spectra of the field (top right) and conjugate momentum (bottom left) for the ensemble of simulations at $T = 1.2m$. In the top left panel we show the ratio (3.12) as well as the dispersion relation $\omega_k^2 = m_{\rm eff}^2 + k^2$ with the best-fit value of $m_{\rm eff}^2$. There is an excellent fit for $m_{\rm eff}/m = 0.80$, demonstrating that at late times the field fluctuations renormalize the mass parameter for IR modes to be *less* than the input value. In the left panel of Fig. 3.6, we show the time-dependence of the best-fit $m_{\rm eff}$ at each temperature. There is a stage immediately following initialization where the mass measured from (3.12) abruptly decreases between 15% and 25%, with the effect being stronger for larger T. After this stage, the mass starts to increase slowly until it reaches a plateau. For all ensembles, the effective mass reaches steady state around $mt \approx 160$. We treat the late-time value for the mass as the effective equilibrium field mass in each ensemble.

As the power 'cascades' from the IR towards the UV, the field and conjugate momentum achieve a state of local thermodynamic equilibrium with an effective temperature determined by the long-wavelength modes [194]. The modes which are in equilibrium will satisfy the Rayleigh-Jeans distribution defined by: $\left\langle |\delta\varphi_k|^2 \right\rangle \propto T_{\rm eff}/\omega_k^2, \left\langle |\delta\Pi_k|^2 \right\rangle \propto T_{\rm eff}$. Note that the low-k limit of these relations implies that a decrease in the effective mass must come with a corresponding decrease in the effective temperature at fixed field variance. The measured effective temperature of the low-k modes as a function of time in each ensemble is shown in the right panel of Fig. 3.6. Assuming thermal equilibrium is reached on scales $k \leq 3.3m$, we use the Rayleigh-Jeans distribution to find the best-fit effective temperature from the field power spectra. In this procedure we fix the mass to the value given by our late-time measurement of the dispersion relation from the ratio (3.12). We find that the temperature drops abruptly after initialization, reaching a constant at late times. On time scales $mt > 160$ the temperature is constant, up to statistical fluctuations due to limited sample size. We estimate the systematic error on the effective temperature measurement

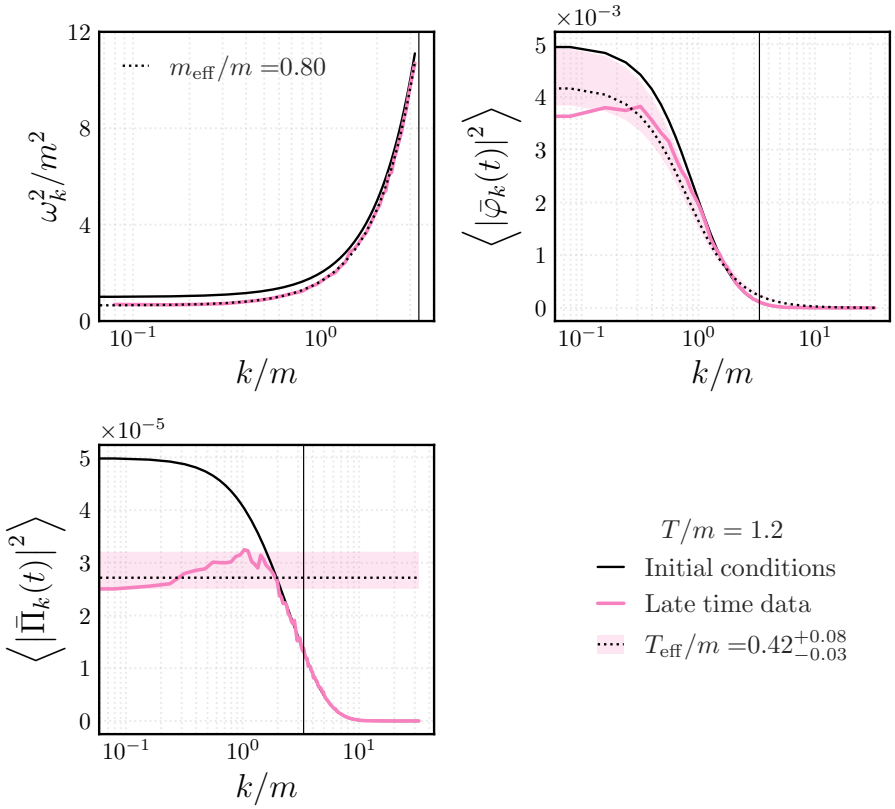

Figure 3.5: Measurement of the effective mass and temperature from the ensemble initialized with $T = 1.2m$. Solid black curves show the dispersion relation with the bare mass in the upper left panel and the initial auto-power spectra (3.8) in the top right and bottom panels. The pink curves represent the ensemble-average of all surviving simulations and over the time interval $160 \lesssim mt \lesssim 400$. The fit of the empirical dispersion relation with (3.12) is shown with the dotted line in the upper left panel and provides a precise determination of the effective mass. With the effective mass fixed from the dispersion relation, the field power spectrum is used to obtain a best-fit estimate of the effective temperature, assuming a Rayleigh-Jeans distribution on scales $k \sim R_{\rm crit}^{-1} \leq 3.3m$. The value also gives a good fit to the average power spectrum of the conjugate momentum in the same range of scales. The faded pink interval illustrates the bounds of the systematic error on the $T_{\rm eff}$ measurement. Over the time interval considered, the empirical effective temperature is constant up to statistical fluctuations. This is evidence that the modes relevant for bubble formation have reached an approximate thermal equilibrium.

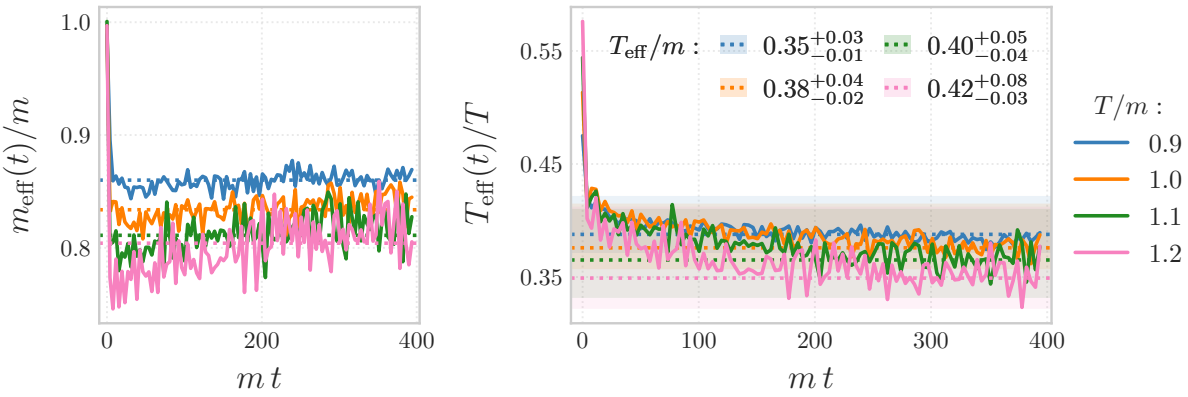

Figure 3.6: In the left panel we show the time-evolution of the effective mass measured by fitting (3.12) to the dispersion relation for a massive scalar $\omega_k^2 = m_{\rm eff}^2 + k^2$. In the right panel we show the time-evolution of the effective temperature measured by fitting the field variance to the Rayleigh-Jeans distribution with the dispersion relation fixed by the value of $m_{\rm eff}$ measured in the left panel.

by looking at the spread of the conjugate momentum power spectrum on large scales, which is a direct measurement of $T_{\rm eff}$. Fig. 3.5 illustrates the measurement of the effective temperature and its error bars for the case $T = 1.2m$. We observe that $T_{\rm eff}$ is about three times lower than the 'temperature' parameter T in the input Bose-Einstein distribution.

For the rest of this Chapter, we will use the values of the effective temperatures measured in this way, as well as the interpretation of local thermal equilibrium described above, to estimate the false vacuum decay rate and explain quantitatively the measured observables that we introduce.

3.4.2 Decay rate

The probability of the field remaining in the false vacuum centered at $\varphi_{\rm fv}$ after a time t can be parametrized as:

$$\Pr(\text{survive}) = e^{-\Gamma L(t-t_0)}, \tag{3.13}$$

where Γ is the probability per unit time per unit length to form a bubble and t_0 is a free parameter. The instanton prediction for Γ in (3.4) depends on the temperature and the critical bubble configuration. We empirically determine ΓL by measuring the survival probability as a function of time in our ensemble of simulations. To do so, we implement a

similar technique as described in previous studies [21, 43] where the survival probability is defined as the number of realizations out of an ensemble that have not nucleated a bubble by time t. The nucleation time is determined by the condition that the quantity $\langle \cos \bar{\varphi} \rangle$, where here $\langle \cdot \rangle$ denotes a lattice volume average, has reached a value greater than -0.7. The survival fraction is fit by an exponential according to (3.13), and the slope of the exponent is identified with the decay rate ΓL.

The survival fraction for all choices of T is shown in left panel of Fig. 3.7. After a transient phase, the survival probability is well fitted by an exponential. We take the transient to be the time interval over which the power spectrum adjusts to the effective mass and temperature parameters, as measured in the previous section. We perform the fit over the shaded region in the figure, which excludes the transient region and encompasses three lattice crossing times, i.e. for $160 < mt < 400$. We find the best-fit value from 4000 simulations for ΓL and t_0 in expression (3.13) for each input power spectrum. In the right panel of Fig. 3.7 we show the trend of the decay rate with temperature compared against the instanton prediction. Specifically, the solid black line represents the best-fit curve with a functional expression given by (3.4), where $B = E_{\rm crit}/T_{\rm eff}$ is fixed, and only the prefactor A is a free parameter. The effective temperature is fixed by the analysis of the previous subsection. By inspection, the decay rate agrees well with the Euclidean prediction.

3.4.3 Center-of-mass velocity distribution

Examining individual nucleation events in the simulations it is evident that bubbles do not nucleate at rest; several examples are shown in Fig. 3.8 and Fig. A.1. This was also noticed in Chapter 2. For the potential and range of temperatures studied here, we find that bubbles materialize with center-of-mass velocities ranging from 0 up to 80% the speed of light on the lattice. In this section we describe an algorithm to identify bubble nucleation events, and determine the Lorentz boost necessary to transform to the rest frame of the nucleation event.

In section 3.2 we described how a critical bubble formed from the thermal ensemble is unstable to either growth or collapse. Here, we focus on nucleation events that lead to expanding bubbles. Once a critical bubble begins expanding, the surfaces of constant field describing the bubble walls asymptote to timelike hyperbolae (studied quantitatively in Ref. [186]). We first identify simulations where the field value achieves this for one of the two true vacua at $\bar{\varphi}_{\rm tv} = 0$ and $\bar{\varphi}_{\rm tv} = 2\pi$. Because our potential is symmetric about the false vacuum, transitions to either of these true vacua are identical for our purposes. For realizations where bubbles nucleate to $\bar{\varphi}_{\rm tv} = 0$, we reflect about the mean

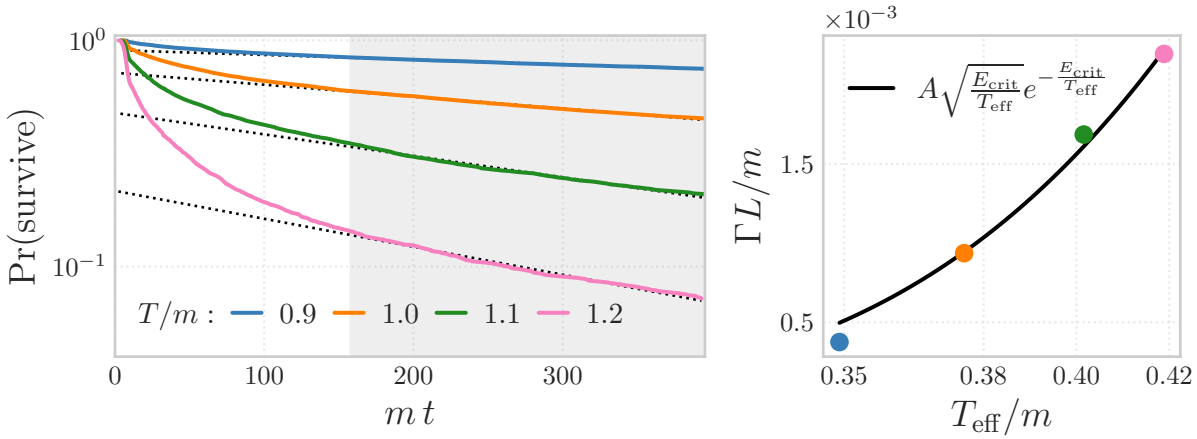

Figure 3.7: *Left:* False vacuum survival probability as the fraction of simulations that have not produced a bubble as a function of time, estimated from ensembles of 4000 realizations for each of the four initial power spectra differing by the value of the parameter T. The grey shaded region denotes the range used to fit an exponential decay rate of the form (3.13) used to extract ΓL in each curve. This is the time range over which the effective temperature $T_{\rm eff}(t)$ has reached a plateau (see Fig. 3.6). *Right:* Decay rate as a function of effective temperature, determined from the field power spectrum as explained in section 3.4.1. The prediction from instanton theory is shown in black, where the prefactor A has been adjusted to provide the best fit to the data and $E_{\rm crit}$ is fixed by the critical bubble configuration in the bare potential.

field and momentum values to produce a nucleation event to the true vacuum at $\bar{\varphi}_{\rm tv} = 2\pi$. This doubles our sample size. In cases where we find more than one nucleation event, we truncate the simulations to encompass spacetime regions containing only the earliest expanding bubble.

From this sample, we follow a procedure similar to the one proposed in the previous Chapter to identify bubble nucleation centers and the bubble center-of-mass velocities. The technique is based on finding the Lorentz boost that produces hyperbolic bubble walls with symmetric expansion away from a common reference point. Such symmetric expansion is what one expects to observe in the bubble's rest frame (center-of-mass frame) in absence of fluctuations. Any deviation from this symmetry indicates there is a preferred direction for the expansion, sourced by a center-of-mass velocity component. The total velocity needed to bring the bubble from the initial frame of nucleation into its rest frame via a Lorentz boost is its center-of-mass velocity $v_{\rm COM}$. The sign of the velocity indicates whether the

expanding bubble is moving to the left or to the right in the lattice frame. To estimate it, we define a measure for the asymmetry between the expansions of the left- and right-traveling walls. In its rest-frame, the bubble is fully symmetric, so the goal is to treat this asymmetric expansion as a residual and minimize it. The full details of the procedure can be found in Appendix A.2.

Out of the four ensembles of 4000 realizations at each value of $T/m \in \{0.9, 1, 1.1, 1.2\}$, we detected a total of $\{1003, 2192, 3165, 3711\}$ bubbles, respectively. We exclude bubbles that formed before $mt \approx 80$, to allow for thermal state to be reached. This filters out a large fraction of simulations, especially at high values of T. As discussed earlier, the effective temperature plateaus after $mt \geq 160$, however we keep a looser cutoff here to gain statistical power; we do not expect this choice to significantly affect our results. For each realization, we checked visually that de-boosted bubbles from the procedure described above appeared symmetric against a central axis. These requirements leave $\{559, 956, 997, 591\}$ bubbles at rest, which made up the ensembles considered throughout the rest of this study. Out of these, in the simulation frame $\{49.91\%, 51.15\%, 51.65\%, 49.41\%\}$ were right-movers, and the rest were left-movers - a nearly even distribution as expected. In absolute value, $\{31.48\%, 33.58\%, 38.72\%, 42.81\%\}$ were moving faster than $v = 0.3$, showing a clear increase with temperature. This trend continues with a larger velocity threshold, as $\{7.69\%, 10.98\%, 13.94\%, 16.58\%\}$ of all bubbles were moving faster than half the speed of light.

The full distribution of velocities found in each ensemble is shown in Fig. 3.9 for each initial power spectrum. The mean of these distributions is near zero; the variance is plotted in Fig. 3.10. To obtain an estimate for the magnitude of the error in our result, we divided each ensemble into 15 sub-ensembles and computed the variance. Then we used the standard deviation of the resulting distribution as an estimate for the error.

This distribution is described by the following simple theoretical model. A boosted bubble has total energy

$$E = \gamma E_{\text{crit}} \approx E_{\text{crit}}(1 + v^2/2), \tag{3.14}$$

where in the second equality we have replaced the boost factor $\gamma = (1 - v^2)^{-1/2}$ by its non-relativistic approximation which is accurate for the majority of the bubbles used in our analysis. In a thermal ensemble with temperature T_{eff} the probability to find such bubble must obey the Boltzmann distribution,

$$P(v) = \mathcal{N}^{-1} e^{-\frac{v^2 E_{\text{crit}}}{2T_{\text{eff}}}}, \tag{3.15}$$

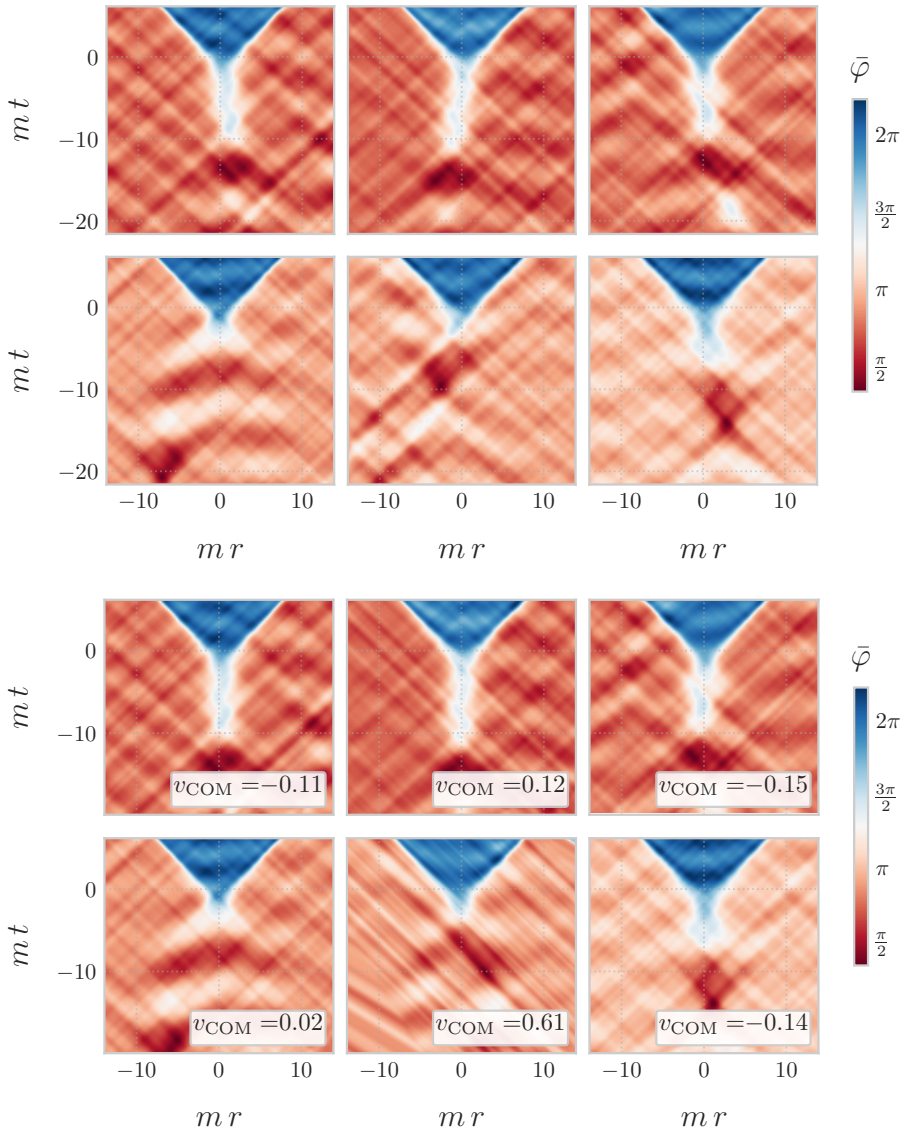

Figure 3.8: *Top panel*: Six examples of original bubbles from the $T/m = 0.9$ ensemble. *Bottom panel:* The same bubbles as the top panel, after going through the de-boosting procedure described in Appendix A.2. The bubble center-of-mass velocity is indicated in each case. The purpose of the Lorentz boost is to maximize the symmetry of expansion of the bubble walls.

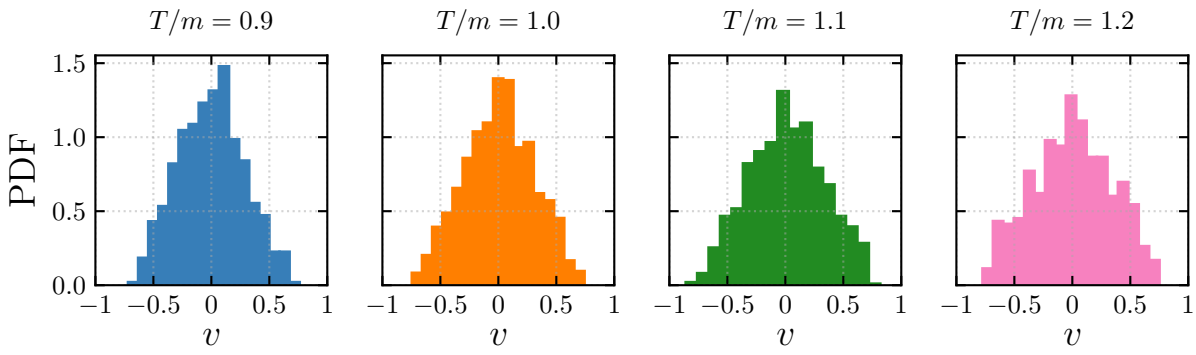

Figure 3.9: The normalized distributions for the measured center-of-mass velocities.

with the normalization factor[3] $\mathcal{N} = \sqrt{\frac{2\pi T}{E}}$. The expectation value for the variance is:

$$\langle v^2 \rangle = \int dv\, v^2 P(v) = \frac{T_{\text{eff}}}{E_{\text{crit}}}. \tag{3.16}$$

Note that this expression coincides with the inverse critical bubble action (3.5), $\langle v^2 \rangle = B^{-1}$. Using the energy of the critical bubble obtained by solving (3.3) and the empirical values for the effective temperature, this expression gives us a theoretical prediction for the center-of-mass velocity. This is compared with the variance measured in the simulations in Fig. 3.10. The agreement is within one sigma of the empirically determined variance.

The relativistic Klein-Gordon field has two associated conserved charges: the total energy and the total momentum. These remain conserved to near machine precision over the entire time of the evolution. They are defined on the lattice as:

$$H(\bar{\varphi}) = \sum_r^L \left[\frac{1}{2}\bar{\Pi}^2 + \frac{1}{2}|\partial_r \bar{\varphi}|^2 + V(\bar{\varphi}) \right] = H(\varphi)/\varphi_0^2, \tag{3.17}$$

$$P(\bar{\varphi}) = -\sum_r^L \bar{\Pi} \partial_r \bar{\varphi} = P(\varphi)/\varphi_0^2. \tag{3.18}$$

Both quantities are fixed by the initial conditions. However, different realizations have a spread in the initial energy and momentum due to the stochastic sampling of the field and

[3]We formally extended the range of integration in the normalization condition $\int dv P(v) = 1$ from $-\infty$ to $+\infty$, which is justified if $E_{\text{crit}} \gg T_{\text{eff}}$, so that the distribution is peaked at $v \ll 1$.

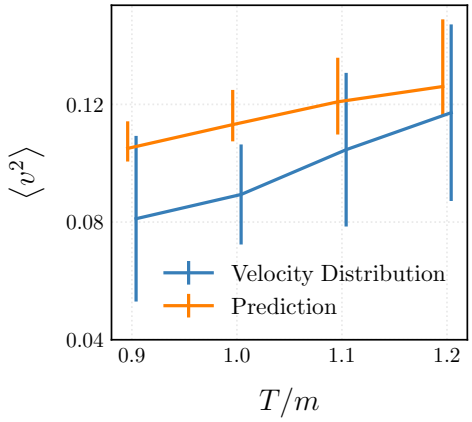

Figure 3.10: Comparison between the measured variance in the distribution of bubble center-of-mass velocities depicted in Fig. 3.9 versus the prediction in (3.16). E_{crit} is the energy of the critical solution from instanton theory and T_{eff} is given by the effective temperatures at late time in each ensemble. There is good agreement between the two.

momentum mode amplitudes. In Fig. 3.11 we plot the initial relativistic momentum defined in (3.18) versus the measured center-of-mass velocity v_{COM} for each realization. The best-fit linear correlation between the total momentum and measured center-of-mass velocity is nearly the same in each ensemble. The spread about the mean correlation increases with T, as expected from the expression for the variance in initial momenta (see (3.9)). This indicates that the initial conditions influence the dynamics of the bubble at nucleation. The average relativistic momentum is zero across the ensemble. However, the local surplus of momentum associated with the random initial conditions in a given realization selects a preferred frame of reference for bubble nucleation.

3.4.4 Average bubble

In this section, we define an ensemble-averaged bubble measured on the lattice and compare this to the critical bubble predicted by the thermal Euclidean instanton described in section 3.2. A non-zero center-of-mass velocity at nucleation leads to morphological changes in the critical bubble, e.g. its size at nucleation is length-contracted, while the total energy is increased. We must therefore first transform to the frame where bubbles are at rest as described above. Even after boosting to the rest frame, there is still great diversity in the details of individual nucleation events. For example, in Fig. 3.8 some bubbles loiter around

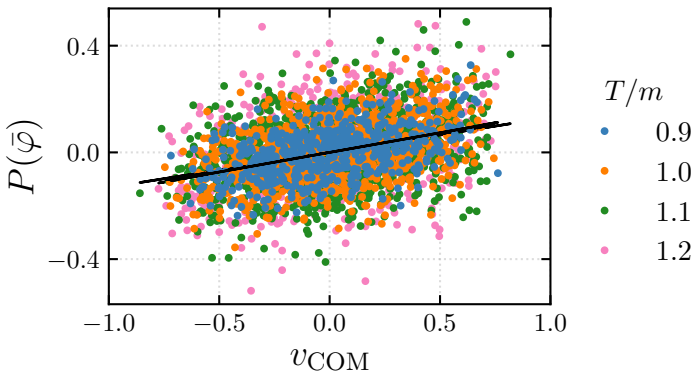

Figure 3.11: A scatter plot of the total conserved relativistic momentum on the lattice at initialization versus bubble center-of-mass velocity. For reference, the initial variance of fluctuations in each ensemble was $\sigma_{\bar{\varphi}} \approx \{0.27, 0.30, 0.33, 0.36\}$ respectively. There are four solid black lines that represent the best linear fit through the data from each ensemble. They all share the same slope to within the thickness of the lines, showing that the degree of correlation remains constant with temperature. The root-mean-square in momentum increases as a function of T, as expected.

the turnover value of the potential, while others make the transition from false vacuum to true vacuum much faster. The variance between different realizations is greatest near the nucleation center, where one would like to make direct comparison with the critical bubble solution. Here, we define a stacking procedure to compute the ensemble-averaged bubble. Our algorithm is fully automated, and does not use any prior information about the expected profile.

The main idea is based on the observation that the walls of a stationary bubble start off at rest, then expand with acceleration asymptoting to $c = 1$. The walls undergo Lorentz contraction, becoming thinner as they accelerate, and gain a momentum far greater than the typical momenta in the fluctuations about the false vacuum. Therefore, relativistic walls become insensitive to fluctuations about the false vacuum and expand at the same rate across all realizations. Essentially, bubbles have different formation histories, but expand in a universal manner at late times.

To stack the bubbles we need a reference point that is common in all cases. We call this reference point the spacetime location of the bubble 'nucleation' and label its coordinates by $(r_{\mathrm{N}}, t_{\mathrm{N}})$. These coordinates are different for every bubble in the ensemble. To find t_{N}, we search for the time-slice where the bubble has reached a fixed radius R where the field

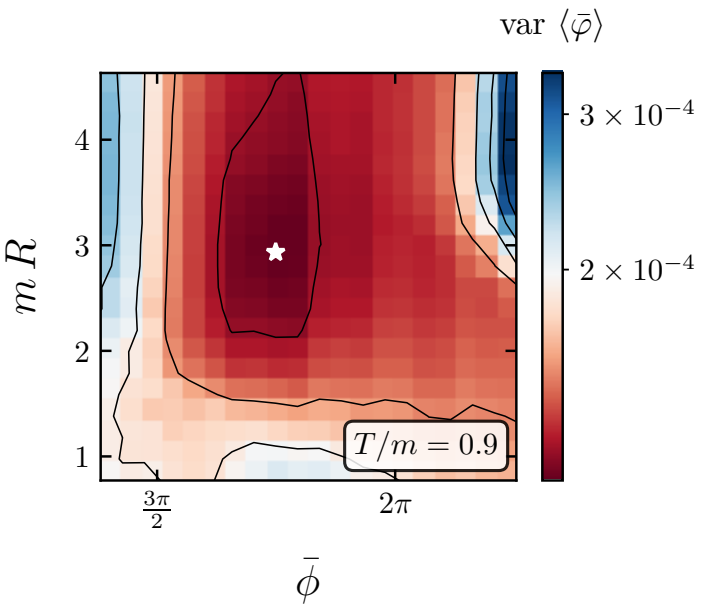

Figure 3.12: Sample variance (defined in (3.19)) around the nucleation region of the stacked average bubble at $T = 0.9m$, function of fluctuation height and width. Each point on the graph shows the value of the variance as a function of the field amplitude threshold $\bar{\phi}$ and bubble size R. These two parameters control where the coordinates of the nucleation center are assigned in each simulation. The white star shows the location where the minimum variance is achieved. Each ensemble yields a different combination that satisfies this condition. The average bubble is produced by stacking bubble nucleation events defined by the $(\bar{\phi}, R)$ pair at this point.

amplitude is above some fixed threshold $\bar{\phi}$. We also need to define $r_{\rm N}$ for each simulation. Since all bubbles have been already de-boosted and are assumed to be at rest, we make use of their symmetry and define the nucleation center as the middle of the region of size $2R$ delineated by the points where the walls reach a field amplitude of at least $\bar{\phi}$. The bubbles are all translated to grids centered at $(r_{\rm N}, t_{\rm N})$, and the field can now be averaged.

To find the best choice for $\bar{\phi}$ and R, we scanned over a large and physically motivated range of values. We choose mR between 0.77 (slightly smaller than the instanton prediction) and 4.63 (roughly three times the instanton prediction). For $\bar{\phi}$, we choose a range between $\bar{\varphi}_{\rm fv} + \sigma_{\bar{\varphi}}$ (far lower amplitude than expected from the instanton prediction) and $\bar{\varphi}_{\rm fv} + 6\sigma_{\bar{\varphi}}$ (far larger in amplitude than the instanton prediction). To estimate the goodness of fit we minimize the sample variance over a finite spacetime region centered at the

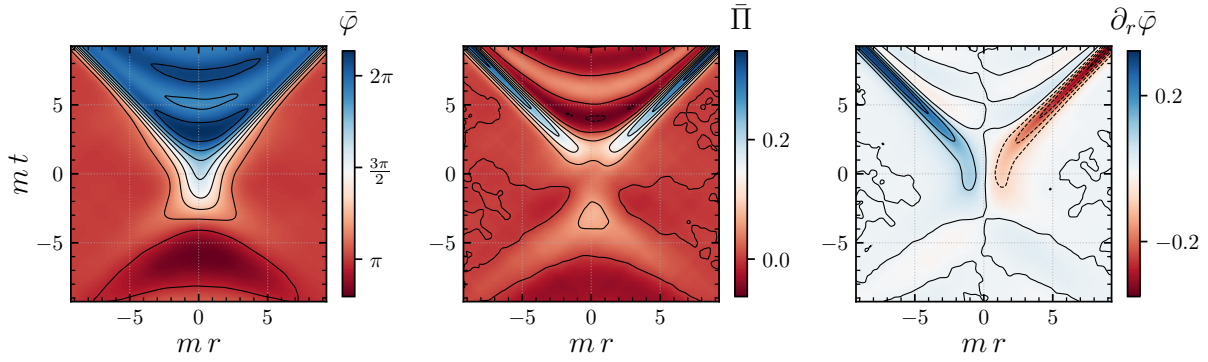

Figure 3.13: From left to right, we show the average bubble, average conjugate momentum and average field gradient for $T = 0.9m$. The black contours are added to help visualize surfaces of constant field amplitude. Qualitatively, beyond the nucleation time shown here at $t = 0$, the features of the three fields match the characteristics of the critical saddle point solution pictured in the left panel of Fig. 3.3. Moreover, the average fields look similar, up to sample variance, among all four ensembles with different values of T.

nucleation center. The sample variance is computed as

$$\text{var}\,\langle\bar{\varphi}\rangle = \frac{1}{(2\Delta r)^2}\sum_{r,t}\left|\frac{1}{S}\sum_{i=1}^{S}\left[\bar{\varphi}_i(r,t) - \langle\bar{\varphi}(r,t)\rangle\right]^2\right|, \tag{3.19}$$

where S is the total number of samples in the stack. The variance is computed for every pair of field amplitude value $\bar{\phi}$ and bubble width R considered. The nucleation region is taken to be the spacetime volume defined by $r \in [r_{\rm N} - \Delta r, r_{\rm N} + \Delta r]$ and $t \in [t_{\rm N} - \Delta r, t_{\rm N} + \Delta r]$ with $\Delta r = 30\mathrm{d}r$ around the nucleation site at coordinates $(r_{\rm N}, t_{\rm N})$ uniquely defined by the pair $\left(\bar{\phi}, R\right)$. For reference, in mass units $m\Delta r \approx 2.4$. The sample variance for all combinations of R and $\bar{\phi}$ in the case of the $T = 0.9m$ ensemble is shown in Fig. 3.12. The variance is largest around the boundaries where the parameters take un-physical values. The white star denotes the combination of parameters that minimizes the variance and has been used to obtain the average bubble. This pair is different for each choice of T.

The average bubble is shown in Fig. 3.13 alongside its momentum and gradient on equivalent coordinate grids. The momentum and gradient fields have been obtained in the same manner as the procedure applied to the field. Namely, the Lorentz boosts were done with respect to the same definition of the coordinate grid and gamma factor in each simulation, and the stacking was with respect to the same set of reference points $(r_{\rm N}, t_{\rm N})$. Notice that the bubble profile has common features with the canonical result shown in the

left hand panel of Fig. 3.3. In particular, after a region of space where the field briefly loiters around the potential maximum, expanding bubble walls form and the bubble interior rolls down to the true vacuum at $\bar{\varphi}_{\rm tv} = 2\pi$. The wall trajectories are best visible in the gradient plot, where it can be seen that they quickly asymptote to null and that the gradient increases as the walls length-contract as they achieve increasingly high velocity. From the momentum plot, we see that the magnitude of momentum remains small until the bubble is well-formed. Finally, in the field plot note that prior to the bubble nucleation event, there is a coherent field configuration with $\bar{\varphi} < \bar{\varphi}_{\rm tv}$ – the opposite direction in field space than the false vacuum. We will discuss this bubble precursor in the next section.

To make a comparison with the Euclidean instanton prediction for the critical bubble, we must choose a corresponding time-slice through the average bubble in Fig. 3.13. To find it, we use the following method. We sample the time-slices around the region identified as $t = 0$ in the plot. We take the average field configuration at each time step and time evolve it using the equations of motion, in the absence of thermal fluctuations. We define the critical bubble profile $\bar{\varphi}_{\rm crit}(r, t_{\rm crit})$ as the earliest time-slice that evolves into an expanding bubble solution in the absence of fluctuations and with zero initial momentum everywhere. The profile for the $T/m = 0.9$ case is shown in Fig. 3.14 alongside the solution found using the Euclidean instanton. The two agree quite well. The time evolution of the empirical critical bubble configuration is shown in the left panel of Fig. 3.15. After a brief loitering period, the configuration develops into an expanding bubble. Further, inputting as an initial condition the field configuration one simulation time step prior at $t = t_{\rm crit} - {\rm d}t_{\rm out}$ yields an oscillon configuration as depicted in the right panel of Fig. 3.15. The critical bubble defined in this way is nearly identical across all four ensembles with different T. Notice also the striking resemblance between Fig. 3.15 and Fig. 3.3 – the ensemble average bubble in our lattice simulations matches well with the expectation from the thermal Euclidean instanton.

In Fig. 3.16 we show the time evolution of the average field and average momentum from Fig. 3.13, for all values of T, and at a fixed $r = 0$, the location of the nucleation center. The critical time has been identified for each of the four ensembles using the method described above. The curves in Fig. 3.13 have been matched so that $t = 0$ corresponds to $t_{\rm crit}(T)$. First, note that the average evolution around this time is nearly identical for all values of T, although each curve was formed by averaging a completely different ensemble of bubble nucleation events. The field first oscillates about the true vacuum at $\bar{\varphi}_{\rm fv} = \pi$, transitions across the potential barrier, and oscillates about the false vacuum at $\bar{\varphi}_{\rm tv} = 2\pi$. Around $mt = 0$, there is a local minimum in the field momentum, as it briefly loiters around $\bar{\varphi} \simeq 3\pi/2$.

However, note from the right panels in Figs. 3.14 and 3.16, and also from the middle

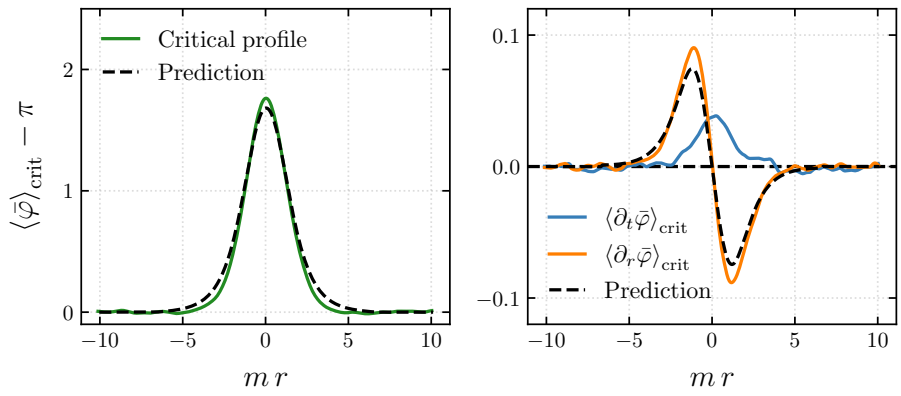

Figure 3.14: *Left:* We show in solid green the critical average bubble profile obtained empirically. The critical profile $\bar{\varphi}(r, t_{\rm crit})$ is the field configuration taken from the average bubble in Fig. 3.13 that produces an expanding bubble when time-evolved under the equations of motion. We refer to this particular field profile as $\bar{\varphi}_{\rm crit}$, and the associated time-slice as $t_{\rm crit}$. Comparing against the Euclidean prediction shown in dashed black, we find excellent agreement. The Euclidean profile represents also the initial condition for the field configuration as a function of lattice site $\bar{\varphi}(r, t = 0)$ that was used to obtain the left-hand side panel in Fig. 3.3. *Right:* The average gradient and momentum on the critical time-slice compared to their theoretical predictions: the gradient of the Euclidean solution and the uniformly null momentum respectively.

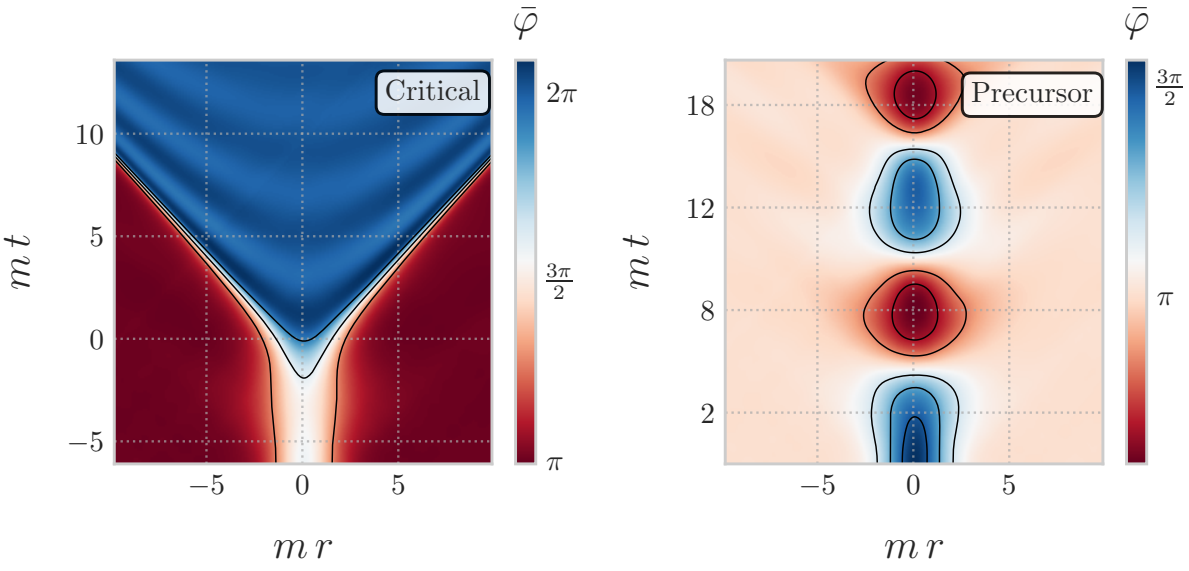

Figure 3.15: On the left we show the time evolution in the absence of field or momentum fluctuations of the empirical critical profile depicted in Fig. 3.14. On the right, we plot the time evolution of the field configuration corresponding to $\bar{\varphi}(r, t_{\rm crit} - {\rm d}t_{\rm out})$. The resemblance with Fig. 3.3 using the Euclidean critical bubble as initial conditions is striking.

panel of Fig. 3.13 that the average momentum around the critical nucleation time $t_{\rm crit}$ does not vanish across the lattice. This is in contrast to the prediction of the Euclidean instanton solution, where the momentum vanishes everywhere. The extreme case where decays are driven entirely by a momentum profile was studied in [196]. Here, we certainly do not find that this is the dominant channel, and furthermore, the critical bubble solution we have identified does not require initial momentum to produce an expanding bubble. Since the amplitude of momentum at $(r = 0, t = t_{\rm crit})$ from both Fig. 3.14 and Fig. 3.16 is of order the average root-mean-square of momentum fluctuations in the initial conditions $\sigma_{\overline{\Pi}} \approx \{0.040, 0.045, 0.051, 0.056\}$, it is possible that this is a residual of the de-boosting procedure or even a bias owing to the fact that we only average critical profiles which result in expanding bubbles, and neglect solutions that collapse back into the false vacuum via oscillons. Nevertheless, it is clear that field dynamics are an important component of bubble nucleation since the average bubble includes precursor fluctuations. We now turn to study these precursors in more detail.

3.4.5 Bubble precursors

The Euclidean instanton formalism provides a prediction for the critical bubble profile, but offers no guidance into how this configuration comes about from an ensemble of fluctuations around the false vacuum. General theoretical considerations can yield some insight, as described in Ref. [30]. In short, the most probable formation history of a rare configuration from a thermal ensemble is the time-reverse of its decay. For thermal vacuum decay, the critical bubble is in unstable equilibrium between expansion and collapse. As we demonstrated in Fig. 3.15, time-evolving the slightly subcritical average bubble yields an oscillon (a stable and compact oscillating field configuration), which after long times would decay back to un-bound plane-wave fluctuations about the false vacuum. Time-reversing, the prediction is that the most probable formation history of an expanding thermal bubble is for plane waves about the false vacuum to scatter, producing an oscillon, which propagates for a long time, eventually interacting with thermal fluctuations to produce a critical expanding bubble. Indeed, oscillon precursors have been observed previously in lattice simulations [28], where they were shown to enhance the decay rate in a quench.

We can test the hypothesis that the most likely bubble formation history starts with an oscillon by using our lattice simulations to empirically measure the dynamics prior to bubble nucleation. In Fig. 3.13 we see that the average bubble configuration has a large under-density in field space, followed by a peak in momentum. Looking closely at each realization, empirically we observe that many bubbles form from oscillons; several examples are shown in Fig. 3.17.

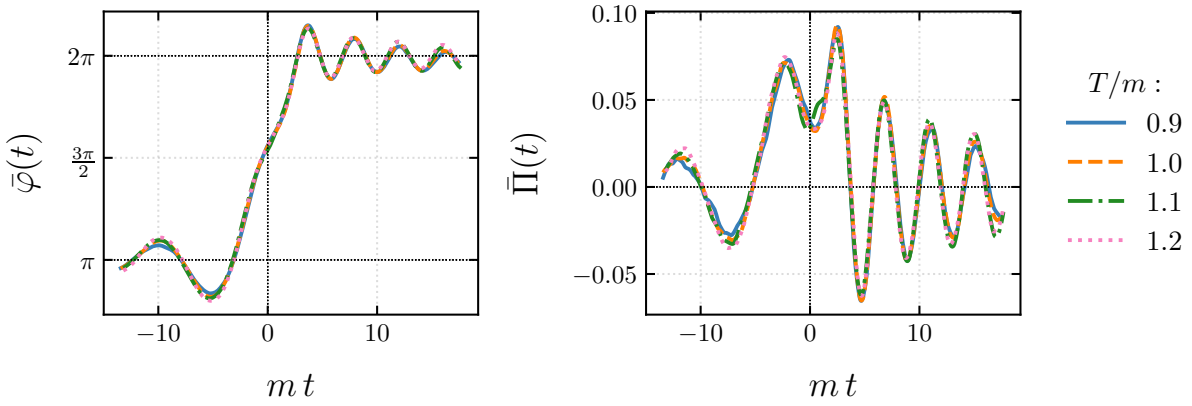

Figure 3.16: The time evolution of the average bubble field amplitude (on the left) and the average momentum amplitude (on the right) depicted in Fig. 3.13 along the $r = 0$ axis. For each ensemble labeled by the value of T, we identified the critical time t_{crit} separately as the time-slice where the field profile evolves into the expanding bubble solution and is the earliest time-slice that evolves into a bubble. In this figure, we offset the time evolution so that in each case the critical time lies at $t = 0$. The four profiles look extremely similar, even though they are obtained by averaging entirely different ensembles of bubbles. In particular, before the critical time, the average field oscillates around $\bar{\varphi}_{\text{fv}}$, while afterwards it oscillates around $\bar{\varphi}_{\text{tv}}$ with decreasing amplitude as it settles into equilibrium. Around the critical time, the one-point function of the field amplitude makes a jump, while simultaneously the momentum temporarily acquires a non-zero amplitude, of roughly $\sigma_{\bar{\Pi}}$ in magnitude. At the critical time $t = 0$, the momentum one-point function is at a local minimum.

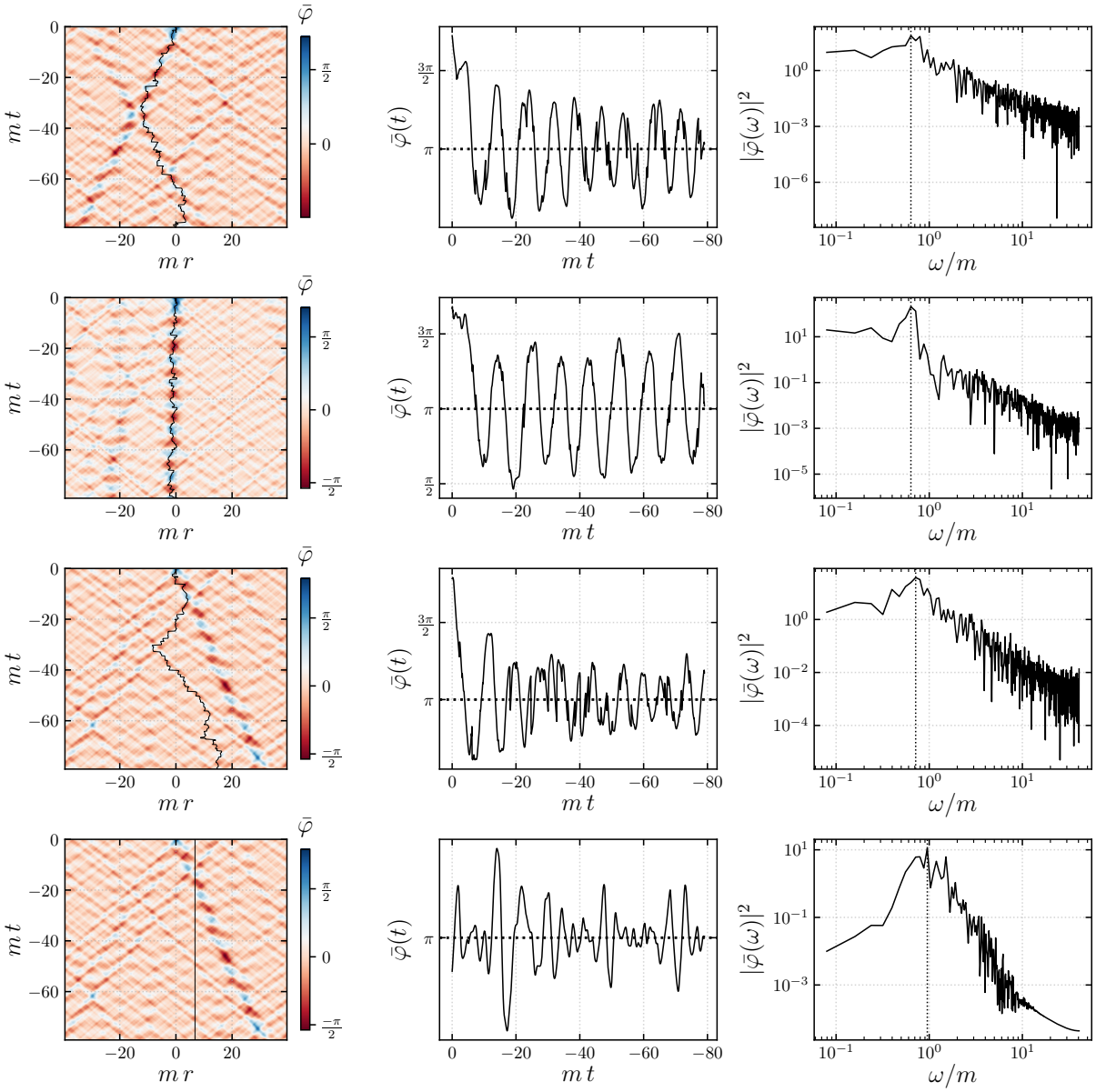

Figure 3.17: The image caption is on the next page.

Figure 3.17: *Left:* Examples of field configurations preceding the bubble nucleation at $(r, t) = (0, 0)$. The trajectories of the oscillon precursors are shown in black. The bubble precursors are not the only structures evolving on the lattice and in fact in many cases it is collisions of such objects that trigger bubble nucleation. The oscillon collisions also make it difficult, in general, to track the long-term evolution of the precursor, as exemplified in the third row where the trajectory seems to diverge from the dominant oscillon in that simulation at around $mt = -20$ and instead random background fluctuations are being picked up. The bottom row shows the same realization as above, but instead of the oscillon we analyze an example null trajectory. *Middle:* The field amplitude along the oscillon trajectory as a function of time. A large amplitude sinusoidal stands out in the top two cases. The bottom case exemplifies that the typical background field does not, in general, show the same phase coherence. *Right:* Taking the time-domain Fourier transform of the field shown in the middle panel, we compute its power spectrum. The peak frequency $\omega_{\rm osc}$ is identified by the vertical dotted line. Interestingly, the frequency corresponding to this peak is below the mass scale of the field everywhere, except in the null test case. This demonstrates that the oscillons are bound structures, since they are characterized by a lower energy per particle, $\omega_{\rm osc} < m_{\rm eff}$, than a collection of free waves with $\omega \geq m_{\rm eff}$. Moreover, since the critical bubble is a static solution, it has $\omega_{\rm crit} \to 0$. In this sense, oscillons are an intermediate state between propagating field degrees of freedom and the critical bubble solution.

We now explain how to disentangle these structures from the background field fluctuations. First we select the simulations where the bubble nucleates after at least a duration $mt = 80$, equivalent to a full lattice crossing time. This allows us to trace the long-term evolution of the precursors. Throughout this section we limit our discussion to the case $T/m = 0.9$ where the field fluctuations are smallest, but the results presented below apply also to the other ensembles.

Oscillons stand out as large amplitude long-wavelength fluctuations. As they evolve slowly in time, they bounce around the lattice subject to a random Brownian-like motion. To isolate their trajectory in a consistent way across realizations, we compute the Hilbert transform of the field $\bar{\varphi}(r, t)$ and take the absolute value. This produces the instantaneous amplitude (envelope) of the field as a function of time [197]. The trajectory is simply given by the location r on the lattice where the envelope has peaked in amplitude. The starting point for the procedure is the location of the bubble nucleation, shown as $(r, t) = (0, 0)$ in the figures on the left panel of Fig. 3.17. Then we trace the trajectory backwards in time, imposing the additional requirement that the maximum at t should not be farther than

$mr = 2$ away from the maximum computed at $t + \mathrm{d}t_{\mathrm{out}}$. The time evolution is truncated at $mt = -80$. In the middle panels of this figure, we plot the time-development of the field along this trajectory. In the right panels, we show the spectral content of the field along this trajectory.

Notice from the middle and right panels of Fig. 3.17 that the field along the trajectory oscillates with a characteristic oscillon frequency ω_{osc}. This stands out as a peak in the power spectrum. We associate a characteristic ω_{osc} to each bubble precursor in our ensemble. Their distribution is shown in blue in the left panel of Fig. 3.18. To highlight the difference between oscillons and the background fluctuations, we pick random field trajectories through each simulation and select the frequency where their respective power spectra peak. This distribution is plotted in orange. Note that the peak of the power spectrum for oscillon trajectories is lower than the peak on random trajectories (appropriately centered on $\omega = m_{\mathrm{eff}}$, the prediction from the dispersion relation for plane waves about the false vacuum). This is consistent with the interpretation that oscillons are bound states.

Next, we compute the average power spectrum of all oscillons and the average power spectrum of random trajectories and plot them side by side in the right panel of Fig. 3.18. We also plot, for comparison, the power spectra of the field trajectories $\bar{\varphi}_{\mathrm{crit}}(r = 0, t)$ for both the subcritical bare lattice solution in Fig. 3.3 and the precursor to the average bubble critical solution shown in Fig. 3.15. These are shown in green and pink, respectively. Notice that these peak at the same frequency as the average oscillon signal. This is highlighted by the green band in both plots. This is strong evidence that the formation history of bubbles in our simulations includes an oscillon precursor matching the oscillon that results from collapse of a subcritical bubble (as in e.g. Fig. 3.3).

Here we considered the trajectory of the oscillons in the original simulations, before de-boosting. In principle the distribution of velocities for the oscillons should obey $\langle v_{\mathrm{osc}}^2 \rangle \propto T_{\mathrm{eff}}/E_{\mathrm{osc}}$ but the frequent collisions make it difficult to systematically measure their velocities (such a collision which changes the direction of motion of the oscillon is clearly visible in the top panel in Fig. 3.17). We will perform a more detailed study of the properties of oscillon precursors in future studies.

3.4.6 Critical bubble energy

We can compare the observables we introduced up to this point by looking at how they relate to the critical bubble action $B = E_{\mathrm{crit}}/T_{\mathrm{eff}}$. In section 3.4.2 we have already shown that in the effective IR temperature interpretation we find good agreement with the Euclidean expectation for the decay rate. Here we show that the measurements of the average critical

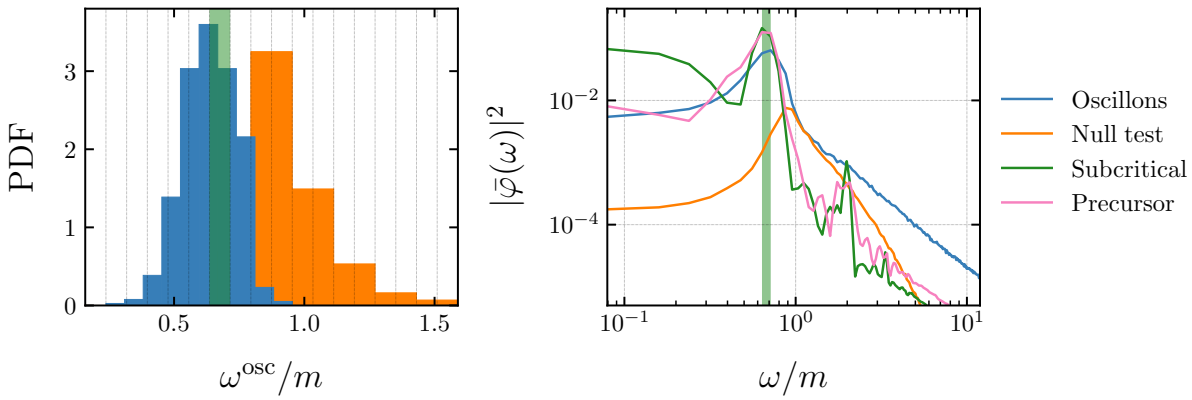

Figure 3.18: *Left:* In blue is the distribution of characteristic frequencies of the bubble precursors $\omega_{\rm osc}$. In orange is the distribution of the peak frequencies in the power spectrum of null field trajectories drawn from the same realizations. The oscillon distribution has smaller variance and peaks at lower frequency than the null trajectories. This is consistent with the bubble precursors being bound states of similar properties across the ensemble. *Right:* The average oscillon (in blue) and the average null trajectory (orange) power spectra. We also show in green the spectrum of the $\bar{\varphi}_{\rm crit}(r=0,t)$ trajectory of the precursor in Fig. 3.3 and in pink the subcritical average bubble solution from Fig. 3.15, for comparison. With the exception of the null test line which peaks around $\omega \approx m_{\rm eff}$, all other spectra peak over the same frequency range, highlighted by the faded green band in both images. The occupation numbers are also much larger on large scales for the three spectra that measure oscillons, which supports their identification as bubble precursors.

bubble and the velocity distribution are also compatible with the theoretical prediction. The critical bubble energy is

$$E_{\rm crit}(\varphi) = \sum_r^L \frac{1}{2}\Pi_{\rm crit}^2 + \frac{1}{2}\left(\partial_r \varphi_{\rm crit}\right)^2 + \varphi_0^2 V(\varphi_{\rm crit}) - \varphi_0^2 V(\varphi_{\rm fv}). \tag{3.20}$$

The kinetic energy term is zero for the static Euclidean solution. Taking the Euclidean solution $\bar{\varphi}_{\rm crit}$ computed for the bare potential (used as initial condition for the left panel of Fig. 3.3 and plotted in dashed black in Fig. 3.14), we obtain a baseline value for the critical energy. Dividing by the empirical effective temperature of each ensemble determined in section 3.4.1, we arrive at our theoretical predictions for the action. The predictions are plotted in blue in Fig. 3.19. Next, we can estimate the energy of the empirical average critical bubble by taking the average field, gradient and momentum profiles on the critical slice shown in Fig. 3.14 and integrating (3.20). Repeating the exercise for all four ensembles differing by the value of T, we obtain the points shown in orange in Fig. 3.19. Lastly, according to (3.16), the variance of the velocity distribution is a direct measurement of the critical bubble action. This is shown in green. Overall, we find good agreement between all measurements in each ensemble.

We have implicitly assumed that the critical energy is independent of temperature, or even effective mass. We postpone a more detailed analysis of the effects related to the running of these variables on the bubble solution to future work. However we note that this approximation is supported by our empirical finding that the average bubble as well as the time evolution of the field and conjugate momentum one-point functions shown in Fig. 3.16 are identical, up to statistical error bars, between the four different ensembles. This is in spite of the fact that the averaging is done with respect to different set of parameters $(\bar{\phi}, R)$ (see section 3.4.4).

3.5 Discussion

In this Chapter we have identified the center-of-mass velocity distribution of bubbles, the ensemble-averaged bubble in the nucleation rest frame, and oscillon precursors as promising observables for vacuum decay. We investigated the properties of these observables using ensembles of classical simulations in 1+1 dimensions. The initial conditions for the simulations are drawn from a non-equilibrium distribution over phase space which we took to be Bose-Einstein (as opposed to the equilibrium Rayleigh-Jeans spectrum). Generalizing our results, we expect bubbles to have a distribution of center-of-mass velocities in any number

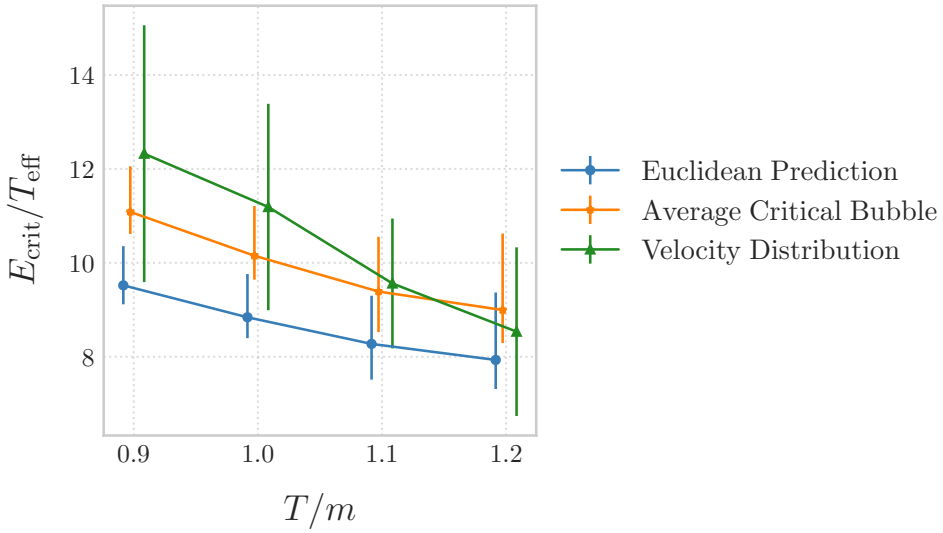

Figure 3.19: The energy of the critical bubble solution, as measured from three different lattice observables and compared against the Euclidean prediction shown in blue. The prediction is given by (3.20) computed for φ_{crit} corresponding to the solution to the static equation of motion (3.3). The orange line corresponds to the critical field profile obtained empirically from the average bubbles, as explained in section 3.4.4. The error bars on the blue and orange are proportional to the systematic uncertainty on the effective temperature, as explained in section 3.4.1. Finally, the green curve is obtained from taking the inverse of the measured values for $\langle v^2 \rangle$. Here the error bars are the same as in Fig. 3.10, percentage-wise. The data points have been offset slightly along the horizontal axis to help with visualizing the error bars.

of spatial dimensions and for any ensemble defining the initial conditions. The distribution likely depends on the ensemble from which the initial conditions are drawn, but it is reasonable to expect that it is given by the Boltzmann factor involving the total bubble energy if the ensemble is close to thermal. This will be a topic of future investigation. We also expect that oscillon precursors play a role in thermal bubble nucleation in any number of spatial dimensions. Here, there could be interesting phenomenology related to the potential, since this determines the properties of oscillons. There may also be dependence on the ensemble of initial conditions, since the oscillons are infrared-sensitive objects. For the ensemble-averaged bubble, there may also be important differences that depend on the potential and the ensemble of initial conditions. For example, vacuum decay at zero temperature is not described by the static thermal critical bubble, but by the $O(4)$-invariant Euclidean bounce, which gives rise to an expanding bubble in real time. Can this be the average bubble observed in semi-classical simulations such as those performed in [21]?

Our study could also have interesting implications for a number of phenomenological scenarios involving first-order phase transitions. Models of electroweak baryogenesis involve a first-order phase transition (see e.g. [198] for a review). The terminal velocity of the bubble wall through the primordial plasma is a crucial element of these models, determining if a sufficient baryon asymmetry can be accumulated. Incorporating the velocity distribution outlined in this Chapter could have implications for this calculation if the expected velocity of bubbles is comparable to the terminal wall velocity which is typically non-relativistic and can be as low as $v \sim \mathcal{O}(.1)$ [199, 200, 201] (though in some models can be close to the speed of light, see e.g. [202]). Our results imply that the root-mean-square bubble center-of-mass velocity is $\sqrt{\langle v^2 \rangle} \sim 1/\sqrt{B}$, where $B \gg 1$ is Euclidean critical bubble action controlling the false vacuum decay rate. We can estimate B by requiring that the phase transition occurs when $\Gamma \sim H(T)^4$, which for $H^2 \sim T^4/M_{\rm pl}^2$ and assuming $\Gamma \sim T^4 B^{3/2} e^{-B}$ (appropriate in 3+1 dimensions) yields $B \sim 150$ for a temperature of order TeV. The expected root-mean-square velocity of a bubble during electroweak baryogenesis is therefore $\sqrt{\langle v^2 \rangle} \sim .1$ - comparable to the terminal wall velocity! This simple estimate undoubtedly misses important physical effects, but it certainly motivates the inclusion of bubble velocities in these models. Note that in existing simulations of electroweak baryogenesis e.g. [203], bubbles are inserted by hand and do not include this effect. These simulations could be augmented to include the velocity distribution outlined in this Chapter. The velocity distribution may also have implications for the spectrum of stochastic gravitational waves produced during electroweak baryogenesis or other early-Universe phase transitions observable by LISA [158].

The oscillon precursor to bubble nucleation could also have implications for baryogenesis. This is because the oscillon core can sample regions of a symmetry-breaking phase.

The role of oscillons in electroweak baryogenesis was discussed in [204], whose title reflects their conclusion: oscillons are not present during an electroweak phase transition. Here, we have shown that whenever bubbles are present, so are oscillons. This motivates revisiting the question of whether a long-lived oscillon precursor could contribute significantly to the dynamics and outcome of baryogenesis.

Early work on oscillons showed that their presence could affect the decay rate of a false vacuum [29]. Here, we highlight that for thermal decay they are an essential component of the nucleation process. What is their role in the Euclidean formalism - are they implicitly captured in the saddle point corresponding to the critical bubble? The answer to this question could have implications for the decay rate computation at zero temperature as well: is vacuum decay preceded by a 'virtual' oscillon, or is vacuum decay fundamentally different in this respect? We hope to investigate these, and other questions, in future work.

Part II

Anisotropic Screening of the Cosmic Microwave Background with Hidden-Sector Particles

Summary of Part II

In this Part we introduce a new type of Cosmic Microwave Background (CMB) secondary anisotropy – which we termed patchy dark screening – induced by dark photons and axions with masses in the range $10^{-13} - 10^{-11}$ eV interacting with primordial photons inside large scale structure (LSS).

We begin Chapter 4 by first reviewing photon to dark photon kinetic mixing and describe quantitatively the phenomenology of resonant conversion inside LSS. Next, we use a halo model-based approach to statistically model the anisotropies due to a dark screening optical depth. We derive correlation functions of CMB temperature and polarization fluctuations induced by the conversion of photons into dark photons, and between these CMB observables and LSS tracers. Next, we present a Fisher forecast to estimate the sensitivity of existing and future CMB data on the various two- and three-point correlation functions. The possibility to construct analogous correlation functions with various cosmological observables is discussed. In the appendices associated to this Chapter, we present details about the modelling of dark matter and gas halos, and the technical details related to the computation of correlation functions.

In Chapter 5 we extend the analysis introduced in Chapter 4 to the case of CMB photons resonantly converting into axion particles. This Chapter is structured in analogy with Chapter 4. Here, the background magnetic field inside virialized halos plays an important role in the phenomenology and we investigate this aspect in detail. We include several appendices including technical details of calculations and discussions on the domain of validity of our analysis and methods, as well as an extension to the case of massless axions.

Chapter 4

Patchy Screening of the CMB with Dark Photons

4.1 Introduction

Cosmic microwave background (CMB) and large scale structure (LSS) surveys have provided some of the most important evidence for physics beyond the Standard Model (BSM) of particle physics – dark matter and dark energy, as well as early-Universe cosmological models such as inflation. These observations also provide powerful constraints on BSM physics, such as the number of relativistic degrees of freedom, neutrino masses, and the strength of interactions during an inflationary era. The next generation of CMB experiments such as the upcoming Simons Observatory [205], as well as CMB-S4 [206] and CMB-HD [89], and LSS surveys like DESI [207], Euclid [208], and LSST [209] promise to further expand our ability to detect and characterize BSM physics. These new surveys motivate the exploration of new observables that can exploit their full potential. In particular, a promising avenue of current and future effort is to use the CMB as a back-light through which to study the intervening LSS (see e.g. [210, 211]).

Within the Standard Model of cosmology and particle physics, CMB photons can interact with LSS via gravity (e.g. weak lensing or the integrated Sachs-Wolfe effect) and electromagnetism (e.g. Sunyaev Zel'dovich effects). These effects lead to additional temperature and polarization anisotropies in the CMB, the so-called secondary CMB, as well as new correlations with tracers of LSS such as galaxy surveys. The slew of associated new observables, and in particular cross-correlations between CMB and LSS, can be used to extract valuable information about the initial conditions and the formation and growth of

structure in the early Universe. Several examples include: lensing reconstruction (see e.g. [81] for a review), kinetic Sunyaev Zel'dovich velocity reconstruction [82, 83, 84, 212, 86], moving-lens velocity reconstruction [87], and patchy reionization optical depth reconstruction [88].

In this Chapter, we discuss the possibility of using the CMB and its cross-correlation with tracers of LSS to extract information about BSM physics that manifest in the low-redshift Universe. In particular, we will discuss how a new type of CMB secondary anisotropy and its correlation with LSS can be used to extend the reach in the parameter space of kinetically mixed dark photons [105, 106] by orders of magnitude.

As discussed briefly in Chapter 1, the dark photon is a hypothetical vector boson that arises in various extensions of the Standard Model [99, 100]. An ultra-light dark photon is an essential ingredient in dark matter models, either as a light bosonic dark matter candidate [101, 102, 103], or as a mediator to a sector of dark matter particles (see [104] and reference within). Despite recent evidence of various collective effects which cast doubt on the validity of some of the models (vortex production during production of dark photon dark matter [114] and the two stream instability in the case of freeze-in dark matter models [213]), it is still of great interest to probe the existence of ultra-light dark photons regardless of their cosmological abundance through superradiance [111, 112, 113, 114, 115], cosmology [116, 117, 118, 119], stellar objects [120, 121, 122] and laboratory searches [123, 124, 125, 126, 127].

A dark photon and its coupling to the Standard Model can be described by the Lagrangian

$$\mathcal{L} = -\frac{1}{4}F_{\mu\nu}F^{\mu\nu} - \frac{1}{4}F'_{\mu\nu}F'^{\mu\nu} - \frac{m_{\mathrm{A}'}^2}{2}\mathrm{A}'_{\mu}\mathrm{A}'^{\mu} - \frac{\varepsilon}{2}F_{\mu\nu}F'^{\mu\nu} + \mathrm{A}^{\mu}J_{\mu}, \tag{4.1}$$

where A^{μ} and A'^{μ} are the photon and dark photon fields respectively, with $F^{\mu\nu}$ and $F'^{\mu\nu}$ their field strengths, and J^{μ} is the Standard Model electromagnetic current. The dark photon has a mass $m_{\mathrm{A}'}$ and couples to the Standard Model photon through a kinetic mixing parameter ε. This simple coupling leads to a plethora of observable consequences (see [15] and references within). Most of these are based on the conversion, in particular resonant conversion, between the photon and the dark photon in a medium. In the lab, resonant conversion is facilitated with carefully prepared small scale experiments. In the early Universe, resonant conversion happens in different astrophysical and cosmological environments, as the dispersion relation of the photon (plasma frequency) is naturally scanned. When the plasma frequency of the photon m_{γ}^2 over its trajectory $\vec{x}$ matches the mass of the dark photon

$$m_{\gamma}^2(\vec{x}) = m_{\mathrm{A}'}^2, \tag{4.2}$$

CMB photons resonantly convert into dark photons.

In [116, 117, 118, 119, 214], the resonant conversion between CMB photons and dark photons was studied both in the homogeneous early-time and inhomogeneous late-time limits. Cosmic expansion and the inhomogeneous distribution of ionized gas were identified as important scanners of the plasma frequency. In this Chapter, we examine the conversion from CMB photons into dark photons inside non-linear structure, after the epoch of reionization, where the amplitude of the density profile of ionized gas within dark matter halos provides the primary scanner.

Resonant conversion leads to a frequency-dependent disappearance of CMB photons that traces the distribution of matter in the Universe. Hence it can be treated as a frequency (ω) and angle ($\hat{n}$) dependent optical depth $\tau(\varepsilon, \omega, \hat{n})$, after integrating along the line of sight. The optical depth from resonant conversion can be extracted or constrained from cosmological data, and we present five methods to search for dark photons, along with the projected sensitivity on ε:

- **Spectral distortions of the CMB**: The spatially averaged $\langle \tau(\varepsilon, \omega) \rangle$ manifests as a distortion of the blackbody spectrum of the CMB, and as a result is constrained by COBE/FIRAS [77]. This effect, the late-time component of the effect studied in [116, 117, 118, 119], scales as ε^2.

- **CMB temperature and polarization anisotropies**: The optical depth correlation function $\langle \tau(\varepsilon, \omega, \hat{n})\, \tau(\varepsilon, \omega, \hat{n}') \rangle$ can be obtained from the measured CMB through the screening of the temperature and polarization anisotropies by resonant conversion. Data from CMB experiments can be used to extract the amplitude of dark screening, which scales like ε^4. We show how the large signal-to-noise ratio of CMB surveys, along with the characteristic frequency dependence of the screening signal, implies that this method outperforms the COBE/FIRAS constraint.

- **Correlating CMB anisotropies with templates from LSS**: As described in greater detail below, the morphology of the dark photon optical depth anisotropy depends on the distribution of ionized gas in halos. With assumptions about the galaxy-gas connection, a galaxy survey can be used to create a template for the dark photon optical depth field $\hat{\tau}(\omega, \hat{n})$. Cross-correlating the CMB measurement with this template $\langle \tau(\varepsilon, \omega, \hat{n})\, \hat{\tau}(\omega, \hat{n}') \rangle$ scales as ε^2, improving greatly on the CMB-only reach.

- **Correlation with Thomson screening**: The standard optical depth due to Thomson scattering by free electrons (we will denote by $\tau^{\rm Th}$) is also present as a source

of screening in the measured CMB. Since this anisotropic signal traces the same distribution of ionized matter as the dark screening component, the two signals will be correlated yet distinguishable due to the latter being frequency dependent. The cross-correlation $\langle \tau(\varepsilon, \omega, \hat{n})\, \tau^{\rm Th}(\hat{n}') \rangle$ also scales as ε^2.

- **The CMB bispectrum and optical depth reconstruction**: Both conversion to dark photons and Thomson screening induce non-Gaussian statistics in the CMB anisotropies. The combined effect can be modelled via three-point correlation functions (bispectra) that also scale as ε^2. These bispectra hold additional information compared to two-point functions since there are more modes; the associated statistical anisotropy can additionally be used to reconstruct the dark screening optical depth, allowing for its study at the field level.

In this Chapter, we demonstrate the possibility of using the aforementioned methods to improve the reach on kinetically mixed dark photon in the mass range (10^{-13} eV $\lesssim m_{\rm A'} \lesssim 10^{-11}$ eV). The Chapter is organized as follows. We first review resonant photon to dark photon conversion and compute the properties of conversion inside individual halos in Section 4.2, before summing over halos to obtain a frequency dependent dark screening optical depth in Section 4.3. In Section 4.4, we discuss the anisotropies of this dark screening optical depth, correlation functions, and CMB observables. In Section 4.5 we study the cross-correlation between this dark screening optical depth and the LSS of our Universe, and construct two-point cross-correlation functions between the CMB and LSS, as well as three-point cross-correlation functions of CMB observables. In Section 4.6, we present a forecast of the sensitivity of existing and future CMB data-sets to the various correlation functions studied in this Chapter. The result of these forecasts are shown in Section 4.7, along with a discussion of the prospect for constructing similar correlation functions in other new physics scenarios. In the appendix, we present details about the modelling of dark matter and gas halos (Appendix B.1) and the computation of correlation functions of dark screening (Appendix B.2), as well as a list of useful two-point correlation functions and quadratic estimators for the optical depth and other quantities (Appendix B.3).

4.2 Photon to dark photon conversion

In this section, we discuss how photons resonantly convert into dark photons within non-linear structure in the context of the halo model of LSS, where matter is organized into virialized dark matter halos populated by gas (see e.g. [59, 60] for a review). Resonant conversion can be modelled via the same formalism that describes neutrino oscillation

in medium, that is, the Mikheyev-Smirnov-Wolfenstein (MSW) effect [215, 216]. In the following, we review the resonant conversion of photons into dark photons and present our prescription for modelling the conversion probability as a sum over halos.

4.2.1 Resonant conversion probability

In an ionized medium, the Lagrangian in (4.1) leads to resonant conversion of photons to dark photons. This can be described by the Schrödinger equation [116]:

$$i\frac{\mathrm{d}}{\mathrm{d}t}\begin{pmatrix}\gamma\\ \mathrm{A}'\end{pmatrix} = \frac{1}{4\omega(t)}\begin{pmatrix}m_\gamma^2(\vec{x}(t)) - m_{\mathrm{A}'}^2 & 2\varepsilon m_{\mathrm{A}'}^2\\ 2\varepsilon m_{\mathrm{A}'}^2 & -m_\gamma^2(\vec{x}(t)) + m_{\mathrm{A}'}^2\end{pmatrix}\begin{pmatrix}\gamma\\ \mathrm{A}'\end{pmatrix}, \tag{4.3}$$

where γ is an incident photon with frequency $\omega(t)$ that follows a trajectory $\vec{x}$ parameterized by time t. The photon acquires an effective mass $m_\gamma^2(\vec{x}(t))$ (plasma frequency) as it crosses an ionized medium due to its interaction with the collective oscillations in the free electron density. Hence, to first order, the mass depends on the number density of electrons $n_e(\vec{x}(t))$ along its trajectory:

$$m_\gamma^2(\vec{x}(t)) \simeq 1.4\times10^{-21}\ \mathrm{eV}^2\left(\frac{n_e(\vec{x}(t))}{\mathrm{cm}^{-3}}\right). \tag{4.4}$$

Here we assume all baryonic matter is ionized and therefore ignore an additional negative contribution due to interactions with neutral atoms [116].

In the small-ε limit where conversion from dark photons back to photons can be safely neglected, the conversion probability is given by

$$P_{\gamma\to\mathrm{A}'} = \sum_{t_{\mathrm{res}}}\frac{\pi\varepsilon\, m_{\mathrm{A}'}^2}{\omega(t_{\mathrm{res}})}\times\varepsilon\left|\frac{\mathrm{d}}{\mathrm{d}t}\ln m_\gamma^2(\vec{x}(t))\right|^{-1}_{t=t_{\mathrm{res}}}, \tag{4.5}$$

where t_{res} are the times when the resonance condition $m_\gamma^2(t_{\mathrm{res}}) = m_{\mathrm{A}'}^2$ is met along the path $\vec{x}$. This expression for the total probability is a combination of the conversion rate $\Gamma_{\mathrm{res}} = \pi\varepsilon\, m_{\mathrm{A}'}^2/\omega(t_{\mathrm{res}})$ and the resonance time scale $\Delta t_{\mathrm{res}} \simeq \varepsilon\left|\frac{\mathrm{d}}{\mathrm{d}t}\ln m_\gamma^2(\vec{x}(t))\right|^{-1}_{t=t_{\mathrm{res}}}$.

4.2.2 Photon to dark photon conversion in non-linear structure

In the homogeneous and weakly inhomogeneous early Universe ($z \gg 10$), the slowly diluting charged particle density caused by cosmic expansion provides a natural scanner of the dark photon mass, and ensures efficient conversion for a wide range of dark photon masses.

At low redshift ($z \lesssim 10$), the scanner is mainly provided by the spatially varying electron density inside non-linear structure, e.g. halos, which also ensures efficient conversion over a range of dark photon masses due to the large density contrast.

Expression (4.5) is the integrated probability to convert along the line of sight. Working in the halo model for LSS [59], this expression becomes a sum over halos, where each term represents the probability that a photon converts within each. We re-write the probability per halo in terms of the mass and redshift:

$$P_i(\vec{x}|z_i, m_i) = \frac{\pi\varepsilon^2 m_{\mathrm{A}'}^2}{\omega(z_i)} \left| \frac{\mathrm{d}}{\mathrm{d}t} \ln m_\gamma^2(\vec{x}|z_i, m_i) \right|_{t=t_{\mathrm{res}}}^{-1} . \tag{4.6}$$

This expression holds for any type of photon, but in what follows we will focus on the conversion of CMB photons along their path from the surface of last scattering to the Earth. In the remainder of this sub-section we explain how to simplify the term in the modulus to account for a photon's path across each halo.

The effective photon mass $m_\gamma^2(\vec{x})$ depends on the baryon number density as well as the ionization fraction. In a galactic halo, baryonic matter represents a fraction $\Omega_b/\Omega_c \sim 0.19$ of the total halo mass m. Since baryonic matter is predominantly protons by mass, and the Universe is electrically neutral, we approximate the number density of the electrons to be the same as the number density of baryons. Furthermore, we are interested in the period after reionization ($z \lesssim 6-10$) therefore we assume throughout that the ionization fraction is unity everywhere. Where relevant, we treat reionization as instantaneous at a redshift in the range $6 < z < 10$ to encapsulate uncertainties about the history of reionization. Finally, we neglect the impact of He reionization. Further details of our modelling of reionization and other assumptions can be found in Appendix B.1.

For the density profile of baryons, we use the Battaglia et al. 'AGN Feedback' gas density profiles introduced in [217], which are based on hydrodynamic cosmological simulations. We use a version of the profile where the fit parameters are based on simulations that include a sub-grid model for active galactic nuclei (AGN) feedback. The profile is given by an expression that parametrically resembles the standard Navarro-Frenk-White (NFW) density profile of dark matter in halos [218]:

$$\rho_{\mathrm{gas}} = \frac{\Omega_b}{\Omega_c}\rho_c(z)\rho_0(z,m) \left(\frac{x}{x_c}\right)^\gamma \left[1 + \left(\frac{x}{x_c}\right)^{\alpha(z,m)}\right]^{-\frac{\beta(z,m)+\gamma}{\alpha(z,m)}}, \quad x \equiv \frac{r}{r_{200}(z,m)}. \tag{4.7}$$

The quantity $\rho_c(z)$ is the critical density for a flat FRW Universe and r_{200} is the radius where the gas density reaches $200\rho_c$. The exponents α, β, γ fix the slope in the regimes

where $x \sim 1, x \gg 1$ and $x \ll 1$, respectively. There are two fixed quantities $\gamma = -0.2$ and the core scale $x_c = 0.5$ that control the central region in each halo. The remaining functions $\rho_0(z,m), \alpha(z,m)$ and $\beta(z,m)$ are fit with power laws:

$$A = a \left(\frac{m_{200}}{10^{14} M_\odot} \right)^b (1+z)^c, \quad m_{200} = \frac{4\pi}{3} r_{200}^3, \tag{4.8}$$

where the best-fit parameters $\{a, b, c\}$ are in each case as follows: for ρ_0 $\{4000, 0.29, -0.66\}$, for α $\{0.88, -0.03, 0.19\}$, and finally for β $\{3.83, 0.04, -0.025\}$. These values are taken from Table 2 of [217][1].

As discussed in detail in later sections, the assumptions about how gas inhabits dark matter halos has a significant effect on the signal and the resulting sensitivity. An extreme case to contrast with is to assume that baryons track the dark matter density everywhere. The parametric expression for the standard NFW profile is [218]:

$$\rho_{\rm NFW} = \frac{\rho_s}{\frac{r}{r_s}\left(1 + \frac{r}{r_s}\right)^2}. \tag{4.9}$$

Each halo has a physical scale radius and density that depend on its mass and redshift, i.e. $r_s(z_i, m_i)$ and $\rho_s(z_i, m_i)$. The assumption that the baryons follow dark matter is expected to be reasonable in the outer regions of halos (e.g. beyond the scale radius). However it is no longer valid in the inner regions where baryonic feedback processes are non-negligible. We present a discussion on the model uncertainty in our sensitivity due to varying assumptions about the electron profile in Appendix B.1, using the NFW and AGN Feedback models as a proxy for the span of models.

The effective mass of a photon crossing a halo i centered at redshift z_i with mass m_i depends on the number density of electrons n_e along its path as defined in (4.4). Assuming all baryonic mass inside halos is contained within protons, that are as numerous as electrons, we can write this in terms of the halo gas density profile:

$$m_\gamma^2(\vec{x}|z_i, m_i) = \kappa \left[\frac{\rho_{\rm gas}(\vec{x}|z_i, m_i)}{\rm M_\odot/Mpc^3} \right], \tag{4.10}$$

where the term in brackets is dimensionless and we have defined $\kappa = 5.7 \times 10^{-38}$ eV^2.

[1]Throughout Part II of this Thesis, unless m_{200} is written explicitly (e.g. when we define the gas profile in (4.7) from [217]), the symbol m denotes the halo virial mass, defined such that within the virial radius the halo density is 178 times the critical density of the universe, i.e. $r_{\rm vir} \equiv r_{178}$ and $m \equiv m_{178}$.

For resonant conversion that occurs at a radius $r_{\rm res}$, the resonance time scale can be broken into a radial and an angular part:

$$\Delta t_{\rm res} \equiv \varepsilon \left| \frac{{\rm d} \ln m_\gamma^2}{{\rm d}t} \right|^{-1}_{t_{\rm res}} = \frac{\varepsilon}{\kappa} m_{\rm A'}^2 \left| \frac{{\rm d}\rho(\vec{x})}{{\rm d}t} \right|^{-1}_{t_{\rm res}} = \frac{\varepsilon}{\kappa} \frac{m_{\rm A'}^2}{|{\rm d}r(t_{\rm res})/{\rm d}t|} \left| \frac{{\rm d}\rho}{{\rm d}r} \right|^{-1}_{r_{\rm res}}, \tag{4.11}$$

where the velocity term $|{\rm d}r(t)/{\rm d}t|$ in (4.11) depends on the precise photon trajectory through the halo and encapsulates the angular dependence of the probability. As shown in Fig. 4.1, the direction to the center of halo i is $\hat{n}_i$ and the direction of the test photon is $\hat{n}$. We assume each halo is located at a single redshift z_i throughout the photon's crossing time (e.g. the halo size does not encompass cosmologically relevant distances), and take advantage of azimuthal symmetry around the $\hat{n}_i$ direction.

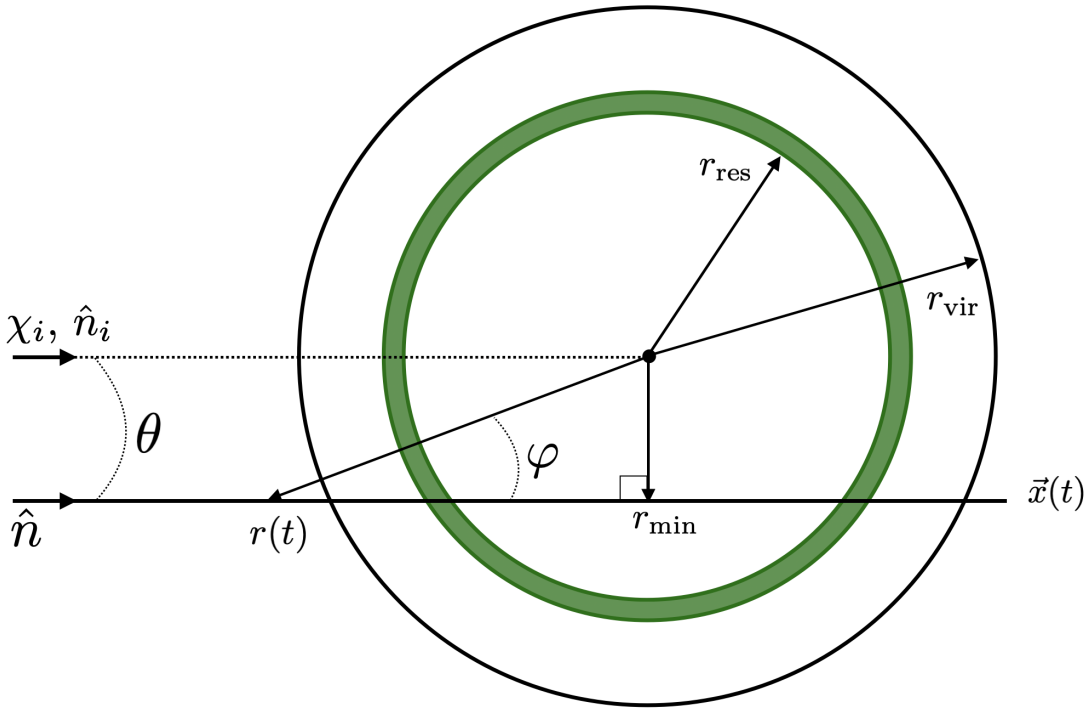

Figure 4.1: The trajectory of a photon $\vec{x}(t)$ through a dark matter halo centered at $\chi_i, \hat{n}_i$ on an observer's sky. In a coordinate system whose origin is at the halo center, the photon trajectory follows $r(\vec{x}(t)) \equiv r(t)$. Resonant conversion to a dark photon occurs when the photon crosses through a spherical shell at $r_{\rm res}$ over a timescale $\Delta t_{\rm res}$; each trajectory has two crossings. We define the boundary of each halo by the virial radius $r_{\rm vir}$.

In the small angle approximation where $\hat{n}||\hat{n}_i$, the minimum comoving distance between the halo center and the photon's path is $(1+z_i)\, r_{\rm min} = \chi_i\, \theta$, where χ_i is the radial comoving distance to the halo center at redshift z_i and θ is a small angle. The velocity $|{\rm d}r(t)/{\rm d}t| = \cos\varphi(t)$, where $\sin\varphi(t) = r_{\rm min}/r(t)$.

Using this geometry, the conversion probability due to halo i is separable into a radial part and an angular part. The latter one is a measure of how long the photon spends inside the resonance region $\sim \Delta t_{\rm res}$. We have:

$$P^i_{\gamma\to {\rm A}'}(\chi_i, m_i) = P(\chi_i, m_i)\, u(\hat{n} - \hat{n}_i|\chi_i, m_i), \tag{4.12}$$

where we define

$$\begin{aligned} P(\chi_i, m_i) &= \frac{2\pi\varepsilon^2 m_{\rm A'}^4}{\kappa\, \omega(z_i)}\, \frac{{\rm d}\rho_i}{{\rm d}r}\Big|^{-1}_{r_{\rm res}}\, \Theta(r_{\rm res} - r_{\rm vir}), \\ u(\hat{n} - \hat{n}_i|\chi_i, m_i) &= \left[1 - \frac{(\chi_i\theta/r_{\rm res})^2}{(1+z_i)^2}\right]^{-1/2}. \end{aligned} \tag{4.13}$$

The Heaviside step function $\Theta(r_{\rm res} - r_{\rm vir})$ arises since we consider only photon to dark photon conversion happening inside the boundary of each halo, which we take here to be the virial radius $r_{\rm vir}$. The step function is normalized so that $\Theta(r_{\rm res} - r_{\rm vir}) = 2$ for $r_{\rm res} < r_{\rm vir}$ and $\Theta(r_{\rm res} - r_{\rm vir}) = 1$ for $r_{\rm res} = r_{\rm vir}$ to account for the fact that a photon crosses a resonance twice, going in and then out of a halo, except when it exactly grazes the edge of the virial radius. The effect of the sharp truncation at the boundary of the halo is significant for masses $m_\gamma \sim 10^{-13}$ eV that probe low densities. Note that the function $u(\hat{n} - \hat{n}_i|\chi_i, m_i)$ has the apparent singularity when $\theta = (1+z_i) r_{\rm res}/\chi_i$, where the conversion probability blows up. However, the integral over the profile is finite and equal to

$$\int d^2\hat{n}\; u(\hat{n} - \hat{n}_i|\chi_i, m_i) = 2\pi(1+z_i)^2 r_{\rm res}^2/\chi_i^2\ . \tag{4.14}$$

We close this section by noting that within the halo model, we make the rather drastic assumptions that each halo (dark matter and gas) is spherically symmetric, identical at each mass and redshift, and has properties independent of their formation history and local environment. These assumptions will fail for individual halos. However, we expect that quantities dependent on the statistical properties of the full distribution of halos, such as power spectra, will be well-approximated (see e.g. recent analyses such as [219]). We are primarily concerened with such statistical quantities in the following.

4.3 The photon to dark photon conversion monopole

The total probability for a photon to convert over its trajectory is the sum of contributions from each individual halo. In this section we focus on the sky-averaged probability and explain why this effect induces a new type of optical depth. In the next section we introduce the two-point function of optical depth fluctuations owing to the halos' shapes on the sky.

The overall conversion probability is

$$\mathbf{P}_{\gamma\to \mathrm{A}'} = \left\langle \sum_i P^i_{\gamma\to \mathrm{A}'}(\chi_i, m_i) \right\rangle = \int \mathrm{d}m \int \mathrm{d}^3\chi \, n(\chi, m) P(\chi, m) \, u(\hat{n}|\chi, m), \tag{4.15}$$

where $\mathrm{d}^3\chi = \chi^2 \mathrm{d}\chi \mathrm{d}^2\hat{n}$ and we have separated the resonant conversion probability $P_{\gamma\to \mathrm{A}'}$ into its radial and angular components that depend on each halo's characteristics. To obtain the expression above we also identified the number density of halos of mass m at redshift χ as

$$\left\langle \sum_i \delta(m - m_i)\delta(\chi - \chi_i)\delta^2(\hat{n} - \hat{n}_i) \right\rangle \equiv n(\chi, m), \tag{4.16}$$

where $\langle \ldots \rangle$ denotes a sky-wide ensemble average and the delta functions are evaluated at each halo position and mass. The halo number density per volume per halo mass $n(\chi, m)$ is the halo mass function. We use the Tinker mass function throughout [220].

Integrating the angular profile $u(\hat{n}|\chi, m)$ over the sky we implicitly weight the probability by the effective projected area of each halo. Evaluating the angular integral and simplifying we obtain:

$$\mathbf{P}_{\gamma\to \mathrm{A}'} = 4\pi \int_{0.01}^{z^{\mathrm{reio}}} \mathrm{d}z \, \frac{\chi(z)^2}{H(z)} \int \mathrm{d}m \, n(z, m) P(z, m) \, u_{00}(z, m), \tag{4.17}$$

where $u_{00} = \int \mathrm{d}^2\hat{n} \, u(\hat{n})/4\pi$ is the monopole of $u(\theta)$, and we changed the integration variable to redshift z from radial comoving distance χ. Within our assumption of instantaneous reionization, we impose a sharp upper limit on the integral over redshift at z^{reio}.

Photon to dark photon conversion manifests itself as a frequency dependent optical depth, encoding the removal of CMB photons along their path from recombination to CMB telescopes on Earth. The sky-averaged magnitude of this optical depth is the integrated probability in (4.17):

$$\bar{\tau}(\varepsilon, \omega) \equiv \mathbf{P}_{\gamma\to \mathrm{A}'} \propto \varepsilon^2 \omega^{-1}, \tag{4.18}$$

where from here onward the bar notation stands for the projected, i.e. integrated over redshift, sky average. We introduce a new notation for the dimensionful average optical depth

$$\bar{\eta} = \bar{\tau}\varepsilon^{-2}\omega \text{ [eV]}, \tag{4.19}$$

such that $\bar{\eta}$ depends only on the dark photon mass $m_{A'}^2$ and the cosmology. It is useful to make this distinction because both ε and ω are parameters we vary later.

In Fig. 4.2, we show several examples of the differential optical depth along the line of sight for a range of dark photon masses. Notice in this plot that the light dark photons are only produced at low redshift. Light dark photons probe the outer-most regions of halos and the abrupt fall-off is due to the truncation of halos at the virial radius. Physically, this falloff would be broadened by the softer boundaries between halos and the intergalactic medium. In contrast, the heaviest dark photons probe regions near the core of halos where the gas density is highest. Since the gas profile is nearly flat near the core of halos, only the heaviest and rarest halos contribute to the optical depth of photons with $m_{A'} \geq 10^{-12}$ eV.

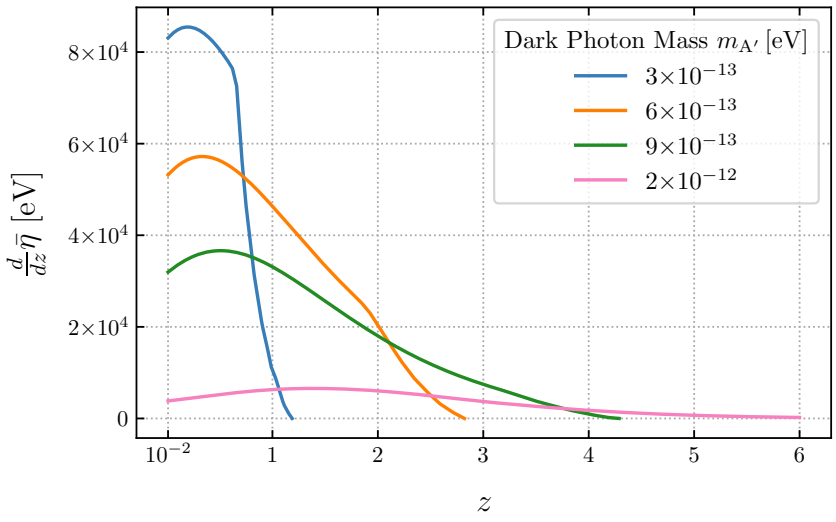

Figure 4.2: The average dimensionful optical depth defined in (4.19) as a function of redshift, for a range of dark photon masses. To obtain the full optical depth, one needs to integrate over redshift and multiply by the unknown mixing parameter divided by the frequency of the photon, ε^2/ω. Notice that the lighter masses produce the strongest signal at low redshift. Meanwhile, heavier dark photons probe redshifts all the way to reionization but require crossing large densities in order for the resonant conversion to take place. These are found within more massive halos whose number density is suppressed.

In Fig. 4.3 we plot the total (e.g. integrated over the line of sight) dimensionful optical depth assuming both $z^{\rm reio} = 6$ and $z^{\rm reio} = 10$. The change in magnitude is less than the thickness of the blue curve, meaning that our model is insensitive to uncertainties related to when the end of reionization takes place. From now on, unless otherwise stated, we assume that reionization takes place instantaneously at $z^{\rm reio} = 6$. Notice that, unless $\varepsilon \ll 1$ photon to dark photon conversion is in the optically thick regime. For example, $\bar{\tau} = \bar{\eta}\,\varepsilon^2/\omega = 1$ for ~ 100 GHz photons (near the peak of the CMB blackbody) at $\varepsilon \sim 10^{-4}$. This is a preliminary indicator that photon to dark photon conversion at low redshift can be a sensitive probe. The dark photon mass range over which there is a significant effect spans roughly one order of magnitude, peaking at $m_{\rm A'} \sim 6 \times 10^{-13}$ eV.

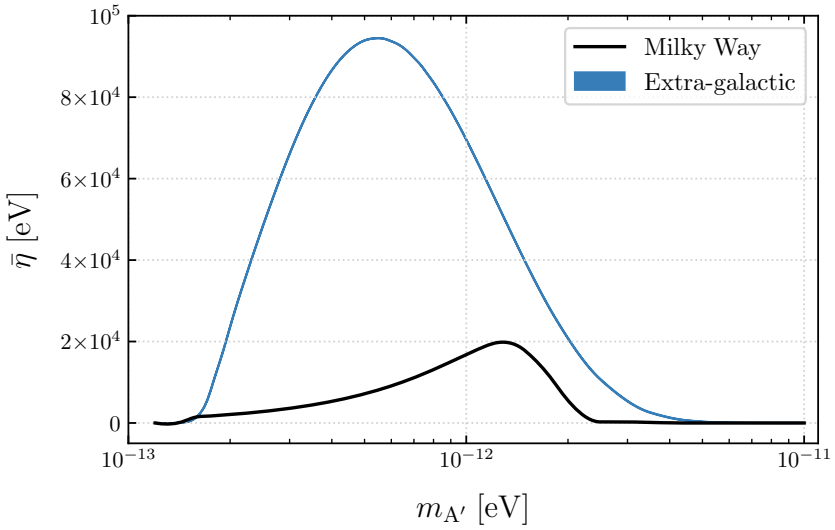

Figure 4.3: The dimensionful optical depth monopole as a function of dark photon mass $m_{\rm A'}$. The extra-galactic contribution $\bar{\eta}$ (*blue*) is defined by (4.19). Under our assumptions, resonant conversion occurs once reionization is completed and here we plot the case where $z^{\rm reio} = 6$ and where $z^{\rm reio} = 10$. The maximum change in the amplitude of $\bar{\eta}$ is of order 10^2 eV, less than the thickness of the blue line, and we conclude that the model is insensitive to the details of reionization over the range of masses we are probing. We therefore assume $z^{\rm reio} = 6$ in the remainder of this Chapter. At low mass, $\bar{\eta} \to 0$ due to the constraint that conversion only happens within the virial radius in each halo. The upper bound is set by the shape of the gas profile and details about the halo model. The contribution due to gas in the Milky Way $\eta^{\rm MW}$ (*black*) is defined in (4.20).

Baryonic feedback can affect the accessible dark photon mass range and strength of

the photon to dark photon conversion monopole, in principle contributing a source of modelling uncertainty in the expected signal. We explore this modelling uncertainty in more detail in Appendix B.1 by comparing the AGN gas model used here [217] with the results obtained by assuming that baryons trace the dark matter NFW density profile [218]. We show that the two models give nearly identical results for low masses $m_{\mathrm{A}'}$ where the resonant conversion condition is met near the outermost region of a halo. This can be understood as a consequence of the fact that the AGN gas profile and the NFW profile are only different near the core of halos where the NFW density increases without bound, while the gas density achieves a maximum; beyond the scale radius, the two density profiles are nearly the same. Also for this reason, the predictions for the two models differ most at large dark photon mass. Here, details about the gas population in each halo can have a significant effect on the projected signal and resulting sensitivity, and it is important to incorporate this modelling uncertainty in the interpretation of our results below. As we will demonstrate in more detail below, the monopole signal is more strongly influenced by this modelling uncertainty than correlation functions.

4.3.1 Contribution from the Milky Way

The gas halo surrounding the Milky Way is also a source of resonant photon to dark photon conversion. In this section we model its contribution to the overall optical depth. The Earth's distance from the galactic center is well below the scale radius of the Milky Way halo, therefore in our model we assume that there is only an appreciable contribution to the optical depth monopole and not to optical depth anisotropies. We further assume that the Milky Way is an average spherical halo, with average AGN feedback and model it with the same gas profile of (4.7) computed for $z^{\mathrm{MW}} = 0$ and m^{MW} from [221]. In reality, the details of the gas distribution can affect both the monopole and anisotropies in the optical depth. Nevertheless, we can estimate the relative magnitude of the galactic versus extra-galactic conversion under these assumptions.

The expression for the optical depth is simply the contribution from a single halo with appropriate properties:

$$\tau^{\mathrm{MW}} \equiv P^{\mathrm{MW}}_{\gamma\to\mathrm{A}'} = \frac{2\pi\varepsilon^2 m^4_{\mathrm{A}'}}{\kappa\,\omega}\,\frac{\mathrm{d}\rho_{\mathrm{gas}}}{\mathrm{d}r}\bigg|^{-1}_{r_{\mathrm{res}}}\Theta(r_{\mathrm{res}} - r^{\mathrm{MW}}_{\mathrm{vir}}), \tag{4.20}$$

where we discard the angular component by assuming the Earth is near the center of the halo, and ω is the frequency of the CMB photons today. Assuming a virial radius and virial mass for the Milky Way as found in [221], as well as the concentration-mass relation

at redshift zero from [222], we calculate the conversion probability for the relevant range of dark photon masses. The result is plotted in Fig. 4.3. Given the assumptions made in this Chapter, the extra-galactic optical depth dominates the contribution due to conversion in the Milky Way for all dark photon masses considered.

Since the Milky Way does not host an AGN, the gas profile assumed here may be too diffuse. In the extreme scenario where gas traces dark matter, the magnitude of the Milky Way contribution increases monotonically for higher dark photon masses. The increase is cutoff at the core when gas no longer traces dark matter. The high dark photon mass regime is where the extra-galactic contribution to the optical depth becomes small, and the Milky Way therefore introduces additional modelling uncertainties at the upper end of dark photon masses we consider. Note that such effects will only increase the reach in sensitivity to conversion, making the neglect of contributions from the Milky Way a conservative assumption.

4.4 Patchy dark screening

When photon to dark photon conversion occurs in non-linear structure, the associated optical depth for conversion is strongly anisotropic on the sky. These anisotropies in the optical depth serve as a screen of varying opacity through which the CMB must propagate on the way from decoupling to our telescopes here on Earth. In addition to the sky-averaged suppression in the intensity of CMB photons, new temperature and polarization anisotropies are introduced due to the different conversion probability of CMB photons to dark photons across different lines of sight.

The analogous effect in the standard cosmological model is the 'screening' of CMB anisotropies due to the Thomson scattering of CMB photons by free electrons. For Thomson scattering, anisotropies in the optical depth couple to *anisotropies* in the CMB temperature and polarization. This is known as 'patchy screening' of the CMB. Notably, there is no coupling of optical depth anisotropies to the CMB temperature monopole – Thomson scattering doesn't change the energy of photons and for every photon scattered out of the line of sight, another is scattered into the line of sight. Therefore, patchy screening of the CMB is always a small effect, i.e. second order in perturbations of the CMB and optical depth anisotropies. Although small, the detection of *patchy screening* during [88] and after [223] reionization is within the reach of future CMB experiments.

Photon to dark photon conversion produces *patchy dark screening*, which has two crucial differences to Thomson screening: conversion does not preserve the blackbody spectrum

and conversion only removes photons from the line of sight. *Therefore, patchy dark screening couples the CMB monopole to fluctuations in the optical depth, and is a 1st order effect* (in anisotropies). Since the CMB monopole is $\sim 10^4$ times larger than the temperature anisotropies, patchy dark screening is far stronger at fixed optical depth than Thomson screening. Furthermore, the characteristic frequency-dependence of patchy dark screening can be used to separate it from the primary CMB and astrophysical foregrounds. In the remainder of this section and the next section, we derive various correlation functions that will be used to forecast the sensitivity of CMB experiments to the kinetic mixing parameter and dark photon mass, assuming the frequency dependent dark screening anisotropies can be *separated* from the primary CMB anisotropies. A detailed discussion of how well this separation can be performed is presented in Section 4.6.2.

4.4.1 Anisotropic screening

Before computing CMB correlators, we must first describe anisotropies in the photon to dark photon conversion optical depth, the anisotropies in the Thomson optical depth, and the cross-correlation between these two fields. The halo model for large-scale structure is a useful tool for these computations, since it is straightforward to populate dark matter halos with the electron density (for Thomson screening) and the conversion probability (for dark screening).

The standard optical depth to reionization is the integrated electron density along the line of sight:

$$\tau^{\rm Th} = \sigma_T \int \mathrm{d}\chi \, a(\chi) n_e(\chi, \hat{n}), \tag{4.21}$$

where σ_T is the Thomson cross-section and a is the local scale factor. The inhomogeneous matter distribution introduces spatial fluctuations in the electron number density $n_e(\chi, \hat{n})$. This can be measured via the directional dependence they introduce on the optical depth field. The local perturbations in the electron density induce small fluctuations $\delta\tau^{\rm Th}(\hat{n})$ in the optical depth profile

$$\tau^{\rm Th}(\hat{n}) = \bar{\tau}^{\rm Th} + \delta\tau^{\rm Th}(\hat{n}), \tag{4.22}$$

where $\bar{\tau}^{\rm Th}$ is the standard cosmological parameter. Once again we work under the assumptions of the halo model where the integral above can be written as an average over halos whose number density depends on mass and redshift, where the electron number density fluctuations are related to the gas density profile. In the Limber approximation, the multipole expansion of the electron density from one halo centered on the north celestial pole

(such that the azimuthal angular momentum $m = 0$) is [224]:

$$\rho^e_\ell(z,m) = \frac{a(z)}{\chi(z)^2}\int 4\pi r^2 \mathrm{d}r \frac{\sin\left((\ell+1/2)\, r/\chi(z)\right)}{(\ell+1/2)\, r/\chi(z)} \rho^{\rm gas}(r|z,m), \tag{4.23}$$

where the $\rho^{\rm gas}$ is the Battaglia et al. AGN gas density profile [217] and $\rho_e = n_e\, m_p$. The Limber approximation works best for $\ell \gg 1$, which is the regime we are in.

We now introduce the optical depth for photon to dark photon conversion. Consider small anisotropic perturbations to the average extra-galactic optical depth $\bar{\tau}$:

$$\tau(\hat{n}, \varepsilon, \omega) = \bar{\tau}(\varepsilon, \omega)\left(1 + \delta\tau(\hat{n})\right). \tag{4.24}$$

Note that with this convention $\delta\tau(\hat{n})$ is independent of ε and ω. The next step is to compute the two-point angular power spectra for these fields. Projecting onto spherical harmonics, we define the power spectrum $C_\ell^{\delta\tau\delta\tau}$:

$$\langle \delta\tau_{\ell m}\, \delta\tau^*_{\ell' m'}\rangle = \delta_{\ell\,\ell'}\delta_{m\,m'} C_\ell^{\delta\tau\delta\tau}, \tag{4.25}$$

In the context of the halo model, the power spectrum can be described by a sum of an intra-halo (1-halo) and an inter-halo (2-halo) contributions:

$$C_\ell^{\delta\tau\delta\tau} = C_\ell^{\tau\tau}/\bar{\tau}^2 = C_\ell^{1-\rm halo} + C_\ell^{2-\rm halo}, \quad \ell \geq 1. \tag{4.26}$$

The quantity $C_\ell^{\tau\tau}$ is the angular power spectrum of the optical depth due to photon to dark photon conversion (which depends on ε and ω). The terms on the right hand side of (4.26) are computed in detail in Appendix B.2. The final expressions are:

$$\begin{aligned}
\bar{\tau}^2 C_\ell^{1-\rm halo} &= \frac{4\pi}{2l+1}\int \mathrm{d}z\, \frac{\chi(z)^2}{H(z)} \int \mathrm{d}m\, n(z,m)\left[P(z,m)\, u_{\ell 0}(z,m)\right]^2, \\
\bar{\tau}^2 C_\ell^{2-\rm halo} &= \frac{4\pi}{2\ell+1}\left[\prod_{i=1,2}\int \mathrm{d}z_i\, \frac{\chi(z_i)^2}{H(z_i)} \int \mathrm{d}m_i\, n(z_i,m_i) b(z_i,m_i) P(z_i,m_i) u_{\ell 0}(z_i,m_i)\right] C_\ell^{\rm lin}(z_1,z_2), \\
C_\ell^{\rm lin}(z_1,z_2) &= \frac{2}{\pi}\int \mathrm{d}k\, k^2 j_\ell(k\chi_1)\, j_\ell(k\chi_2)\, \sqrt{P^{\rm lin}(k,\chi_1) P^{\rm lin}(k,\chi_2)}.
\end{aligned} \tag{4.27}$$

The quantity $j_\ell(k\chi)$ is the spherical Bessel function and $b(z,m)$ is the linear halo bias. $P^{\rm lin}(k,\chi)$ is the linear matter power spectrum calculated using CAMB [69]. All quantities are computed for fixed cosmology. Throughout this Chapter we used the following set of parameters: dark matter density $\Omega_c h^2 = 0.12$, baryon density $\Omega_b h^2 = 0.022$, Hubble

constant $H_0 = 67.3\,\mathrm{km\,s^{-1}\,Mpc^{-1}}$, scalar spectral index $n_s = 0.96$, scalar amplitude $A_s = 2.2 \times 10^{-9}$, and optical depth to reionization $\bar{\tau}^{\mathrm{Th}} = 0.06$.

In Fig. 4.4 we plot the optical depth power spectrum of $\delta\tau$ fluctuations for a range of dark photon masses, assuming $z^{\mathrm{reio}} = 6$. In the left panel, we show the relative importance of the 1-halo term compared to the total. The 1-halo term dominates at high ℓ, while the 2-halo term dictates the shape and amplitude on large scales $\ell \lesssim 1000$. The 1-halo term is larger at the upper end of the dark photon mass range we consider. This is consistent with the fact that conversion happens near the halo core in this regime. In the right panel we show the total power spectrum $C_\ell^{\delta\tau\delta\tau}$ for 4 choices of $m_{\mathrm{A}'}$ that span the parameter space we probe for. Any changes can be attributed to the radius of the resonance surface at that mass given the gas density profile ρ^{gas} as well as details about the halo model, for e.g. the population of halos $n(z, m)$, which also dictates the bias function $b(z, m)$. The total magnitude of the power spectrum, $C_\ell^{\tau\tau}$, depends strongly on the dark photon mass through $\bar{\eta}$. Hence, it will be maximized by masses near the peak in the monopole $\bar{\tau}(m_{\mathrm{A}'})$, which was depicted in Fig. 4.3.

Repeating the computation presented in Appendix B.2 for the dark screening case, we find the 1-halo and 2-halo contributions to the Thomson screening auto-power spectrum. The full expression is

$$C_\ell^{\tau^{\mathrm{Th}}\tau^{\mathrm{Th}}} = \frac{\sigma_T^2}{m_p^2}\left(\int \frac{\mathrm{d}z}{H(z)}\frac{\chi(z)^2}{(1+z)^2}\int \mathrm{d}m\, n(z,m)\,\rho_{\ell 0}^{e}(z,m)^2 + \left[\prod_{i=1,2}\int \frac{\mathrm{d}z_i}{H(z_i)}\frac{\chi(z_i)^2}{(1+z_i)}\int \mathrm{d}m_i\, n(z_i,m_i) b(z_i,m_i)\rho_{\ell 0}^{e}(z_i,m_i)\right] C_\ell^{\mathrm{lin}}(z_1,z_2)\right). \tag{4.28}$$

The quantities have the same meaning as in expressions (4.27) above.

Anisotropies in the Thomson screening and dark screening optical depth fields trace similar matter density profiles over the sky and across the line of sight. It is therefore expected that the fluctuations in either field are correlated. The two-point function $\langle \tau\tau^{\mathrm{Th}} \rangle \sim \varepsilon^2$ has

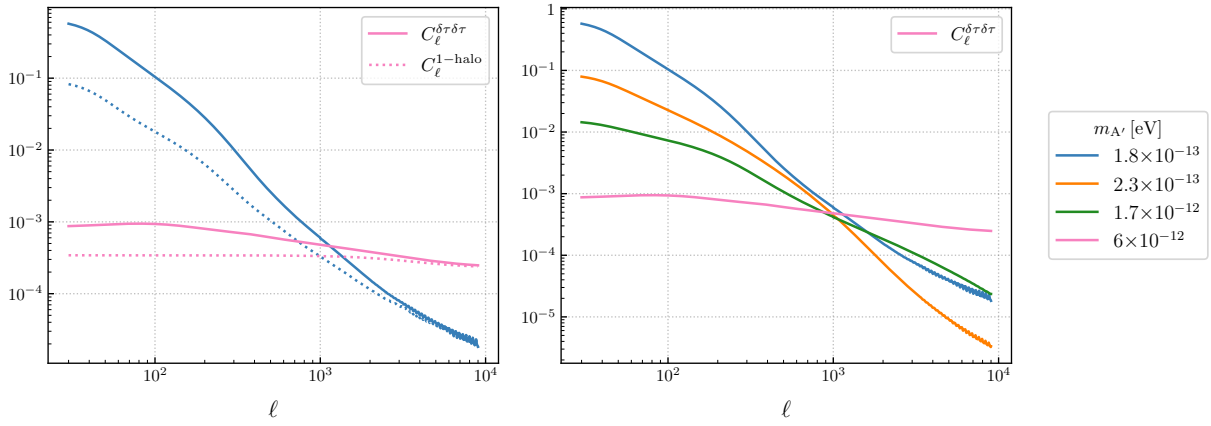

Figure 4.4: The angular power spectrum of dark screening fluctuations, $C_\ell^{\delta\tau\delta\tau}$, which is independent of ε and ω, for a range of dark photon masses that span the parameter space we are probing. In the left panel, we compare the 1-halo term with the sum in (4.26) to show that most power on large scales is due to the 2-halo term, while on small scales the 1-halo term dominates. At large mass, when the transition from photon to dark photon occurs nearer to the halo core where gas densities are largest, the two terms become comparable and the spectrum is scale invariant. This feature also affects the signal amplitude hierarchy: although at large $m_{\mathrm{A}'} > 10^{-12}$ eV the monopole is subdominant (e.g. Fig. 4.3), the additional structure on small scales causes $C_\ell^{\tau\tau}$ in this regime to be equivalent in terms of constraining power for ε to spectra for $m_{\mathrm{A}'} < 10^{-12}$ eV. This will be relevant in Section 4.6 where we present our forecasts.

the following angular power spectrum:

$$\bar{\tau} C_\ell^{\delta\tau\tau^{\mathrm{Th}}} = \frac{\sigma_T}{m_p}\sqrt{\frac{4\pi}{2\ell+1}}\left(\int \frac{\mathrm{d}z}{H(z)}\frac{\chi(z)^2}{(1+z)}\int \mathrm{d}m\, n(z,m)\,\mathcal{F}(z,z,m,m)\right.$$
$$\left. + \left[\prod_{i=1,2}\int \frac{\mathrm{d}z_i}{H(z_i)}\frac{\chi(z_i)^2}{(1+z_i)}\int \mathrm{d}m_i\, n(z_i,m_i) b(z_i,m_i)\right]\mathcal{F}(z_1,z_2,m_1,m_2)\, C_\ell^{\mathrm{lin}}(z_1,z_2)\right), \tag{4.29}$$

$$\mathcal{F}(z_1,z_2,m_1,m_2) = P(z_1,m_1)\, u_{\ell 0}(z_1,m_1)\, \rho^e_{\ell 0}(z_2,m_2), \tag{4.30}$$

where all quantities are real. The Thomson auto-power spectrum is shown in Fig. 4.5, alongside examples for the power spectrum of the dark screening optical depth and their cross-correlation for fixed $m_{\mathrm{A}'}$ and ε ($C_\ell^{\tau^{\mathrm{Th}}\tau^{\mathrm{Th}}}$ is independent of ε). The power spectra

involving dark screening scale differently with ε, so that for ε around 7×10^{-7}, $C_\ell^{\tau\tau^{\rm Th}} > C_\ell^{\tau\tau}$. The magnitude of $C_\ell^{\tau\tau}$ varies over the range of dark photon masses we study such that it peaks around $m_{\rm A'} \simeq 10^{-12}$ eV and falls abruptly for mass values towards both ends of the interval.

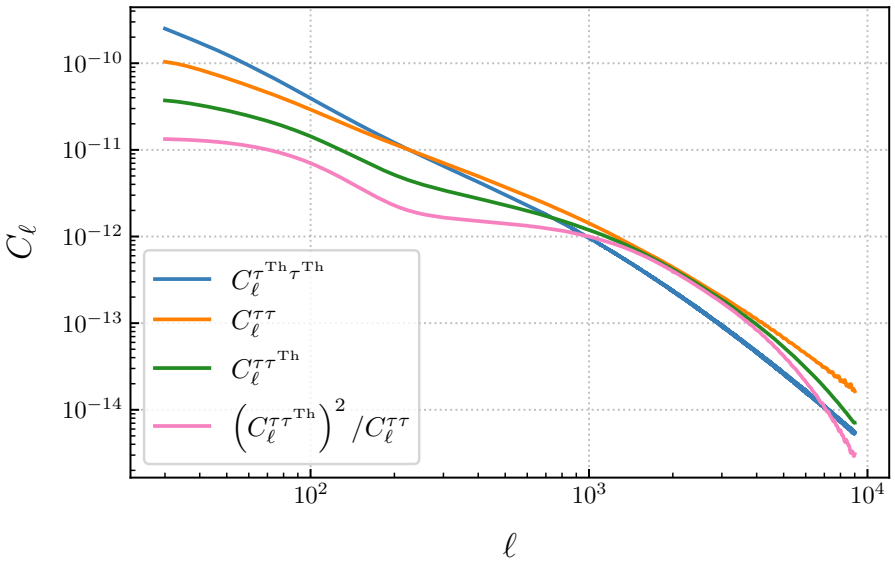

Figure 4.5: We show the angular power spectrum of the two-point function of Thomson screening (*blue*), dark screening (*orange*), as well as their cross-correlation (*green*). We chose the value of $\varepsilon = 10^{-6}$ and fixed $m_{\rm A'} = 6\times10^{-13}$ eV and $\omega = 30$ GHz. We also present the ε-independent combination $\left(C_\ell^{\tau\tau^{\rm Th}}\right)^2/C_\ell^{\tau\tau}$ (*pink*), which will be useful for the sensitivity forecast in Section 4.6.

4.4.2 Patchy dark screening of the CMB

We now describe in detail how the optical depth anisotropies of the previous section manifest as anisotropic spectral distortions in the CMB temperature and polarization. The largest effect arises from patchy dark screening of the CMB temperature monopole. In addition to this, there are new spectral anisotropies from the screening of temperature and polarization anisotropies. An additional novel signature of patchy dark screening is the production of B-modes (curl) from pure E-mode (divergence) polarization anisotropies, as occurs in any scenario with screening [225]. This leads to statistically anisotropic correla-

tions between the temperature, E modes, and B modes dependent on the specific realization of the anisotropic optical depth and CMB anisotropies in our Universe.

In analogy with patchy screening from Thomson scattering, the photon to dark photon optical depth fluctuations suppress the CMB temperature fluctuations and polarization Stokes parameters. The combined effect of dark and Thomson screening on the observed temperature and polarization are

$$\begin{aligned} T^{\rm obs}(\hat{n},\omega) &= \bar{T} + T^{\rm Sc}(\hat{n}) + T^{\rm dSc}(\hat{n},\omega), \\ (Q \pm iU)^{\rm obs}(\hat{n},\omega) &= (Q \pm iU)^{\rm Sc}(\hat{n}) + (Q \pm iU)^{\rm dSc}(\hat{n},\omega), \end{aligned} \tag{4.31}$$

where

$$\begin{aligned} T^{\rm Sc}(\hat{n}) &\simeq \left[1 - \tau^{\rm Th}(\hat{n})\right] T(\hat{n}), \\ T^{\rm dSc}(\hat{n},\omega) &\simeq -\tau(\hat{n},\omega)\left[\bar{T} + T(\hat{n})\right], \\ (Q \pm iU)^{\rm Sc}(\hat{n}) &\simeq \left[1 - \tau^{\rm Th}(\hat{n})\right](Q \pm iU)(\hat{n}), \\ (Q \pm iU)^{\rm dSc}(\hat{n},\omega) &\simeq -\tau(\hat{n},\omega)(Q \pm iU)(\hat{n}). \end{aligned} \tag{4.32}$$

The label *obs* stands for observed anisotropies, *Sc* for screening from Thomson scattering, and *dSc* for dark screening. We have explicitly isolated the dependence on the CMB blackbody temperature monopole $\bar{T} = 2.725K$, where in our notation the sky average of $T(\hat{n})$ is zero while the sky average of $T^{(\rm obs)}$ is not. As our first approximation, we assume that $T(\hat{n})$ and $(Q \pm iU)(\hat{n})$ are the lensed CMB temperature and polarization anisotropies. This neglects the lensing of the screened CMB along the line of sight, which is a small higher order effect. We neglect extra-galactic foregrounds, such as the cosmic infrared background, point sources, and Sunyaev Zel'dovich effects. We assume that no significant kinetic mixing happened between recombination and the end of reionization. Finally, we work in the limit where $\tau(\hat{n},\omega), \tau^{\rm Th}(\hat{n}) \ll 1$.

The total spectral distortion to the blackbody spectrum due to photons' conversion into dark photons is given by

$$B(\hat{n},\omega,T) = B^0(\omega,T)\left(1 - P_{\gamma\to {\rm A}'}(\hat{n},\omega)\right), \tag{4.33}$$

where $P_{\gamma\to {\rm A}'}$ is the overall conversion probability and $B^0(\omega,T)$ represents the intensity of the theoretical Planckian spectrum. In natural units this is:

$$B^0(\omega,T) = \frac{\omega^3}{2\pi^2}\left(e^{\frac{\omega}{T}} - 1\right)^{-1}. \tag{4.34}$$

The dependence on frequency ω in (4.32) is relative to the blackbody spectrum of the CMB in units of temperature, not intensity (see, e.g. also [226]). To convert, we take the

leading order expansion in temperature fluctuations $\delta T(\hat{n})$ of (4.33):

$$\begin{aligned} B(\omega, \hat{n}) &= B^0(\omega, \bar{T}) + \delta B(\omega, \hat{n}) \\ &\simeq B^0(\omega, \bar{T}) + \left.\frac{\partial B^0(\omega, T)}{\partial T}\right|_{T=\bar{T}} \delta T(\hat{n}) - B^0(\omega, \bar{T}) P_{\gamma \to \mathrm{A}'}(\hat{n}, \omega). \end{aligned} \tag{4.35}$$

Therefore, in CMB temperature units, the temperature fluctuation function of frequency is

$$\frac{1}{\left.\frac{\partial B(\omega,T)}{\partial T}\right|_{T=\bar{T}}} \delta B = \delta T - \frac{1}{\left.\frac{\partial B(\omega,T)}{\partial T}\right|_{T=\bar{T}}} B(\omega, \bar{T}) P_{\gamma \to \mathrm{A}'} = \delta T - \frac{1 - e^{-x}}{x} \bar{T} P_{\gamma \to \mathrm{A}'}, \tag{4.36}$$

where $x = \omega / \bar{T}$ in natural units. A factor of

$$\zeta(\omega) = \frac{1 - e^{-x}}{x}, \tag{4.37}$$

appears when converting the frequency dependence in the absorption optical depth to the frequency dependence in the standard temperature units, and the full frequency dependence of the dark screening signal in units of temperature is $\zeta(\omega)/\omega$.

Next, we decompose the lensed CMB temperature and optical depths into spherical harmonics and the Stokes parameters into spin-2 spherical harmonics:

$$\begin{aligned} T(\hat{n}) &= \sum_{\ell m} T_{\ell m} Y_{\ell m}(\hat{n}), \\ \tau(\hat{n}) &= \sum_{\ell m} \tau_{\ell m} Y_{\ell m}(\hat{n}), \\ (Q \pm iU)(\hat{n}) &= \sum_{\ell m} \left[E_{\ell m} \pm i B_{\ell m}\right] {}_{\pm 2}Y_{\ell m}(\hat{n}), \end{aligned} \tag{4.38}$$

where $E_{\ell m}$ and $B_{\ell m}$ are the moments of the E- and B-mode polarization anisotropies. Note that the latter is induced only by lensing in the absence of primordial gravitational waves and is therefore substantially smaller than E-mode polarization. We neglect the dark screening of lensing B-modes below.

Given multi-frequency observations of the CMB, it is possible to separate the blackbody and dark screening components of the temperature and polarization anisotropies. Assuming perfect separation of the blackbody and patchy dark screening components (we discuss the scenario where this separation is imperfect in Section 4.6.2), we construct correlation functions between Thomson-screened and dark-screened temperature and polarization anisotropies, that is, T^{Sc} and T^{dSc}, respectively. Note that there will be both statistically isotropic and statistically anisotropic components of the correlation functions.

4.4.3 Dark screening auto-correlation functions

As a warm up, in the Standard Model ($\varepsilon = 0$ and hence $T^{\rm dSc} = 0$), the anisotropies in optical depth $\tau^{\rm Th}$ lead to temperature anisotropies, which are captured in the auto-correlation function for the Thomson-screened blackbody anisotropies:

$$\begin{aligned}\langle T^{\rm Sc}_{\ell m} T^{\rm Sc}_{\ell' m'}\rangle &= (-1)^m C_\ell^{T^{\rm Sc}T^{\rm Sc}}\delta_{\ell\ell'}\delta_{m-m'} \\ &\quad - \sum_{\ell_1 m_1}(-1)^{m_1}\begin{pmatrix}\ell & \ell' & \ell_1\\ m & m' & -m_1\end{pmatrix}\sqrt{2\ell_1+1}W^{000}_{\ell\ell'\ell_1}\left[C_\ell^{TT}+C_{\ell'}^{TT}\right]\tau^{\rm Th}_{\ell_1 m_1},\end{aligned} \tag{4.39}$$

where we have defined

$$W^{mm'm_1}_{\ell\ell'\ell_1} = \sqrt{\frac{(2\ell+1)(2\ell'+1)}{4\pi}}\begin{pmatrix}\ell & \ell' & \ell_1\\ m & m' & -m_1\end{pmatrix}. \tag{4.40}$$

The statistically isotropic component of the correlator is [225]

$$C_\ell^{T^{\rm Sc}T^{\rm Sc}} \equiv C_\ell^{TT} + \sum_{\ell'\ell''} C_{\ell''}^{\tau^{\rm Th}\tau^{\rm Th}} C_{\ell'}^{TT}(W^{000}_{\ell\ell'\ell''})^2 + N_\ell^{T^{\rm Sc}T^{\rm Sc}}. \tag{4.41}$$

C_ℓ^{TT} is the lensed primary CMB temperature power spectrum, $C_\ell^{\tau^{\rm Th}\tau^{\rm Th}}$ is the Thomson optical depth power spectrum, and $N_\ell^{T^{\rm Sc}T^{\rm Sc}}$ encompasses all other contributions to the blackbody CMB such as instrumental noise, foregrounds, etc. The statistically anisotropic component of the correlator is induced by the particular realization of patchy Thomson screening in our Universe. We have explicitly kept this term, which would vanish for a full ensemble average over all fields. As we describe in detail below, this statistical anisotropy can be used to reconstruct the anisotropies of optical depth $\tau^{\rm Th}$, and induces various three-point correlation functions.

Similarly, anisotropies in the dark screening optical depth $\tau(\hat{n},\omega)$ lead to anisotropies in $T^{\rm dSc}(\omega)$, which is captured by the auto-correlation function of the dark screening component of the observed CMB temperature:

$$\begin{aligned}&\left\langle T^{\rm dSc}_{\ell m}(\omega) T^{\rm dSc}_{\ell' m'}(\omega')\right\rangle = (-1)^m C_\ell^{T^{\rm dSc}T^{\rm dSc}}(\omega,\omega')\delta_{\ell\ell'}\delta_{m-m'} + \\ &+\sum_{\ell_1 m_1}(-1)^{m_1}\begin{pmatrix}\ell & \ell' & \ell_1\\ m & m' & -m_1\end{pmatrix}\sqrt{2\ell_1+1}W^{000}_{\ell\ell'\ell_1}\left[C_\ell^{\tau\tau}(\omega,\omega')+C_{\ell'}^{\tau\tau}(\omega,\omega')\right]\bar{T}T_{\ell_1 m_1},\end{aligned} \tag{4.42}$$

where $C_\ell^{\tau\tau}(\omega,\omega')$ is the dark screening optical depth, for which we have retained the frequency dependence with respect to the blackbody, namely a factor of $(\zeta(\omega)/\omega)^2$. The

statistically isotropic contribution to the correlator is

$$C_\ell^{T^{\rm dSc}T^{\rm dSc}}(\omega,\omega') \equiv \bar{T}^2\, C_\ell^{\tau\tau}(\omega,\omega') + \sum_{\ell'\ell''} C_{\ell''}^{\tau\tau}(\omega,\omega') C_{\ell'}^{TT} (W_{\ell\ell'\ell''}^{000})^2 + N_\ell^{T^{\rm dSc}T^{\rm dSc}}(\omega,\omega') \\ \simeq \bar{T}^2\, C_\ell^{\tau\tau}(\omega,\omega') + N_\ell^{T^{\rm dSc}T^{\rm dSc}}(\omega,\omega'). \tag{4.43}$$

The contribution from instrumental noise and foregrounds is $N_\ell^{T^{\rm dSc}T^{\rm dSc}}(\omega,\omega')$. Because the CMB anisotropies are so small in comparison to the monopole, the first term completely dominates the statistically isotropic contribution to the correlator. As a result, measuring $C_\ell^{T^{\rm dSc}T^{\rm dSc}}$ can be extremely sensitive to photon to dark photon conversion. However, such an auto-correlation function is proportional to the small kinetic mixing parameter ε^4, which limits the reach of measurements of the dark-screened CMB power spectrum. We forecast the reach of such an analysis in Section 4.6.3.

Similar dark-screened auto-correlations can be computed for the TE, EE and BB CMB spectra. These are listed in Appendix B.3. In determining the sensitivity of CMB experiments to ε in Section 4.6, we use all isotropic components of the two-point auto-correlators. However, the temperature auto-correlation provides the best sensitivity because of the coupling of τ to $\bar{T}$.

The statistically anisotropic component of the dark screening auto-correlation is proportional to the un-screened temperature anisotropies, and we explore in the next section how this can be used to search for photon to dark photon conversion. We can also construct cross-correlations functions in the form of $\langle T_{\ell m}^{\rm dSc}(\omega) T_{\ell' m'}^{\rm Sc}\rangle$, the discussion of which we also leave to the next section.

4.5 Cross-correlating dark screening

In this section, we study the cross-correlation between observables that contain the dark screening optical depth $\tau(\hat{n},\omega)$ and those that do not. The essential qualitative understanding that motivates the construction of these correlation functions is the following: *Dark screening occurs in halos, and is therefore correlated with observables (within the Standard Model) that are sensitive to either the halos' locations or their electron density distributions.* As we showed, both Thomson screening and photon to dark photon conversion depend on the electron density profile. Therefore, there is a non-zero cross-correlation between the Thomson-screened and dark-screened temperature and polarization anisotropies. In the following, we discuss two ways of combining these maps: we consider first cross-correlation between the Thomson-screened and dark-screened CMB, and then their correlation with

LSS tracers. We compute the relevant two- and three- point correlation functions for each method and identify the ones that are most sensitive to dark screening.

4.5.1 Two-point cross-correlation

Based on the discussions in the last section, an obvious candidate for the correlation function we want is:

$$\begin{aligned}\langle T^{\rm dSc}_{\ell m}(\omega) T^{\rm Sc}_{\ell' m'}\rangle &= (-1)^m C_\ell^{T^{\rm dSc}T^{\rm Sc}}(\omega)\delta_{\ell\ell'}\delta_{m-m'} \\ &\quad - \sum_{\ell_1 m_1}(-1)^{m_1}\begin{pmatrix}\ell & \ell' & \ell_1\\ m & m' & -m_1\end{pmatrix}\sqrt{2\ell_1+1}W^{000}_{\ell\ell'\ell_1}C_{\ell'}^{TT}\tau_{\ell_1 m_1}(\omega) \\ &\quad + \bar{T}\sum_{\ell_1 m_1}(-1)^{m_1}\begin{pmatrix}\ell & \ell' & \ell_1\\ m & m' & -m_1\end{pmatrix}\sqrt{2\ell_1+1}W^{000}_{\ell\ell'\ell_1}C_\ell^{\tau\tau^{\rm Th}}(\omega)T_{\ell_1 m_1},\end{aligned} \tag{4.44}$$

where $C_\ell^{\tau\tau^{\rm Th}}(\omega)$ was defined in (4.29) and

$$C_\ell^{T^{\rm dSc}T^{\rm Sc}}(\omega) \;\equiv\; \sum_{\ell'\ell''} C_{\ell''}^{\tau\tau^{\rm Th}}(\omega) C_{\ell'}^{TT}(W^{000}_{\ell\ell'\ell''})^2. \tag{4.45}$$

Note that for this correlator there are statistically anisotropic contributions proportional to both the dark screening optical depth and the un-screened temperature anisotropies. The cross-correlation between the Thomson-screened and dark-screened temperature scales as $\bar{\tau} \sim \varepsilon^2$. This is more favorable than the ε^4 scaling found in (4.42). However, unlike for (4.42), only the second statistically anisotropic term depends on the temperature monopole $\bar{T}$ (Thomson screening doesn't couple to the temperature monopole). The consequence is that this cross-correlation is less competitive than the dark-screened autocorrelation at fixed noise.

Before moving on, let's turn to polarization. E and B modes are defined with the relation in (4.38). Combined with the assumption that the Thomson-screened temperature anisotropies can be separated from the dark-screened anisotropies through the frequency dependence, we can construct a variety of two-point correlation functions – 12 in total! These can be found in Appendix B.3. Unlike for temperature auto- and cross-correlations, some correlators involving polarization vanish in the absence of screening, and only receive statistically anisotropic contributions. These include

$$\left\langle T^{\rm dSc}_{\ell_1 m_1} i B^{\rm Sc}_{\ell_2 m_2}\right\rangle = \sum_{\ell m} E_{\ell m}(-1)^m \begin{pmatrix}\ell_1 & \ell_2 & \ell\\ m_1 & m_2 & -m\end{pmatrix}\sqrt{2\ell+1}o_{\ell_1\ell_2\ell}W^{220}_{\ell_2\ell\ell_1}\bar{T}C_{\ell_1}^{\tau\tau^{\rm Th}} \tag{4.46}$$

and

$$\left\langle E^{\rm Sc}_{\ell_1 m_1} i B^{\rm dSc}_{\ell_2 m_2} \right\rangle = -\sum_{\ell m} \tau_{\ell m} (-1)^m \begin{pmatrix} \ell_1 & \ell_2 & \ell \\ m_1 & m_2 & -m \end{pmatrix} \sqrt{2\ell+1} o_{\ell_1 \ell_2 \ell} W^{220}_{\ell_2 \ell_1 \ell} C^{EE}_{\ell_1}, \tag{4.47}$$

where C_ℓ^{EE} is the lensed primary CMB E-mode power spectrum and

$$o_{\ell\ell'\ell''} \equiv \frac{1}{2}\left[1 - (-1)^{\ell+\ell'+\ell''}\right]. \tag{4.48}$$

These correlations are also potential sensitive probes of patchy dark screening, as demonstrated in greater detail below.

4.5.2 Correlating patchy dark screening with LSS

Expanding our focus beyond CMB observables, photon to dark photon conversion happens inside halos, and therefore the patchy dark screening signal is correlated with the LSS. It is most natural to look for correlations between patchy dark screening and tracers of LSS, such as galaxy redshift surveys. Given a tracer and various model assumptions, one can build a template for patchy dark screening, which we will denote by $\hat{\tau}(\varepsilon_0)$. In this section we build the intuition of how to use such a template to improve our sensitivity to ε. As one example, the template can be built in the following way:

$$\hat{\tau}^g_{\ell m}(\varepsilon_0, \omega) = \left[(C^{\tau\tau}_\ell(\varepsilon_0, \omega)\mathbf{C}^{gg}_\ell)^{-1} \cdot \mathbf{C}^{g\tau}_\ell(\varepsilon_0, \omega)\right] \cdot \mathbf{g}_{\ell m}, \tag{4.49}$$

where $\mathbf{g}_{\ell m}$ are the moments of the galaxy overdensity field and the vector notation denotes the redshift information; $C^{\tau\tau}_\ell$ is the model photon to dark photon optical depth power spectrum, $\mathbf{C}^{gg}_\ell$ is the redshift $\times$ redshift galaxy overdensity covariance matrix, and $\mathbf{C}^{g\tau}_\ell$ is a vector of the dark photon optical depth $\times$ galaxy overdensity cross-spectra at each redshift. We have explicitly indicated that the model power spectra involving the patchy dark screening optical depth depends on the fiducial choice ε_0 for the kinetic mixing parameter. Note that the template defined in (4.49) can be improved by going beyond this simple linear filter, for example using machine learning techniques as in Ref [227].

The largest contribution to the cross-correlation of the template with the patchy dark screening component of the CMB is statistically isotropic and given by

$$\langle T^{\rm dSc}_{\ell m} \hat{\tau}^g_{\ell' m'}(\varepsilon_0, \omega)\rangle_{\rm isotropic} = -\bar{T} C^{\tau\hat{\tau}^g}_\ell(\varepsilon, \varepsilon_0, \omega)\ \delta_{\ell\ell'}\delta_{mm'}, \tag{4.50}$$

where $C^{\tau\hat{\tau}^g}_\ell$ is the cross-power spectrum between the template and real photon to dark photon optical depth. Importantly, $C^{\tau\hat{\tau}^g}_\ell(\varepsilon, \varepsilon_0, \omega) \propto \varepsilon^2$, and therefore this quantity scales

more favorably with ε in the small-ε limit than the monopole contribution to the temperature auto-spectrum (which scales $\propto \varepsilon^4$). In addition to the more favorable scaling with the mixing parameter, cross-correlation with a template can be beneficial for mitigating systematic effects and galactic or extra-galactic foregrounds in the observed CMB. We forecast the reach of such analysis in Section 4.6.4.

4.5.3 Reconstruction

Coming back to the CMB, the discussion in the previous section suggests searching for correlation functions that would allow us to reconstruct the map $\tau^{\rm Th}(\hat{n})$ from CMB observables. $\tau^{\rm Th}(\hat{n})$, depending on the same electron density distribution in the Universe as $\tau(\hat{n},\omega)$, would be correlated with $T^{\rm dSc}$, just like $\hat{\tau}^g$. The statistically anisotropic components of the two-point correlation functions in (4.39) can be used to construct quadratic estimators for patchy Thomson screening optical depth $\tau^{\rm Th}(\hat{n})$. Similarly, patchy dark screening, as well as the un-screened primary CMB temperature and polarization anisotropies can be reconstructed e.g. from equations (4.42), (4.44), (4.47). An exhaustive list of quadratic estimators is presented in Appendix B.3. Similar quadratic estimators are used to measure weak lensing of the CMB (see e.g. [81] for a review), and are employed in a wide variety of other contexts in CMB science, in particular for the reconstruction of patchy Thomson screening during reionization [88] and kinetic Sunyaev Zel'dovich velocity reconstruction [82, 83, 84, 212, 86].

Starting again with a Standard Model example, the reionization optical depth can be found from (4.39) as:

$$\hat{\tau}^{\rm Th}_{LM} = - N_L^{\tau^{\rm Th};T^{\rm Sc}T^{\rm Sc}} \sum_{\ell m}\sum_{\ell' m'} (-1)^M \begin{pmatrix} \ell & \ell' & L \\ m & m' & -M \end{pmatrix} \sqrt{2L+1}\, G^{\tau^{\rm Th};T^{\rm Sc}T^{\rm Sc}}_{\ell\ell' L} T^{\rm Sc}_{\ell m} T^{\rm Sc}_{\ell' m'}, \quad (4.51)$$

where

$$N_L^{\tau^{\rm Th};T^{\rm Sc}T^{\rm Sc}} = \left[\sum_{\ell\ell'} \frac{\left(W^{000}_{\ell\ell' L}\left[C^{TT}_\ell + C^{TT}_{\ell'}\right]\right)^2}{2\, C_\ell^{T^{\rm Sc}T^{\rm Sc}} C_{\ell'}^{T^{\rm Sc}T^{\rm Sc}}}\right]^{-1}, \quad G^{\tau^{\rm Th};T^{\rm Sc}T^{\rm Sc}}_{\ell\ell' L} = \frac{W^{000}_{\ell\ell' L}\left[C^{TT}_\ell + C^{TT}_{\ell'}\right]}{2\, C_\ell^{T^{\rm Sc}T^{\rm Sc}} C_{\ell'}^{T^{\rm Sc}T^{\rm Sc}}}. \quad (4.52)$$

The weights and prefactor are chosen such that the estimator is unbiased if the input power spectra provide an accurate model, i.e.

$$\langle \hat{\tau}^{\rm Th}_{LM} \rangle = \tau^{\rm Th}_{LM}, \quad (4.53)$$

as well as has minimum variance when all fields in the problem are Gaussian:

$$\langle \hat{\tau}^{\rm Th}_{LM} \hat{\tau}^{\rm Th}_{L'M'} \rangle = (C_L^{\tau^{\rm Th}\tau^{\rm Th}} + N_L^{\hat{\tau}^{\rm Th};T^{\rm Sc}T^{\rm dSc}}) \delta_{LL'} \delta_{MM'}. \tag{4.54}$$

The prefactor $N_L^{\hat{\tau}^{\rm Th};T^{\rm Sc}T^{\rm dSc}}$ is the noise on the reconstruction.

Similarly, one can reconstruct $\hat{\tau}^{\rm Th}$ from measurements of polarization, notably from $E^{\rm Sc}B^{\rm Sc}$. The relevant quadratic estimators are presented in Appendix B.3. Estimators for the Thomson optical depth found there are equivalent those presented in Ref. [88]. The two-point function that would result from cross-correlating the dark-screened CMB temperature with the Thomson optical depth map, i.e. $\langle \hat{\tau}^{\rm Th} T^{\rm dSc} \rangle$, is another means to construct the correlation function in (4.50).

More quadratic estimators can be built from the dark screening anisotropies $T^{\rm dSc}$. The leading term that contains the dark screening optical depth is:

$$\hat{\tau}^{qe\,*}_{LM} = -N_L^{\hat{\tau};T^{\rm dSc}T^{\rm Sc}} \sum_{\ell m} \sum_{\ell' m'} (-1)^M \begin{pmatrix} \ell & \ell' & L \\ m & m' & -M \end{pmatrix} \sqrt{2L+1}\, G^{\hat{\tau};T^{\rm dSc}T^{\rm Sc}}_{\ell\ell' L} T^{\rm dSc}_{\ell m} T^{\rm Sc}_{\ell' m'}, \tag{4.55}$$

where

$$N_L^{\hat{\tau}^{qe};T^{\rm Sc}T^{\rm dSc}} = \left(\sum_{\ell\ell'} \frac{(W^{000}_{L\ell\ell'})^2 (C^{TT}_{\ell'})^2}{C_\ell^{T^{\rm Sc}T^{\rm Sc}} C_{\ell'}^{T^{\rm dSc}T^{\rm dSc}}} \right)^{-1}, \tag{4.56}$$

$$\begin{aligned} G^{\hat{\tau}^{qe};T^{\rm Sc}T^{\rm dSc}}_{\ell\ell' L} &= \frac{C_{\ell'}^{T^{\rm Sc}T^{\rm Sc}} C_\ell^{T^{\rm dSc}T^{\rm dSc}} W^{000}_{L\ell\ell'} C^{TT}_{\ell'} - (-1)^{\ell+\ell'+L} C_\ell^{T^{\rm Sc}T^{\rm dSc}} C_{\ell'}^{T^{\rm Sc}T^{\rm dSc}} W^{000}_{L\ell'\ell} C^{TT}_{\ell}}{C_\ell^{T^{\rm Sc}T^{\rm Sc}} C_{\ell'}^{T^{\rm Sc}T^{\rm Sc}} C_\ell^{T^{\rm dSc}T^{\rm dSc}} C_{\ell'}^{T^{\rm dSc}T^{\rm dSc}} - (C_\ell^{T^{\rm Sc}T^{\rm dSc}})^2 (C_{\ell'}^{T^{\rm Sc}T^{\rm dSc}})^2} \\ &\simeq \frac{W^{000}_{L\ell\ell'} C^{TT}_{\ell'}}{C_\ell^{T^{\rm Sc}T^{\rm Sc}} C_{\ell'}^{T^{\rm dSc}T^{\rm dSc}}}. \end{aligned} \tag{4.57}$$

We used the fact that the product of the screened auto-spectra is larger than the product of the screened cross-spectra in the second line.

It is important to note that in constructing the weights $G^{\hat{\tau};T^{\rm Sc}T^{\rm dSc}}_{\ell\ell' L}$ and the prefactor $N_L^{\hat{\tau};T^{\rm Sc}T^{\rm dSc}}$ that the input power spectra come from a *theoretical* model for the un-screened CMB temperature power spectrum C_ℓ^{TT} as well as contributions from noise and foregrounds to both $C_\ell^{T^{\rm Sc}T^{\rm Sc}}$ and $C_{\ell'}^{T^{\rm dSc}T^{\rm dSc}}$. The model for $C_\ell^{T^{\rm Sc}T^{\rm Sc}}$ and $C_{\ell'}^{T^{\rm dSc}T^{\rm dSc}}$ can be checked against the measured power spectra of these maps. However, since we cannot directly measure C_ℓ^{TT}, there is inevitably some residual model uncertainty. This manifests as a bias on the reconstruction:

$$\langle \hat{\tau}^{qe}_{LM} \rangle = b^\tau_L\, \tau_{LM}, \quad b^\tau_L = N_L^{\hat{\tau};T^{\rm Sc}T^{\rm dSc}} \sum_{\ell\ell'} \frac{(W^{000}_{L\ell\ell'})^2 (C^{TT}_{\ell'})_{\rm model} (C^{TT}_{\ell'})_{\rm actual}}{C_\ell^{T^{\rm Sc}T^{\rm Sc}} C_{\ell'}^{T^{\rm dSc}T^{\rm dSc}}}. \tag{4.58}$$

When the model and actual power spectra are identical, the bias factor is unity. Importantly, it is possible to measure this bias by comparing e.g. $\hat{\tau}^{qe}_{LM}$ to $\hat{\tau}^{g}_{LM}$. In principle, the bias can be measured without cosmic variance since the comparison is done at the level of the modes and not the power spectra; this is an example of 'sample variance cancellation' (e.g. [228]). This procedure is elucidated in greater detail in Section 4.6.

As a third example, a quadratic estimator for the un-screened temperature anisotropies is

$$\hat{T}_{LM} = N_L^{\hat{T};T^{\rm dSc}T^{\rm Sc}} \sum_{\ell m} \sum_{\ell' m'} (-1)^M \begin{pmatrix} \ell & \ell' & L \\ m & m' & -M \end{pmatrix} \sqrt{2L+1}\, G^{\hat{T};T^{\rm dSc}T^{\rm Sc}}_{\ell\ell' L} T^{\rm dSc}_{\ell m} T^{\rm Sc}_{\ell' m'}, \qquad (4.59)$$

where

$$N_L^{\hat{T};T^{\rm dSc}T^{\rm Sc}} = \left[\sum_{\ell\ell'} \frac{\bar{T}^2 \left| W^{000}_{\ell\ell' L} C_\ell^{\tau T^{\rm Th}} \right|^2}{C_\ell^{T^{\rm dSc}T^{\rm dSc}} C_{\ell'}^{T^{\rm Sc}T^{\rm Sc}}} \right]^{-1}, \qquad G^{\hat{T};T^{\rm dSc}T^{\rm Sc}}_{\ell\ell' L} \simeq \frac{W^{000}_{\ell\ell' L} \bar{T} C_\ell^{\tau\tau^{\rm Th}}}{C_\ell^{T^{\rm dSc}T^{\rm dSc}} C_{\ell'}^{T^{\rm Sc}T^{\rm Sc}}}. \qquad (4.60)$$

The weights and reconstruction noise in this case depend on a theoretical model for $C_\ell^{\tau\tau^{\rm Th}}$, an object we have no prior knowledge of and hope to search for. This implies that the reconstruction of the un-screened temperature anisotropies will be significantly biased. However, as described above, one can measure the bias by comparing to a template for T_{LM}, which at least on large angular scales, can be provided by $T^{\rm Sc}$. That is, a correlation function $\langle \hat{T} T^{\rm Sc} \rangle$, can also be used to search for anisotropic dark screening.

4.5.4 Three-point correlation functions

The discussion in the previous section suggests that one should correlate maps reconstructed from CMB observables, such as $\hat{\tau}^{\rm Th}$, $\hat{\tau}$ and $\hat{T}$, with CMB observables (e.g. $T^{\rm Sc}$ or $T^{\rm dSc}$) or itself. In terms of CMB observables, these correlation functions will be three-point or four-point correlation functions. In other words, the statistically anisotropic contributions to the two-point correlation functions in the previous section imply that there are many non-vanishing three-point correlation functions even in the case where the temperature, polarization, and optical depth fields are Gaussian.

For example, the correlation functions

$$\langle \hat{\tau}^{\rm Th} T^{\rm dSc} \rangle \sim \langle \langle T^{\rm Sc} T^{\rm Sc} \rangle T^{\rm dSc} \rangle \quad \text{and} \quad \langle \hat{T} T^{\rm Sc} \rangle \sim \langle \langle T^{\rm dSc} T^{\rm Sc} \rangle T^{\rm Sc} \rangle \qquad (4.61)$$

both come from the three-point correlation function $\langle T^{\rm dSc}T^{\rm Sc}T^{\rm Sc}\rangle$. Therefore, rather than working with the more intuitive two-point correlation functions involving reconstructed maps, we can forecast the sensitivity directly using three-point functions; we present this forecast in Section 4.6.5.

Three-point functions are described by the angle-average bispectrum, defined as

$$\mathcal{B}^{XYZ}_{\ell\ell'\ell''} = \sum_{mm'm''} \begin{pmatrix} \ell & \ell' & \ell'' \\ m & m' & -m'' \end{pmatrix} \langle X_{\ell m} Y_{\ell' m'} Z_{\ell'' m''}\rangle. \tag{4.62}$$

There are many bispectra to consider between temperature, polarization, and templates for the optical depth. Here we focus on the largest bispectra that scale like ε^2, since these will be most sensitive to photon to dark photon conversion.

The most relevant bispectra involving only CMB temperature and polarization are (see (4.44) and (4.46))

$$\mathcal{B}^{T^{\rm dSc}T^{\rm Sc}T^{\rm Sc}}_{\ell\ell'\ell''} = \bar{T}\sqrt{2\ell''+1}W^{000}_{\ell\ell'\ell''}\left(C^{TT}_{\ell'} + C^{TT}_{\ell''}\right) C^{\tau\tau^{\rm Th}}_{\ell}(\omega) \tag{4.63}$$

and

$$\mathcal{B}^{T^{\rm dSc}E^{\rm Sc}B^{\rm Sc}}_{\ell\ell'\ell''} = \bar{T}\sqrt{2\ell''+1}W^{022}_{\ell\ell'\ell''}o_{\ell\ell'\ell''}\left(C^{EE}_{\ell'} + C^{EE}_{\ell''}\right) C^{\tau\tau^{\rm Th}}_{\ell}(\omega). \tag{4.64}$$

Note that both are proportional to the CMB monopole. The most relevant bispectra that scale like ε^2 and involve both the CMB and an optical depth template are

$$\mathcal{B}^{E^{\rm Sc}B^{\rm dSc}\hat{\tau}}_{\ell\ell'\ell''} = \sqrt{2\ell''+1}W^{220}_{\ell\ell'\ell''}o_{\ell\ell'\ell''}\left(C^{EE}_{\ell} + C^{EE}_{\ell'}\right) C^{\tau\hat{\tau}}_{\ell''}(\omega) \tag{4.65}$$

and

$$\mathcal{B}^{T^{\rm Sc}E^{\rm dSc}\hat{\tau}}_{\ell\ell'\ell''} = \mathcal{B}^{T^{\rm dSc}E^{\rm Sc}\hat{\tau}}_{\ell\ell'\ell''} = \sqrt{2\ell''+1}W^{000}_{\ell\ell'\ell''}e_{\ell\ell'\ell''}\left(C^{TE}_{\ell} + C^{TE}_{\ell'}\right) C^{\tau\hat{\tau}}_{\ell''}(\omega). \tag{4.66}$$

These bispectra, similar to the cross-correlation with LSS in (4.50), are proportional to the CMB monopole $\bar{T}$, while at the same time, scales as ε^2. This, as we will demonstrate in more detail in Section 4.6, makes these bispectra almost as sensitive as the two-point functions $\langle T^{\rm dSc}T^{\rm dSc}\rangle$ (scaling as ε^4), and more sensitive than $\langle T^{\rm dSc}T^{\rm Sc}\rangle$ (proportional to C^{TT}_{ℓ}).

4.6 Forecast

In this section we forecast the projected sensitivity of several CMB experiments to the mixing parameter ε over a range of fixed values for the dark photon mass $m_{\rm A'}$. We consider

each of the five techniques mentioned in the introduction, and identify the most promising observables for each experimental configuration. These relevant correlation functions are summarized in Table 4.1. We first compute the constraint on ε from the monopole spectral distortion using COBE/FIRAS. We then describe our forecast assumptions, and compute the reach of existing and future CMB anisotropy experiments.

	ε	C_ℓ^{TT}	$\tau^{\rm Th}$	C_ℓ^{EE}
$\langle T^{\rm dSc}\rangle$	2	0	0	-
$\langle T^{\rm Sc}T^{\rm Sc}\rangle$	0	1	2	-
$\langle T^{\rm dSc}T^{\rm dSc}\rangle$	4	0	0	-
$\langle T^{\rm Sc}T^{\rm dSc}\rangle$	2	1	1	-
$\langle T^{\rm dSc}\hat{\tau}^g\rangle$	2	0	0	-
$\langle T^{\rm Sc}T^{\rm Sc}T^{\rm dSc}\rangle$	2	1	1	-
$\langle T^{\rm dSc}E^{\rm Sc}B^{\rm Sc}\rangle$	2	-	1	1

Table 4.1: The scaling of various correlation functions with the small parameters: kinetic mixing ε, primary CMB power C_ℓ^{TT}, primary E-mode polarization power C_ℓ^{EE} and optical depth of Thomson screening $\tau^{\rm Th}$. The correlation functions $\langle T^{\rm Sc}T^{\rm Sc}\rangle$ and $\langle T^{\rm Sc}T^{\rm dSc}\rangle$ are also shown for comparison.

4.6.1 FIRAS bounds

First we look at the CMB monopole constraint given by the COBE satellite. This method has been used in the past to forecast the constraint on ε from different models for the distribution of ionized gas since recombination [119, 116, 214].

The CMB monopole was measured by the FIRAS instrument on the COBE satellite and was discovered to have a near perfect blackbody spectrum [77]. The data consists of 43 measurements of the sky-averaged temperature over frequencies in the range $\omega = 68.05 - 639.46$ GHz [2]. This gives a best fit blackbody temperature of $\bar{T} = 2.725 \pm 0.002\,\mathrm{K}$, with residuals of order roughly 10^{-4} below the peak intensity and 1σ uncertainties of the same magnitude. This remarkable precision already gives a constraint on the amplitude of the conversion probability for CMB photons of order the uncertainty $P_{\gamma\to \mathrm{A}'} \lesssim 10^{-4}$. In

[2]Data was taken from `https://lambda.gsfc.nasa.gov/data/cobe/firas/monopole_spec/firas_monopole_spec_v1.txt`

this section we improve this bound by considering the full available frequency spectrum. To constrain our model we use the method described in [116].

Assuming an isotropic conversion of photons into dark photons, the CMB blackbody spectrum is distorted according to

$$B(\omega, T, \varepsilon, m_{\mathrm{A}'}) = B^0(\omega, T)\left(1 - P_{\gamma\to\mathrm{A}'}(\bar{\tau}_{\mathrm{tot}}, m_{\mathrm{A}'})\right), \tag{4.67}$$

where $B^0(\omega, T)$ is the theoretical blackbody spectrum defined in (4.34) and $\bar{\tau}_{\mathrm{tot}}$, the total dark screening monopole including the galactic component, implicitly depends on ω and ε. The reduced χ^2 estimator is an average over all available frequency channels of the difference between the measured data and the expected signal B^{exp} in each frequency bin:

$$\chi^2 = \frac{1}{N-1}\sum_i^N \frac{1}{\sigma_i^{\mathrm{exp}}}\left(B_i^{\mathrm{exp}} - B_i(T, \varepsilon, m_{\mathrm{A}'})\right). \tag{4.68}$$

This estimator is minimized by some value of T at each point in the plane spanned by ε and $m_{\mathrm{A}'}$. In Fig. 4.6 we show the 95% and 99% confidence limit contours in this parameter space, for the χ^2 of a distribution with 42 degrees of freedom. The exclusion regions are similar in both cases, indicating that the regression method is robust, i.e. the χ^2 changes rapidly with temperature around the minimum.

Over the accessible range of dark photon masses, the constraint on ε reaches up to $\simeq 10^{-6}$, roughly two orders of magnitude better than the naive limit set by the error bar on the blackbody temperature. In Appendix B.1 we explore the model uncertainty implicit in our constraint, which arises primarily from our lack of knowledge of the gas profile. Comparing the constraints obtained in our fiducial model for gas profiles with those obtained for a model in which gas perfectly tracks dark matter (e.g. a model without any baryonic feedback), we conclude that the constraints at low dark photon mass are robust. At high dark photon mass, the constraint is strengthened in a model where baryons perfectly track dark matter. We can extrapolate that if our fiducial gas model has too little baryonic feedback, the constraints could further weaken at high dark photon mass. Incorporating information from measurements of the Sunyaev Zel'dovich effect (e.g. [229]), the dispersion measure of fast radio bursts (e.g. [230, 231])), 21 cm intensity mapping (e.g. [232]), and other tracers of baryons will be helpful in mitigating this modelling uncertainty and will be explored in future work.

4.6.2 Forecast assumptions for CMB anisotropy experiments

In Section 4.4.2, we assumed that the frequency-dependent anisotropies due to resonant conversion (T^{dSc}, E^{dSc}, B^{dSc}) could be perfectly separated from the blackbody Thomson-

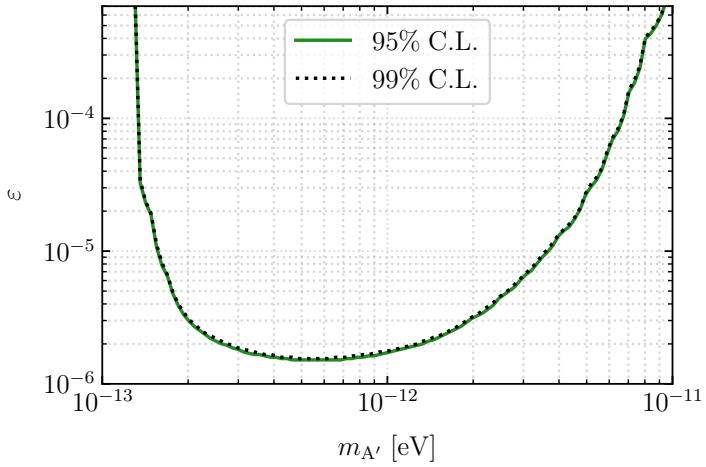

Figure 4.6: Exclusion contours on coupling constant ε function of dark photon mass $m_{A'}$ from COBE/FIRAS [77] data. We see that the uncertainty in the measurement of $\bar{T}$ gives a constraint on the magnitude of the dark-screened temperature monopole $\langle T^{\rm dSc} \rangle$. Here we used the total dark screening optical depth due to both galactic and extra-galactic contributions $\bar{\tau} + \tau^{\rm MW}$. This constraint provides an upper bound on ε of at most 10^{-6}.

screened anisotropies ($T^{\rm Sc}$, $E^{\rm Sc}$, $B^{\rm Sc}$). Here, we explore the degree to which this separation can be made in the presence of instrumental noise and measurements in only a small number of frequency channels. We estimate the residual noise on the dark-screened and Thomson-screened maps achievable with existing and future CMB experiments, which is used in the following forecasts based on two- and three-point correlation functions.

We consider three different CMB experiments: the combination of the Low Frequency Instrument (LFI) [233] and High Frequency Instrument (HFI) [234] on the Planck satellite, CMB Stage-4 [206] and CMB-HD [89, 235]. In the context of our analysis, a CMB experiment is characterized by the sensitivity and resolution at a set of measured frequencies.Throughout, we assume Gaussian beam and white uncorrelated noise for all instruments, as well as full-sky coverage and no foregrounds.

Before proceeding, it is important to comment on the potential impact of CMB foregrounds. There are a variety of galactic foregrounds (see e.g. [236] for an overview) that fall with frequency, with a similar power law in the power spectra to the patchy dark screening signal (falling as $\omega^{-2} - \omega^{-3}$) including: synchrotron, free-free, and spinning dust. These are strongest in the galactic plane, and their influence can be mitigated by masking the most contaminated regions of the sky, or by incorporating information about the morphology of

the signal. Nevertheless, these foregrounds can in principle add significant extra power at low-frequencies and on large angular scales. Extra-galactic radio point sources, which are dominated by synchrotron emission, are also a potentially important foreground to consider. Resolved point sources can again be dealt with by masking, however the unresolved point sources can add power at low frequencies and on small angular scales. This signal is also correlated with other tracers of LSS, limiting the power of cross-correlations to mitigate foregrounds. The extent to which galactic and extra-galactic foregrounds degrade the forecast we present below requires a detailed analysis, which we defer to future work.

The instrumental noise considered throughout our analysis is modelled as:

$$\begin{aligned} N_\ell^{TT} &= \Delta_T^2 \exp\left[\ell(\ell+1)\,\frac{\theta^2_{\rm FWHM}}{8\log 2}\right]\left[1+(\ell/\ell_{\rm knee})^{\alpha_{\rm knee}}\right], \\ N_\ell^{EE} &= N_\ell^{BB} = \sqrt{2}N_\ell^{TT}, \quad N_\ell^{TE} = 0. \end{aligned} \tag{4.69}$$

Here, $\Delta_T\,[\mu\mathrm{K\,rad}]$ represents the sensitivity in temperature, while $\theta_{\rm FWHM}\,[\mathrm{rad}]$ is the full width at half maximum of our assumed Gaussian beam, which characterizes the resolution of the instrument. The sensitivity and resolution vary with frequency. Furthermore, ground-based measurements are subject to atmospheric contamination on large angular scales. To account for this effect, in the analysis for both CMB-S4 and CMB-HD we include the additional 'red noise' term in the second bracket with $\alpha_{\rm knee} = -3$ and $\ell_{\rm knee} = 100$ in all frequency bins. This contribution diverges at low-ℓ, and becomes increasingly irrelevant for $\ell > \ell_{\rm knee}$. The values we choose to represent each experiment are shown in Table 4.2. Note, throughout this section, we denote by ν the photon frequency in GHz such that $\nu \equiv \omega/2\pi$.

Later, when we compute the Fisher information, we will need to estimate the noise covariance for the dark screening two-point functions of Section 4.4.3. These power spectra have an intrinsic inverse frequency squared dependence $C_\ell^{X^{\rm dSc}X^{\rm dSc}} \propto \varepsilon^4/\omega^2$. It is possible to disentangle this signal from the measured CMB by cross-correlating measurements across multiple frequency channels. We do this by applying a harmonic Internal Linear Combination (ILC) algorithm [237] which we now describe.

Recall that the expected *isotropic* measured CMB signal consists of the primary CMB which is screened by the inhomogeneous field τ plus instrumental noise. For example, in the temperature case we have from equations (4.31), (4.32), (4.43):

$$\begin{aligned} C_\ell^{TT\,\rm obs}(\omega_i,\omega_j) &= C_\ell^{TT} - C_\ell^{T^{\rm dSc}T^{\rm dSc}}(\omega_i,\omega_j) + N_\ell^{TT}(\omega_i)\delta_{\omega_i\omega_j} \\ &\simeq C_\ell^{TT} - \bar{T}^2 C_\ell^{\tau\tau}(\omega_i,\omega_j) + N_\ell^{TT}(\omega_i)\delta_{\omega_i\omega_j}, \end{aligned} \tag{4.70}$$

Frequency ν (GHz)	30	44	70	100	143	217	353	545	857
Δ_T (μK arcmin)	195.1	226.1	199.1	77.4	33.	46.8	153.6	818.2	40090.7
$\theta_{\rm FWHM}$ (arcmin)	32.41	27.1	13.32	9.69	7.3	5.02	4.94	4.83	4.64

(a) Parameters used for the Planck forecast. Sensitivities and temperatures taken from [234] for frequencies 100 GHz and higher (HFI instrument), and [233] for the lowest three frequencies (LFI instrument).

Frequency ν (GHz)	20	27	39	93	145	225	278
Δ_T (μK arcmin)	10.41	5.14	3.28	0.50	0.46	1.45	3.43
$\theta_{\rm FWHM}$ (arcmin)	11.0	8.4	5.8	2.5	1.6	1.1	1.0

(b) Sensitivity and resolution for CMB-S4 V3R0 configuration.

Frequency ν (GHz)	30	40	90	150	220	280	350
Δ_T (μK arcmin)	6.5	3.4	0.7	0.8	2.0	2.7	100.0
$\theta_{\rm FWHM}$ (arcmin)	1.25	0.94	0.42	0.25	0.17	0.13	0.11

(c) CMB-HD forecast parameters, taken from Table 2 of [235].

Table 4.2: Noise parameters for Fisher forecasts. We model the noise covariance as in (4.69) where in the case of ground-based CMB-S4 and CMB-HD we include the red noise term with parameters $\alpha_{\rm knee} = -3$ and $\ell_{\rm knee} = 100$ in all frequency bins.

The instrumental noise term is frequency dependent as displayed in Table 4.2, where the i and j labels above denote each available channel. Let us re-write the dark screening two-point function term in the frequency explicit form $C_\ell^{\tau\tau}(\omega_i = 1, \omega_j = 1)/\omega_i\omega_j$. To build the covariance matrix for all temperature measurements we simply choose a frequency for the signal, ω_0, and measure all entries in reference to it. Overall we find:

$$\mathbf{C}_\ell = \mathbf{\Omega}^{-1}\mathbf{C}_\ell^{TT} - \mathbf{e}\mathbf{e}^\dagger \bar{T}^2 \frac{\zeta(\omega_0)^2}{\omega_0^2} C_\ell^{\tau\tau}(\omega = 1) + \text{diag}\left(\mathbf{\Omega}^{-1}\mathbf{N}_\ell^{TT}(\omega)\right). \tag{4.71}$$

The frequency-dependent matrix has entries $\Omega_{ij}^{-1} = (\zeta(\omega_0)^2/\omega_0^2)\,(\omega_i\omega_j/\zeta(\omega_i)\zeta(\omega_j))$ and $\mathbf{e} = (1, 1, \ldots, 1)$. The ILC method consists of weighting each matrix element appropriately in order to minimize a frequency-independent residual. This is constructed like

$$\tilde{N}_\ell^{T^{\rm dSc}T^{\rm dSc}} = \mathbf{w}_\ell^\dagger \cdot \left(\mathbf{\Omega}^{-1}C_\ell^{TT} + \mathbf{\Omega}^{-1}\mathbf{N}_\ell^{TT}\right) \cdot \mathbf{w}_\ell, \tag{4.72}$$

where the weights $\mathbf{w}_\ell$ satisfy

$$\mathbf{w}_\ell = \frac{(\mathbf{C}_\ell)^{-1}\,\mathbf{e}}{\mathbf{e}^\dagger\,(\mathbf{C}_\ell)^{-1}\,\mathbf{e}}. \tag{4.73}$$

In our analysis, we use a fixed baseline frequency $\omega_0 = 30$ GHz. For the C_ℓ^{XX} terms of the primary CMB we compute the lensed temperature and polarization power spectra using CAMB [69], using the cosmological parameters listed in Section 4.4. Fig. 4.7 shows the weights computed for CMB-S4 specifications. On large scales, the 93 and 145 GHz maps, which are the lowest noise, are used to subtract off the blackbody CMB, with the other channels weighted inversely with frequency.

A similar computation can be used to find the weights and residual noise for polarization. The ILC-cleaned spectrum of the temperature map includes the frequency-dependent term, computed at the baseline frequency ω_0, plus the noise residual:

$$\tilde{C}_\ell^{T^{\rm dSc}T^{\rm dSc}} = \frac{\zeta(\omega_0)^2}{\omega_0^2} C_\ell^{T^{\rm dSc}T^{\rm dSc}}(\omega = 1) + \tilde{N}_\ell^{T^{\rm dSc}T^{\rm dSc}}. \tag{4.74}$$

Henceforth, the $\tilde{\cdot}$ notation will refer to an ILC-cleaned map, or its associated residual defined as in (4.72). Note the factor of $\zeta(\omega)$ defined in (4.37). The CMB peaks in intensity around 160 GHz. The factor of $\zeta(\omega)$ approaches unity for frequencies below the CMB peak, and vanishes for frequencies $\omega \gg 160$ GHz. Since a ω^{-1} scaling weighs small frequencies more strongly, the additional $\zeta(\omega)$ factor does not affect the analysis significantly.

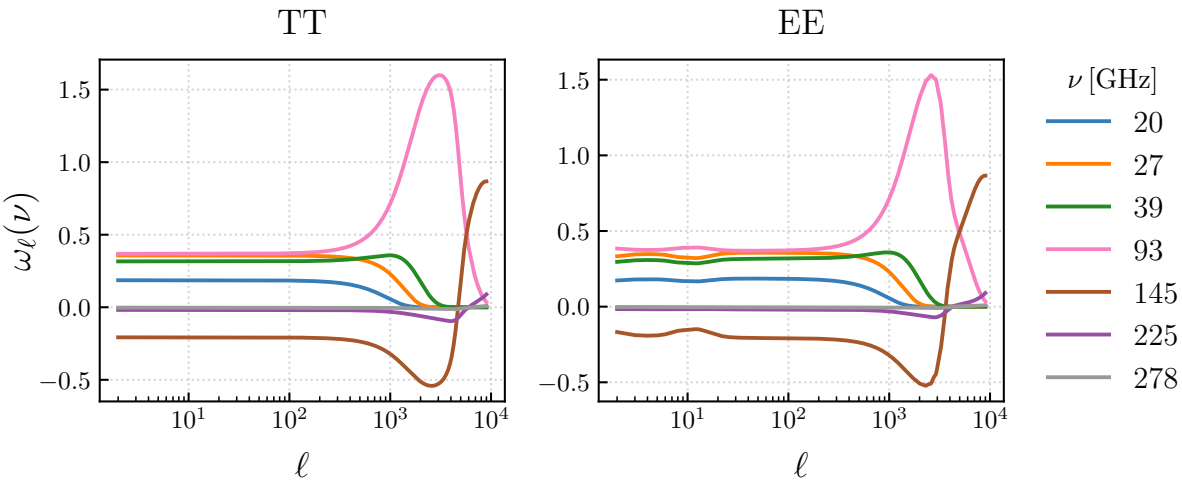

Figure 4.7: Illustration of the weight functions $\mathbf{w}_\ell$ as defined in (4.73) for the frequencies of CMB-S4 with noise parameters defined in Table 4.2. Notice that the dominant frequency is the $\omega = 93$ GHz channel, but this changes at higher ℓ. This is because the ILC favors the $N_\ell(\omega)$ with the lowest magnitude at a given ℓ.

Not only does $\tilde{N}_\ell^{T^{\rm dSc}T^{\rm dSc}}$ do a good job of removing the primary CMB signal, it also gives a lower noise amplitude at high ℓ compared to the noisiest frequency channels. This can be seen by comparing the solid purple line in Fig. 4.8 depicting $\tilde{N}_\ell^{T^{\rm dSc}T^{\rm dSc}}$ with the dotted lines that show $N_\ell^{TT}(\omega)$ for CMB-S4. In the limit of infinitely many frequency measurements, one could in principle fully isolate the frequency-dependent signal from the blackbody component.

Finally, to compute the ILC for the strictly blackbody signal of the Thomson-screened CMB of (4.39), we set $\Omega_{ij}^{-1} = 1$. The residual $\tilde{N}_\ell^{T^{\rm Sc}T^{\rm Sc}}$ in this case is a linear combination of the instrumental noise spectra, once again weighted heavily by the middle frequencies with lowest magnitude, but this time all weights are positive. Again, if we had access to infinitely many frequency channels, the ILC would perfectly recover the Thomson-screened CMB.

4.6.3 CMB auto-correlation

The first method we look at considers the cross-correlation of all dark-screened CMB auto-power spectra. The covariance matrix takes the following form:

$$\mathbf{C}_\ell = \begin{pmatrix} \tilde{C}_\ell^{T^{\rm dSc}T^{\rm dSc}} & \tilde{C}_\ell^{T^{\rm dSc}E^{\rm dSc}} & 0 \\ \tilde{C}_\ell^{T^{\rm dSc}E^{\rm dSc}} & \tilde{C}_\ell^{E^{\rm dSc}E^{\rm dSc}} & 0 \\ 0 & 0 & \tilde{C}_\ell^{B^{\rm dSc}B^{\rm dSc}} \end{pmatrix}, \tag{4.75}$$

where each noise term contained in $\tilde{C}_\ell$ is the post-ILC residual for the particular T, E or B measurement. The Fisher matrix is defined as:

$$F_{ij} = f_{\rm sky} \sum_\ell \frac{2\ell+1}{2} {\rm Tr}\left[(\mathbf{C}_\ell)^{-1} \cdot \partial_i \mathbf{C}_\ell \cdot (\mathbf{C}_\ell)^{-1} \cdot \partial_j \mathbf{C}_\ell\right]. \tag{4.76}$$

where $(\mathbf{C}_\ell)^{-1}$ is the matrix inverse of $\mathbf{C}_\ell$ evaluated at a fiducial value for parameters i and j; $\partial_i \mathbf{C}_\ell$ is the derivative of the covariance matrix with respect to parameter i evaluated at the fiducial parameters i and j. The observed sky-fraction is assumed to be $f_{\rm sky} = 0.7$ for Planck and $f_{\rm sky} = 0.5$ for CMB-S4 and CMB-HD. We are interested in expanding the reach for the mixing parameter ε at a variety of values for $m_{\rm A'}$. Since in this case we only have access to dark screening power spectra, we are constraining ε^4. The Fisher 'matrix' has a single entry given by $F_{\varepsilon^4\varepsilon^4}$. To find the exclusion region, we compute the the 1-sigma constraint on ε^4, given a fiducial value $\varepsilon^4 = 0$: $\sigma_{\varepsilon^4} = 1/\sqrt{F_{\varepsilon^4\varepsilon^4}}$. The Fisher matrix

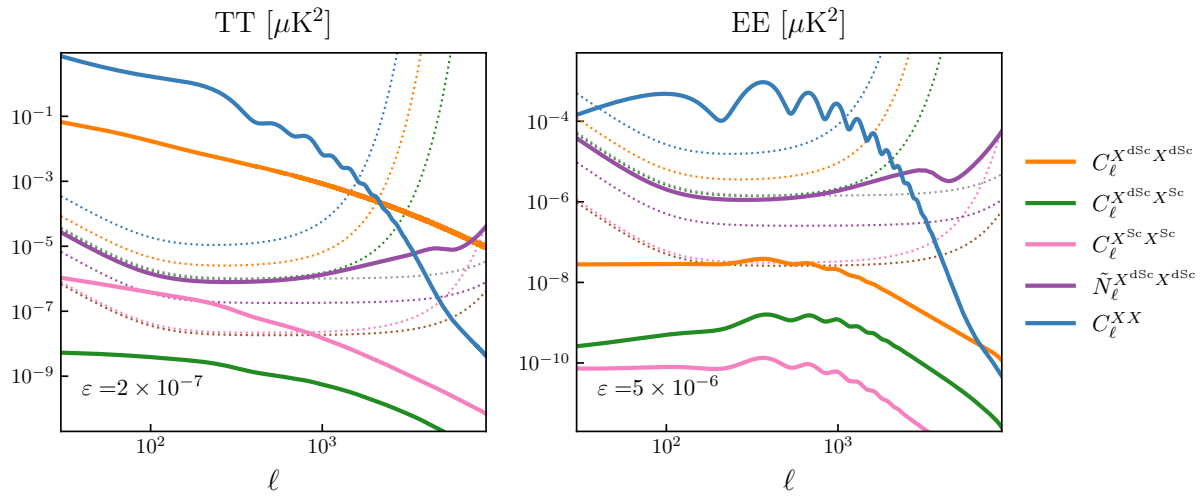

Figure 4.8: Scale comparison between the primary CMB, screening two-point functions, CMB-S4-like instrumental noise and total noise remainder after ILC. We fixed $m_{\rm A'} = 10^{-12}$ eV and ε as shown in each panel. We show the isotropic component to the $XX = TT, EE$ power spectra due to dark screening $C_\ell^{X^{\rm dSc}X^{\rm dSc}} \propto \varepsilon^4$ (*orange*), Thomson screening $C_\ell^{X^{\rm Sc}X^{\rm Sc}}$ (*pink*), and their cross-correlation $C_\ell^{X^{\rm Sc}X^{\rm dSc}} \propto \varepsilon^2$ (*green*). Notice $C_\ell^{T^{\rm dSc}T^{\rm dSc}}$ dominates due to the additional factor $\propto \bar{T}^2$. Due to the different scaling with ε, the cross-spectrum $C_\ell^{T^{\rm Sc}T^{\rm dSc}}$ in *green* is comparable in magnitude to the *orange* curve around a value $\varepsilon \sim 8 \times 10^{-11}$. In the case of EE, the switch happens around $\varepsilon \sim 7 \times 10^{-7}$. The lensed primary CMB spectra (*blue*) and the ILC leftover noise (*purple*) computed at the baseline $\omega_0 = 30$ GHz are shown for comparison. The dotted lines represent the instrumental noise $N_\ell(\omega)$ for each channel in CMB-S4, as defined in Table 4.2. The colors of the dotted lines are the same as their corresponding weights' in Fig. 4.7.

simplifies in this case to:

$$F_{\varepsilon^4\varepsilon^4}|_{\varepsilon^4=0} = f_{\rm sky} \sum_\ell \frac{2\ell+1}{2} \sum_{X=T,E,B} \left(\frac{C_\ell^{X^{\rm dSc}X^{\rm dSc}}(\varepsilon^4 = 1)}{\tilde{N}_\ell^{X^{\rm dSc}X^{\rm dSc}}} \right)^2 , \tag{4.77}$$

and the 1-sigma sensitivity is roughly given by $\sigma_{\varepsilon^4} \sim 1/(S/N)_{\varepsilon^4=0}$.

To obtain the variance on ε, we assume a Gaussian posterior for the probability distribution of the positive real-valued ε^4. The sensitivity on ε is then well approximated

by:

$$\sigma_\varepsilon \simeq 0.7 \left[f_{\rm sky} \sum_\ell \frac{2\ell+1}{2} \left(\frac{\bar{T}^2\, C_\ell^{\tau\tau}(\varepsilon^4=1)}{\tilde{N}_\ell^{T^{\rm dSc}T^{\rm dSc}}} \right)^2 \right]^{-1/8} . \tag{4.78}$$

Notice from the expression above that the value of σ_ε improves as $\sim \ell^{-1/4}$ with the number of modes with significant S/N. This feature is general, regardless of the observable we use in the forecast. In terms of signal, most of the sensitivity of the CMB auto-correlation is due to the $C_\ell^{T^{\rm dSc}T^{\rm dSc}} \sim \bar{T}^2$ term. Finally, the shape of the sensitivity as a function of mass $m_{\rm A'}$ will trace the optical depth monopole as $\bar{\eta}^{-1/2}$. This sensitivity is shown in Fig. 4.9 for Planck and CMB S4. As explained above, the sensitivity is bounded at low dark photon mass from imposing a hard cutoff at the virial radius in each halo, while at high mass it is given by the fact that the halo mass function $n(z,m)$ falls to zero. The boundaries of the contours are also sensitive to our assumptions about the lower bound on the mass of halos described by the AGN gas profiles. We comment on the impact of this modelling uncertainty in Appendix B.1. Overall, the sensitivity is superior to the FIRAS bound due to the dependence on the CMB monopole $\bar{T}$.

4.6.4 CMB cross-correlation with a conversion template

Cross-correlating the measured CMB with other probes increases the forecasted sensitivity to ε. To investigate the degree of improvement that could eventually be possible, we assume in this section that a perfect template for patchy screening occurring at $z < 2$ is available. Such a template could be created from a massive galaxy survey and a detailed model for the relation between galaxy density and ionized gas density, as described in Section 4.5.2. The choice of $z < 2$ is motivated by the redshift range that will be covered by near-term surveys. When referring to the template, we will write $\hat{\tau}$ and its amplitude will depend on a fiducial choice of coupling strength denoted by ε_0^2. In the presence of a dark photon, the measured dark-screened CMB depends on an unknown 'true' $\tau \propto \varepsilon^2$.

One can write the first order in $\delta\tau$ contributions to the two-point function between the template $\hat{\tau}$ and the dark-screened temperature $T^{\rm dSc}$ from (4.32) as:

$$C_\ell^{\hat{\tau}T^{\rm dSc}} = \varepsilon^2\varepsilon_0^2\, \bar{T}\, C_\ell^{\hat{\tau}\tau}(\varepsilon=1,\varepsilon_0=1). \tag{4.79}$$

Notice that another advantage of this method is that it allows us to be sensitive to ε^2 directly, which is the same power of the coupling that appears in the dark screening optical depth monopole (in Section 4.6.1). There is no statistically isotropic component of the

cross-correlation between polarization and the template, and so we do not discuss them here. Note that for the template power spectrum, anisotropies are calculated up to $z = 2$ but the monopole $\hat{\bar{\tau}}$ corresponds to the full contribution up to reionization, i.e. $\bar{\tau} = \hat{\bar{\tau}}$. Breaking up the two-point function into an integral over redshift, one can see that $C_\ell^{\hat{\tau}\tau}$ simplifies to $C_\ell^{\hat{\tau}\hat{\tau}}$ for a perfect template. For an imperfect template, this result would include a (scale-dependent) correlation coefficient describing the imperfect overlap of the template with the actual dark screening optical depth.

The covariance matrix assuming a perfect template is the following:

$$\mathbf{C}_\ell = \begin{pmatrix} C_\ell^{\hat{\tau}\hat{\tau}} & C_\ell^{\hat{\tau}T^{\rm dSc}} \\ C_\ell^{\hat{\tau}T^{\rm dSc}} & \tilde{C}_\ell^{T^{\rm dSc}T^{\rm dSc}} \end{pmatrix}. \tag{4.80}$$

With a fiducial $\varepsilon \to 0$, the Fisher estimator in this case simplifies to:

$$\varepsilon_0^4 F_{(\varepsilon/\varepsilon_0)^2(\varepsilon/\varepsilon_0)^2} = f_{\rm sky} \sum_\ell (2\ell+1)\, \bar{T}^2\, \frac{C_\ell^{\hat{\tau}\hat{\tau}}(\varepsilon^2=1)}{\tilde{N}_\ell^{T^{\rm dSc}T^{\rm dSc}}}, \tag{4.81}$$

and the uncertainty on the coupling constant is

$$\sigma_\varepsilon = 0.76 \left[f_{\rm sky} \sum_\ell (2\ell+1)\, \bar{T}^2\, \frac{C_\ell^{\hat{\tau}\hat{\tau}}(\varepsilon^2=1)}{\tilde{N}_\ell^{T^{\rm dSc}T^{\rm dSc}}} \right]^{-1/4}. \tag{4.82}$$

This sensitivity is plotted in Fig. 4.9 for the various CMB experiments we consider. Notice here that the sensitivity contour corresponding to this estimator is improved by around one order of magnitude compared to the dark-screened CMB-only result. In short, this is due to the ε^2 scaling instead of ε^4 that brings about a more favorable scaling $\sim \ell^{-1/2}$ with the number of modes that are measured with appreciable S/N.

4.6.5 Correlations with Thomson screening, the bispectrum and reconstruction

Recall from Section 4.4.3 that there are statistically anisotropic contributions to the two-point function between the CMB temperature and polarization anisotropies. These statistically anisotropic contributions form the basis of the reconstruction of the un-screened CMB temperature and polarization anisotropies as well as the Thomson and photon to dark photon optical depth introduced in Section 4.5.3 and enumerated in Appendix B.3.

These statistical anisotropies also imply the existence of the three-point functions introduced in Section 4.5.4. In this section, we explore how this non-Gaussian information can be used to search for dark photons.

We first consider the $\left\langle T^{\rm dSc}T^{\rm Sc}T^{\rm Sc}\right\rangle$ bispectrum, which is proportional to $C_\ell^{\tau\tau^{\rm Th}}(\omega)$. Factoring out the dependence on ε:

$$\mathcal{B}^{T^{\rm dSc}T^{\rm Sc}T^{\rm Sc}}_{\ell\ell'\ell''} = \varepsilon^2\bar{T}\sqrt{2\ell''+1}W^{000}_{\ell\ell'\ell''}\left(C^{TT}_{\ell'}+C^{TT}_{\ell''}\right)C_\ell^{\tau\tau^{\rm Th}}(\varepsilon=1), \tag{4.83}$$

we see that forecasting the limits on ε^2 is a straightforward exercise in estimating the amplitude of this bispectrum, a problem whose optimal solution is already known from studies of primordial non-Gaussianity (for an overview, see e.g. [238]). The simplest bispectrum estimator is

$$\hat{\varepsilon}^2 = \sigma^2_{\varepsilon^2}\sum_{\ell m}\sum_{\ell' m'}\sum_{\ell'' m''}\frac{\mathcal{B}^{T^{\rm dSc}T^{\rm Sc}T^{\rm Sc}}_{\ell\ell'\ell''}(\varepsilon^2=1)}{\tilde{C}_\ell^{T^{\rm dSc}T^{\rm dSc}}\tilde{C}_{\ell'}^{T^{\rm Sc}T^{\rm Sc}}\tilde{C}_{\ell''}^{T^{\rm Sc}T^{\rm Sc}}}\begin{pmatrix}\ell & \ell' & \ell''\\ m & m' & -m''\end{pmatrix}T^{\rm dSc}_{\ell m}T^{\rm Sc}_{\ell' m'}T^{\rm Sc}_{\ell'' m''}, \tag{4.84}$$

where the resulting constraint is related to the estimator variance by

$$\sigma_\varepsilon \approx 0.76\sqrt{\sigma_{\varepsilon^2}} = 0.76\left[f_{\rm sky}\sum_{\ell\ell'\ell''}\frac{1}{2}\frac{\left(\mathcal{B}^{T^{\rm dSc}T^{\rm Sc}T^{\rm Sc}}_{\ell\ell'\ell''}(\varepsilon^2=1)\right)^2}{\tilde{N}_\ell^{T^{\rm dSc}T^{\rm dSc}}\tilde{N}_{\ell'}^{T^{\rm Sc}T^{\rm Sc}}\tilde{N}_{\ell''}^{T^{\rm Sc}T^{\rm Sc}}}\right]^{-1/4}. \tag{4.85}$$

Note that just as for the quadratic estimators discussed above, the weights in the bispectrum estimator are constructed from models for C_ℓ^{TT} and $C_\ell^{\tau\tau^{\rm Th}}(\omega,\varepsilon=1)$. The factor of $1/2$ comes from having two indistinguishable $T^{\rm Sc}$ fields.

An alternative starting point would be to first use $T^{\rm dSc}$ and $T^{\rm Sc}$ to reconstruct T (see (4.59)) and then correlate this with $T^{\rm Sc}$. If we assume that the model for $C_\ell^{\tau\tau^{\rm Th}}$ is known up to the value of ε^2 then the reconstruction of T will have a bias of ε^2 such that:

$$\langle\hat{T}_{LM}\hat{T}_{LM}\rangle \simeq \varepsilon^4 C_L^{TT} + N_L^{T;T^{\rm dSc}T^{\rm Sc}}(\varepsilon=1), \quad \langle\hat{T}_{LM}T^{\rm Sc}_{LM}\rangle \simeq \varepsilon^2 C_L^{TT}, \tag{4.86}$$

where we have neglected small contributions that appear at higher order in ε, higher order in $\tau^{\rm Th}$ or lower order in $\bar{T}$. Computing the Fisher matrix we have:

$$\begin{aligned} F_{\varepsilon^2\varepsilon^2} &= \sum_L f_{\rm sky}(2L+1)\frac{(C_L^{TT})^2}{N_L^{T;T^{\rm dSc}T^{\rm Sc}}(\varepsilon=1)\tilde{C}_L^{T^{\rm Sc}T^{\rm Sc}}} \\ &= \sum_{\ell\ell' L}\bar{T}^2 f_{\rm sky}(2L+1)(W^{000}_{\ell\ell' L})^2\frac{C_\ell^{\tau\tau^{\rm Th}}(\varepsilon=1)^2(C_L^{TT})^2}{\tilde{C}_\ell^{T^{\rm dSc}T^{\rm dSc}}\tilde{C}_{\ell'}^{T^{\rm Sc}T^{\rm Sc}}\tilde{C}_L^{T^{\rm Sc}T^{\rm Sc}}}, \end{aligned} \tag{4.87}$$

It is informative to compare this result to the variance on the bispectrum estimator in (4.85). Since $\ell^2 C_\ell^{TT}$ falls with ℓ (at sufficiently high ℓ), the two results agree in the limit where the dominant contributions to the sum in (4.85) come from squeezed configurations with $\ell \gg 1$ – the triangle rule then implies that either the term proportional to $C_{\ell'}^{TT}$ or $C_{\ell''}^{TT}$ dominates the bispectrum. Said differently, because the reconstruction of T improves by measuring many small-scale modes, we mainly capture information about squeezed configurations of the bispectrum where $T^{\rm Sc}$ is evaluated at low-ℓ while the other power of $T^{\rm Sc}$ and $T^{\rm dSc}$ are evaluated at high-ℓ. We expect to be in this regime, since screening occurs mainly on small scales (e.g. it is associated with halos). Note that a completely analogous situation arises in kinetic Sunyaev Zel'dovich velocity reconstruction, as described in detail in Ref. [212].

Including polarization, the best sensitivity on ε can be obtained from the $\left\langle T^{\rm dSc} E^{\rm Sc} B^{\rm Sc} \right\rangle$ bispectrum, where the estimator variance is

$$\sigma_\varepsilon = 0.76 \left[f_{\rm sky} \sum_{\ell\ell'\ell''} \frac{\left(\mathcal{B}^{T^{\rm dSc} E^{\rm Sc} B^{\rm Sc}}_{\ell\ell'\ell''}(\varepsilon^2 = 1) \right)^2}{\tilde{N}_\ell^{T^{\rm dSc} T^{\rm dSc}} \tilde{N}_{\ell'}^{E^{\rm Sc} E^{\rm Sc}} \tilde{N}_{\ell''}^{B^{\rm Sc} B^{\rm Sc}}} \right]^{-1/4} , \tag{4.88}$$

where $\mathcal{B}^{T^{\rm dSc} E^{\rm Sc} B^{\rm Sc}}_{\ell\ell'\ell''}$ was defined in (4.64). This bispectrum can yield a competitive sensitivity compared to the temperature-only bispectrum above since $C_{\ell''}^{B^{\rm Sc} B^{\rm Sc}} \ll C_{\ell''}^{EE}$ in the signal-dominated regime.

The sensitivities to ε using the $\left\langle T^{\rm dSc} T^{\rm Sc} T^{\rm Sc} \right\rangle$ and $\left\langle T^{\rm dSc} E^{\rm Sc} B^{\rm Sc} \right\rangle$ bispectra are shown in Fig. 4.9. The sensitivity of the bispectrum estimator for the experimental configurations studied here is slightly weaker than the result from the CMB auto-correlation. This is due to the smallness of $\tau^{\rm Th}$, which, parametrically, suppresses the sensitivity compared to CMB auto-correlation as well as LSS cross-correlation by an ε-independent factor of $(C_\ell^{\tau\tau^{\rm Th}})^2 / C_\ell^{\tau\tau} \sim 10^{-11} - 10^{-12}$, depending on $m_{\rm A'}$ (see Fig. 4.5). However, this estimator also scales as ε^2, and brings about the most favorable scaling $\sim \ell^{-3/4}$ with the number of modes measured at significant S/N. Notable is also the improvement of $\left\langle T^{\rm dSc} E^{\rm Sc} B^{\rm Sc} \right\rangle$ over $\left\langle T^{\rm dSc} T^{\rm Sc} T^{\rm Sc} \right\rangle$ between the analyses for Planck and HD-like noise, due to predicted noise drop especially in polarization measurements.

To explore the improved sensitivity on ε from small-scale modes we evaluate he bispectrum estimators (4.85) and (4.88) for Planck and CMB-HD. For Planck we capture most of the SNR by summing from $\ell = 2$ up to $\ell = 3000$, while for CMB-HD there is significant SNR up to $\ell = 6000$. From Fig. 4.4, at large dark photon mass, there is a lot of structure at high ℓ in the dark screening optical depth coming from the 1-halo term. Due to the

favorable scaling with ℓ in the bispectrum constraints, the CMB-HD sensitivity is greatly enhanced by the additional support on small scales of the cross-power spectrum, despite the decreasing monopole $\bar{\tau}$ and the smallness of $\bar{\tau}^{\rm Th}$. Note that if we extended the range of halo masses in our halo model below the conservative $10^{11} M_\odot$, the sensitivity on ε would increase. However, this would also bring about larger uncertainties in what the appropriate gas profile to be used on those small scales might be.

4.7 Discussion

In this Chapter, we have studied the resonant conversion of CMB photons to a hypothetical dark photon inside LSS at low redshift. Conversion leads to a frequency dependent patchy 'dark' screening of the CMB. Observationally, dark screening manifests as an anisotropic and frequency dependent optical depth $\tau(\omega, \hat{n})$, which can in principle be extracted from CMB data. The sensitivity to ε for a variety of two- and three-point correlation functions are shown in Fig. 4.9, which we summarize in the following (see also Table 4.1).

The patchy dark screening optical depth $\tau(\omega, \hat{n})$ can be measured using CMB data alone. The global signal, i.e. the $\overline{\tau}(\omega)$ monopole, leads to a spectral distortion which is constrained by COBE/FIRAS [77] and can potentially be measured with future experiments targeting spectral distortions. The constraint from conversion at low-redshift in non-linear structure that we obtain using existing FIRAS data [77] is consistent with previous limits obtained from conversion over a wider range of redshift and a different treatment of inhomogeneities.

Extending previous analyses, we have demonstrated that CMB and LSS correlation functions are in principle a far more powerful probe of photon to dark photon conversion. The two-point function of dark screening ($\langle \tau(\omega, \hat{n}) \tau(\omega, \hat{n}') \rangle$) can be extracted from existing and future CMB data by measuring $\langle T^{\rm dSc}(\omega, \hat{n}) T^{\rm dSc}(\omega, \hat{n}') \rangle$. The patchy dark screening map $T^{\rm dSc}(\omega, \hat{n})$ can be separated from the blackbody CMB by taking advantage of multi-frequency observations of the CMB. As shown in Fig. 4.9, such a correlation function can be more sensitive than the existing FIRAS constraints by up to 2 orders of magnitude despite scaling with the small kinetic mixing parameter as ε^4.

A better reach on the mixing parameter can be obtained by cross-correlating $\tau(\omega, \hat{n})$ with other observables that are sensitive to the underlying distribution of electron density in the Universe. One such correlation function is $\langle T^{\rm dSc}(\omega, \hat{n}) \hat{\tau}(\hat{n}') \rangle$, where $\hat{\tau}(\hat{n}')$ is a template for the dark screening optical depth. This correlation function takes advantage of the fact that for a dark photon with mass $\lesssim 10^{-12}$ eV, conversion mostly happens at late times,

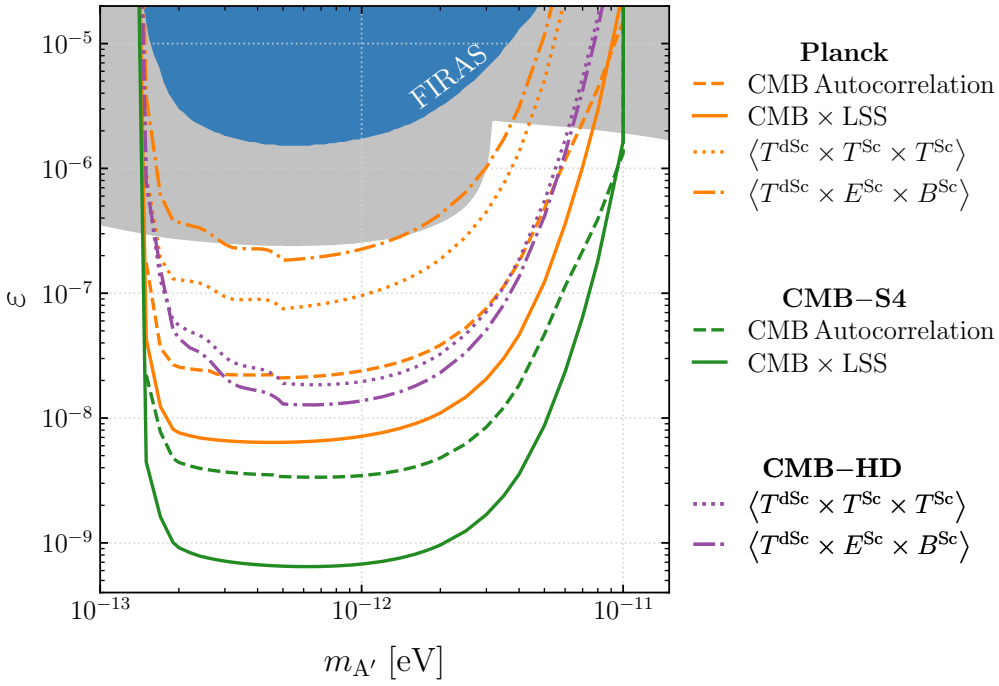

Figure 4.9: The projected sensitivity of several estimators for Planck, as well as future surveys CMB-S4 and CMB-HD. The gray shaded region is excluded from analysis [119, 116] with data from COBE/FIRAS [77]. The blue shaded region shows the equivalent constraint using our model, as explained in Section 4.6.1. The solid lines show the projected sensitivity of the CMB auto-correlation functions in Section 4.4.3 and 4.6.3 with uncertainty given by (4.78). The dashed contours were computed using (4.82) and show the projected sensitivity from the cross-correlation between CMB and LSS in Section 4.5.2 and 4.6.4. The dotted and dot-dashed contours given by (4.85) and (4.88) respectively show the projected sensitivities of the bispectra presented in Section 4.5.4 and 4.6.5. The projected sensitivity from CMB-S4 and CMB-HD are similar for the CMB auto-correlation and cross-correlation between CMB and LSS, whereas bispectra sensitivity with CMB-HD is superior to CMB-S4. We used $f_{\rm sky} = 0.7$ for Planck and $f_{\rm sky} = 0.5$ for CMB-S4 and CMB-HD.

creating a strong correlation between tracers of LSS and patchy dark screening. As shown in Fig. 4.9, the reach obtained from this correlator can be an order of magnitude better than the CMB-only result.

Cross-correlation functions can also be constructed from the dark-screened and Thomson-screened CMB alone. Qualitatively, these correlation functions can be understood as a

correlation between the dark screening $\tau(\omega, \hat{n})$ and the Thomson screening optical depth $\tau^{\rm Th}$ from halos. Three-point correlation functions offer the best sensitivity to this correlation. In particular, the $\left\langle T^{\rm dSc} T^{\rm Sc} T^{\rm Sc} \right\rangle$ and $\left\langle T^{\rm dSc} E^{\rm Sc} B^{\rm Sc} \right\rangle$ bispectra (both shown in Fig. 4.9) offer the best sensitivity, and are comparable to the reach anticipated with CMB auto-correlation functions. Compared to the cross-correlation with a template, the reduction in sensitivity is mainly a result of the smallness of the Thomson screening optical depth $\tau^{\rm Th}$, which suggests that these three-point correlation functions could be better probes of photon to dark photon conversion in the weakly inhomogeneous Universe around recombination, when $\tau^{\rm Th}$ was much larger. Compared to the CMB auto-correlation functions, the sensitivity of these three-point correlation function scales much more favorably with ℓ, and hence improves with increased sensitivity and high resolution – the regime targeted by future surveys. The similarity in the reach of the CMB auto-correlation functions and these three-point correlation functions for future CMB survey is a numerical coincidence, and the relative strength of these two methods in a real data analysis likely depend on systematics and foregrounds, an investigation that we postpone to future work. Finally, we note that in the event of a detection, a combination of the two-point and three-point functions can be used to break degeneracies between the dark photon mass, kinetic mixing parameter and electron density profile, which is essential for extracting detailed information about the dark screening optical depth and how it correlates with the distribution of ionized gas. The methodologies we developed in this Chapter can be used to search for conversions of photon to dark photon in various other environment in the early-Universe, the details of which we will work out in a few follow up studies.

The study presented in this Chapter is a novel example of using cross-correlations between an observable in the Standard Model (SM) of cosmology (ΛCDM) and signals of a model beyond the Standard Model (BSM) of particle physics. Experimentally, the measurement of these correlators is enabled by the rapid improvement of cosmological experiments. Theoretically, these $\langle {\rm SM} \times {\rm BSM} \rangle$ correlators allow us to use the ultra-high precision cosmological data on the anisotropic Universe to study BSM signals at the same order of the small BSM parameter as the monopole signal $\langle {\rm BSM} \rangle$. We expect similar $\langle {\rm SM} \times {\rm BSM} \rangle$ correlators will allow us to better probe other BSM signals with the rapidly improving cosmological CMB and LSS datasets, and take advantage of the synergy between the upcoming CMB experiments like the Simons Observatory [205], as well as future experiments CMB-S4 [206] and CMB-HD [89], with upcoming LSS surveys like DESI [207], Euclid [208], and LSST [209]. Constructing new observables of this kind can allow us to better search for new interactions between the Standard Model and dark sectors, including dark matter annihilation, decay, and mixing between the visible and dark sector particles. In the next Chapter, we extend this analysis to the case of axions coupling to CMB photons.

Chapter 5

Axion Dark Screening

5.1 Introduction

As discussed briefly in Chapter 1, the QCD axion and axion-like particles, generally referred to as axions, are among the most well-motivated additions to the Standard Model (SM) [128, 129, 130, 131, 132, 99]. Axions provide a solution to the strong CP problem [128, 129, 130, 131], and can be good dark matter candidates [135, 239, 240]. Axions can couple to the SM through the strong or electromagnetic force. Here, we will be concerned with the coupling between the axion and the photon, described by the Lagrangian:

$$\mathcal{L}_{\mathrm{a}\gamma} = -\frac{1}{4} g_{\mathrm{a}\gamma\gamma}\, \mathrm{a}\, F^{\mu\nu}\tilde{F}_{\mu\nu} = g_{\mathrm{a}\gamma\gamma}\, \mathrm{a}\, \mathbf{E}\cdot\mathbf{B}, \tag{5.1}$$

where $F^{\mu\nu}$ is the electromagnetic field-strength tensor and $\tilde{F}^{\mu\nu} \equiv 1/2\, \epsilon_{\mu\nu\alpha\beta}F^{\alpha\beta}$ its dual. The above coupling allows the photon to oscillate into an axion in the presence of an external magnetic field transverse to the photon three-momentum.

Searches for photon-axion conversion have been conducted over a wide range of the electromagnetic spectrum and axion parameter space both in terrestrial laboratory experiments and through astrophysical observations [1]. These efforts have probed axions from effectively zero mass to masses up to a TeV, and down to a coupling of $g_{\mathrm{a}\gamma\gamma} \sim 10^{-11}\,\mathrm{GeV}^{-1}$. In this Chapter, we focus on very low-mass axions, $m_{\mathrm{a}} \sim \mathcal{O}(\mathrm{peV})$, where the best existing limit on the axion-photon couplings $g_{\mathrm{a}\gamma\gamma}$ comes from the CERN Axion Solar Telescope (CAST) experiment [241] and various astrophysical observations. CAST uses a large

[1] For a comprehensive summary of ongoing effort to look for axions, see [136, 16].

magnetic field to induce the conversion of axions produced in the Sun to photons, placing a limit of $g_{a\gamma\gamma} < 6.6 \times 10^{-11}\,\mathrm{GeV}^{-1}$ [242] at low mass. The strongest astrophysical constraints arise from scenarios where sources of axions (from stars [137, 243] or supernovae [138]) are converted to photons in the galactic magnetic field or scenarios where photons from a background source are converted to axions in extragalactic magnetic fields (e.g. [139]). The strongest existing astrophysical constraints are from the latter category, yielding $g_{a\gamma\gamma} < 6 - 8 \times 10^{-13}\,\mathrm{GeV}^{-1}$ for $m_a \lesssim 10$ peV, from the impact on AGN spectra of photons converting to axions in the magnetized intracluster medium [139]. Constraints that are independent of the axion-photon coupling in this mass range also comes from black hole superradiance [244], which can be affected by axion self-interactions [245].

The cosmic microwave background (CMB) is an exquisitely calibrated source: it has an almost perfect blackbody frequency spectrum, anisotropies are small and follow simple, Gaussian statistics, and it is only weakly polarized. Measurements of the CMB are therefore extremely sensitive to *secondary* anisotropies and spectral distortions produced by the interactions of CMB photons with large-scale structure (LSS) as they propagate through cosmic history to our telescopes. Secondary anisotropies are a primary target of future CMB surveys such as Simons Observatory [205] (SO), CMB-S4 [206], and CMB-HD [89] which lie on the high-resolution, low-noise frontier; their true potential will be unleashed through cross-correlation with upcoming galaxy surveys performed by Vera Rubin Observatory Legacy Survey of Space and Time (LSST) [209], Dark Energy Spectroscopic Instrument [207] (DESI), Euclid [208], and Spectro-Photometer for the History of the Universe, Epoch of Reionization, and Ices Explorer [246] (SPHEREx). Standard Model sources of secondary anisotropies include Sunyaev Zel'dovich effects (scattering from charges) and weak lensing (scattering from masses). Measurements of these secondaries have broad application, from determining the sum of neutrino masses to narrowing down the properties of inflationary cosmology [205, 206, 89]. Any beyond the SM (BSM) physics scenarios that involves new interactions between CMB photons and LSS will lead to new sources of secondary anisotropies. The high sensitivity and resolution of existing and upcoming surveys motivates identifying the range of BSM models that lead to new CMB secondaries and designing optimal search techniques for their signatures.

In this Chapter we investigate scenarios where CMB photons are converted to axions in magnetic fields associated with LSS. As CMB photons transit a magnetic field $\mathbf{B}_\perp$, perpendicular to the photon's direction of propagation, the polarization state along $\mathbf{B}_\perp$, $A_\parallel$, mixes with an ultra-relativistic axion ($\omega \gg m_a$) according to the equation of motion [247, 248, 249]

$$\left[\omega - i\partial_z + \frac{1}{2}\begin{pmatrix} -m_\gamma^2/\omega & g_{a\gamma\gamma}|\mathbf{B}_\perp| \\ g_{a\gamma\gamma}|\mathbf{B}_\perp| & -m_a^2/\omega \end{pmatrix}\right]\begin{pmatrix} A_\parallel \\ a \end{pmatrix} = 0, \tag{5.2}$$

where $m_{\rm a}$ is the axion mass and $m_\gamma^2 = e^2 n_e/m_e$ denotes the photon plasma mass in an ionized medium with electron density n_e. The probability for a CMB photon to resonantly convert to an axion is computed using the Landau-Zener expression [250, 251, 252]:

$$P^{\rm res}_{A_\parallel \to {\rm a}} \simeq \frac{\pi \omega g_{{\rm a}\gamma\gamma}^2 |\mathbf{B}_\perp|^2}{m_{\rm a}^2} \left| \frac{{\rm d} \ln m_\gamma^2}{{\rm d}t} \right|^{-1}_{t_{\rm res}}, \tag{5.3}$$

which is a good approximation for the scenarios considered throughout this Chapter [2]. CMB photons propagating along different lines of sight encounter varying magnetic fields in media with varying density. From (5.3), the removal of CMB photons due to conversion into axions therefore leads to an anisotropic spectral distortion of the CMB intensity and polarization.

Early work on the imprint of photon-axion conversion in the CMB used the absence of significant spectral distortions of the CMB monopole observed by COBE/FIRAS [77] to rule out proposals for axion-induced supernova dimming [253] [3]. Ref. [254] proposed to look for *anisotropic* spectral distortions of the CMB due to inhomogeneous plasma densities and magnetic fields, but assumed unrealistically shallow plasma density gradients to maintain the resonance condition over long distances, leading to an overestimate and incorrect frequency dependence of the conversion probability. Ref. [255] studied the spectral distortion in intensity from individual clusters, and obtained upper limits from Planck CMB temperature anisotropies of $g_{{\rm a}\gamma\gamma} \lesssim \mathcal{O}(10^{-11}\,{\rm GeV}^{-1})$, subject to assumptions about magnetic field profile in clusters.

Subsequently, Ref. [256] performed a detailed study of the CMB polarization and intensity signature from resonant and non-resonant conversion in the Milky Way's magnetic fields (with resonant conversion happening in coherent magnetic domains and non-resonant conversion in turbulent domains). Achieving a strong constraint from this signal requires high spectral resolution. The near-term space-based Lite-Bird [257] mission was forecasted to yield limits down to $g_{{\rm a}\gamma\gamma} \sim 10^{-12}\,{\rm GeV}^{-1}$ [256], with stronger limits requiring futuristic missions such as PIXIE [258]. An analysis of the non-resonant signal using Planck temperature anisotropies provided a far weaker constraint of $g_{{\rm a}\gamma\gamma} \lesssim 10^{-9}\,{\rm GeV}^{-1}$ [256]. Ref. [259] revisited the extragalactic signal first examined in [255], modeling the detectability of the polarization signal. Subject to assumptions about magnetic fields, gas profiles, and the number of detectable clusters, they demonstrate that sensitivity of beyond $g_{{\rm a}\gamma\gamma} \sim 10^{-13}\,{\rm GeV}^{-1}$

[2] We provide a detailed derivation of this formula and its range of validity in the context of this work in App. B.4. A complimentary scenario where the axion mass is too light (effective massless) to satisfy the resonant condition anywhere in the universe is discussed in App. B.9.

[3] It was also pointed out that, due to the photon plasma mass, the conversion probability acquires a frequency dependence, making it hard to account for achromatic dimming of SNe [248].

could be achieved with next-generation CMB experiments such as CMB-S4. These works indicate that the CMB signature of photon to axion conversion could be competitive with the laboratory and astrophysical constraints described above.

This Chapter proposes a new framework to look for the spectral secondary CMB temperature and polarization anisotropies, sourced by the resonant conversion of CMB photons into axion radiation within the magnetic field of structure in the late universe. The effect is analogous to the case of CMB photons converting into dark photons studied in the previous Chapter, and manifests as an *anisotropic* absorption optical depth with a characteristic *linear frequency dependence*, $\tau^{\rm a}(\omega, \hat{n}) \propto \omega$ that is strongly correlated with LSS. The radial profile of the electron density inside halos provides a natural scanner of the photon plasma mass, which allows for resonant conversion between CMB photons and light axions in the halo magnetic fields for more than a decade in axion masses around $m_{\rm a} \simeq 10^{-12}\,{\rm eV}$. Following Chapter 4, we use the halo model to compute two-point correlation functions of the resulting secondary CMB temperature anisotropies, and their correlations with tracers of LSS. Photon-axion conversion generates an anisotropic polarization signal from the unpolarized CMB monopole. We derive the corresponding CMB two-point function and the CMB polarization-LSS three-point function. To compute the signal strength, halo magnetic fields are modeled according to state of the art hydrodynamical cosmological simulations. Depending on the axion mass, photon-axion conversion predominantly occurs at different halo radii, inducing a characteristic scale dependence in the correlations. Our results provide a simple framework for computing correlation functions, which can be easily adapted to future analyses with differing assumptions. As in Chapter 4, the known frequency dependence of the signal is crucial to disentangle the axion-induced CMB secondary anisotropies from the primary anisotropies. We use the signal two- and three-point functions to project the sensitivity of CMB and LSS surveys to the axion-photon coupling.

We forecast that current data from Planck and unWISE galaxies are complementary to the best existing constraints from AGN spectra described above. The component-separated temperature-galaxy correlator $\langle T^{\rm a} g \rangle$ is the most sensitive, and can in principle achieve $g_{{\rm a}\gamma\gamma} \lesssim 3 \times 10^{-12}\,{\rm GeV}^{-1}$. Other correlators have a slightly weaker sensitivity, which can be helpful in confirming any possible detection. This strongly motivates an analysis using existing measurements, which we pursue in a separate publication [260]. Even though the region in the axion parameter space that can be currently probed seems disfavoured by other astrophysical searches, we stress that, given the assumptions required to derive those bounds, it is nevertheless interesting to have complementary probes which rely on a different set of assumptions and completely different observations. Moreover, we find that a future search using results from the CMB-S4 experiment could be sensitive to up to an order of magnitude smaller couplings compared to Planck, providing the most sensitive

probe of axions in this mass range. Data from ACT [261] and Simons Observatory [205] will continuously extend the reach in parameter space as we approach the S4 era.

The Chapter is organized as follows. We describe photon-axion conversion inside an individual halo in Sec. 5.2.1 and the resulting sky-averaged optical depth in Sec. 5.2.2. In Sec. 5.3 we derive the CMB temperature and polarization anisotropies, computing the temperature and polarization auto-correlation functions in Sec. 5.3.1, the temperature-galaxy cross-correlation function in Sec. 5.3.2, and the polarization-galaxy bispectrum in Sec. 5.3.3. In Sec. 5.4.1 we investigate how CMB maps at different frequencies can be used to separate the photon-axion conversion signal from the primary CMB as well as galactic and extragalactic foregrounds. We forecast the sensitivity of existing and future CMB and galaxy surveys to photon-axion conversion in Sec. 5.4.2 and comment on the limit of (effectively) massless axions in Sec. 5.4.3. Finally, we conclude in Sec. 5.5. We include a set of appendices containing various technical discussions and derivations. In App. B.4 we derive the photon-axion conversion probability and discuss the domain of validity in the context of our analysis. In App. B.5 and B.7 we derive the two- and three-point correlators involving polarization. In App. B.6 we detail the model used for the galaxy distribution and their power spectra. In App. B.8 we describe the foreground and instrumental noise models used in our forecasts. In App. B.9 we sketch the utility of our formalism to the study of photon-axion conversion for (effectively) massless axions. In App. B.10 we provide a qualitative order-of-magnitude estimate of the effect and the expected sensitivity. Finally, in App. B.11 we derive the likelihood for the axion signal. Natural units are used throughout, with $\hbar = c = k_B = 1$.

5.2 Photon-axion conversion inside large-scale structure

To model photon-to-axion conversion, we first need a model for the distribution of LSS. Here, we work within the halo model (see e.g. [262, 60] for a review), where dark and baryonic matter is assumed bound in virialized halos. The mass and redshift of halos determines the properties of the baryonic matter and galaxies that inhabit them. Correlation functions are then computed from the distribution of matter between and within halos. The halo model is extremely flexible, allowing for a unified framework to incorporate a wide variety of observables. Below, we first compute the photon-axion conversion probability in individual halos and then compute the sky-averaged (monopole) signal over all halos.

5.2.1 Individual halo conversion

In this section, we derive the rate for resonant photon-axion conversion inside an individual halo, which is the main ingredient needed to compute the axion-induced CMB spectral distortions and anisotropies we study in the following sections. An important feature of the conversion into axions is that only the photon polarization parallel to the magnetic field mixes with the axion [247]; therefore there are two types of signal that can be looked for: a reduction (screening) in the intensity of the CMB and an induced polarization.

In analogy with Chapter 4, we compute the probability that photons traveling along the direction $\hat{n}$ convert to axions inside a halo with mass m_i, at comoving distance $\chi_i(z_i)$, and redshift z_i according to the Landau-Zener expression (5.3). We assume halos to be spherically symmetric and centered at $\hat{n}_i$. While individual halos could be far from spherical, we will only be concerned with ensemble averages below, where spherical symmetry is a good approximation. Due to the gradient in the halo's gas density profile, at some distance $r_{\rm res}(\chi_i, m_i)$ from the halo center, the resonance condition will be satisfied, with $m_\gamma(r_{\rm res}) = m_{\rm a}$. Within these assumptions, the conversion probability is azimuthally symmetric with respect to the halo center, and can be written as

$$P^i_{\gamma\to{\rm a}}(\chi_i, m_i, \hat{n}_i - \hat{n}) = P(\chi_i, m_i)\, N_{\rm res}(\chi_i, m_i)\, u(\hat{n}_i - \hat{n}|\chi_i, m_i)\, \gamma(\hat{n}|\chi_i), \tag{5.4}$$

where

$$P(\chi_i, m_i) = \pi\omega(1+z_i) g^2_{{\rm a}\gamma\gamma} |\mathbf{B}(r_{\rm res}, z_i, m_i)|^2 \left|\frac{{\rm d}m^2_\gamma(r, z_i, m_i)}{{\rm d}r}\right|^{-1}_{r_{\rm res}}, \tag{5.5}$$

$$N_{\rm res}(\chi_i, m_i) = \begin{cases} 2, & r_{\rm res} < r_{\rm vir}, \\ 1, & r_{\rm res} = r_{\rm vir}, \end{cases} \tag{5.6}$$

$$u(\hat{n}_i - \hat{n}|\chi_i, m_i) = \left[1 - \frac{(\chi_i\theta/r_{\rm res})^2}{(1+z_i)^2}\right]^{-1/2}. \tag{5.7}$$

In the above expressions, $\theta \simeq |\hat{n}_i - \hat{n}| \leq r_{\rm res}(1+z_i)/\chi_i \ll 1$ is the small angle between the halo center and the photon trajectory. $N_{\rm res}$ counts the number of resonance crossings for $r_{\rm res}$ within the virial radius $r_{\rm vir}$; it is set to one for $r_{\rm res} = r_{\rm vir}$ to smooth the sharp transition, i.e. the conversion only happens half of the time at the edge. $|\mathbf{B}(r_{\rm res}, z_i, m_i)|$ denotes the magnitude of the magnetic field inside the halo at the resonance radius. In general, the magnetic field within the halo has a finite coherence length – much smaller than $r_{\rm vir}$ or $r_{\rm res}$ – and will take a random orientation in different domains. To account for the random angle of the magnetic field along each photon propagation direction, we

multiply the conversion probability by $\gamma(\hat{n})$. This function takes a different form – and has different statistical properties – depending on whether we are computing the contribution of the conversion to the intensity or polarization signals, since a different combination of the magnetic field components enters in each case. We will therefore write $\gamma(\hat{n})$ explicitly in Sec. 5.3, when computing the axion-induced signal to CMB intensity and polarization anisotropies.

The radial profile of the photon plasma mass within a spherically symmetric halo can be modeled using the baryonic gas density profile $\rho_{\rm gas}(r, z_i, m_i)$ based on hydrodynamical cosmological simulations from Ref. [217], the widely-used Battaglia et al. AGN Feedback profile (see e.g. Ref. [85] for an example in a different context). Assuming that protons account for all the baryonic mass and that there is an equal number of electrons and protons, $m_\gamma^2(r, z_i, m_i) = e^2\rho_{\rm gas}(r, z_i, m_i)/(m_e m_p)$, where e is the electric charge, m_e and m_p the electron and proton masses, and the expression for $\rho_{\rm gas}$ is given in Sec. 4.2 of Chapter 4.

To model the magnetic field profile within halos we use recent results from the high resolution cosmological magneto-hydrodynamical zoom simulations from the Auriga project. The structure of the magnetic field in the circumgalactic medium and its time evolution has been analysed for Milky Way-like galaxies [263] and a broad range of halo masses [264]. We use the interpolated magnetic field radial profiles provided by the authors of Ref. [264] for $z < 1.9$ in 7 halo mass bins between $10^{10}\,{\rm M}_\odot$ and $10^{13}\,{\rm M}_\odot$; for heavier halos, we conservatively use a flat extrapolation, i.e. we assume the same magnetic field profile for all halo masses above the highest mass bin available. The magnetic field we use only includes the smooth halo component and no contributions from sub-structure (such as satellite galaxies) within the halos, which represent additions to the smooth density profile. For Milky Way-like halos, the magnetic field at $z = 0$ reaches a value of about $0.1\,\mu$G at the virial radius, with larger (smaller) values for heavier (lighter) halos. While in an individual halo the magnetic field is far from being spherically symmetric, we are only interested in statistically averaged quantities, in which case the averaged $|\mathbf{B}(r)|$ profiles should give a good approximation.

Similar to Chapter 4, we compute only the conversion in the smooth circumgalactic medium, in regions where the density is well characterized by the Battaglia density profile [217]. Making use of, for example, the central region of disk galaxies will extend the sensitivity to higher axion masses. Similarly, the sensitivity can be extended to lighter axions by utilizing the regions outside the virial radius of a halo, where the baryon density slowly decreases to the average density of the universe. Both extensions come with more modeling uncertainties associated with the density profile of matter and amplitude of the magnetic field in these regions. As a result, we defer these studies to a future publication.

We emphasise that the resonance conversion formula in (5.4) is valid even for a finite coherence length of the magnetic field, as long as it varies slowly compared to the oscillation length between the two mass eigenstates in vacuum, $4\pi\omega/m_{\rm a}^2$. For the smallest axion masses considered here, this is equivalent to a minimum coherence length of about a parsec, which is much smaller than the smallest spatial resolution of the cosmological simulations, of $\mathcal{O}$(kpc). The magnetization of the circumgalactic medium is driven by galactic outflows transporting magnetised gas from the disk into the halo and later amplified by a turbulent dynamo acting in the halo. Both of these processes operate at length scales much larger than a parsec and strongly suggests that the magnetic field to be coherent over long enough length scales for (5.4) to be valid. The results of the simulations additionally show that the magnetic energy power spectra are dominated by scales $\gtrsim 10$ kpc [263], which support the assumption made here that the magnetic field is dominated by relatively large-scale fluctuations, while rapidly oscillating components can be neglected. Importantly, in this regime, the conversion probability scales linearly with frequency and it is insensitive to the exact value of the magnetic field coherence length. For a more detailed discussion on the derivation of the conversion probability and its range of validity see App. B.4.

5.2.2 Conversion monopole and optical depth

The total photon-axion conversion probability is given by the sum of the individual halo contributions from (5.4) along the line of sight. Since the magnetic field orientation changes randomly in each halo (and also between the two resonance crossings in the same halo), the axion-induced polarization will have a random positive or negative sign at each crossing of the conversion surface, yielding a zero mean but non-zero variance. The photon-axion conversion always removes photons, therefore reducing the intensity and *screening* the CMB monopole [4]. On average, only one component of the magnetic field contributes to the intensity axion-induced screening, such that the γ factor in (5.4) averages to 1/3. We define the axion-induced screening optical depth in the direction $\hat{n}$ as

$$\begin{aligned}\tau^{\rm a}(\hat{n}) &\equiv \sum_i P^i_{\gamma\to{\rm a}}(\chi_i, m_i, \hat{n}_i - \hat{n}) = \sum_i P(\chi_i, m_i) N_{\rm res}(\chi_i, m_i) u(\hat{n}_i - \hat{n}|\chi_i, m_i)\gamma(\hat{n}|\chi_i) \\ &= \int_{z_{\rm max}}^{z_{\rm max}} {\rm d}z \, \frac{{\rm d}\tau^{\rm a}(\hat{n}, \chi)}{{\rm d}z}, \end{aligned} \tag{5.8}$$

[4] This is analogous to Thomson scattering of CMB photons from free electrons in the post-reionization universe screening the primary CMB anisotropies. Two crucial differences here are that while Thomson screening preserves the blackbody spectrum, axion-induced screening does not and while Thomson screening couples only to temperature anisotropies, axion-induced screening couples to the temperature *monopole*.

where we have defined the differential optical depth as a function of redshift

$$\frac{\mathrm{d}\tau^{\mathrm{a}}}{\mathrm{d}z} \equiv \frac{\chi^2}{H}\int \mathrm{d}^2\hat{n}'\,\mathrm{d}m \sum_i \frac{\delta(\chi-\chi_i)}{\chi^2}\delta^2(\hat{n}'-\hat{n}_i)\delta(m-m_i)\,\frac{1}{3}P(\chi,m)N_{\mathrm{res}}(\chi,m)u(\hat{n}'-\hat{n}|\chi,m), \tag{5.9}$$

where H is the Hubble parameter at redshift z, we performed a change of variables from comoving distance $\chi(z)$ to redshift, and we replaced explicitly the average value of the γ factor. Notice that, similarly to the dark photon case of Chapter 4, the axion-induced screening has a simple scaling with frequency and photon-axion coupling, in this case $\tau^{\mathrm{a}} \propto \omega g_{\mathrm{a}\gamma\gamma}^2$. We will leverage this frequency dependence to appropriately combine CMB measurements across multiple frequency channels and maximize the signal-to-noise ratio, as described in Sec. 5.3. The ensemble average of the optical depth is

$$\begin{aligned}\langle\tau^{\mathrm{a}}(\hat{n})\rangle &= \int_{z_{\mathrm{max}}}^{z_{\mathrm{max}}} \mathrm{d}z \left\langle \frac{\mathrm{d}\tau^{\mathrm{a}}(\hat{n},z)}{\mathrm{d}z}\right\rangle \\ &= \int_{z_{\mathrm{max}}}^{z_{\mathrm{max}}} \mathrm{d}z \frac{\chi^2}{H}\int \mathrm{d}m\, n(\chi,m)\frac{1}{3}P(\chi,m)N_{\mathrm{res}}(\chi,m)\int \mathrm{d}^2\hat{n}'\, u(\hat{n}'-\hat{n}|\chi,m),\end{aligned} \tag{5.10}$$

where $n(\chi,m)$ denotes the isotropic average halo number density per volume per halo mass, i.e. the halo mass function. Since the halo number density is isotropic, the average optical depth in (5.10) does not depend on the direction and we can evaluate it at the north pole, $\hat{n}=\hat{z}$, to get the expected screening monopole

$$\begin{aligned}\bar{\tau}^{\mathrm{a}} \equiv \langle\tau^{\mathrm{a}}(0)\rangle &= \int_{z_{\mathrm{max}}}^{z_{\mathrm{max}}} \mathrm{d}z \frac{\chi^2}{H}\int \mathrm{d}m\, n(\chi,m)\frac{1}{3}P(\chi,m)N_{\mathrm{res}}(\chi,m)\int \mathrm{d}^2\hat{n}\, u(\hat{n}|\chi,m) \\ &= \int_{z_{\mathrm{min}}}^{z_{\mathrm{max}}} \mathrm{d}z \frac{\chi^2}{H}\int \mathrm{d}m\, n(\chi,m)\tau_{00}(z,m).\end{aligned} \tag{5.11}$$

For later convenience, we have introduced the notation

$$\tau_{00}(z,m) \equiv \frac{\sqrt{4\pi}}{3}N_{\mathrm{res}}(\chi,m)P(z,m)u_{00}(z,m), \tag{5.12}$$

$$u_{00}(z,m) \equiv \frac{1}{\sqrt{4\pi}}\int \mathrm{d}^2\hat{n}\, u(\theta|z,m) = \sqrt{\pi}\frac{(1+z)^2 r_{\mathrm{res}}^2}{\chi(z)^2}, \tag{5.13}$$

for the optical depth monopole at each redshift and halo mass, and the monopole of the angular part of the conversion probability u, respectively. In the next sections, these will be generalized to higher multipoles.

We choose the limits of integration to range between a minimum redshift of $z_{\rm min} = 0.005$ and up to a maximum redshift for which the halo magnetic field profile is available $z_{\rm max} = 1.9$, which is well below the redshift at which reionization is complete. We checked for all our observables that the lowest redshift bins give a subdominant contribution; however note that, in general, the effect from individual particularly nearby objects can be significant [255], in particular, if we can resolve and model the central regions of these objects, for the upper end of the axion masses. To perform numerical computations we assume the mass-function of [220] that fixes the bias function [265], and the concentration-mass relation from [266], which fixes the free parameters in the halo density profile. We also work under the assumption that the halo boundary is at the virial radius where the overdensity is ≈ 178 greater than the background density, so that the halo mass is defined in a sphere of radius $r_{\rm vir}$ in units of $M_\odot$. We assume 100 halo mass bins logarithmically spaced in the $10^{11} - 10^{17}\,{\rm M}_\odot$ interval. Finally, throughout this Chapter we assume a flat ΛCDM cosmology, with parameters fixed by the best-fit Planck 2018 data [10]: $\Omega_{\rm cdm} = 0.11933$, $\Omega_{\rm b} = 0.02242$, $H_0 = 67.66$ km/s/Mpc, $\ln(10^{10} A_s) = 3.047$, $n_s = 0.9665$ and $\tau_{\rm reio} = 0.0561$. Note, these parameters are slightly different from those assumed in Chapter 4.

Fig. 5.1 shows the differential optical depth $\mathrm{d}\bar{\tau}^{\rm a}/\mathrm{d}\ln z$, the integrand of (5.11), as a function of redshift for three choices of axion masses. The conversion mostly happens at low redshifts for the smallest masses and at high redshift for the heavier masses, as expected following the redshift evolution of the photon plasma mass. The range of redshifts where we have a reliable model for the circumgalactic magnetic field limits the range of heavy axion masses accessible in our analysis. Therefore, our result for the integrated optical depth is conservative, as it would in principle receive additional contributions at higher redshifts.

The total optical depth over the sky from (5.11) represents a spectral distortion of the blackbody CMB spectrum from photon-axion conversion inside structure in the late universe, and can be used to derive a bound on the axion-photon coupling from COBE/FIRAS [77]. The resulting constraint obtained from a chi-square test identical to what was implemented in Chapter 4 is shown in Fig. 5.2. Spectral distortions can only probe couplings as small as $10^{-9}\,{\rm GeV}^{-1}$, which are well within the excluded region from the axion helioscope CAST [242]. Note that COBE/FIRAS can only exclude an optical depth of $\bar{\tau}^{\rm a} \gtrsim 10^{-2}$ (see Fig. 5.1); the reason for such a weak bound is that the effect from an optical depth with linear frequency scaling can be partially compensated by increasing the best fit black body temperature. In fact, in the high frequency tail, where the axion-induced screening effect is strongest, $\exp\big[-\omega/(\bar{T}+\Delta\bar{T})\big] \simeq \exp\big(-\omega/\bar{T}\big)(1+\omega\,\Delta\bar{T}/\bar{T}^2)$; for example, we find that a change of the best fit CMB temperature $\bar{T}$ by a small fractional amount of $\Delta\bar{T}/\bar{T} \lesssim 10^{-4}$ is enough to wash out the axion screening spectral distortions for $g_{\rm a\gamma\gamma} = 10^{-10}$ GeV. The

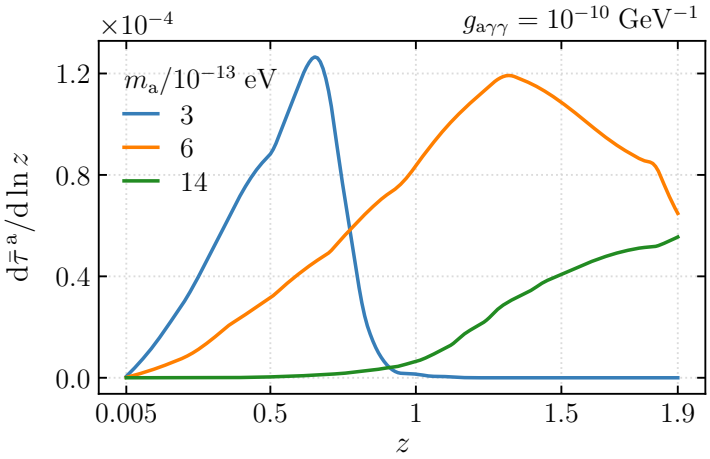

Figure 5.1: The axion-induced differential optical depth (see (5.11)) as a function of redshift for three choices of axion mass m_a. The coupling constant $g_{a\gamma\gamma}$ is fixed as labeled and we use a reference frequency $\omega/(2\pi) = 145$ GHz. The latter is adopted for all the figures throughout this Chapter. At the low-end of the axion masses accessible in our analysis, the conversion takes place in the outermost regions of low-redshift halos, where electron densities reach the lowest amplitude. For heavier axions, the density required to undergo resonant conversion increases, and a broader range of redshift becomes relevant. The non-smooth features in these curves are due to the magnetic field profiles evaluated in discrete coarse halo mass bins as provided by Ref. [264]. We work under the assumption that there are no significant magnetic fields in the circumgalactic medium for virialized halos beyond $z > 1.9$. This represents a boundary on the axion-induced screening that results in a natural cutoff at $m_a \simeq 3 \times 10^{-12}$ eV for the range of axion masses accessible with this method.

bound is therefore coming from higher order terms and from the low frequency tail, where the effect is weaker. This constraint could be strengthened slightly if additional contributions to the spectral distortion were taken into account, such as contributions from higher redshift, the conversion in the intercluster medium (which contains a larger volume compared to structure, but also weaker magnetic fields), and the contribution to the conversion inside the Milky Way.

However, as shown in the rest of this Chapter, the sensitivity to the photon-axion coupling can be improved by a few orders of magnitude by considering the *anisotropies* induced by the photon-axion conversion inside structure. In the next section, we introduce the anisotropic axion-screened CMB temperature and polarization fields and compute the most promising observables to look for an axion signal: the two-point auto-correlation functions, the two-point temperature and LSS cross-correlation function, and the polarization and LSS three-point function.

5.3 Axion-induced patchy screening

Conventionally, the CMB temperature and polarization anisotropies are given with respect to the mean brightness temperature, i.e. the CMB blackbody temperature $\bar{T} = 2.726\,\mathrm{K}$. The photon-axion conversion effect from (5.4) removes CMB photons, or equivalently reduces the intensity of the blackbody spectrum, in a frequency dependent way. The corresponding axion-induced fluctuations to the temperature and polarization Stokes parameters are:

$$T^{\mathrm{a}}(\hat{n}) = -\frac{1-e^{-x}}{x}\bar{T}\int_{z_{\mathrm{min}}}^{z_{\mathrm{max}}} \mathrm{d}z\, \frac{\mathrm{d}\tau^{\mathrm{a}}(\hat{n},\chi)}{\mathrm{d}z}\gamma^{I}(\hat{n},\chi), \tag{5.14}$$

$$(Q \pm iU)^{\mathrm{a}}(\hat{n}) = -\frac{1-e^{-x}}{x}\bar{T}\int_{z_{\mathrm{min}}}^{z_{\mathrm{max}}} \mathrm{d}z\, \frac{\mathrm{d}\tau^{\mathrm{a}}(\hat{n},\chi)}{\mathrm{d}z}\gamma^{\pm}(\hat{n},\chi), \tag{5.15}$$

where $x \equiv \omega/\bar{T}$, the multiplicative factor arises when converting from intensity to temperature units [254], and the differential contribution to axion-induced screening is defined in (5.9). Throughout this Chapter and in the associated appendices, we keep explicit the factor of $(1-e^{-x})/x$ when defining axion screening induced CMB power spectra. In the equations above we have considered only the dominant contributions proportional to the CMB temperature monopole $\bar{T}$, neglecting the screening of CMB anisotropies; because the axion-induced screening couples to the monopole, we can hope to differentiate it from the primordial CMB anisotropies, which are about 5 orders of magnitude smaller, despite the suppression from the small photon-axion coupling.

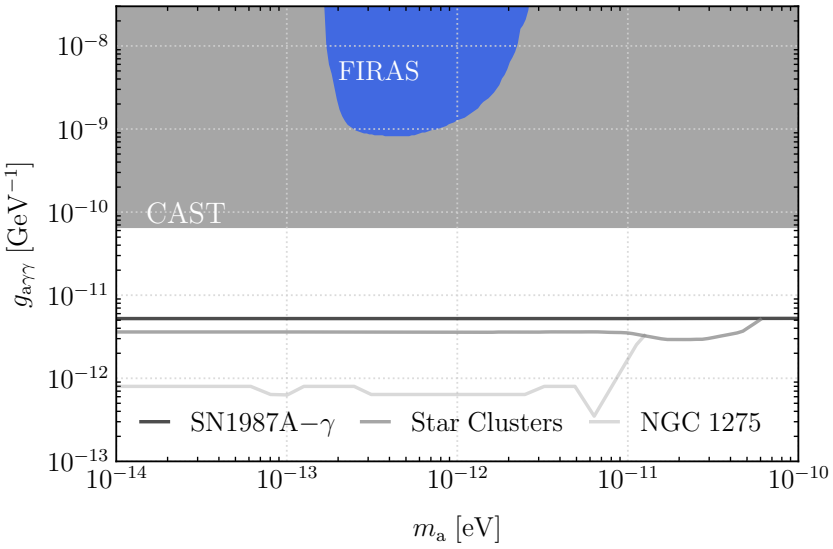

Figure 5.2: The region of interest in the parameter space of axion mass $m_{\rm a}$ and coupling to photons $g_{\rm a\gamma\gamma}$. In grey we show the existing bounds reproduced from the repository [16], which include: the CAST helioscope [242] (shaded gray), the non-observation of γ-rays from axions produced in the SN1987A that convert to photons in the galactic magnetic field [138] (solid dark gray), the non-observation of X-rays from axions produced in stars that convert to photons in the galactic magnetic field [137] (solid gray), and the absence of spectral distortions in the X-ray spectra of cluster-hosted quasars due to photon-axion conversion [139] (solid light gray). Note that Ref. [243] recently placed a limit comparable to the NCG 1275 line from the non-observation of X-rays from stellar axions produced in M82 and M87 which is not shown here. The blue shaded region represents the parameters excluded at 99% confidence level from requiring that the CMB spectral distortions from photon-axion conversion inside halos is compatible with the COBE/FIRAS measurements [77], using the optical depth described in Sec. 5.2.2 (see (5.11)) and a χ^2-squared test identical to what was implemented in Chapter 4.

The fields $\gamma^{I,\pm}(\hat{n},\chi)$ in (5.14) and (5.15) encode the information about the magnetic field components perpendicular to the line of sight that contribute to the conversion. Explicitly,

$$\begin{aligned}\gamma^{I}(\hat{n},\chi) &= 3\frac{B_\theta(\hat{n},\chi)^2 + B_\phi(\hat{n},\chi)^2}{|\mathbf{B}(\hat{n},\chi)|^2},\\ \gamma^{\pm}(\hat{n},\chi) &= \frac{3}{2}\frac{(B_\theta(\hat{n},\chi) \mp iB_\phi(\hat{n},\chi))^2}{|\mathbf{B}(\hat{n},\chi)|^2},\end{aligned} \tag{5.16}$$

where $B_{\theta,\phi}$ are the polar and azimuthal components along each line of sight $\hat{n}$ and $|\mathbf{B}|$ is total magnitude (evaluated at the location of the resonance at comoving distance χ). The overall factor of 3 is just due to the choice of normalization of $\mathrm{d}\tau^{\rm a}/\mathrm{d}z$ to include a factor of 1/3 (see (5.9)). For simplicity, we model the magnetic field as a random Gaussian field roughly constant over a domain of characteristic physical size $r_{\rm dom} \in [1, 10]$ kpc, which is independent of halo mass and redshift. If the magnetic fields have a random orientation in each domain, averaging over many domains gives

$$\left\langle \gamma^I(\hat{n},\chi)\right\rangle = 1, \quad \left\langle \gamma^{\pm}(\hat{n},\chi)\right\rangle = 0. \tag{5.17}$$

The corresponding two-point functions are

$$\left\langle \gamma^I(\hat{n}_1,\chi)^*\gamma^I(\hat{n}_2,\chi)\right\rangle \simeq \left\langle \left|\gamma^I(\hat{n}_1)\right|^2\right\rangle = 1, \tag{5.18}$$

$$\left\langle \gamma^{\pm}(\hat{n}_1,\chi)^*\gamma^{\pm}(\hat{n}_2,\chi)\right\rangle = \left\langle \left|\gamma^{\pm}(\hat{n}_1,\chi)\right|^2\right\rangle \times e^{-|\hat{n}_1-\hat{n}_2|^2/(2\theta^2_{\rm dom})} = \frac{9}{N_{\rm res}}\frac{2}{15}e^{-|\hat{n}_1-\hat{n}_2|^2/(2\theta^2_{\rm dom})}, \tag{5.19}$$

where $\theta_{\rm dom}(z) = r_{\rm dom}(1+z)/\chi(z)$. Any cross-correlation between $I, +$ or $-$ vanishes[5]. The factor of $N_{\rm res}$ in the denominator of (5.19) is to account for the fact that, for polarization, there is no cross-correlation between the resonant crossings going in and out of the halo (so that the polarization correlation should scale as $N_{\rm res}$ and not $N^2_{\rm res}$)[6].

In the following subsections we present the expressions for the signal contribution to the relevant two- and three- point functions in harmonic space. These will be used to forecast the sensitivity of current and future CMB and LSS surveys to axions that couple to photons in Sec. 5.4. A schematic representation of the terms that enter the axion-signal n-point statistics computed here is given in Fig. 5.3 for illustrative purposes.

[5]For the temperature two-point function $\left\langle \gamma^I(\hat{n}_1)^*\gamma^I(\hat{n}_2)\right\rangle$ we neglect a second, sub-leading, contribution of $4/5\, e^{-|\hat{n}_1-\hat{n}_2|^2\theta^2_{\rm dom}/2}$ that is non-zero only for small angular separations $|\hat{n}_1-\hat{n}_2|$ inside the same domain, which are mostly unresolved. Depending on the domain size and the resolution of the CMB experiment, this term could contribute detectable small-scale power.

[6]Strictly speaking, $N_{\rm res}$ is not the same in each halo, so it cannot be factorized outside of the sum over halos; however it is just equal to 2 in most cases and we adopt this factorization for simplicity, so as to use the same $\mathrm{d}\tau^{\rm a}/\mathrm{d}z$ in Eqs. (5.14)-(5.15) and keep the same notation in the computation of the temperature and polarization power spectra. Operationally, this means that we use the $\tau^{\rm a}$ power spectra with the appropriate power of $N_{\rm res}$ in each case.

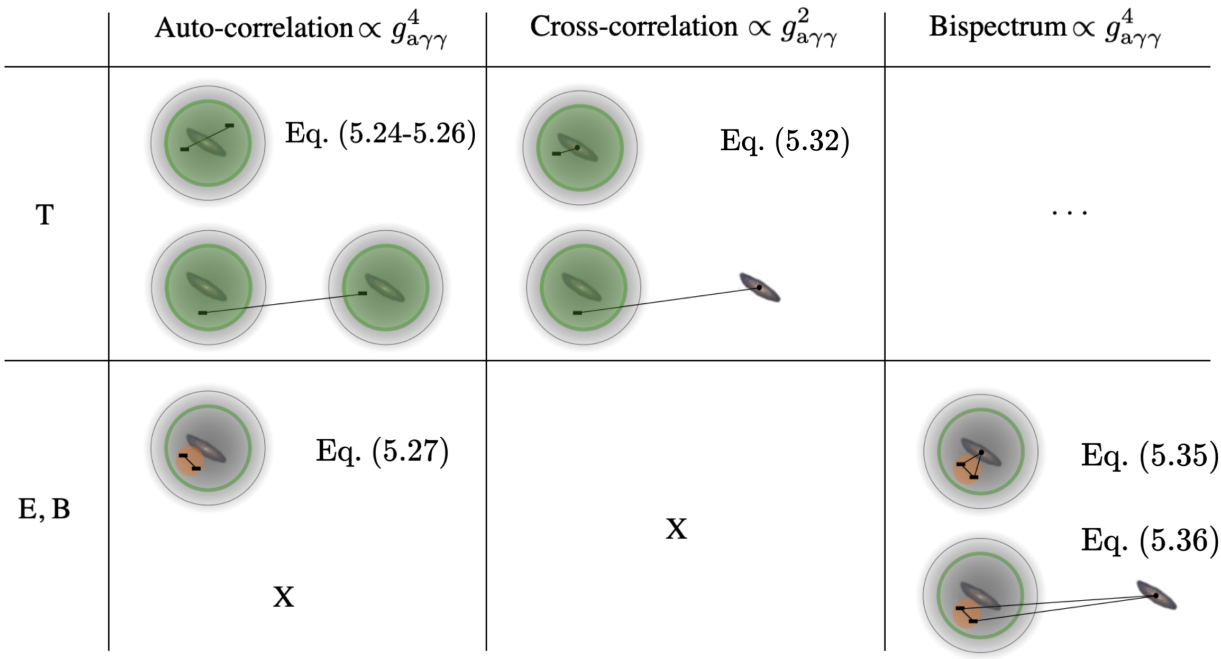

Figure 5.3: Schematic representation of the axion-induced screening n-point functions considered in this Chapter. The green circle represents the distance from the halo's center at which $m_\gamma = m_a$; all the photon trajectories crossing the halo within the circle undergo resonant photon-axion conversion. For the temperature (top row) the leading-order observables in $g_{a\gamma\gamma}$ are: $\langle T^a T^a \rangle$ auto-correlation (left, see Sec. 5.3.1) and $\langle T^a g \rangle$ cross-correlation (center, see Sec. 5.3.2), both with non-vanishing 1-halo and 2-halo terms. We checked that the bispectrum $\langle T^a T^a g \rangle$ does not improve the sensitivity compared to the two-point functions considered. For polarization (bottom row) the leading-order observables are: $\langle B^a B^a \rangle$ auto-correlation (left, see Sec. 5.3.1), with the 1-halo term only, and $\langle B^a B^a g \rangle$ bispectrum (right, see Sec. 5.3.3), with 1-halo and 2-halo terms (both dominated by squeezed triangles). The orange shaded region in the bottom row represents a magnetic field domain, where the polarization signal is correlated (see (5.19)). Note that the figures are not to scale and are given for illustrative purposes only.

5.3.1 CMB temperature and polarization auto-correlation functions

In the previous section we explored the effect of resonant axion-photon conversion on the temperature and polarization of the CMB at the field level. Here, we derive the two-point angular correlation functions of these fields. In analogy with Chapter 4 we use a halo model approach [267, 268, 262, 60]. Below we report power spectra in harmonic space following the usual notation for statistically isotropic correlators, with

$$\langle X^*_{\ell m} X'_{\ell' m'} \rangle = C_\ell^{XX'} \delta_{\ell\ell'} \delta_{mm'}, \tag{5.20}$$

where $X^{(\prime)}$ denotes a general field on the sky, $X^{(\prime)}_{\ell m}$ its corresponding spherical harmonic coefficients and $\delta_{\ell\ell'}$ is a Kronecker delta. Real space correlators can be written in terms of their power spectra as

$$\xi^{XX'}(\hat{n}_1 - \hat{n}_2) = \sum_{\ell=0}^{\ell_{\rm max}} \sum_{m=-\ell}^{\ell} C_\ell^{XX'} Y^*_{\ell m}(\hat{n}_1) Y_{\ell m}(\hat{n}_2) = \sum_{\ell=0}^{\ell_{\rm max}} \frac{4\pi}{2\ell+1} C_\ell^{XX'} \mathcal{P}_\ell(\hat{n}_1 \cdot \hat{n}_2), \tag{5.21}$$

where $Y_{\ell m}$ are the spherical harmonic functions and $\mathcal{P}_\ell$ denotes the Legendre polynomial of degree ℓ and $\ell_{\rm max}$ is set by the angular resolution of the survey. If X is a spin-2 function, analogous expressions hold for expansions in spin-2 spherical harmonics.

The first quantities to model are anisotropies in axion-induced screening $\tau^{\rm a}$, specifically the angular power spectrum, $C_\ell^{\tau\tau}$. This quantity carries two crucial features of the signal: the small-scale dependence on the halo profile and the large-scale clustering of structure. In the halo model, these are captured by the 1-halo and 2-halo terms contributing to the power spectrum, respectively. The full expression was derived in detail in Chapter 4 and the associated appendices. Here we simply report the result, expressing the harmonic-space screening optical depth as

$$\tau^{\rm a}_{\ell 0}(z, m) \equiv \sqrt{\frac{4\pi}{2\ell+1}} \frac{1}{3} N_{\rm res}(z, m) P(z, m) u_{\ell 0}(z, m), \tag{5.22}$$

$$u_{\ell 0}(z, m) \equiv \sqrt{\frac{2\ell+1}{4\pi}} \int {\rm d}^2\hat{n}\, u(\theta|z, m) \mathcal{P}_\ell(\cos\theta), \tag{5.23}$$

which generalizes Eqs. (5.12) and (5.13) to higher multipoles. The power spectrum is given

by

$$
\begin{aligned}
C_\ell^{\tau\tau} &= C_\ell^{\tau\tau,\,1-\mathrm{halo}} + C_\ell^{\tau\tau,\,2-\mathrm{halo}}, \\
C_\ell^{\tau\tau,\,1-\mathrm{halo}} &= \int_{z_{\rm min}}^{z_{\rm max}} \mathrm{d}z\, \frac{\chi(z)^2}{H(z)} \int \mathrm{d}m\, n(z,m)\, [\tau^{\rm a}_{\ell 0}(z,m)]^2\,, \\
C_\ell^{\tau\tau,\,2-\mathrm{halo}} &= \int_{z_{\rm min}}^{z_{\rm max}} \mathrm{d}z\, \frac{\chi(z)^2}{H(z)} \left[\int \mathrm{d}m\, n(z,m) b(z,m) \tau^{\rm a}_{\ell 0}(z,m)\right]^2 P^{\rm lin}\left(\frac{\ell+\frac{1}{2}}{\chi(z)}, z\right).
\end{aligned}
\tag{5.24}
$$

where $P^{\rm lin}$ is the linear matter power spectrum evaluated at comoving wavenumbers $k = \left(\ell+\frac{1}{2}\right)/\chi$ and redshift z, $b(z,m)$ is the linear halo bias and $n(z,m)$ is the halo mass function. The expression given here is the result obtained after taking the Limber approximation to simplify the halo-halo power spectrum [269, 270].[7]

The axion-induced screening CMB power spectra are based on $C_\ell^{\tau\tau}$ and the properties of the $\gamma^{I,\pm}$ coefficients. Due to the latter, the only non-vanishing terms are the temperature and polarization auto-correlations, while any cross-correlation vanishes.

The temperature auto-correlation function takes a simple form, given that the coefficients γ^I are defined with unit variance and do not add any angular dependence. Therefore, the temperature power spectrum is simply proportional to the $\tau^{\rm a}$ screening auto-power spectrum and reads

$$
C_\ell^{T^{\rm a}T^{\rm a}} = \left(\frac{1-e^{-x}}{x}\bar{T}\right)^2 C_\ell^{\tau\tau},
\tag{5.26}
$$

including both 1-halo and 2-halo contributions.[8]

The polarization auto-correlation has a slightly more involved expression. Due to the finite magnetic field coherence length, the polarization signal is correlated only on small angular scales, at or below the angular size of the projected magnetic field domain – see (5.19). In recent simulations, the magnetic field energy power spectra are dominated

[7] We have verified numerically that, over the range of scales considered here, the Limber approximation is equivalent to the full expression given in App. B.2.2 of Chapter 4,

$$
\begin{aligned}
C_\ell^{\tau\tau,\,2-\mathrm{halo}} &= \left[\prod_{i=1,2}\int_{z_{\rm min}}^{z_{\rm max}} \mathrm{d}z_i\, \frac{\chi(z_i)^2}{H(z_i)} \int \mathrm{d}m_i\, n(z_i,m_i) b(z_i,m_i) \tau^{\rm a}_{\ell 0}(z,m_i)\right] \mathcal{C}_\ell^{\rm lin}(z_1,z_2)\,, \\
\mathcal{C}_\ell^{\rm lin}(z_1,z_2) &= \frac{2}{\pi}\int \mathrm{d}k k^2 j_\ell(k\chi_1) j_\ell(k\chi_2) \sqrt{P^{\rm lin}(k,\chi_1) P^{\rm lin}(k,\chi_2)}.
\end{aligned}
\tag{5.25}
$$

Further details on how to reduce the result above to (5.24) are also given in App. B.7 (see (B.128)-(B.129)).

[8] The monopole of the axion-induced temperature is given by $\langle T^{\rm a}\rangle = -(1-e^{-x})/x\,\bar{T}\,\bar{\tau}^{\rm a}$.

by scales between 1 and 100 kpc over the halo masses considered [264]. Therefore, except for the nearest and more massive halos, the projected angular size of a magnetic field domain, $\theta_{\rm dom}$, is small and will not be resolved with existing and future surveys ($\ell \sim 10^4$ corresponds to a physical scale of about 100 kpc at a distance of 1 Gpc).

The scaling of the axion-induced polarization with magnetic field domain size can be understood as follows: the contribution to the signal integrated over the angular area of one halo of size $\theta_{\rm vir}$ adds up incoherently from the unresolved $N_{\rm dom}$ domains within the halo and scales as $B^{\rm a} \propto \theta_{\rm dom}^2 \sqrt{N_{\rm dom}}$; on the effectively two dimensional conversion surface there are $N_{\rm dom} \simeq (\theta_{\rm vir}/\theta_{\rm dom})^2$ domains; therefore, the polarization two-point function will scale as $(\theta_{\rm dom}\theta_{\rm vir})^2$. Despite the suppression from the small angle $\theta_{\rm dom}$, there are several handles on the polarization signal that can be leveraged for detection: it induces B-modes (the signal contributes equally to E (curl-free) and B (gradient-free) modes, but as we see below, the noise is lower for B-modes), it has a characteristic frequency dependence, and it is correlated with the location of galaxies. For these reasons, we find it can be competitive and complementary to the temperature observables, although it is sensitive to the unknown value of the magnetic field coherence length.

Here we report the power spectra for the E and B modes. These are derived in App. B.5 from the two-point functions of the Stokes parameters Q and U, following the standard expansion in spin-2 spherical harmonics for the polarization tensor. The final result is[9]

$$\begin{aligned} &C_\ell^{E^{\rm a}E^{\rm a}} = C_\ell^{B^{\rm a}B^{\rm a}} = \\ &= \left(\frac{1-e^{-x}}{x}\bar{T}\right)^2 \int {\rm d}z\, \frac{\chi(z)^2}{H(z)} \int {\rm d}m\, n(z,m) \sum_{LL'} \left(W^{220}_{\ell L' L}\right)^2 \left[\tau^{\rm a}_{L0}(z,m)\right]^2 C^{\rm pol}_{L'}(z,m), \end{aligned} \tag{5.27}$$

where the factor $W^{220}_{\ell L' L}$, defined in (B.99), arises due to the appropriate weighting by Wigner 3j-symbols when combining the product of spherical harmonics, and $C_\ell^{\rm pol}$ denotes the power spectrum of the appropriate combination of γ functions from (5.16) with two-point function from (5.19), which captures the correlation length of magnetic domains. These are

$$\begin{aligned} C_\ell^{\rm pol}(z,m) &\equiv \frac{1}{4}\left[C_\ell^+(z,m) + C_\ell^-(z,m)\right] \\ &= \frac{9}{N_{\rm res}(z,m)} \frac{1}{15}\, 2\pi\theta^2_{\rm dom}(z) \exp\left[-\ell(\ell+1)\theta^2_{\rm dom}(z)/2\right] \end{aligned} \tag{5.28}$$

where $\theta_{\rm dom}(z) = r_{\rm dom}(1+z)/\chi(z)$ and we fix the physical size of the magnetic field domain $r_{\rm dom} \in [1, 10]$ kpc. Comparing (5.24) with (5.27), notice that there is no contribution from

[9]Note that within this assumption of randomly oriented magnetic field in each domain, the correlation function $\langle E^{\rm a} B^{\rm a}\rangle$ vanishes.

the 2-halo term for the polarization screening. Since the magnetic field direction varies randomly in different domains, the polarization signal has a non-zero correlation only for points within the same domain.

The resulting power spectra are shown in Fig. 5.4, where the temperature power spectrum from (5.26) is compared to the polarization power spectra spectra from (5.27), for one choice of axion mass and coupling. From the flat shape of the $C_\ell^{E^{\rm a}E^{\rm a}}/C_\ell^{B^{\rm a}B^{\rm a}}$, we see that the polarization signal is predominantly coming from unclustered positive and negative sources. At large-scales, where the 2-halo term dominates, the signal in $\langle T^{\rm a}T^{\rm a}\rangle$ is significantly larger than $\langle E^{\rm a}E^{\rm a}\rangle, \langle B^{\rm a}B^{\rm a}\rangle$. Notice that the relative size between the temperature and polarization power spectra will change slightly at different values of the axion mass: lighter axions correspond to conversions at smaller redshifts, when the angular size of the magnetic field domain is less suppressed for nearby halos; therefore the polarization signal is stronger (relative to $\langle T^{\rm a}T^{\rm a}\rangle$) for smaller masses and becomes more suppressed at larger masses. This will be apparent when comparing the sensitivity to photon-axion couplings from $\langle T^{\rm a}T^{\rm a}\rangle$ and $\langle B^{\rm a}B^{\rm a}\rangle$, whose relative importance will depend on the axion mass (see Sec. 5.4.2). Finally, the fact that the signal in polarization is weaker than the one in temperature at almost all scales, does not mean that the polarization does not contribute to the overall signal sensitivity. In fact, $\langle B^{\rm a}B^{\rm a}\rangle$ gives a much cleaner channel to look for non-SM effects, due to the small amplitude of lensing B-modes, making it possible to distinguish a smaller signal compared to the $\langle T^{\rm a}T^{\rm a}\rangle$ channel.

5.3.2 CMB temperature-LSS cross-correlation

Since axion-induced screening occurs inside LSS, the cross-correlation of the CMB with a tracer of LSS will be more sensitive than the CMB auto-correlations discussed in the previous section. On one hand, the cross-correlation contains only one power of the small coupling squared $g_{\rm a\gamma\gamma}^2$ - compared to the double insertion in the auto-correlation functions - which translates into a more favourable scaling of the sensitivity with the highest accessible multipole $\ell_{\rm max}$, as can be seen from the signal-to-noise ratio described below in Sec. 5.4.2 (see also App. B.10 for a qualitative order-of-magnitude comparison of the sensitivity of different observables). Additionally, having a template based on the distribution of LSS helps in the detection of a weak signal. Finally, cross-correlation minimizes the impact of uncorrelated foregrounds and systematics that contribute strongly to the individual auto-spectra, increasing the sensitivity of the measurement. The simple cross-correlation between the axion-induced polarization signal and LSS vanishes due to the random orientation of the magnetic field in different domains (there are, however, non-vanishing higher-point functions that will be described in Sec. 5.3.3). Therefore, here we

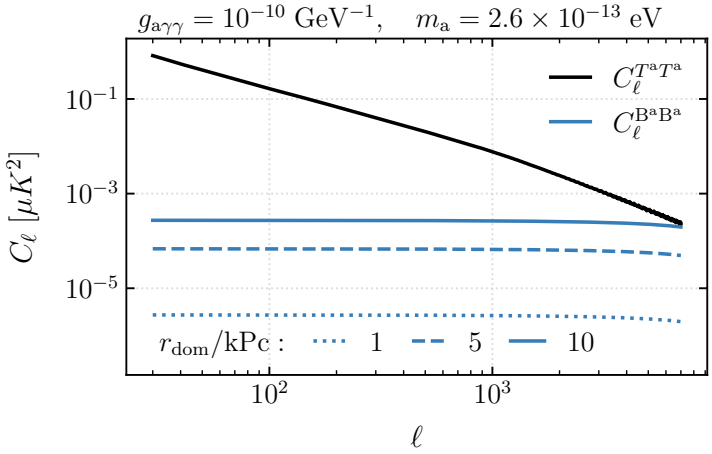

Figure 5.4: Axion-screening induced CMB power spectra for fixed axion parameters as labeled and reference frequency $\omega/(2\pi) = 145$ GHz. The temperature power spectrum $C_\ell^{T^aT^a}$ is given in (5.26) and shown by the black solid line, while the polarization power spectrum $C_\ell^{B^aB^a}$ is given in (5.27) and shown by the blue dotted, dashed, and solid lines, for magnetic domain size of $r_{dom} = 1, 5$, and 10 kpc, respectively. The amplitude of the power spectrum scales as r_{dom}^2, as expected. The ratio between the temperature and polarization power spectra at fixed ℓ changes depending on the axion mass. In general, for the range of magnetic domain sizes chosen, the temperature power spectrum is stronger on all scales. This is in part due to the fact that the polarization auto-correlator does not receive inter-halo contributions proportional to the linear matter power spectrum. On small scales of $\ell > \mathcal{O}(10^3)$, where the 1-halo term dominates, the polarization signal can be competitive with the temperature, especially at low axion mass where there is no redshift-dependent suppression from C_ℓ^{pol} (see (5.28)).

focus on the two-point correlation function between the axion-induced temperature signal and LSS,

$$\langle T^{\rm a}(\hat{n}_1) g(\hat{n}_2) \rangle \,, \tag{5.29}$$

where $T^{\rm a}(\hat{n})$ is defined in (5.14) and $g(\hat{n})$ represents the projected galaxy overdensity field. Since the axion-induced screening signal in the CMB is projected along the line-of-sight and receives contribution from a wide range of redshifts, we do not require precise redshift measurements. The ideal tracer has a high number-density, to leverage both the clustering signal on large angular scales and the small-scale structure within halos. In the following, we adopt the unWISE galaxy sample [271, 272] as our fiducial tracer. We focus on the blue sample, which contains $\sim$ 50 million objects over roughly 60% of the sky with a well-characterized redshift distribution. The galaxy field template $g(\hat{n})$ is defined as an overdensity in the counts of a galaxy survey, weighted by the fractional number of galaxies in the sample per redshift bin and integrated over the line-of-sight [273, 274]:

$$g(\hat{n}) = \int {\rm d}z \, \frac{{\rm d}N_g}{{\rm d}z} \frac{n_g(z,\hat{n}) - \bar{n}_g(z)}{\bar{n}_g(z)}, \tag{5.30}$$

where $\bar{n}_g$ is the mean number density of galaxies per redshift bin and ${\rm d}N_g/{\rm d}z$ is the galaxy redshift distribution normalized so that $\int {\rm d}z \frac{{\rm d}N_g}{{\rm d}z} = 1$. To model how the observed galaxies populate the underlying dark matter halo distribution, we use the Halo Occupation Distribution (HOD) [275] as described in Ref. [276]. The full details of the HOD can be found in App. B.6; here we report only the resulting galaxy field auto power-spectrum and the cross-correlation with the axion-induced signal.

Within this framework, the unWISE galaxy sample is modeled by a population of galaxies at the center of their dark matter halo, 'centrals', and a population of 'satellite' galaxies distributed according to the dark matter density profile in each halo. Following Ref. [277], the result is

$$\begin{aligned} C_\ell^{gg} &= C_\ell^{gg,\,1-{\rm halo}} + C_\ell^{gg,\,2-{\rm halo}} + A_{\rm SN}, \\ C_\ell^{gg,\,1-{\rm halo}} &= \int {\rm d}z \frac{\chi(z)^2}{H(z)} \int {\rm d}m \, n(z,m) \left\langle |u_\ell^g(z,m)|^2 \right\rangle, \\ C_\ell^{gg,\,2-{\rm halo}} &= \int {\rm d}z \frac{\chi(z)^2}{H(z)} \left[\int {\rm d}m \, n(z,m) b(z,m) u_\ell^g(z,m) \right]^2 P^{\rm lin}\left(\frac{\ell + \frac{1}{2}}{\chi(z)}, z \right), \end{aligned} \tag{5.31}$$

where $u_\ell^g(z,m)$ describes the mean distribution of galaxies and their distribution inside halos, $\left\langle |u_\ell^g(z,m)|^2 \right\rangle$ is the second moment of the distribution, and $A_{\rm SN}$ denotes the shot noise

contribution and is an empirically determined parameter of the model. These functions depend on the details of the HOD, and are defined in App. B.6.

The cross-power between the axion-induced screening temperature anisotropies and unWISE galaxies is a straightforward generalization of the galaxy-galaxy power spectrum. Noting that $T_\ell^{\rm a}(z,m) \propto \tau_\ell^{\rm a}(z,m)$, the cross-power is

$$\begin{aligned} C_\ell^{T^{\rm a}g} &= \frac{1-e^{-x}}{x}\bar{T}\left[C_\ell^{g\tau,\,1-{\rm halo}} + C_\ell^{g\tau,\,2-{\rm halo}}\right], \\ C_\ell^{g\tau,\,1-{\rm halo}} &= \int {\rm d}z \frac{\chi(z)^2}{H(z)} \int {\rm d}m\, n(z,m)\tau_\ell^{\rm a}(z,m)u_\ell^g(z,m), \\ C_\ell^{g\tau,\,2-{\rm halo}} &= \int {\rm d}z \frac{\chi(z)^2}{H(z)} \left[\prod_{i=1,2}\int {\rm d}m_i\, n(z,m_i)b(z,m_i)\right] \tau_\ell^{\rm a}(z,m_1)u_\ell^g(z,m_2)P^{\rm lin}\left(\frac{\ell+\frac{1}{2}}{\chi(z)},z\right). \end{aligned} \tag{5.32}$$

The cross-power depends on the redshift overlap in the axion-induced optical depth and the distribution of unWISE galaxies described by $u_\ell^g(z,m)$. As discussed in App. B.6, $u_\ell^g(z,m)$ is proportional to the redshift distribution of galaxies in the unWISE blue sample, which spans the range $0.2 \lesssim z \lesssim 0.8$. Comparing with Fig. 5.1, the overlap is greatest at low axion mass $m_{\rm a}$. The strength of the auto- and cross-correlations depends on the statistical power of the halo model: when the distribution of structure is known to high precision, the signal-to-noise of the estimator is enhanced. In principle, the best sensitivity is achieved when the location of all halos and distribution of galaxies therein is known.

An example of the axion-induced cross-correlation power spectra $C_\ell^{T^{\rm a}g}$ at fixed coupling constant $g_{{\rm a}\gamma\gamma}$ is shown in Fig. 5.5 for three different values of the axion mass $m_{\rm a}$. For $\ell < 1000$, the curves follow the linear matter power spectrum $P_\ell^{\rm lin}$ (through the 2-halo term) and have similar shapes but different amplitudes. On smaller angular scales, where the 1-halo term dominates, the cross-spectra hold information about the resonance scale characteristic of each mass.

Fig. 5.5 also shows the galaxy auto-spectra corresponding to the full unWISE sample C_ℓ^{gg} defined in (5.31), as well as for central galaxies only $C_\ell^{gg,{\rm cen}}$ defined in (B.110). As explained in the next section, when deriving expressions for the axion-induced bispectrum, we use a centrals-only galaxy template to simplify the calculation. This simplification should be a conservative choice, which only mildly affects the forecasted sensitivity to the axion coupling strength. Notice that on large-scales both curves trace the matter power spectrum, but with a slightly larger amplitude for the full galaxy power spectrum; the reason for this discrepancy is that both the number of satellite galaxies and the bias function are larger for heavier halos, while the number of centrals is constant above a

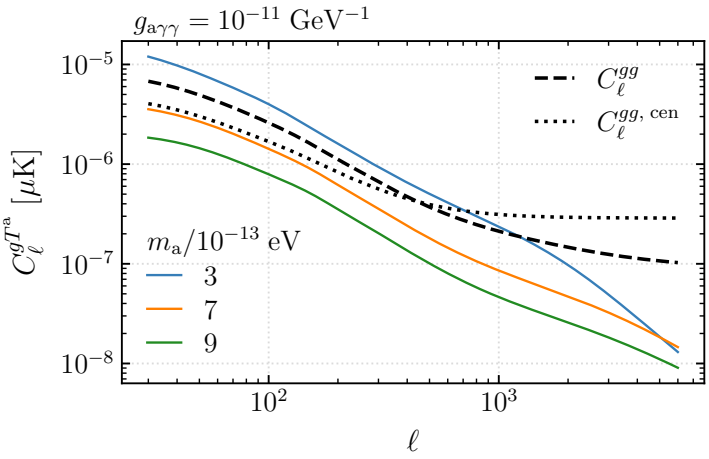

Figure 5.5: Cross-correlation of the axion-induced CMB temperature screening with a tracer of LSS for fixed photon-axion coupling as labeled and reference frequency $\omega/(2\pi) = 145$ GHz. The signal angular cross-power spectrum is defined in (5.32) and shown by the blue, orange, and green solid lines for $m_a = 3, 7$, and 9×10^{-13} eV, respectively. On large scales, the main difference in the three spectra is the amplitude, while the spectral shape is dictated by the proportionality with the linear matter power spectrum $P_\ell^{\rm lin}$. On small scales, the spectra hold some information about the conversion radius $r_{\rm res}$ characteristic for each axion mass. Also shown are the galaxy-galaxy and centrals-only power-spectra C_ℓ^{gg} (black dashed line) and $C_\ell^{gg,\,\rm cen}$ (black dotted line), defined in (5.31) and (B.110) respectively. On large-scales, the galaxy auto-spectra trace the linear matter power spectrum, while at small scales they asymptote to the shot noise terms ($A_{\rm SN}$ and $A_{\rm SN}^{\rm cen}$). The HOD parameters used to model the properties of the galaxies are the best-fit values from the unWISE blue catalog obtained in Ref. [276] (see App. B.6).

certain mass threshold; therefore, removing satellites removes a preferential weighting of large-bias halos, in turn reducing the amplitude of the 2-halo term (cf. definitions (5.31) and (B.110)). At small scales, on the other hand, $C_\ell^{gg,\mathrm{cen}}$ becomes larger due to a larger shot noise term in a sample with fewer galaxies, $A_{\mathrm{SN}}^{\mathrm{cen}} > A_{\mathrm{SN}}$.

5.3.3 CMB polarization and LSS bispectrum

Similarly to the CMB-LSS cross-correlation observable constructed in the previous section for the axion-induced temperature map, it is possible to leverage the fact that the polarization signal originates in structure. In this case, however, the leading-order non-vanishing observable is the three-point function containing two polarization fields and one galaxy field. The simple cross-correlation vanishes because it has only one insertion of the polarization field. Therefore we are interesting in obtaining the signal contribution to

$$\langle (Q \pm iU)^{\mathrm{a}}(\hat{n}_1)(Q \pm iU)^{\mathrm{a}}(\hat{n}_2) g(\hat{n}_3) \rangle \,, \tag{5.33}$$

where $(Q \pm iU)^{\mathrm{a}}(\hat{n})$ is defined in (5.15) and $g(\hat{n})$ represents the projected galaxy overdensity field as defined in (5.30). To simplify the calculation of the bispectrum, we only include galaxies at the center of each halo, neglecting satellite galaxies. The HOD modeling with centrals-only is outlined in App. B.6 and the corresponding auto-power spectrum is given in (B.110) and shown in Fig. 5.5.

Since the polarization signal is non-zero only for small angular separations that fall within the same magnetic field domain (within the same halo), the three point function above will receive a non-vanishing contribution only for $|\hat{n}_1 - \hat{n}_2| \lesssim \theta_{\mathrm{dom}}(\chi)$. There are then two contributions to (5.33): a 1-halo term, where $\hat{n}_3$ is taken to be at the center of a halo while $\hat{n}_1$ and $\hat{n}_2$ are two points in the same halo, and a 2-halo term, where $\hat{n}_3$ is taken to be at the center of a different halo than $\hat{n}_1$ and $\hat{n}_2$. Since the magnetic domain size is typically much smaller than both the characteristic resonance conversion radius and the separation between two halos, both 1-halo and 2-halo terms are dominated by squeezed configurations of the bispectrum. Similar to the case of the auto-correlation functions, the 1-halo term will be sensitive to the small-scale shape of the halos, while the 2-halo term holds information about the modulation of small-scale power by the density field as traced by LSS. We find the the two terms are comparable, but the 2-halo terms slightly dominates across the full range of axion masses considered.

The full derivation is presented in App. B.7 and here we report the final expressions for the angle-averaged bispectrum, which is the quantity appearing in the signal-to-noise ratio

used for the sensitivity forecast. In terms of the B-mode (the same expression applies to the E-mode), the result is

$$\mathcal{B}^{B^{\rm a}B^{\rm a}g}_{\ell\ell'\ell''} = \mathcal{B}^{B^{\rm a}B^{\rm a}g,\,1-{\rm halo}}_{\ell\ell'\ell''} + \mathcal{B}^{B^{\rm a}B^{\rm a}g,\,2-{\rm halo}}_{\ell\ell'\ell''}, \tag{5.34}$$

$$\begin{aligned}\mathcal{B}^{B^{\rm a}B^{\rm a}g,\,1-{\rm halo}}_{\ell\ell'\ell''} =& \sqrt{\frac{(2\ell+1)(2\ell'+1)(2\ell''+1)}{4\pi}} \begin{pmatrix} \ell & \ell' & \ell'' \\ +2 & -2 & 0 \end{pmatrix} e_{\ell\ell'\ell''} \times \\ & \left(\frac{1-e^{-x}}{x}\bar{T}\right)^2 \int {\rm d}z\, \frac{\chi(z)^2}{H(z)} \int {\rm d}m\, n(\chi,m) u^{g,{\rm cen}}(\chi,m) \times \\ & \sum_{LL'} \left(W^{000}_{\ell''LL'}\right)^2 \tau^{\rm a}_{L0}(\chi,m) \tau^{\rm a}_{L'0}(\chi,m) \frac{\mathcal{C}^{\rm pol}_{\ell}(\chi) + \mathcal{C}^{\rm pol}_{\ell'}(\chi)}{2},\end{aligned} \tag{5.35}$$

$$\begin{aligned}\mathcal{B}^{B^{\rm a}B^{\rm a}g,\,2-{\rm halo}}_{\ell\ell'\ell''} =& \sqrt{\frac{(2\ell+1)(2\ell'+1)(2\ell''+1)}{4\pi}} \begin{pmatrix} \ell & \ell' & \ell'' \\ +2 & -2 & 0 \end{pmatrix} e_{\ell\ell'\ell''} \times \\ & \left(\frac{1-e^{-x}}{x}\bar{T}\right)^2 \int {\rm d}z\, \frac{\chi(z)^2}{H(z)} \left[\prod_{i=1,2} \int {\rm d}m_i\, n(z,m_i) b(z,m_i)\right] u^{g,\,{\rm cen}}(\chi,m_2) \times \\ & \sum_{LL'} \frac{\left(W^{220}_{\ell L'L}\right)^2 + \left(W^{220}_{\ell' L'L}\right)^2}{2} \left[\tau^{\rm a}_{L0}(\chi,m_1)\right]^2 \mathcal{C}^{\rm pol}_{L'}(\chi)\, P^{\rm lin}\left(\frac{\ell''+\frac{1}{2}}{\chi(z)}, z\right),\end{aligned} \tag{5.36}$$

where $W^{220}_{\ell L'L}$ is defined in (B.99) and $e_{\ell\ell'\ell''}$ in (B.120) and all the other quantities have been introduced in Sec. 5.3.1- 5.3.2. Since we have included central galaxies only in our LSS tracer for the bispectrum calculation, our prediction of the signal is conservative, and additional contributions are expected from satellites galaxies in the sample. The above bispectrum contribution to the signal have been derived in the limit of the squeezed triangles $\ell, \ell' \gg \ell''$ and are symmetric under the exchange of $\ell \leftrightarrow \ell'$, as expected.

The axion-induced n-point statistics derived above will be used in the next section to estimate the sensitivity of Planck and CMB-S4 measurements, together with the unWISE galaxy catalog, to photon-axion couplings.

5.4 Sensitivity forecasts

In this section, we forecast the ability of existing and near-term datasets to detect the axion-induced screening signal. We first assess how measurements of the CMB at multiple frequencies can be used to isolate the spectral dependence of the axion-induced screening

signal from foregrounds and the primary CMB. We then determine the sensitivity of the correlation functions described in the previous section to $g_{a\gamma\gamma}$ as a function of m_a for existing CMB data from Planck and the unWISE blue galaxy distribution, as well as for a future CMB experiment – CMB-S4 [206].

5.4.1 Isolating the axion-induced screening signal using CMB component separation

The multi-frequency information available in a CMB experiment can be used to enhance the axion-induced screening signal relative to the primary CMB and astrophysical foregrounds. Similar to the approach taken in Chapter 4, we estimate the ability of the harmonic internal linear combination (ILC) method [237] to isolate this signal. The ILC is a weighted sum of individual frequency maps in harmonic space, with weights chosen to minimize the variance of a signal with known frequency dependence. The ability of this method to isolate the axion-induced screening signal is limited by the available frequency channels, instrumental noise, and the spectral dependence/amplitude of foregrounds. Inevitably, there will be some residual with which the signal must compete. We estimate the residual contribution to the ILC for two CMB experiments: the completed Planck satellite mission and CMB-S4. The assumed resolution of each frequency channel, quantified by the width of a Gaussian beam, for each experiment is recorded in the top two panels of Table 4.2 as follows: the top panel shows the frequency bins and beam parameters used for the Planck forecast, while the middle panel shows frequencies, sensitivity and resolution parameters for the CMB-S4 V3R0 configuration. Recall that ν denotes the photon frequency in GHz such that $\nu \equiv \omega/2\pi$.

The input to the ILC is the full $N_{\rm freq} \times N_{\rm freq}$ covariance matrix between the power spectra measured in $N_{\rm freq}$ channels:

$$\mathbf{C}_\ell = \mathbf{\Omega}^{-1}\mathbf{C}_\ell^{TT} + \mathbf{e}\mathbf{e}^\dagger \zeta(\omega_0)^2 C_\ell^{T^{\rm a}T^{\rm a}}(\omega = 1) + \mathbf{\Omega}^{-1}\left(\mathbf{N}_\ell^{TT}(\omega)/\mathbf{G}_\ell(\omega)\right), \tag{5.37}$$

where $\mathbf{C}_\ell^{TT}$ is the primary blackbody CMB angular power spectrum,$\mathbf{C}_\ell^{T^{\rm a}T^{\rm a}}$ was defined in (5.26), $\mathbf{N}_\ell^{TT}$ is the overall noise covariance (defined to include instrumental noise and astrophysical foregrounds) and $\mathbf{G}_\ell$ the beam model. We also used the notation $\zeta(\omega) \equiv \left(1 - e^{-x(\omega)}\right)\omega/x(\omega)$ for $x \equiv \omega/\bar{T}$. The second term in (5.37) represents the axion-induced screening contribution in temperature. This term can be neglected in the small-signal limit we are interested in when computing the ILC. Equivalent expressions can be written for the E and B-mode polarization spectra. We also defined the matrix $\mathbf{\Omega^{-1}}$ with entries $\Omega_{ij}^{-1} = \zeta(\omega_0)^2/\left(\zeta(\omega_i)\zeta(\omega_j)\right)$, $\mathbf{e} = (1, 1, \ldots, 1)$ which characterize the frequency dependence

of the axion-induced screening signal. The ILC method identifies the linear combination of harmonic coefficients that minimizes the variance of a map with the target frequency dependence. This residual is given by

$$\tilde{N}_\ell^{T^{\rm a}T^{\rm a}} = \mathbf{w}_\ell^\dagger \cdot \left(\mathbf{\Omega}^{-1}\mathbf{C}_\ell^{TT} + \mathbf{\Omega}^{-1}\mathbf{N}_\ell^{TT}/\mathbf{G}_\ell\right) \cdot \mathbf{w}_\ell, \tag{5.38}$$

where the weights $\mathbf{w}_\ell$ satisfy

$$\mathbf{w}_\ell = \frac{(\mathbf{C}_\ell)^{-1}\,\mathbf{e}}{\mathbf{e}^\dagger\,(\mathbf{C}_\ell)^{-1}\,\mathbf{e}}. \tag{5.39}$$

To evaluate the residual (5.38) we need the lensed primary CMB contribution $\mathbf{C}_\ell^{TT}$, which is independent of experiment and computed using CAMB [69] with cosmological parameters described in Sec. 5.3.1. Additionally, we need a model for the noise covariance $\mathbf{N}_\ell^{TT}$. We refer the reader to App. B.8 for a complete description of our methodology. For Planck, we estimate $\mathbf{N}_\ell^{TT}$ from publicly available CMB-subtracted maps from the Public Data Release 3 [278] (PR3) at 30, 44, 70, 100, 143, 217, and 353 GHz (we do not include the strongly foreground-dominated 545 and 857 GHz channels in our analysis; we confirmed that including them does not change our results). The entries of $\mathbf{N}_\ell^{TT}$ are simply the auto and cross-power spectra of these maps after applying a galactic cut retaining 40% of the sky. An analogous analysis is performed for polarization. For CMB-S4, the low-ℓ spectra are expected to be the same as those measured by Planck. We fit the low-ℓ CMB-subtracted spectra from Planck to a power law. We add this component to a noise power spectrum incorporating atmospheric effects, with parameters appropriate for CMB-S4 (see Table 4.2). On small-angular scales and at high frequencies, the cosmic infrared background (CIB) is expected to be the dominant foreground. We use simulated CIB maps from the Websky suite of simulations [279] to compute the contributions to $\mathbf{N}_\ell^{TT}$ at high-ℓ. For polarization, we include the Planck low-ℓ power-law spectra and instrumental noise only. For both Planck and CMB-S4, we chose a baseline frequency $\omega/(2\pi) = 145$ GHz, and assume 40% sky coverage in the forecasts below, together with a maximum resolution of $\ell_{\rm max} = 3000$ for Planck and $\ell_{\rm max} = 6000$ for S4.

For both experiments, the frequencies in the $\sim 100 - 200$ GHz range are weighted most strongly in the ILC, as they have the lowest overall noise, and they are favoured by the increase of the axion signal with frequency. The highest frequencies, i.e. 353 GHz for Planck and 278 GHz for S4, suffer from large foreground contamination (mainly CIB) and are penalized. Together with frequencies below ~ 70 GHz, these channels do not contribute significantly to the sensitivity. Fig. 5.6 illustrates the total noise level for the ILC used in our CMB-S4 forecast. As mentioned, the scaling of the axion-induced screening signal with frequency causes the ILC residuals $\tilde{N}_\ell^{T^{\rm a}T^{\rm a}}$ and $\tilde{N}_\ell^{B^{\rm a}B^{\rm a}}$ to trace the least noisy and highest-frequency channels.

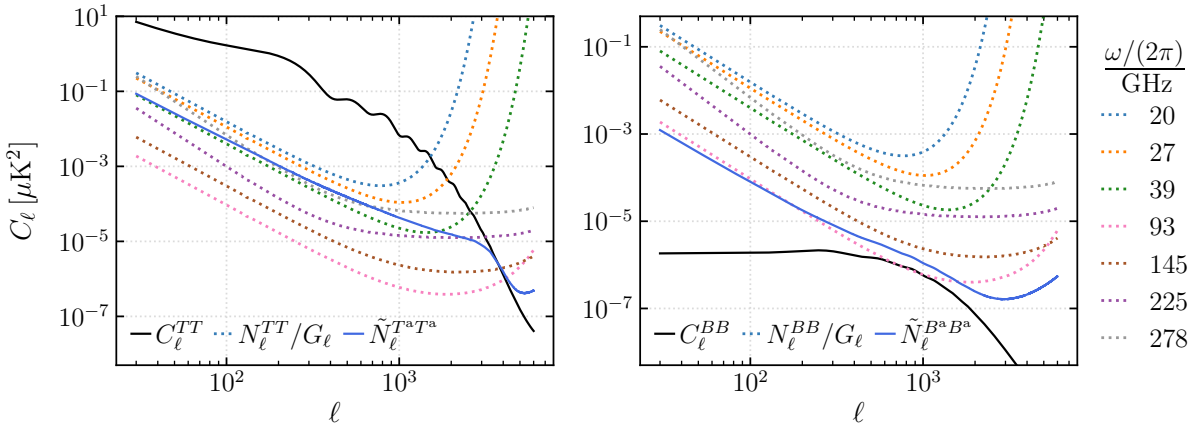

Figure 5.6: Comparison between lensed blackbody CMB and noise model before and after implementing the ILC for CMB-S4 temperature (left panel) and polarization (right panel). Without an ILC procedure, the axion-induced screening signal competes against the sum of the measured CMB C_ℓ^{XX} (solid black) and our estimate for the noise model in each frequency channel N_ℓ^{XX}/G_ℓ (coloured dotted), where $X \in \{T, E, B\}$. The residual noise post-ILC is $\tilde{N}_\ell^{X^aX^a}$ (solid blue). Note that its amplitude is proportional to the Ω^{-1} matrix defined in the text. In the temperature case shown on the left, at our chosen baseline frequency $\omega/(2\pi) = 145$ GHz, the ILC removes three orders of magnitude in the total noise amplitude (cf. the sum of the dotted lines with the black line versus the blue line). For polarization, the ILC simply minimizes the total noise so that it follows the optimal (i.e. least noisy) channel at any given scale.

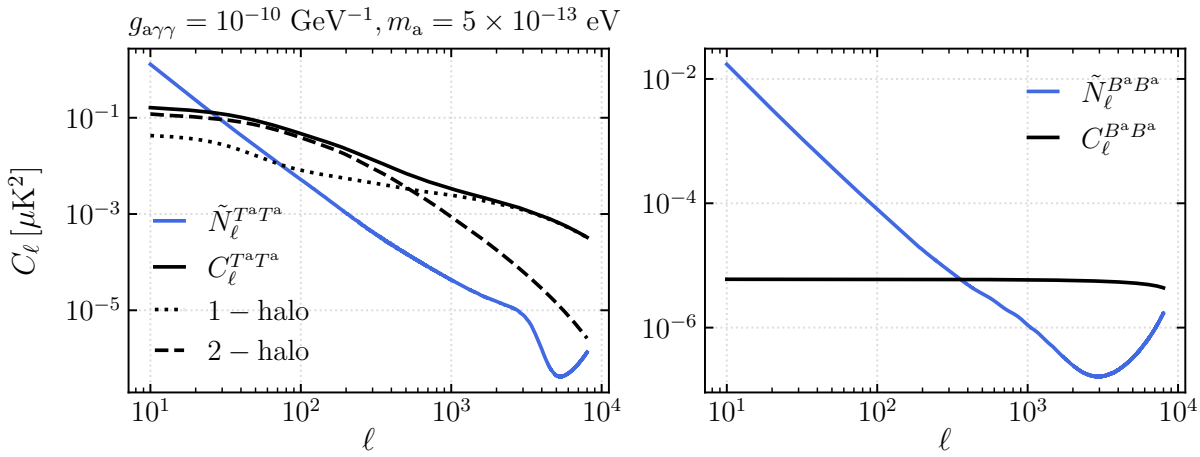

Figure 5.7: Axion-induced auto-correlation functions for temperature (black lines, left) and polarization (black line, right) compared to the corresponding ILC residual noise (blue lines). The signal amplitude is calculated for fixed axion parameters as labeled; both signal and noise are evaluated at the reference frequency $\omega/(2\pi) = 145$ GHz. The noise residuals are given in (5.37) and correspond to CMB-S4 observations. The signal is clearly detectable in both channels for this choice of parameters and can be rescaled as $g_{a\gamma\gamma}^4$ to infer the magnitude at different couplings. For temperature, we show the total $C_\ell^{T^aT^a}$ (solid black) as well as the 1-halo (dotted black) and 2-halo (dashed black) terms individually – see Eqs. (5.24) and (5.26). The signal-to-noise ratio is driven by small angular scales (high-ℓ modes), where the 1-halo term dominates. For polarization B-modes, the signal contains only the 1-halo term – see (5.27) – and is above the noise level on small angular scales.

In Fig. 5.7 we compare the ILC residual noise in temperature and polarization B-mode with a sample curve for each auto-correlation axion signal $C_\ell^{T^{\rm a}T^{\rm a}}$ and $C_\ell^{B^{\rm a}B^{\rm a}}$ respectively, at fixed coupling and axion mass. The ratio between the axion-induced dark screening signal and residual noise is most favourable on small angular scales, $\ell > 1000$, where most of the sensitivity of a CMB experiment will come from.

5.4.2 Results

To determine the sensitivity of the two- and three-point correlation functions described above to the coupling constant $g_{\rm a\gamma\gamma}$ as a function of $m_{\rm a}$, we assume that the measurements follow a Gaussian likelihood and are compatible with the hypothesis of no axion-signal, i.e. $g_{\rm a\gamma\gamma} = 0$. For a given axion mass, all the observables considered in this Chapter have a simple dependence on the coupling $\propto g_{\rm a\gamma\gamma}^n$, with $n = 2$ or 4. The likelihood in this case takes the form $\langle \log \mathcal{L} \rangle \propto g_{\rm a\gamma\gamma}^{2n}$. Following a Bayesian approach and adopting a flat prior for $g_{\rm a\gamma\gamma} \geq 0$, we derive the posterior over $g_{\rm a\gamma\gamma}$ in App. B.11. To define the sensitivity of a measurement, we compute the value of $g_{\rm a\gamma\gamma}$ containing 68% of the posterior probability (for the Gaussian case, equivalent to a 1-σ bound). The best sensitivity would be given by summing over all observables that contain an axion signal. However, to understand which one is the most sensitive, here we consider them separately.

The results for CMB auto-correlation functions $C_\ell^{X^{\rm a}X^{\rm a}}$, with $X \in \{T, E, B\}$ – see (5.26) and (5.27), CMB temperature-LSS cross-correlation function $C_\ell^{T^{\rm a}g}$ – see (5.29), and CMB polarization-LSS bispectrum $\mathcal{B}^{B^{\rm a}B^{\rm a}g}$ – see (5.34), are

$$\sigma_{g_{\rm a\gamma\gamma}} \simeq 0.7 \left(\sigma_{4,XX}\right)^{1/4}, \qquad \sigma^2_{4,XX} = \left\{ f_{\rm sky} \sum_\ell \frac{2\ell+1}{2} \left[\frac{C_\ell^{X^{\rm a}X^{\rm a}}(g_{\rm a\gamma\gamma}=1)}{\tilde{N}_\ell^{X^{\rm a}X^{\rm a}}} \right]^2 \right\}^{-1}, \tag{5.40}$$

$$\sigma_{g_{\rm a\gamma\gamma}} \simeq 0.76 \left(\sigma_{2,Tg}\right)^{1/2}, \qquad \sigma^2_{2,Tg} = \left\{ f_{\rm sky} \sum_\ell (2\ell+1) \frac{\left[C_\ell^{T^{\rm a}g}(g_{\rm a\gamma\gamma}=1) \right]^2}{C_\ell^{gg} \tilde{N}_\ell^{T^{\rm a}T^{\rm a}}} \right\}^{-1}, \tag{5.41}$$

$$\sigma_{g_{\rm a\gamma\gamma}} \simeq 0.7 \left(\sigma_{4,BBg}\right)^{1/4}, \qquad \sigma^2_{4,BBg} = \left\{ f_{\rm sky} \sum_{\ell\ell'\ell''} \frac{1}{2} \frac{\left[\mathcal{B}_{\ell\ell'\ell''}^{B^{\rm a}B^{\rm a}g}(g_{\rm a\gamma\gamma}=1) \right]^2}{\tilde{N}_\ell^{B^{\rm a}B^{\rm a}} \tilde{N}_{\ell'}^{B^{\rm a}B^{\rm a}} C_{\ell''}^{gg,\,\rm cen}} \right\}^{-1}. \tag{5.42}$$

where the derivation of the expressions for $\sigma_{g_{\rm a\gamma\gamma}}$ is presented in App. B.11. In the equations above, $f_{\rm sky}$ represents the fraction of the sky covered and is fixed to 0.4 throughout.

The CMB noise terms $\tilde{N}^{X^{\rm a}X^{\rm a}}$ are the corresponding ILC-minimized noise levels defined in (5.38), while the LSS noise terms C_ℓ^{gg} and $C_{\ell''}^{gg,\,\rm cen}$ correspond to the unWISE galaxy auto-power spectra described in App. B.6 and given in (5.31) (all) and (B.110) (centrals-only). Here we have neglected the noise contribution to $\langle T^{\rm a} g\rangle$ and $\langle B^{\rm a} g\rangle$, but we note that residual foregrounds in the component-separated CMB, in particular the CIB, have non-negligible correlation with unWISE galaxies [280], which should be taken into account in a data analysis. The factor of 1/2 in the signal-to-noise ratio of the bispectrum in (5.42) comes from having two indistinguishable $B^{\rm a}$ fields (see e.g. Ref. [238] for an overview).

From Eqs. (5.40), (5.41) and (5.42), it can be seen that the sensitivity to the photon-axion coupling from CMB auto-correlation functions and the bispectrum scale as signal-to-noise ratio squared to the negative power of 1/8, while for CMB temperature-galaxy cross-correlation there is a negative power of 1/4. For this reason, the latter observable benefits more from the sum over many ℓ modes and will give the best sensitivity.

Fig. 5.8 and Fig. 5.9 show the sensitivities for the observables computed above in the $g_{\rm a\gamma\gamma}$-$m_{\rm a}$ parameter space for Planck and CMB-S4 respectively. We project that, with current data, our method can be complementary to existing astrophysical searches for axions, improving significantly compared to the most sensitive existing laboratory experiment, while future observations can marginally exceed the strongest astrophysical bounds currently in place.

Regarding auto-correlators, we show results for $X = T$ (blue dashed) and $X = B$ (orange dashed-dotted), since the signal for E and B modes is the same, but the latter has lower noise. The three auto-correlators can be easily combined by summing the individual signal-to-noise ratios squared, if one neglects TE correlations in the primary CMB, which provide a negligible contribution to the final answer. The signal-to-noise ratio for both temperature and polarization is dominated by very high ℓ-modes (see Fig. 5.7). This is different from the dark photon case considered in Chapter 4, where the ILC residual noise was more suppressed at large scales and the signal-to-noise ratio in TT was dominated by intermediate values of ℓ where the 2-halo term dominates. For polarization, the strength of the axion-induced signal is suppressed and sensitive to the small size of the coherent magnetic domains. We incorporate this uncertainty as a shaded band whose upper and lower bounds correspond to $r_{\rm dom} = 1$ and $r_{\rm dom} = 10\,{\rm kpc}$, respectively. Unless a significant component of the magnetic field is coherent on larger scales, the TT channel always dominates the total sensitivity of CMB auto-correlation functions (with the exception of axion masses at the lower boundary of the range considered, where TT and BB have comparable sensitivities).

As expected, the CMB temperature cross-correlation with the unWISE galaxy catalog

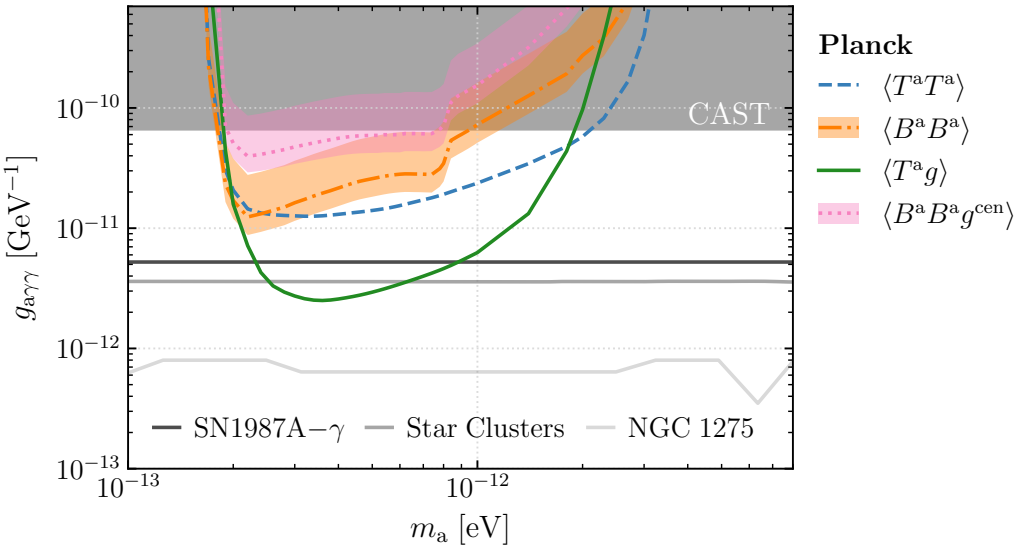

Figure 5.8: Forecasted sensitivity to the axion-photon coupling for Planck CMB measurements and the unWISE blue galaxy sample. The $\langle T^{\rm a}T^{\rm a}\rangle$ (blue dashed) and $\langle B^{\rm a}B^{\rm a}\rangle$ (orange dashed-dotted) sensitivities are obtained from (5.40) for $X = T$ and $X = B$, respectively. The strongest sensitivity is from $\langle T^{\rm a}g\rangle$ (solid green), which is obtained from (5.41). We also show the three point function (pink dotted) between CMB B-modes and the unWISE template for central galaxies, from (5.42). For both observables involving polarization fields, the coloured shaded band shows the effect of varying the magnetic domain size $r_{\rm dom}$ between 1 and 10 kpc, and the central line corresponds to 5 kpc. The bump in the orange and pink contours around $m_{\rm a} \approx 8 \times 10^{-13}$ is due to jumps in the magnetic field amplitude between discrete and wide bins in halo mass at a redshift $z \approx 1.3$; the effect does not appear in all the observables due to different weightings of each halo contribution in each case. Existing bounds on the photon-axion coupling (all in gray) are also shown and described in Fig. 5.2.

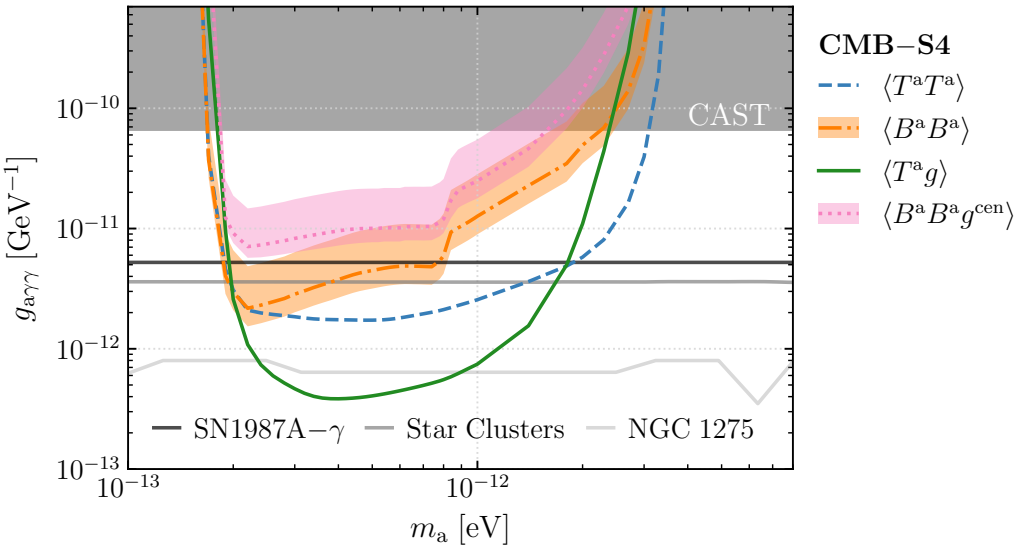

Figure 5.9: Same as Fig. 5.8, but assuming CMB-S4 measurements and the unWISE blue galaxy sample. The lower CMB instrumental noise level and higher angular resolution translate into an improved sensitivity by a factor of $\mathcal{O}(10)$ compared to the Planck forecast, with a similar hierarchy between different observables.

is more sensitive than CMB auto-correlators, as can be seen from the green solid lines in Fig. 5.8 and 5.9. The performance of this observable should improve as catalogs with larger number of galaxies become available. Additionally, with a catalog that has better redshift resolution, one could properly weight the cross-correlators in different redshift bins leveraging the redshift dependence of the photon-axion conversion at different axion masses (see Fig. 5.1) to further increase the signal-to-noise ratio. For CMB-S4 (Fig. 5.9), the increased sensitivity is enough to go beyond existing astrophysical constraints on $g_{a\gamma\gamma}$ by a factor of up to ≈ 1.7 for axion masses around $m_a \approx 4 \times 10^{-13}\,\mathrm{eV}$.

Finally, the pink dotted lines in Fig. 5.8 and 5.9 show the sensitivity of the CMB polarization-galaxy bispectrum $\langle B^a B^a g\rangle$. Similarly to the $\langle B^a B^a\rangle$ observable, the shaded region corresponds to magnetic field correlation lengths between $r_{\rm dom} = 1$ and $r_{\rm dom} = 10\,\mathrm{kpc}$. We find that the three-point function including a tracer of LSS does not improve the sensitivity compared to the CMB-only polarization auto-spectrum. Naively, this finding seems to contradict the expectation that the correlation with galaxies should enhance the signal-to-noise ratio, by properly weighting regions of the sky where the signal is expected. In practice, however, existing galaxy catalogs are incomplete and therefore the signal from the halos whose central galaxy is not seen by unWISE is effectively removed in $\langle B^a B^a g\rangle$. We checked that computing the bispectrum with a 'perfect' galaxy catalog that contains all central galaxies, improves the sensitivity beyond the auto-spectrum. Future surveys could be expected to lie between these two limiting cases. We find that the 1-halo and 2-halo terms in the bispectrum (see (5.35) and (5.36)) give a comparable contribution to the total signal, with the latter larger by a factor of a few. Note that, since we have included central galaxies only to simplify the derivation of the bispectrum, we are not leveraging the fact that axion-induced screening traces the angular profile of the satellite distribution and we are neglecting part of the signal, particularly at small scales where most of the signal-to-noise ratio should come from. If a signal is present in the data, it could therefore be larger than what is estimated here. Finally, we would like to stress the importance of having multiple correlators involving different maps of comparable sensitivity, in particular to confirm any possible future detection.

The results described in this section are consistent with, and complementary to the study of axion-induced polarization signals in clusters presented in Ref. [259]. There, the authors propose to use aperture photometry on identified clusters to detect the square of the polarization signal induced by resonant photon-axion conversion. The bispectrum $\langle B^a B^a g\rangle$ considered here should be similar in spirit to the stacking technique considered in Ref. [259][10]. However, it is difficult to perform a direct comparison due to differing assumptions about the coherence length of the magnetic field, a parameter which strongly affects

[10]For CMB-LSS bispectra involving the kinematic Sunyaev Zel'dovich contribution to CMB temperature,

the magnitude of the signal. Another crucial difference is that the correlators considered here target statistical signals, while aperture photometry or other filtering techniques target only the objects contributing most strongly to the signal. Arguably, the statistical signal is less sensitive to assumptions about the magnetic field and density profiles around individual halos, a primary uncertainty in any approach. Finally, the authors of Ref. [259] cite the difficulty in distinguishing extragalactic CMB foregrounds from the signal as a challenge for using temperature data in correlation with LSS. Although our analysis does not account for this correlation explicitly in the $\langle T^a g \rangle$ correlator, we note that it is possible to exactly deproject foregrounds with known spectral energy distribution (see e.g. Ref. [281]), and that the axion signal in temperature always corresponds to a reduction in intensity (in contrast to e.g. radio or CIB *emission*). An interesting future direction would be to study in more detail the synergy of n-point correlators and various filtering and stacking techniques for both the temperature and polarization axion-induced screening signals.

5.4.3 Extension to the case of effectively massless axions

So far, we have focused on axion masses where resonant conversion happens inside galactic halos. For lighter axion masses, between $2 \times 10^{-13}\,\mathrm{eV}$ and roughly $10^{-15}\,\mathrm{eV}$, the resonance condition can be met in regions outside the boundary of halos, where diffuse ionized gas traces the cosmic web. Independent of the exact location where resonant conversion occurs, axion-induced screening has the same frequency scaling and can therefore be searched for using the same maps obtained with the procedure outlined in Sec. 5.4.1, and cross correlating with the appropriate tracers of LSS.

For axions with even lighter masses, resonant conversion cannot happen in any astrophysical medium in the late universe (nor in the early universe, where densities were higher). However, non-resonant conversion can still occur in the presence of magnetic fields and we describe this scenario in some detail in App. B.9. In this case, the conversion probability still depends strongly on the photon plasma mass (scaling as m_γ^{-4}) and can therefore also give rise to axion-induced patchy screening. The axion-induced screening optical depth in the effectively massless axion case also has a characteristic dependence on the CMB photon frequency

$$\tau^{\mathrm{a}} \sim \omega^2, \tag{5.43}$$

it is possible to demonstrate that constraints from the bispectrum are formally equivalent to constraints from a variety of estimators [85]. A similar set of equivalences may be identified in the context of axion-induced screening as well.

and the ILC method [237] can be used to isolate anisotropies with this spectral dependence. In contrast to resonant conversion, for an effectively massless axion, the sign and size of the axion-induced screening signal strongly depends on the detailed properties of the inter-cluster gas density profile, and magnetic field power spectrum, neither of which are well-known. We provide an estimate for the amplitude of this signal in App. B.9, demonstrating that, in principle, anisotropies can improve upon existing constraints from the CMB monopole [249]. Future measurements sensitive to the distribution of ionized gas [282, 231] or numerical simulations could be used to build more reliable models of photon-axion conversion in this regime and therefore extend the region of axion masses probed by the CMB.

5.5 Discussion

In this Chapter, we projected the sensitivity of current and future CMB experiments combined with LSS surveys to probe light axions that couple to the photon. The axion-photon coupling leads to axion-induced screening of the CMB, which is imprinted in new spectral anisotropies in temperature and polarization. We computed the resulting temperature auto-correlation $\langle T^{\rm a} T^{\rm a} \rangle$, polarization auto-correlation $\langle B^{\rm a} B^{\rm a} \rangle$, CMB temperature-galaxy cross-correlation $\langle T^{\rm a} g \rangle$ and the polarization-galaxy bispectrum $\langle B^{\rm a} B^{\rm a} g \rangle$. The reach of the existing Planck and unWISE datasets on the axion photon coupling is significantly better than the current laboratory constraints from the axion helioscope CAST [242], and complement astrophysical constraints in the same mass range. Data from upcoming CMB-S4 experiment and future LSS surveys can further improve the sensitivity by up to about a factor of 2 in coupling compared to the best existing bounds, for $m_{\rm a} \approx 4 \times 10^{-13}\,{\rm eV}$.

The search we propose in this Chapter has different systematic uncertainties than other astrophysical probes. Similar to astrophysical searches that look for axion-induced irregularities on the X-ray spectra of AGN and quasars, our search also relies on the effect of photons oscillation into axions in the magnetic field of galaxies. Despite the effect being suppressed by the small frequency of CMB photons (see (5.4)), the high quality of existing and future measurements of CMB anisotropies provides a competitive probe of axions.

The cosmological search proposed in this Chapter is complementary to existing analysis based on X-ray observations of the super star cluster [137] (see also the recent search for X-ray emissions from M82 and M87 [243]), the cluster-hosted quasar H1821+643 [283], AGN NGC 1275 [139], and M87 [284], due to several crucial differences. First, the most sensitive observable considered here – $\langle T^{\rm a} g \rangle$ – is quite insensitive to the unknown magnetic field coherence length, as long as it is larger than $\mathcal{O}(\rm pc)$, because the relevant length scale

for us is the vacuum oscillation length; at higher photon frequency, the latter becomes larger and the conversion probability becomes sensitive to the smallest length scale in the problem, i.e. the size of the magnetic field domain. Second, although our approach also requires a modeling of the magnetized circumgalactic medium, similarly to the models of the intracluster magnetic fields used in [284, 139, 283], the axion-induced screening of CMB photons is a statistically *average* effect from many halos and therefore less affected by systematic uncertainties in the modeling of individual objects. Indeed, Ref. [285] suggested that the bound from NGC 1275 relaxes considerably if the intracluster magnetic field is completely ordered and the unknown contribution from the turbulent and ordered component should be interpreted as a large uncertainty on the constraint. Similar uncertainties also exist for searches for photon to axion conversion with CMB polarization with small numbers of tracers [256, 286, 259]. However, our proposal requires modeling of the magnetic field profiles of distant objects, which are much harder to measure directly compared to the MW magnetic field relevant for the limits obtained in Ref. [137]. Finally, the source property for our search, that is, the spectrum and the polarization of the blackbody CMB, is particularly well-known, compared to studies based on polarization of magnetized stars in [287, 288], and potentially also SN1987A-γ [289, 138] (see also [290]).

For the reasons we listed above, a study based on CMB temperature and polarization anisotropies and their correlations with LSS will complement the existing searches in placing robust constraints on the parameter space of axion like particles. In the event of a discovery, the search proposed in this Chapter can be used to narrow down the exact mass and coupling of the axion that gives rise to this observed signal, by taking advantage of the ℓ-dependence of the signal, the relative size of the different estimators, as well as tomographic information. This is certainly of particular importance for proposed laboratory searches of axion dark matter that are expanding their sensitivity to smaller axion masses [123, 291, 292, 293]. The methodologies in this Chapter can be adapted to different axion masses by correlating with different tracers with a wide range of plasma frequency, such as filaments and voids [294, 295, 296], the details of which we leave to future studies.

The cases presented in Chapter 4, Chapter 5 and App. B.9 are three different examples of a spectral energy distribution (SED) that can be produced by dark screening of the CMB. Whereas Thomson screening produces optical depth $\tau \sim \omega^0$, resonant photon to dark photon conversion produces $\tau \sim \omega^{-1}$, and resonant (non-resonant) photon to axion conversion produces $\tau \sim \omega^1$ ($\tau \sim \omega^2$). Obtaining these different dark screening temperature and polarization maps from current and future CMB observations, and studying their correlations with the underlying large-scale structure tracers, has the potential to reveal the existence of light bosons.

Chapter 6

Conclusions and Outlook

In this Chapter, we summarize the main findings of the work presented in this Thesis and highlight some compelling directions for future study.

In Part I, we introduced the first dynamical observables of bubble nucleation in first-order phase transitions. Specifically, we showed the existence of a clustering scale of nucleation sites. We further showed that bubbles form with a center-of-mass velocity at nucleation and do not arise from free field fluctuations. Instead, they are preceded by coherent structures we termed as oscillons. None of these observables are accessible in standard Euclidean theory due to their fundamentally dynamical nature. We constructed models for these observables starting from statistical and thermodynamic arguments, which generalize our results beyond the assumptions in our work. Our predictions are a function of two quantities: the potential function $V(\varphi)$ that the fields evolve under, and the initial conditions $\langle\varphi^2\rangle$. As long as these quantities are known, our observables can be included in modeling any theory supporting vacuum decay. Our observables should be considered in future studies of cosmological first-order phase transitions and laboratory tests thereof. We justify this statement with a few examples next.

The strongest paradigm shift introduced in Part I is the discovery of oscillons as precursors of bubble nucleation events. Oscillons are non-perturbative solutions that probe the shape of the potential away from the false vacuum and around the turning point in the potential. They represent coherent, long-lived structures that interact with the background field fluctuations and are subject to non-linear evolution. Empirically, oscillons have a spread of center-of-mass velocities, which depends on the statistics of fluctuations in the background field and parameters such as the effective field temperature in the false vacuum state. We also find that their number density correlates with the decay rate of the

false vacuum and prove that these structures source all nucleation events. Remarkably, the Euclidean sphaleron solution matches the shape of the average oscillon, which brings about an analytic prediction for these objects. In our study, oscillons provide a causal mechanism for the nucleation events. This implies that if a theory supports their formation, it becomes possible to predict where and when a bubble might form. Understanding under what circumstances the oscillons form and how they affect other observables, such as the decay rate, is a topic for future work. Also interesting would be to investigate whether oscillons may be relevant in the problem of the stability of the Higgs vacuum today.

Turning to the other two main observables introduced in Part I, we estimated in Chapter 3 that if electroweak baryogenesis were a first-order phase transition, given the predicted temperature at which it would occur, the magnitude of the characteristic center-of-mass bubble velocity would be strong enough to affect the outcome of the dynamics in the new phase of the field. We also argued in Chapter 2 that the clustering scale would change predictions of eternal inflation. Consequently, the existence of both a non-zero correlation function of nucleation sites and a non-zero velocity distribution at nucleation would impact the dynamics of the field undergoing the phase transition in the ensuing true vacuum state. For example, the center-of-mass velocity changes how the energy density is distributed inside the bubble walls by introducing a preferred direction of the bubble's expansion. The wall expansion is no longer spherically symmetric. Together with a clustering scale, these predictions challenge the assumptions of energy transfer in a first-order phase transition.

Because these observables depend on the global shape of the potential, if our dynamical description produces measurable observables, they open up a way to glean the properties of the initial false vacuum state of the decaying field. For example, if a next-generation gravitational wave detector such as LISA [158] finds a primordial component to a gravitational wave background, in the most optimistic scenario, it could place bounds on the three quantities: the decay rate, the clustering scale and the characteristic center-of-mass velocity. Combining all these quantities could constrain the space of theories that led to the phase transition and break degeneracies between different theories. Furthermore, it might tell us about the state of the decaying field before the phase transitions – for example, the temperature and mass in the false vacuum.

Our study of correlation functions and clustering was followed up by the work of Ref. [297], where it was argued that clustering in three dimensions can modify the spectral signature of a stochastic GW background by introducing a new scale to the problem, namely the inter-cluster separation. In the original formulation [179], the stochastic background has a spectral shape that peaks around the scale corresponding to the average distance between bubbles. Since Euclidean instanton methods can not be used to measure correlation functions during a phase transition, a uniform spatial distribution is usually as-

sumed. By introducing a clustering scale, the spectrum of GW would be influenced by two frequencies, and depending on their separation, the effect may be observationally relevant. Simultaneously, a non-zero center of mass velocity distribution would further modify the prediction. Of course, the full treatment of the propagation of waves through the cosmic expansion and interaction with plasma and structure would further change or even mask the signal. However, these are deterministic processes that can be incorporated into the model.

In Part II of this Thesis, we modeled the interaction of hidden sector particles with CMB photons inside LSS based on the property of photons acquiring an effective mass as they cross a charged plasma. In different astrophysical and cosmological environments, the dispersion relation of the photon (plasma frequency) is naturally scanned. The CMB photon can resonantly convert into dark photons via kinetic mixing or an axion in a magnetic field. Using our model, we showed that existing CMB data could increase the reach in the parameter space of the dark photon by orders of magnitude. At the same time, this method is competitive with the current strongest astrophysical bounds on the axion. Upcoming data will increase the sensitivity of both couplings by a further order of magnitude. The study in [298] has used the available Planck CMB and unWISE galaxy survey data to exclude the dark photon-photon coupling to $\varepsilon \approx 4 \times 10^{-8}$ over the mass range 10^{-13} eV $\lesssim m_{A'} \lesssim 10^{-11}$ eV, almost an order of magnitude stronger than previous limits, validating the predictions in this work. Soon, new public data releases in galaxy surveys and CMB data will allow us to explore even further.

In the future, other LSS tracers or secondary CMB observables, such as lensing and the SZ effect, can be used to infer information about the distribution of dark matter of smaller scales and up to higher redshifts, extending the range of hidden-sector particle masses that can be accessed with our method. For example, one can model the epoch of reionization to include the effect of screening up to a redshift $z \approx 15$. Likewise, future measurements of the 21-cm hydrogen line with line intensity mapping could provide a template for the gas distribution up to $z \approx 100$, extending our method to higher densities and larger dark photon and axion masses. The distribution and properties of cosmic voids can also be inferred from LSS data. Since their characteristic densities are below the average matter density, void maps would open up the search for dark matter in the range $< 10^{-13}$ eV.

References

[1] D. Pîrvu, J. Braden, and M. C. Johnson, *Bubble clustering in cosmological first order phase transitions*, *Phys. Rev. D* **105** (2022), no. 4 043510.

[2] D. Pîrvu, M. C. Johnson, and S. Sibiryakov, *Bubble velocities and oscillon precursors in first order phase transitions*, `arXiv:2312.13364`.

[3] D. Pîrvu, J. Huang, and M. C. Johnson, *Patchy screening of the cmb from dark photons*, *J. Cosmol. Astropart. Phys.* **2024** (2024), no. 01 019.

[4] C. Mondino, D. Pîrvu, J. Huang, and M. C. Johnson, *Axion-Induced Patchy Screening of the Cosmic Microwave Background*, `arXiv:2405.08059`.

[5] J. Braden, "1d-scalar." `https://github.com/jonathanbraden/1d-Scalar`, 2019.

[6] M. S. Madhavacheril, "hmvec." `https://github.com/simonsobs/hmvec`, 2019.

[7] C. R. Harris, K. J. Millman, S. J. van der Walt, et al., *Array programming with NumPy*, *Nature* **585** (Sept., 2020) 357–362.

[8] P. Virtanen, R. Gommers, T. E. Oliphant, et al., *SciPy 1.0: Fundamental Algorithms for Scientific Computing in Python*, *Nature Methods* **17** (2020) 261–272.

[9] W. R. Inc., "Mathematica, Version 14.0." https://www.wolfram.com/mathematica. Champaign, IL, 2024.

[10] Planck Collaboration, N. Aghanim, Y. Akrami, et al., *Planck 2018 results. VI. Cosmological parameters*, *Astron. Astrophys.* **641** (2020) A6.

[11] **DESI** Collaboration, A. G. Adame et al., *DESI 2024 VI: Cosmological Constraints from the Measurements of Baryon Acoustic Oscillations*, `arXiv:2404.03002`.

[12] A. G. Riess, L. M. Macri, S. L. Hoffmann, et al., *A 2.4% determination of the local value of the hubble constant**, *Astrophys. J.* **826** (2016), no. 1 56.

[13] D. J. Schwarz, C. J. Copi, D. Huterer, and G. D. Starkman, *Cmb anomalies after planck*, *Classical and Quantum Gravity* **33** (Aug., 2016) 184001.

[14] European Space Agency, *The Planck Legacy Archive*, 2015.

[15] A. Caputo, A. J. Millar, C. A. J. O'Hare, and E. Vitagliano, *Dark photon limits: A handbook*, *Phys. Rev. D* **104** (2021), no. 9 095029.

[16] C. O'HARE, *cajohare/axionlimits: Axionlimits*, July, 2020.

[17] S. Coleman, *The Fate of the False Vacuum. 1. Semiclassical Theory*, *Phys. Rev. D* **15** (1977) 2929–2936. [Erratum: Phys.Rev.D 16, 1248 (1977)].

[18] C. G. Callan, Jr. and S. Coleman, *The Fate of the False Vacuum. 2. First Quantum Corrections*, *Phys. Rev. D* **16** (1977) 1762–1768.

[19] A. Linde, *Fate of the false vacuum at finite temperature: Theory and applications*, *Phys. Lett. B* **100** (1981), no. 1 37–40.

[20] A. Linde, *Decay of the False Vacuum at Finite Temperature*, *Nucl. Phys. B* **216** (1983) 421. [Erratum: Nucl.Phys.B 223, 544 (1983)].

[21] J. Braden, M. C. Johnson, H. V. Peiris, A. Pontzen, and S. Weinfurtner, *New semiclassical picture of vacuum decay*, *Phys. Rev. Lett.* **123** (2019) 031601.

[22] J. M. Bardeen, J. R. Bond, N. Kaiser, and A. S. Szalay, *The statistics of peaks of Gaussian random fields*, *Astrophys. J.* **304** (1986) 15.

[23] V. Makhankov, G. Kummer, and A. Shvachka, *Novel pulsons (or stability from instability)*, *Physica D* **3** (1981), no. 1 344–349.

[24] M. A. Amin and D. Shirokoff, *Flat-top oscillons in an expanding universe*, *Phys. Rev. D* **81** (2010) 085045.

[25] M. C. Johnson and M. Kamionkowski, *Dynamical and Gravitational Instability of Oscillating-Field Dark Energy and Dark Matter*, *Phys. Rev. D* **78** (2008) 063010.

[26] M. Gleiser, E. W. Kolb, and R. Watkins, *Phase transitions with subcritical bubbles*, *Nucl. Phys. B* **364** (1991) 411–450.

[27] M. Gleiser, *Pseudostable bubbles*, *Phys. Rev. D* **49** (1994) 2978–2981.

[28] M. Gleiser and R. C. Howell, *Resonant nucleation*, *Phys. Rev. Lett.* **94** (2005) 151601.

[29] M. Gleiser, B. Rogers, and J. Thorarinson, *Bubbling the False Vacuum Away*, *Phys. Rev. D* **77** (2008) 023513.

[30] A. Aguirre, S. M. Carroll, and M. C. Johnson, *Out of equilibrium: understanding cosmological evolution to lower-entropy states*, *J. Cosmol. Astropart. Phys.* **02** (2012) 024.

[31] J. J. Blanco-Pillado, H. Deng, and A. Vilenkin, *Flyover vacuum decay*, *J. Cosmol. Astropart. Phys.* **12** (2019) 001, [arXiv:1906.09657].

[32] J. Braden, M. C. Johnson, H. V. Peiris, A. Pontzen, and S. Weinfurtner, *Mass renormalization in lattice simulations of false vacuum decay*, *Phys. Rev. D* **107** (2023) 083509.

[33] M. P. Hertzberg and M. Yamada, *Vacuum decay in real time and imaginary time formalisms*, *Phys. Rev. D* **100** (2019), no. 1 016011.

[34] M. P. Hertzberg, F. Rompineve, and N. Shah, *Quantitative Analysis of the Stochastic Approach to Quantum Tunneling*, *Phys. Rev. D* **102** (2020), no. 7 076003, [arXiv:2009.00017].

[35] A. Tranberg and G. Ungersbäck, *Bubble nucleation and quantum initial conditions in classical statistical simulations*, *J. High Energy Phys.* **09** (2022) 206.

[36] S.-J. Wang, *Occurrence of semiclassical vacuum decay*, *Phys. Rev. D* **100** (2019), no. 9 096019.

[37] L. Batini, A. Chatrchyan, and J. Berges, *Real-time dynamics of false vacuum decay*, *Phys. Rev. D* **109** (Jan, 2024) 023502.

[38] T. P. Billam, R. Gregory, F. Michel, and I. G. Moss, *Simulating seeded vacuum decay in a cold atom system*, *Phys. Rev. D* **100** (2019), no. 6 065016.

[39] T. P. Billam, K. Brown, and I. G. Moss, *Simulating cosmological supercooling with a cold atom system*, *Phys. Rev. A* **102** (2020), no. 4 043324.

[40] T. P. Billam, K. Brown, and I. G. Moss, *False-vacuum decay in an ultracold spin-1 Bose gas*, *Phys. Rev. A* **105** (2022), no. 4 L041301.

[41] T. P. Billam, K. Brown, A. J. Groszek, and I. G. Moss, *Simulating cosmological supercooling with a cold atom system. II. Thermal damping and parametric instability*, *Phys. Rev. A* **104** (2021), no. 5 053309.

[42] T. P. Billam, K. Brown, and I. G. Moss, *Bubble nucleation in a cold spin 1 gas*, *New J. Phys.* **25** (2023), no. 4 043028.

[43] A. C. Jenkins, J. Braden, H. V. Peiris, et al., *From the tabletop to the big bang: Analogue vacuum decay from vacuum initial conditions*, `arXiv:2307.02549`.

[44] J. Braden, M. C. Johnson, H. V. Peiris, and S. Weinfurtner, *Towards the cold atom analog false vacuum*, *J. High Energy Phys.* **07** (2018) 014.

[45] J. Braden, M. C. Johnson, H. V. Peiris, A. Pontzen, and S. Weinfurtner, *Nonlinear Dynamics of the Cold Atom Analog False Vacuum*, *J. High Energy Phys.* **10** (2019) 174.

[46] O. Fialko, B. Opanchuk, A. I. Sidorov, P. D. Drummond, and J. Brand, *Fate of the false vacuum: towards realization with ultra-cold atoms*, *Europhys. Lett.* **110** (2015), no. 5 56001, [`arXiv:1408.1163`].

[47] O. Fialko, B. Opanchuk, A. I. Sidorov, P. D. Drummond, and J. Brand, *The universe on a table top: engineering quantum decay of a relativistic scalar field from a metastable vacuum*, *J. Phys. B* **50** (2017), no. 2 024003.

[48] B. Opanchuk, R. Polkinghorne, O. Fialko, J. Brand, and P. D. Drummond, *Quantum simulations of the early universe*, *Annalen Phys.* **525** (2013) 866–876.

[49] K. L. Ng, B. Opanchuk, M. Thenabadu, M. Reid, and P. D. Drummond, *Fate of the false vacuum: Finite temperature, entropy, and topological phase in quantum simulations of the early universe*, *PRX Quantum* **2** (2021) 010350.

[50] A. Zenesini, A. Berti, R. Cominotti, et al., *False vacuum decay via bubble formation in ferromagnetic superfluids*, *Nat. Phys.* **20** (2024), no. 4 558–563.

[51] S. Abel and M. Spannowsky, *Quantum-field-theoretic simulation platform for observing the fate of the false vacuum*, *PRX Quantum* **2** (2021) 010349.

[52] G. Lagnese, F. M. Surace, M. Kormos, and P. Calabrese, *False vacuum decay in quantum spin chains*, *Phys. Rev. B* **104** (2021), no. 20.

[53] G. Lagnese, F. M. Surace, S. Morampudi, and F. Wilczek, *Detecting a long lived false vacuum with quantum quenches*, `arXiv:2308.08340`.

[54] E. A. Martinez, C. A. Muschik, P. Schindler, et al., *Real-time dynamics of lattice gauge theories with a few-qubit quantum computer*, *Nature* **534** (2016), no. 7608 516–519.

[55] B. Xu and W. Xue, *(3+1)-dimensional Schwinger pair production with quantum computers*, *Phys. Rev. D* **106** (2022), no. 11 116007.

[56] N. Christensen, *Stochastic gravitational wave backgrounds*, *Reports on Progress in Physics* **82** (2018), no. 1 016903.

[57] A. Afzal, G. Agazie, A. Anumarlapudi, et al., *The nanograv 15 yr data set: Search for signals from new physics*, *Astrophys. J. Lett.* **951** (June, 2023) L11.

[58] A. Mazumdar and G. White, *Review of cosmic phase transitions: their significance and experimental signatures*, *Reports on Progress in Physics* **82** (2019), no. 7 076901.

[59] A. Cooray and R. Sheth, *Halo Models of Large Scale Structure*, *Phys. Rep.* **372** (2002), no. 1 1–129.

[60] M. Asgari, A. J. Mead, and C. Heymans, *The halo model for cosmology: a pedagogical review*, `arXiv:2303.08752`.

[61] S. Dodelson, *Modern Cosmology*. Academic Press, Elsevier Science, 2003.

[62] V. Mukhanov, *Physical Foundations of Cosmology*. Cambridge University Press, 2005.

[63] V. Mukhanov and S. Winitzki, *Introduction to Quantum Effects in Gravity*. Cambridge University Press, 2007.

[64] P. Peebles, *Principles of Physical Cosmology*. Princeton Series in Physics. Princeton University Press, 1993.

[65] D. Baumann, *Cosmology*. Cambridge University Press, 2022.

[66] E. W. Kolb and M. S. Turner, *The early universe*. Frontiers in physics. Westview Press, Boulder, CO, 1990.

[67] M. C. Johnson, *PSI Cosmology Lecture Notes*, 2019.

[68] F. Bernardeau, S. Colombi, E. Gaztañaga, and R. Scoccimarro, *Large-scale structure of the universe and cosmological perturbation theory*, *Phys. Rep.* **367** (2002), no. 1 1–248.

[69] A. Lewis, A. Challinor, and A. Lasenby, *Efficient computation of cosmic microwave background anisotropies in closed friedmann-robertson-walker models*, *Astrophys. J.* **538** (2000), no. 2 473.

[70] D. Blas, J. Lesgourgues, and T. Tram, *The cosmic linear anisotropy solving system (class). part ii: Approximation schemes*, *J. Cosmol. Astropart. Phys.* **2011** (July, 2011) 034–034.

[71] Planck Collaboration, Akrami, Y., Arroja, F., et al., *Planck 2018 results - x. constraints on inflation*, *Astron. Astrophys.* **641** (2020) A10.

[72] P. J. Peebles, *Large-scale background temperature and mass fluctuations due to scale-invariant primeval perturbations*, *Astrophys. J., Lett. Ed.; (United States)* **263** (12, 1982).

[73] G. R. Blumenthal, S. M. Faber, J. R. Primack, and M. J. Rees, *Formation of galaxies and large-scale structure with cold dark matter*, *Nature* **311** (1984), no. 5986 517–525.

[74] M. Tegmark, M. A. Strauss, M. R. Blanton, et al., *Cosmological parameters from SDSS and WMAP*, *Phys. Rev. D* **69** (May, 2004) 103501.

[75] N. Kaiser, *On the spatial correlations of Abell clusters.*, *Astrophys. J.* **284** (1984) L9–L12.

[76] A. Kosowsky, *Seeing sound waves in the early universe*, `9811163`.

[77] D. J. Fixsen, E. S. Cheng, J. M. Gales, et al., *The Cosmic Microwave Background Spectrum from the Full COBE FIRAS Data Set*, *Astrophys. J.* **473** (1996) 576.

[78] D. Zegeye, T. Crawford, and W. Hu, *Measuring μ distortions from the thermal Sunyaev-Zeldovich effect*, *Phys. Rev. D* **109** (2024), no. 6 063503.

[79] J. Chluba and R. A. Sunyaev, *The evolution of CMB spectral distortions in the early Universe*, *Mon. Not. Roy. Astron. Soc.* **419** (Jan., 2012) 1294–1314.

[80] J. Chluba, M. H. Abitbol, N. Aghanim, et al., *New horizons in cosmology with spectral distortions of the cosmic microwave background*, *Exp. Astron.* **51** (2021), no. 3 1515–1554.

[81] A. Lewis and A. Challinor, *Weak gravitational lensing of the cmb*, *Phys. Rep.* **429** (2006), no. 1 1–65.

[82] P. Zhang and M. C. Johnson, *Testing eternal inflation with the kinetic Sunyaev Zel'dovich effect*, *J. Cosmol. Astropart. Phys.* **1506** (2015), no. 06 046.

[83] A. Terrana, M.-J. Harris, and M. C. Johnson, *Analyzing the cosmic variance limit of remote dipole measurements of the cosmic microwave background using the large-scale kinetic Sunyaev Zel'dovich effect*, *J. Cosmol. Astropart. Phys.* **2017** (2017), no. 02 040–040.

[84] A.-S. Deutsch, E. Dimastrogiovanni, M. C. Johnson, M. Münchmeyer, and A. Terrana, *Reconstruction of the remote dipole and quadrupole fields from the kinetic Sunyaev Zel'dovich and polarized Sunyaev Zel'dovich effects*, *Phys. Rev.* **D98** (2018), no. 12 123501.

[85] K. M. Smith, M. S. Madhavacheril, M. Münchmeyer, et al., *KSZ tomography and the bispectrum*, `arXiv:1810.13423`.

[86] J. Cayuso, R. Bloch, S. C. Hotinli, M. C. Johnson, and F. McCarthy, *Velocity reconstruction with the cosmic microwave background and galaxy surveys*, *J. Cosmol. Astropart. Phys.* **02** (2023) 051.

[87] S. C. Hotinli, J. Meyers, N. Dalal, et al., *Transverse Velocities with the Moving Lens Effect*, *Phys. Rev. Lett.* **123** (2019), no. 6 061301.

[88] C. Dvorkin and K. M. Smith, *Reconstructing Patchy Reionization from the Cosmic Microwave Background*, *Phys. Rev. D* **79** (2009), no. 4 043003.

[89] N. Sehgal et al., *CMB-HD: An Ultra-Deep, High-Resolution Millimeter-Wave Survey Over Half the Sky*, `arXiv:1906.10134`.

[90] A. H. Guth, *Inflationary universe: A possible solution to the horizon and flatness problems*, *Phys. Rev. D* **23** (jan, 1981) 347–356.

[91] A. H. Guth and E. J. Weinberg, *Cosmological consequences of a first-order phase transition in the SU(5) grand unified model*, *Phys. Rev. D* **23** (1981), no. 4 876–885.

[92] A. Linde, *A new inflationary universe scenario: A possible solution of the horizon, flatness, homogeneity, isotropy and primordial monopole problems*, *Phys. Lett. B* **108** (1982), no. 6 389–393.

[93] M. Bucher, A. S. Goldhaber, and N. Turok, *Open universe from inflation*, *Phys. Rev. D* **52** (1995), no. 6 3314–3337.

[94] J. R. Gott, *Creation of open universes from de Sitter space*, *Nature* **295** (1982), no. 5847 304–307.

[95] A. A. Starobinsky, *STOCHASTIC DE SITTER (INFLATIONARY) STAGE IN THE EARLY UNIVERSE*, *Lect. Notes Phys.* **246** (1986) 107–126.

[96] R. Allahverdi, R. Brandenberger, F.-Y. Cyr-Racine, and A. Mazumdar, *Reheating in inflationary cosmology: Theory and applications*, *Annual Review of Nuclear and Particle Science* **60** (Nov., 2010) 27–51.

[97] M. Fabbrichesi, E. Gabrielli, and G. Lanfranchi, *The Physics of the Dark Photon: A Primer*. Springer International Publishing, 2021.

[98] D. J. Marsh, *Axion cosmology*, *Phys. Rep.* **643** (July, 2016) 1–79.

[99] A. Arvanitaki, S. Dimopoulos, S. Dubovsky, N. Kaloper, and J. March-Russell, *String Axiverse*, *Phys. Rev.* **D81** (2010) 123530.

[100] M. Goodsell, J. Jaeckel, J. Redondo, and A. Ringwald, *Naturally Light Hidden Photons in LARGE Volume String Compactifications*, *J. High Energy Phys.* **11** (2009) 027.

[101] M. Pospelov, A. Ritz, and M. B. Voloshin, *Bosonic super-WIMPs as keV-scale dark matter*, *Phys. Rev. D* **78** (2008) 115012.

[102] P. Arias, D. Cadamuro, M. Goodsell, et al., *WISPy Cold Dark Matter*, *J. Cosmol. Astropart. Phys.* **06** (2012) 013.

[103] P. W. Graham, J. Mardon, and S. Rajendran, *Vector Dark Matter from Inflationary Fluctuations*, *Phys. Rev. D* **93** (2016), no. 10 103520.

[104] S. Knapen, T. Lin, and K. M. Zurek, *Light Dark Matter: Models and Constraints*, *Phys. Rev. D* **96** (2017), no. 11 115021.

[105] L. B. Okun, *LIMITS OF ELECTRODYNAMICS: PARAPHOTONS?*, *Sov. Phys. JETP* **56** (1982) 502.

[106] B. Holdom, *Two U(1)'s and Epsilon Charge Shifts*, *Phys. Lett. B* **166** (1986) 196–198.

[107] **CMS** Collaboration, A. M. Sirunyan et al., *Search for new physics in final states with a single photon and missing transverse momentum in proton-proton collisions at* $\sqrt{s} = 13$ *TeV*, *J. High Energy Phys.* **02** (2019) 074.

[108] M. Acciarri, P. Achard, O. Adriani, et al., *Single and multi-photon events with missing energy in electron-positron collisions at s = 189 gev*, *Phys. Lett. B* **470** (1999), no. 1 268–280.

[109] J. H. Chang, R. Essig, and S. D. McDermott, *Revisiting supernova 1987a constraints on dark photons*, *J. High Energy Phys.* **2017** (Jan., 2017).

[110] J. Jaeckel, *A force beyond the Standard Model - Status of the quest for hidden photons*, *Frascati Phys. Ser.* **56** (2012) 172–192.

[111] M. Baryakhtar, R. Lasenby, and M. Teo, *Black Hole Superradiance Signatures of Ultralight Vectors*, *Phys. Rev.* **D96** (2017), no. 3 035019.

[112] N. Siemonsen and W. E. East, *Gravitational wave signatures of ultralight vector bosons from black hole superradiance*, *Phys. Rev. D* **101** (2020), no. 2 024019.

[113] W. E. East, *Vortex String Formation in Black Hole Superradiance of a Dark Photon with the Higgs Mechanism*, *Phys. Rev. Lett.* **129** (2022), no. 14 141103.

[114] W. E. East and J. Huang, *Dark photon vortex formation and dynamics*, `arXiv:2206.12432`.

[115] N. Siemonsen, C. Mondino, D. Egana-Ugrinovic, et al., *Dark photon superradiance: Electrodynamics and multimessenger signals*, *Phys. Rev. D* **107** (2023), no. 7 075025.

[116] A. Mirizzi, J. Redondo, and G. Sigl, *Microwave Background Constraints on Mixing of Photons with Hidden Photons*, *J. Cosmol. Astropart. Phys.* **03** (2009) 026.

[117] S. D. McDermott and S. J. Witte, *Cosmological evolution of light dark photon dark matter*, *Phys. Rev. D* **101** (2020), no. 6 063030.

[118] A. Caputo, H. Liu, S. Mishra-Sharma, and J. T. Ruderman, *Modeling Dark Photon Oscillations in Our Inhomogeneous Universe*, *Phys. Rev. D* **102** (2020), no. 10 103533.

[119] A. Caputo, H. Liu, S. Mishra-Sharma, and J. T. Ruderman, *Dark Photon Oscillations in Our Inhomogeneous Universe*, *Phys. Rev. Lett.* **125** (2020), no. 22 221303.

[120] H. An, M. Pospelov, and J. Pradler, *Dark Matter Detectors as Dark Photon Helioscopes*, *Phys. Rev. Lett.* **111** (2013) 041302.

[121] E. Hardy and R. Lasenby, *Stellar cooling bounds on new light particles: plasma mixing effects*, *J. High Energy Phys.* **02** (2017) 033.

[122] R. Lasenby and K. Van Tilburg, *Dark photons in the solar basin*, *Phys. Rev. D* **104** (2021), no. 2 023020.

[123] S. Chaudhuri, P. W. Graham, K. Irwin, et al., *Radio for hidden-photon dark matter detection*, *Phys. Rev. D* **92** (2015), no. 7 075012.

[124] M. Baryakhtar, J. Huang, and R. Lasenby, *Axion and hidden photon dark matter detection with multilayer optical haloscopes*, *Phys. Rev. D* **98** (2018), no. 3 035006.

[125] J. Chiles et al., *New Constraints on Dark Photon Dark Matter with Superconducting Nanowire Detectors in an Optical Haloscope*, *Phys. Rev. Lett.* **128** (2022), no. 23 231802.

[126] A. Romanenko et al., *New Exclusion Limit for Dark Photons from an SRF Cavity-Based Search (Dark SRF)*, `arXiv:2301.11512`.

[127] **SENSEI** Collaboration, L. Barak et al., *SENSEI: Direct-Detection Results on sub-GeV Dark Matter from a New Skipper-CCD*, *Phys. Rev. Lett.* **125** (2020), no. 17 171802.

[128] S. Weinberg, *A New Light Boson?*, *Phys.Rev.Lett.* **40** (1978) 223–226.

[129] F. Wilczek, *Problem of Strong p and t Invariance in the Presence of Instantons*, *Phys.Rev.Lett.* **40** (1978) 279–282.

[130] R. Peccei and H. R. Quinn, *CP Conservation in the Presence of Instantons*, *Phys.Rev.Lett.* **38** (1977) 1440–1443.

[131] R. Peccei and H. R. Quinn, *Constraints Imposed by CP Conservation in the Presence of Instantons*, *Phys.Rev.* **D16** (1977) 1791–1797.

[132] P. Svrcek and E. Witten, *Axions In String Theory*, *J. High Energy Phys.* **06** (2006) 051.

[133] M. Kuster, G. Raffelt, and B. Beltran, eds., *Axions: Theory, cosmology, and experimental searches. Proceedings, 1st Joint ILIAS-CERN-CAST axion training, Geneva, Switzerland, November 30-December 2, 2005*, vol. 741, 2008.

[134] L. Hui, J. P. Ostriker, S. Tremaine, and E. Witten, *Ultralight scalars as cosmological dark matter*, *Phys. Rev. D* **95** (Feb, 2017) 043541.

[135] J. Preskill, M. B. Wise, and F. Wilczek, *Cosmology of the Invisible Axion*, *Phys. Lett. B* **120** (1983) 127–132.

[136] **Particle Data Group** Collaboration, R. L. Workman et al., *Review of Particle Physics*, *PTEP* **2022** (2022) 083C01.

[137] C. Dessert, J. W. Foster, and B. R. Safdi, *X-ray Searches for Axions from Super Star Clusters*, *Phys. Rev. Lett.* **125** (2020), no. 26 261102.

[138] S. Hoof and L. Schulz, *Updated constraints on axion-like particles from temporal information in supernova sn1987a gamma-ray data*, *J. Cosmol. Astropart. Phys.* **2023** (2023), no. 03 054.

[139] C. S. Reynolds, M. C. D. Marsh, H. R. Russell, et al., *Astrophysical limits on very light axion-like particles from Chandra grating spectroscopy of NGC 1275*, *Astrophys. J.* **890** (2020) 59.

[140] A. Aguirre, *Eternal Inflation, past and future*, .

[141] A. H. Guth, *Eternal inflation and its implications*, *J. Phys. A* **40** (2007), no. 25 6811–6826.

[142] J. Garriga, A. H. Guth, and A. Vilenkin, *Eternal inflation, bubble collisions, and the persistence of memory*, *Phys. Rev. D* **76** (2007) 123512.

[143] A. Aguirre, M. C. Johnson, and A. Shomer, *Towards observable signatures of other bubble universes*, *Phys. Rev. D* **76** (2007) 063509.

[144] S. Chang, M. Kleban, and T. S. Levi, *When worlds collide*, `arXiv:0712.2261`.

[145] V. A. Kuzmin, V. A. Rubakov, and M. E. Shaposhnikov, *On the Anomalous Electroweak Baryon Number Nonconservation in the Early Universe*, *Phys. Lett. B* **155** (1985) 36.

[146] C. Cheung, A. Dahlen, and G. Elor, *Bubble baryogenesis*, *J. High Energy Phys.* **2012** (2012), no. 9.

[147] I. Garcia Garcia, S. Krippendorf, and J. March-Russell, *The string soundscape at gravitational wave detectors*, *Phys. Lett. B* **779** (2018) 348–352.

[148] S. Kachru, R. Kallosh, A. Linde, and S. P. Trivedi, *de Sitter vacua in string theory*, *Phys. Rev. D* **68** (2003), no. 4 046005.

[149] A. Vilenkin, *Anthropic predictions: the case of the cosmological constant*, pp. 163–180. Cambridge University Press, 2007.

[150] A. H. Guth and E. J. Weinberg, *Cosmological consequences of a first-order phase transition in the* su_5 *grand unified model*, *Phys. Rev. D* **23** (Feb, 1981) 876–885.

[151] S. A. Bonometto and O. Pantano, *Physics of the cosmological quark-hadron transition*, *Phys. Rep.* **228** (1993), no. 4 175–252.

[152] M. Pietroni, *The Electroweak phase transition in a nonminimal supersymmetric model*, *Nucl. Phys. B* **402** (1993) 27–45.

[153] N. J. Craig, *Gravitational Waves from Supersymmetry Breaking*, `arXiv:0902.1990`.

[154] H. Goldberg, *Proposal for a constant cosmological constant*, *Phys. Lett. B* **492** (2000), no. 1-2 153–160.

[155] S. Dutta, S. D. H. Hsu, D. Reeb, and R. J. Scherrer, *Dark radiation as a signature of dark energy*, *Phys. Rev. D* **79** (2009), no. 10.

[156] A. Kosowsky, M. S. Turner, and R. Watkins, *Gravitational waves from first-order cosmological phase transitions*, *Phys. Rev. Lett.* **69** (1992) 2026–2029.

[157] M. Kamionkowski, A. Kosowsky, and M. S. Turner, *Gravitational radiation from first-order phase transitions*, *Phys. Rev. D* **49** (Mar, 1994) 2837–2851.

[158] P. A. et. al., *Cosmology with the laser interferometer space antenna*, arXiv:2204.05434.

[159] M. Sher, *Electroweak higgs potential and vacuum stability*, *Phys. Rep.* **179** (1989), no. 5 273–418.

[160] J. Ellis, J. R. Espinosa, G. F. Giudice, A. Hoecker, and A. Riotto, *The probable fate of the Standard Model*, *Phys. Lett. B* **679** (2009), no. 4 369–375.

[161] T. Markkanen, A. Rajantie, and S. Stopyra, *Cosmological aspects of higgs vacuum metastability*, *Front. Astron. Space Sci.* **5** (Dec., 2018).

[162] I. K. Affleck and F. De Luccia, *Induced vacuum decay*, *Phys. Rev. D* **20** (1979) 3168–3178.

[163] S. Coleman, *Fate of the false vacuum: Semiclassical theory*, *Phys. Rev. D* **15** (1977), no. 10 2929–2936.

[164] O. Fialko, B. Opanchuk, A. I. Sidorov, P. D. Drummond, and J. Brand, *The universe on a table top: engineering quantum decay of a relativistic scalar field from a metastable vacuum*, *J. Phys. B* **50** (2017), no. 2 024003.

[165] J. Braden, M. C. Johnson, H. V. Peiris, and S. Weinfurtner, *Towards the cold atom analog false vacuum*, *J. High Energy Phys.* **2018** (2018), no. 7.

[166] E. Wigner, *On the quantum correction for thermodynamic equilibrium*, *Phys. Rev.* **40** (1932) 749–759.

[167] C. W. Gardiner and P. Zoller, *Quantum noise: a handbook of Markovian and non-Markovian quantum stochastic methods with applications to quantum optics*. Springer, 3 ed., 2004.

[168] O. Fialko, B. Opanchuk, A. I. Sidorov, P. D. Drummond, and J. Brand, *Fate of the false vacuum: Towards realization with ultra-cold atoms*, *Europhys Lett.* **110** (2015), no. 5 56001.

[169] A. Milsted, J. Liu, J. Preskill, and G. Vidal, *Collisions of false-vacuum bubble walls in a quantum spin chain*, arXiv:2012.07243.

[170] J. E. Moyal, *Quantum mechanics as a statistical theory*, *Mathematical Proceedings of the Cambridge Philosophical Society* **45** (1949), no. 1 99–124.

[171] A. Polkovnikov, *Phase space representation of quantum dynamics*, *Annals of Physics* **325** (2010), no. 8 1790–1852.

[172] S. Mrówczyński and B. Müller, *Wigner functional approach to quantum field dynamics*, *Phys. Rev. D* **50** (1994), no. 12 7542–7552.

[173] P. Blakie, A. Bradley, M. Davis, R. Ballagh, and C. Gardiner, *Dynamics and statistical mechanics of ultra-cold bose gases using c-field techniques*, *Advances in Physics* **57** (2008), no. 5 363–455.

[174] A. V. Frolov, *Non-linear Dynamics and Primordial Curvature Perturbations from Preheating*, *Class. Quant. Grav.* **27** (2010) 124006.

[175] J. C. Butcher, *Implicit Runge-Kutta processes*, *Math. Comp.* **18** (1964) 50–64.

[176] J. Braden, J. R. Bond, and L. Mersini-Houghton, *Cosmic bubble and domain wall instabilities I: parametric amplification of linear fluctuations*, *J. Cosmol. Astropart. Phys.* **1503** (2015), no. 03 007.

[177] S. L. Lumsden, A. F. Heavens, and J. A. Peacock, *The clustering of peaks in a random Gaussian field*, *Mon. Not. Roy. Astron. Soc.* **238** (1989), no. 2 293–318.

[178] A. R. Rivolo, *The two-point galaxy correlation function of the Local Supercluster*, *Astrophys. J.* **301** (1986) 70.

[179] A. Kosowsky and M. S. Turner, *Gravitational radiation from colliding vacuum bubbles: Envelope approximation to many-bubble collisions*, *Phys. Rev. D* **47** (1993) 4372–4391.

[180] M. Kamionkowski, A. Kosowsky, and M. S. Turner, *Gravitational radiation from first-order phase transitions*, *Phys. Rev. D* **49** (1994), no. 6 2837–2851.

[181] L. Leitao and A. Mégevand, *Hydrodynamics of ultra-relativistic bubble walls*, *Nucl. Phys. B.* **905** (2016) 45–72.

[182] M. Geller, A. Hook, R. Sundrum, and Y. Tsai, *Primordial Anisotropies in the Gravitational Wave Background from Cosmological Phase Transitions*, *Phys. Rev. Lett.* **121** (2018), no. 20 201303.

[183] S. M. Feeney, M. C. Johnson, D. J. Mortlock, and H. V. Peiris, *First observational tests of eternal inflation*, *Phys. Rev. Lett.* **107** (2011) 071301.

[184] E. J. Weinberg, *Classical Solutions in Quantum Field Theory: Solitons and Instantons in High Energy Physics*. Cambridge Monographs on Mathematical Physics. Cambridge University Press, 2012.

[185] M. Hindmarsh, M. Lüben, J. Lumma, and M. Pauly, *Phase transitions in the early universe*, *SciPost Phys. Lect. Notes* (2021) 24.

[186] A. Aguirre, M. C. Johnson, and M. Tysanner, *Surviving the crash: assessing the aftermath of cosmic bubble collisions*, *Phys. Rev. D* **79** (2009) 123514.

[187] D. Y. Grigoriev and V. A. Rubakov, *Soliton Pair Creation at Finite Temperatures. Numerical Study in (1+1)-dimensions*, *Nucl. Phys. B* **299** (1988) 67–78.

[188] D. Y. Grigoriev, V. A. Rubakov, and M. E. Shaposhnikov, *Sphaleron Transitions at Finite Temperatures: Numerical Study in (1+1)-dimensions*, *Phys. Lett. B* **216** (1989) 172–176.

[189] D. Y. Grigoriev, V. A. Rubakov, and M. E. Shaposhnikov, *Topological transitions at finite temperatures: A real time numerical approach*, *Nucl. Phys. B* **326** (1989) 737–757.

[190] M. Alford, H. Feldman, and M. Gleiser, *Thermal activation of metastable decay: Testing nucleation theory*, *Phys. Rev. D* **47** (1993) R2168–R2171.

[191] M. Alford and M. Gleiser, *Metastability in two dimensions and the effective potential*, *Phys. Rev. D* **48** (1993) 2838–2844.

[192] A. Strumia and N. Tetradis, *Testing nucleation theory in two dimensions*, *Nucl. Phys. B.* **560** (1999), no. 1 482–496.

[193] M. Gleiser and H.-R. Müller, *How to count kinks. from the continuum to the lattice and back*, *Phys. Lett. B* **422** (1998), no. 1 69–75.

[194] D. Boyanovsky, C. Destri, and H. J. de Vega, *Approach to thermalization in the classical φ^4 theory in $1+1$ dimensions: Energy cascades and universal scaling*, *Phys. Rev. D* **69** (2004) 045003.

[195] A. Shkerin and S. Sibiryakov, *Black hole induced false vacuum decay from first principles*, *J. High Energy Phys.* **11** (2021) 197.

[196] J. J. Blanco-Pillado, H. Deng, and A. Vilenkin, *Flyover vacuum decay*, *J. Cosmol. Astropart. Phys.* **2019** (2019), no. 12 001.

[197] J. O. Smith, *Mathematics of the Discrete Fourier Transform (DFT)*. W3K Publishing, http://www.w3k.org/books/, 2007.

[198] D. E. Morrissey and M. J. Ramsey-Musolf, *Electroweak baryogenesis*, *New J. Phys.* **14** (2012), no. 12 125003.

[199] P. John and M. Schmidt, *Do stops slow down electroweak bubble walls?*, *Nucl. Phys. B.* **598** (2001), no. 1-2 291–305.

[200] G. D. Moore and T. Prokopec, *How fast can the wall move? a study of the electroweak phase transition dynamics*, *Phys. Rev. D* **52** (1995), no. 12 7182–7204.

[201] G. Moore and T. Prokopec, *Bubble wall velocity in a first order electroweak phase transition*, *Phys. Rev. Lett.* **75** (1995), no. 5 777–780.

[202] J. M. Cline and K. Kainulainen, *Electroweak baryogenesis at high bubble wall velocities*, *Phys. Rev. D* **101** (2020), no. 6 063525.

[203] M. Hindmarsh, S. J. Huber, K. Rummukainen, and D. J. Weir, *Numerical simulations of acoustically generated gravitational waves at a first order phase transition*, *Phys. Rev. D* **92** (2015), no. 12.

[204] A. Riotto, *Oscillons are not present during a first order electroweak phase transition*, *Phys. Lett. B* **365** (1996), no. 1-4 64–71.

[205] **Simons Observatory** Collaboration, J. Aguirre et al., *The Simons Observatory: Science goals and forecasts*, *J. Cosmol. Astropart. Phys.* **1902** (2019) 056.

[206] **CMB-S4** Collaboration, K. N. Abazajian et al., *CMB-S4 Science Book, First Edition*, `arXiv:1610.02743`.

[207] **DESI** Collaboration, M. E. Levi et al., *The Dark Energy Spectroscopic Instrument (DESI)*, `arXiv:1907.10688`.

[208] **EUCLID** Collaboration, R. Laureijs et al., *Euclid Definition Study Report*, `arXiv:1110.3193`.

[209] **LSST Science, LSST Project** Collaboration, P. A. Abell et al., *LSST Science Book, Version 2.0*, `arXiv:0912.0201`.

[210] K. Basu et al., *A space mission to map the entire observable universe using the CMB as a backlight: Voyage 2050 science white paper*, *Exper. Astron.* **51** (2021), no. 3 1555–1591.

[211] D. Scott, J. R. Bond, S. Chapman, et al., *Cosmology in front of the background: studying the growth of structure at CMB wavelengths*, arXiv:1910.05419.

[212] K. M. Smith, M. S. Madhavacheril, M. Münchmeyer, et al., *KSZ tomography and the bispectrum*, arXiv:1810.13423.

[213] R. Lasenby, *Long range dark matter self-interactions and plasma instabilities*, *J. Cosmol. Astropart. Phys.* **11** (2020) 034.

[214] A. A. Garcia, K. Bondarenko, S. Ploeckinger, J. Pradler, and A. Sokolenko, *Effective photon mass and (dark) photon conversion in the inhomogeneous Universe*, *J. Cosmol. Astropart. Phys.* **10** (2020) 011.

[215] S. P. Mikheyev and A. Y. Smirnov, *Resonance Amplification of Oscillations in Matter and Spectroscopy of Solar Neutrinos*, *Sov. J. Nucl. Phys.* **42** (1985) 913–917.

[216] L. Wolfenstein, *Neutrino oscillations in matter*, *Phys. Rev. D* **17** (1978) 2369–2374.

[217] N. Battaglia, *The tau of galaxy clusters*, *J. Cosmol. Astropart. Phys.* **2016** (2016), no. 08 058.

[218] J. F. Navarro, C. S. Frenk, and S. D. M. White, *The Structure of Cold Dark Matter Halos*, *Astrophys. J.* **462** (1996).

[219] A. Kusiak, B. Bolliet, A. Krolewski, and J. C. Hill, *Constraining the galaxy-halo connection of infrared-selected unwise galaxies with galaxy clustering and galaxy-cmb lensing power spectra*, *Phys. Rev. D* **106** (2022) 123517.

[220] J. L. Tinker, A. V. Kravtsov, A. Klypin, et al., *Toward a halo mass function for precision cosmology: The Limits of universality*, *Astrophys. J.* **688** (2008) 709–728.

[221] L. Posti and A. Helmi, *Mass and shape of the Milky Way's dark matter halo with globular clusters from Gaia and Hubble*, *Astron. Astrophys.* **621** (2019) A56.

[222] A. A. Dutton and A. V. Macciò, *Cold dark matter haloes in the Planck era: evolution of structural parameters for Einasto and NFW profiles*, *Mon. Not. Roy. Astron. Soc.* **441** (2014), no. 4 3359–3374.

[223] A. Roy, A. van Engelen, V. Gluscevic, and N. Battaglia, *Probing the circumgalactic medium with CMB polarization statistical anisotropy*, arXiv:2201.05076.

[224] J. C. Hill and E. Pajer, *Cosmology from the thermal sunyaev-zel'dovich power spectrum: Primordial non-gaussianity and massive neutrinos*, *Phys. Rev. D* **88** (2013) 063526.

[225] C. Dvorkin, W. Hu, and K. M. Smith, *B -mode CMB polarization from patchy screening during reionization*, *Phys. Rev. D* **79** (2009), no. 10 107302.

[226] G. D'Amico and N. Kaloper, *Anisotropies in nonthermal distortions of cosmic light from photon-axion conversion*, *Phys. Rev. D* **91** (2015) 085015.

[227] Y. Kvasiuk and M. Münchmeyer, *An Auto-Differentiable Likelihood Pipeline for the Cross-Correlation of CMB and Large-Scale Structure due to the Kinetic Sunyaev-Zeldovich Effect*, `arXiv:2305.08903`.

[228] U. Seljak, *Extracting primordial non-gaussianity without cosmic variance*, *Phys. Rev. Lett.* **102** (2009), no. 2.

[229] S. Amodeo, N. Battaglia, E. Schaan, et al., *Atacama cosmology telescope: Modeling the gas thermodynamics in boss cmass galaxies from kinematic and thermal sunyaev-zel'dovich measurements*, *Phys. Rev. D* **103** (2021) 063514.

[230] J. X. Prochaska and Y. Zheng, *Probing galactic halos with fast radio bursts*, *Mon. Not. Roy. Astron. Soc.* (2019).

[231] M. S. Madhavacheril, N. Battaglia, K. M. Smith, and J. L. Sievers, *Cosmology with the kinematic Sunyaev-Zeldovich effect: Breaking the optical depth degeneracy with fast radio bursts*, *Phys. Rev. D* **100** (2019), no. 10 103532.

[232] J. L. Bernal and E. D. Kovetz, *Line-intensity mapping: theory review with a focus on star-formation lines*, *Astron. Astrophys. Rev.* **30** (2022), no. 1.

[233] Planck Collaboration, Ade, P. A. R., Aghanim, N., et al., *Planck 2015 results - vi. lfi mapmaking*, *A&A* **594** (2016) A6.

[234] Planck Collaboration, Adam, R., Ade, P. A. R., et al., *Planck 2015 results - viii. high frequency instrument data processing: Calibration and maps*, *A&A* **594** (2016) A8.

[235] T. Brinckmann, S. Bryan, C. M. Casey, et al., *Snowmass2021 CMB-HD White Paper*, .

[236] C. Dickinson, *CMB foregrounds - A brief review*, in *51st Rencontres de Moriond on Cosmology*, pp. 53–62, 6, 2016.

[237] M. Tegmark, A. de Oliveira-Costa, and A. J. S. Hamilton, *High resolution foreground cleaned cmb map from wmap*, *Phys. Rev. D* **68** (2003) 123523.

[238] M. Liguori, E. Sefusatti, J. R. Fergusson, and E. P. S. Shellard, *Primordial non-gaussianity and bispectrum measurements in the cosmic microwave background and large-scale structure*, *Adv. Astron.* **2010** (2010) 1–64.

[239] L. F. Abbott and P. Sikivie, *A Cosmological Bound on the Invisible Axion*, *Phys. Lett. B* **120** (1983) 133–136.

[240] M. Dine and W. Fischler, *The Not So Harmless Axion*, *Phys. Lett. B* **120** (1983) 137–141.

[241] **CAST** Collaboration, K. Zioutas et al., *First results from the CERN Axion Solar Telescope (CAST)*, *Phys. Rev. Lett.* **94** (2005) 121301.

[242] **CAST** Collaboration, V. Anastassopoulos et al., *New CAST Limit on the Axion-Photon Interaction*, *Nat. Phys.* **13** (2017) 584–590.

[243] O. Ning and B. R. Safdi, *Leading Axion-Photon Sensitivity with NuSTAR Observations of M82 and M87*, `arXiv:2404.14476`.

[244] A. Arvanitaki, M. Baryakhtar, and X. Huang, *Discovering the QCD Axion with Black Holes and Gravitational Waves*, *Phys. Rev. D* **91** (2015), no. 8 084011.

[245] M. Baryakhtar, M. Galanis, R. Lasenby, and O. Simon, *Black hole superradiance of self-interacting scalar fields*, *Phys. Rev. D* **103** (2021), no. 9 095019.

[246] **SPHEREx** Collaboration, O. Doré et al., *Cosmology with the SPHEREX All-Sky Spectral Survey*, `arXiv:1412.4872`.

[247] G. Raffelt and L. Stodolsky, *Mixing of the Photon with Low Mass Particles*, *Phys. Rev. D* **37** (1988) 1237.

[248] C. Deffayet, D. Harari, J.-P. Uzan, and M. Zaldarriaga, *Dimming of supernovae by photon pseudoscalar conversion and the intergalactic plasma*, *Phys. Rev. D* **66** (2002) 043517.

[249] A. Mirizzi, G. G. Raffelt, and P. D. Serpico, *Photon-axion conversion as a mechanism for supernova dimming: Limits from CMB spectral distortion*, *Phys. Rev. D* **72** (2005) 023501.

[250] S. J. Parke, *Nonadiabatic level crossing in resonant neutrino oscillations*, *Phys. Rev. Lett.* **57** (1986) 1275–1278.

[251] A. Mirizzi, J. Redondo, and G. Sigl, *Constraining resonant photon-axion conversions in the early universe*, *J. Cosmol. Astropart. Phys.* **2009** (2009), no. 08 001.

[252] H. Tashiro, J. Silk, and D. J. E. Marsh, *Constraints on primordial magnetic fields from CMB distortions in the axiverse*, *Phys. Rev. D* **88** (2013), no. 12 125024.

[253] C. Csaki, N. Kaloper, and J. Terning, *Dimming supernovae without cosmic acceleration*, *Phys. Rev. Lett.* **88** (2002) 161302.

[254] G. D'Amico and N. Kaloper, *Anisotropies in nonthermal distortions of cosmic light from photon-axion conversion*, *Phys. Rev. D* **91** (2015), no. 8 085015.

[255] M. Schlederer and G. Sigl, *Constraining ALP-photon coupling using galaxy clusters*, *J. Cosmol. Astropart. Phys.* **01** (2016) 038.

[256] S. Mukherjee, R. Khatri, and B. D. Wandelt, *Polarized anisotropic spectral distortions of the CMB: Galactic and extragalactic constraints on photon-axion conversion*, *J. Cosmol. Astropart. Phys.* **04** (2018) 045.

[257] M. Hazumi, J. Borrill, Y. Chinone, et al., *LiteBIRD: a small satellite for the study of B-mode polarization and inflation from cosmic background radiation detection*, in *Space Telescopes and Instrumentation 2012: Optical, Infrared, and Millimeter Wave*, vol. 8442, p. 844219, Sept., 2012.

[258] A. Kogut, D. Fixsen, D. Chuss, et al., *The primordial inflation explorer (pixie): a nulling polarimeter for cosmic microwave background observations*, *J. Cosmol. Astropart. Phys.* **2011** (July, 2011) 025–025.

[259] S. Mukherjee, D. N. Spergel, R. Khatri, and B. D. Wandelt, *A new probe of Axion-Like Particles: CMB polarization distortions due to cluster magnetic fields*, *J. Cosmol. Astropart. Phys.* **02** (2020) 032.

[260] S. Goldstein, F. McCarthy, D. Pîrvu, et al., *in preparation*, .

[261] T. Louis et al., *The atacama cosmology telescope: two-season actpol spectra and parameters*, *J. Cosmol. Astropart. Phys.* **2017** (June, 2017) 031–031.

[262] A. Cooray and R. Sheth, *Halo models of large scale structure*, *Phys. Rep.* **372** (Dec., 2002) 1–129.

[263] R. Pakmor, F. van de Voort, R. Bieri, et al., *Magnetizing the circumgalactic medium of disc galaxies*, *Mon. Not. Roy. Astron. Soc.* **498** (2020), no. 3 3125–3137.

[264] R. Pakmor, R. Bieri, F. van de Voort, et al., *Magnetic field amplification in cosmological zoom simulations from dwarf galaxies to galaxy groups*, `arXiv:2309.13104`.

[265] J. L. Tinker, B. E. Robertson, A. V. Kravtsov, et al., *The large-scale bias of dark matter halos: Numerical calibration and model tests*, *Astrophys. J.* **724** (2010), no. 2 878.

[266] S. Bhattacharya, S. Habib, K. Heitmann, and A. Vikhlinin, *Dark matter halo profiles of massive clusters: Theory versus observations*, *Astrophys. J.* **766** (2013), no. 1 32.

[267] W. H. Press and P. Schechter, *Formation of Galaxies and Clusters of Galaxies by Self-Similar Gravitational Condensation*, *Astrophys. J.* **187** (Feb., 1974) 425–438.

[268] U. Seljak, *Analytic model for galaxy and dark matter clustering*, *Mon. Not. Roy. Astron. Soc.* **318** (Oct., 2000) 203–213.

[269] D. N. Limber, *The Analysis of Counts of the Extragalactic Nebulae in Terms of a Fluctuating Density Field.*, *Astrophys. J.* **117** (Jan., 1953) 134.

[270] J. C. Hill and E. Pajer, *Cosmology from the thermal sunyaev-zel'dovich power spectrum: Primordial non-gaussianity and massive neutrinos*, *Phys. Rev. D* **88** (Sep, 2013) 063526.

[271] E. F. Schlafly, A. M. Meisner, and G. M. Green, *The unwise catalog: Two billion infrared sources from five years of wise imaging*, *Astrophys. J. Suppl. S.* **240** (2019), no. 2 30.

[272] A. Krolewski, S. Ferraro, E. F. Schlafly, and M. White, *unWISE tomography of Planck CMB lensing*, *J. Cosmol. Astropart. Phys.* **2020** (May, 2020) 047.

[273] N. Koukoufilippas, D. Alonso, M. Bilicki, and J. A. Peacock, *Tomographic measurement of the intergalactic gas pressure through galaxy–tSZ cross-correlations*, *Mon. Not. Roy. Astron. Soc.* **491** (12, 2019) 5464–5480.

[274] F. C. van den Bosch, S. More, M. Cacciato, H. Mo, and X. Yang, *Cosmological constraints from a combination of galaxy clustering and lensing – I. Theoretical framework*, *Mon. Not. Roy. Astron. Soc.* **430** (02, 2013) 725–746.

[275] J. A. Peacock and R. E. Smith, *Halo occupation numbers and galaxy bias*, *Mon. Not. Roy. Astron. Soc.* **318** (Nov., 2000) 1144–1156.

[276] A. Kusiak, K. M. Surrao, and J. C. Hill, *Enhancing measurements of the CMB blackbody temperature power spectrum by removing cosmic infrared background and thermal Sunyaev-Zel'dovich contamination using external galaxy catalogs*, *Phys. Rev. D* **108** (2023), no. 12 123501.

[277] A. Kusiak, B. Bolliet, A. Krolewski, and J. C. Hill, *Constraining the galaxy-halo connection of infrared-selected unwise galaxies with galaxy clustering and galaxy-cmb lensing power spectra*, *Phys. Rev. D* **106** (2022) 123517.

[278] **Planck** Collaboration, N. Aghanim et al., *Planck 2018 results. I. Overview and the cosmological legacy of Planck*, *Astron. Astrophys.* **641** (2020) A1.

[279] G. Stein, M. A. Alvarez, J. R. Bond, A. van Engelen, and N. Battaglia, *The websky extragalactic cmb simulations*, *J. Cosmol. Astropart. Phys.* **2020** (2020), no. 10 012.

[280] Z. Yan, A. S. Maniyar, and L. van Waerbeke, *The star formation, dust, and abundance of galaxies with unWISE-CIB cross-correlations*, *J. Cosmol. Astropart. Phys.* **05** (2024) 058.

[281] F. McCarthy and J. C. Hill, *Component-separated, CIB-cleaned thermal Sunyaev-Zel'dovich maps from Planck PR4 data with a flexible public needlet ILC pipeline*, *Phys. Rev. D* **109** (2024), no. 2 023528.

[282] **CHIME** Collaboration, M. Amiri et al., *An Overview of CHIME, the Canadian Hydrogen Intensity Mapping Experiment*, *Astrophys. J. Supp.* **261** (2022), no. 2 29.

[283] J. S. Reynés, J. H. Matthews, C. S. Reynolds, et al., *New constraints on light axion-like particles using Chandra transmission grating spectroscopy of the powerful cluster-hosted quasar H1821+643*, *Mon. Not. Roy. Astron. Soc.* **510** (2021), no. 1 1264–1277.

[284] M. D. Marsh, H. R. Russell, A. C. Fabian, et al., *A new bound on axion-like particles*, *J. Cosmol. Astropart. Phys.* **2017** (2017), no. 12 036.

[285] M. Libanov and S. Troitsky, *On the impact of magnetic-field models in galaxy clusters on constraints on axion-like particles from the lack of irregularities in high-energy spectra of astrophysical sources*, *Phys. Lett. B* **802** (2020) 135252.

[286] S. Mukherjee, R. Khatri, and B. D. Wandelt, *Constraints on non-resonant photon-axion conversion from the Planck satellite data*, *J. Cosmol. Astropart. Phys.* **06** (2019) 031.

[287] D. Lai and J. Heyl, *Probing Axions with Radiation from Magnetic Stars*, *Phys. Rev. D* **74** (2006) 123003.

[288] C. Dessert, D. Dunsky, and B. R. Safdi, *Upper limit on the axion-photon coupling from magnetic white dwarf polarization*, *Phys. Rev. D* **105** (2022), no. 10 103034.

[289] A. Payez, C. Evoli, T. Fischer, et al., *Revisiting the sn1987a gamma-ray limit on ultralight axion-like particles*, *J. Cosmol. Astropart. Phys.* **2015** (2015), no. 02 006.

[290] N. Bar, K. Blum, and G. D'Amico, *Is there a supernova bound on axions?*, *Phys. Rev. D* **101** (2020), no. 12 123025.

[291] Y. Kahn, B. R. Safdi, and J. Thaler, *Broadband and Resonant Approaches to Axion Dark Matter Detection*, *Phys. Rev. Lett.* **117** (2016), no. 14 141801.

[292] **DMRadio** Collaboration, L. Brouwer et al., *Projected sensitivity of DMRadio-m3: A search for the QCD axion below 1 μeV*, *Phys. Rev. D* **106** (2022), no. 10 103008.

[293] A. Berlin, R. T. D'Agnolo, S. A. R. Ellis, and K. Zhou, *Heterodyne broadband detection of axion dark matter*, *Phys. Rev. D* **104** (2021), no. 11 L111701.

[294] J. Clampitt, B. Jain, M. Takada, and H. Miyatake, *Detection of Stacked Filament Lensing Between SDSS Luminous Red Galaxies*, *Mon. Not. Roy. Astron. Soc.* **457** (2016), no. 3 2391–2400.

[295] D. Galárraga-Espinosa et al., *Evolution of cosmic filaments in the MTNG simulation*, `arXiv:2309.08659`.

[296] R. van de Weygaert and E. Platen, *Cosmic Voids: Structure, Dynamics and Galaxies*, in *International Journal of Modern Physics Conference Series*, vol. 1 of *International Journal of Modern Physics Conference Series*, pp. 41–66, Jan., 2011.

[297] V. De Luca, G. Franciolini, and A. Riotto, *Bubble correlation in first-order phase transitions*, *Phys. Rev. D* **104** (2021), no. 12 123539.

[298] F. McCarthy, D. Pirvu, J. C. Hill, et al., *Dark photon limits from patchy dark screening of the cosmic microwave background*, `arXiv:2406.02546`.

[299] M. P. Hertzberg and M. Yamada, *Vacuum Decay in Real Time and Imaginary Time Formalisms*, *Phys. Rev. D* **100** (2019), no. 1 016011.

[300] Z.-G. Mou, P. M. Saffin, and A. Tranberg, *Quantum tunnelling, real-time dynamics and Picard-Lefschetz thimbles*, *J. High Energy Phys.* **11** (2019) 135.

[301] W.-Y. Ai, B. Garbrecht, and C. Tamarit, *Functional methods for false vacuum decay in real time*, *J. High Energy Phys.* **12** (2019) 095.

[302] F. Michel, *Parametrized Path Approach to Vacuum Decay*, *Phys. Rev. D* **101** (2020), no. 4 045021.

[303] H. Huang and L. H. Ford, *Vacuum decay induced by quantum fluctuations*, *Phys. Rev. D* **105** (2022), no. 8 085025.

[304] G. N. Felder and I. Tkachev, *LATTICEEASY: A Program for lattice simulations of scalar fields in an expanding universe*, *Comput. Phys. Commun.* **178** (2008) 929–932.

[305] R. Micha and I. I. Tkachev, *Turbulent thermalization*, *Phys. Rev. D* **70** (2004) 043538.

[306] A. V. Frolov, *DEFROST: A New Code for Simulating Preheating after Inflation*, *J. Cosmol. Astropart. Phys.* **11** (2008) 009.

[307] R. Easther, H. Finkel, and N. Roth, *PSpectRe: A Pseudo-Spectral Code for (P)reheating*, *J. Cosmol. Astropart. Phys.* **10** (2010) 025.

[308] M. J. Steel, M. K. Olsen, L. I. Plimak, et al., *Dynamical quantum noise in trapped bose-einstein condensates*, *Phys. Rev. A* **58** (Dec, 1998) 4824–4835.

[309] A. Polkovnikov, *Quantum corrections to the dynamics of interacting bosons: Beyond the truncated wigner approximation*, *Phys. Rev. A* **68** (Nov, 2003) 053604.

[310] J. Berges, K. Boguslavski, S. Schlichting, and R. Venugopalan, *Nonequilibrium fixed points in longitudinally expanding scalar theories: infrared cascade, Bose condensation and a challenge for kinetic theory*, *Phys. Rev. D* **92** (2015), no. 9 096006.

[311] J. Berges, M. P. Heller, A. Mazeliauskas, and R. Venugopalan, *QCD thermalization: Ab initio approaches and interdisciplinary connections*, *Rev. Mod. Phys.* **93** (2021), no. 3 035003.

[312] S. Borsanyi, A. Patkos, J. Polonyi, and Z. Szep, *Fate of the classical false vacuum*, *Phys. Rev. D* **62** (2000) 085013.

[313] S. Borsanyi, A. Patkos, D. Sexty, and Z. Szep, *Ising - like dynamical signatures and the endpoint of the QCD transition line*, *Phys. Rev. D* **64** (2001) 125011.

[314] S. Borsanyi, A. Patkos, and D. Sexty, *Goldstone excitations from spinodal instability*, *Phys. Rev. D* **66** (2002) 025014.

[315] I. Y. Kobzarev, L. B. Okun, and M. B. Voloshin, *Bubbles in Metastable Vacuum*, *Yad. Fiz.* **20** (1974) 1229–1234.

[316] M. Sher, *Electroweak Higgs Potentials and Vacuum Stability*, *Phys. Rept.* **179** (1989) 273–418.

[317] M. S. Turner, E. J. Weinberg, and L. M. Widrow, *Bubble nucleation in first-order inflation and other cosmological phase transitions*, *Phys. Rev. D* **46** (1992) 2384–2403.

[318] A. Aguirre and M. C. Johnson, *Towards observable signatures of other bubble universes. ii. exact solutions for thin-wall bubble collisions*, *Phys. Rev. D* **77** (2008) 123536.

[319] J. García-Bellido, *Open inflation models and gravitational wave anisotropies in the cmb*, *Phys. Rev. D* **56** (1997) 3225–3237.

[320] C. L. Wainwright, M. C. Johnson, H. V. Peiris, et al., *Simulating the universe(s): from cosmic bubble collisions to cosmological observables with numerical relativity*, *J. Cosmol. Astropart. Phys.* **2014** (2014), no. 03 030–030.

[321] J. Garriga, X. Montes, Misao Sasaki, and Takahiro Tanaka, *Spectrum of cosmological perturbations in the one-bubble open universe*, *Nucl. Phys. B.* **551** (1999), no. 1 317–373.

[322] R. Jinno and M. Takimoto, *Gravitational waves from bubble collisions: An analytic derivation*, *Phys. Rev. D* **95** (2017) 024009.

[323] A. Linde, *Toy model for open inflation*, *Phys. Rev. D* **59** (1998) 023503.

[324] S. Coleman, V. Glaser, and A. Martin, *Action minima among solutions to a class of Euclidean scalar field equations*, *Communications in Mathematical Physics* **58** (1978), no. 2 211–221.

[325] J. J. Blanco-Pillado, H. Deng, and A. Vilenkin, *Flyover vacuum decay*, *J. Cosmol. Astropart. Phys.* **2019** (2019), no. 12 001–001.

[326] N. Turok, *On quantum tunneling in real time*, *New J. Phys.* **16** (2014).

[327] P. Burda, R. Gregory, and I. G. Moss, *The fate of the Higgs vacuum*, *J. High Energy Phys.* **2016** (2016), no. 6 1–20.

[328] J. Garriga and A. Vilenkin, *Quantum fluctuations on domain walls, strings, and vacuum bubbles*, *Phys. Rev. D* **45** (1992), no. 10 3469–3486.

[329] J. R. Bond and G. Efstathiou, *The Statistics of Cosmic Background Fluctuations*, *Mon. Not. Roy. Astron. Soc.* **226** (1986), no. 3 655–687.

[330] C. G. Callan and S. Coleman, *Fate of the false vacuum. II. First quantum corrections*, *Phys. Rev. D* **16** (1977), no. 6 1762–1768.

[331] A. Linde, *Inflation and quantum cosmology*, *Physica Scripta* **T36** (1991) 30–54.

[332] P. J. E. Peebles, *Statistical Analysis of Catalogs of Extragalactic Objects. I. Theory*, *Astrophys. J.* **185** (1973) 413.

[333] M. Sasaki, T. Tanaka, K. Yamamoto, and J. Yokoyama, *Quantum state inside a vacuum bubble and the creation of an open universe*, *Phys. Lett. B* (1993).

[334] M. Bounakis and I. G. Moss, *Gravitational corrections to Higgs potentials*, *J. High Energy Phys.* **2018** (2018), no. 4 1–32.

[335] P. Burda, R. Gregory, and I. G. Moss, *Gravity and the Stability of the Higgs Vacuum*, *Phys. Rev. Lett.* **115** (2015), no. 7 071303.

[336] A. Linde, *Chaotic inflation*, *Phys. Lett. B* **129** (1983), no. 3-4 177–181.

[337] J. Garcia-Bellido, *Single-bubble Open Inflation: An Overview*, tech. rep., 2nd International Workshop on Birth of the Univers, Rome, Italy, 1997.

[338] T. Banks, *Heretics of the False Vacuum: Gravitational Effects On and Of Vacuum Decay 2*, .

[339] L. M. Widrow, *False-vacuum decay in time-dependent and two-field models*, *Phys. Rev. D* **44** (1991), no. 8 2306–2313.

[340] S. Coleman and F. De Luccia, *Gravitational effects on and of vacuum decay*, *Phys. Rev. D* **21** (1980) 3305–3315.

[341] A. Masoumi, K. D. Olum, and B. Shlaer, *Efficient numerical solution to vacuum decay with many fields*, *J. Cosmol. Astropart. Phys.* **2017** (2017), no. 01 051–051.

[342] W. B. Case, *Wigner functions and Weyl transforms for pedestrians*, *Am. J. Phys.* **76** (2008), no. 10 937–946.

[343] E. Farhi, A. H. Guth, and J. Guven, *Is it possible to create a universe in the laboratory by quantum tunneling?*, *Nucl. Phys. B.* **339** (1990), no. 2 417–490.

[344] S. Coleman and F. De Luccia, *Gravitational effects on and of vacuum decay*, *Phys. Rev. D* **21** (1980), no. 12 3305–3315.

[345] M. Davis, A. Meiksin, M. A. Strauss, L. N. da Costa, and A. Yahil, *On the universality of the two-point galaxy correlation function*, *Astrophys. J.* **333** (1988).

[346] J. Braden, M. C. Johnson, H. V. Peiris, A. Pontzen, and S. Weinfurtner, *Nonlinear dynamics of the cold atom analog false vacuum*, *J. High Energy Phys.* **2019** (2019), no. 10 174.

[347] J. R. Bond, J. Braden, and L. Mersini-Houghton, *Cosmic bubble and domain wall instabilities III: The role of oscillons in three-dimensional bubble collisions*, *J. Cosmol. Astropart. Phys.* **1509** (2015), no. 09 004.

[348] M. Gleiser and A. F. Heckler, *Nonperturbative effects on nucleation*, *Phys. Rev. Lett.* **76** (1996) 180–183.

[349] T. Epelbaum, F. Gelis, and B. Wu, *Nonrenormalizability of the classical statistical approximation*, *Phys. Rev. D* **90** (2014), no. 6 065029.

[350] J. Ambjorn, T. Askgaard, H. Porter, and M. E. Shaposhnikov, *Lattice Simulations of Electroweak Sphaleron Transitions in Real Time*, *Phys. Lett. B* **244** (1990) 479–487.

[351] N. S. Manton and T. Romańczukiewicz, *Simplest oscillon and its sphaleron*, *Phys. Rev. D* **107** (2023), no. 8 085012.

[352] M. Gleiser and D. Sicilia, *A General Theory of Oscillon Dynamics*, *Phys. Rev. D* **80** (2009) 125037.

[353] S. Y. Khlebnikov and I. I. Tkachev, *Classical decay of inflaton*, *Phys. Rev. Lett.* **77** (1996) 219–222.

[354] S. Y. Khlebnikov and I. I. Tkachev, *The Universe after inflation: The Wide resonance case*, *Phys. Lett. B* **390** (1997) 80–86.

[355] S. Y. Khlebnikov and I. I. Tkachev, *Resonant decay of Bose condensates*, *Phys. Rev. Lett.* **79** (1997) 1607–1610.

[356] P. Millington, Z.-G. Mou, P. M. Saffin, and A. Tranberg, *Statistics on Lefschetz thimbles: Bell/Leggett-Garg inequalities and the classical-statistical approximation*, *J. High Energy Phys.* **03** (2021) 077.

[357] A. V. Frolov, *DEFROST: a new code for simulating preheating after inflation*, *J. Cosmol. Astropart. Phys.* **2008** (2008), no. 11 009.

[358] G. Felder and I. Tkachev, *LATTICEEASY: A program for lattice simulations of scalar fields in an expanding universe*, *Computer Physics Communications* **178** (2008), no. 12 929–932.

[359] C. W. Gardiner, J. R. Anglin, and T. I. A. Fudge, *The stochastic gross-pitaevskii equation*, *J. Phys. B* **35** (2002), no. 6 1555.

[360] A. Linde, *Stochastic approach to tunneling and baby universe formation*, *Nucl. Phys. B.* **372** (1992), no. 1-2 421–442.

[361] G. Aarts and J. Smit, *Classical approximation for time-dependent quantum field theory: Diagrammatic analysis for hot scalar fields*, *Nucl. Phys. B.* **511** (1998), no. 1-2 451–478.

[362] J. Berges, S. Borsányi, D. Sexty, and I.-O. Stamatescu, *Lattice simulations of real-time quantum fields*, *Phys. Rev. D* **75** (2007).

[363] T. Hayashi, K. Kamada, N. Oshita, and J. Yokoyama, *Vacuum decay in the Lorentzian path integral*, *J. Cosmol. Astropart. Phys.* **05** (2022), no. 05 041.

[364] J. Nishimura, K. Sakai, and A. Yosprakob, *A new picture of quantum tunneling in the real-time path integral from Lefschetz thimble calculations*, *J. High Energy Phys.* **09** (2023) 110.

[365] K. Blum and O. Rosner, *Unraveling the bounce: a real time perspective on tunneling*, arXiv:2309.07585.

[366] S. F. Bramberger, G. Lavrelashvili, and J.-L. Lehners, *Quantum tunneling from paths in complex time*, *Phys. Rev. D* **94** (2016), no. 6 064032.

[367] A. Cherman and M. Unsal, *Real-Time Feynman Path Integral Realization of Instantons*, arXiv:1408.0012.

[368] S. Y. Khlebnikov, L. Kofman, A. D. Linde, and I. Tkachev, *First order nonthermal phase transition after preheating*, *Phys. Rev. Lett.* **81** (1998) 2012–2015.

[369] M. G. Abed and I. G. Moss, *Bubble nucleation at zero and nonzero temperatures*, *Phys. Rev. D* **107** (2023), no. 7 076027.

[370] E. Garaldi, R. Kannan, A. Smith, et al., *The thesan project: properties of the intergalactic medium and its connection to reionization-era galaxies*, *Mon. Not. Roy. Astron. Soc.* **512** (2022), no. 4 4909–4933.

[371] A. R. Duffy, J. Schaye, S. T. Kay, and C. D. Vecchia, *Dark matter halo concentrations in the wilkinson microwave anisotropy probe year 5 cosmology*, *Mon. Not. Roy. Astron. Soc. Lett.* **390** (2008), no. 1 L64–L68.

[372] **CMB-S4** Collaboration, K. N. Abazajian et al., *CMB-S4 Science Book, First Edition*, arXiv:1610.02743.

[373] J. F. Navarro, C. S. Frenk, and S. D. M. White, *The Structure of Cold Dark Matter Halos*, *Astrophys. J.* **462** (1996) [9508025].

[374] R. Scoccimarro, R. K. Sheth, L. Hui, and B. Jain, *How many galaxies fit in a halo? constraints on galaxy formation efficiency from spatial clustering*, *Astrophys. J.* **546** (jan, 2001) 20.

[375] M. J. Dolan, F. J. Hiskens, and R. R. Volkas, *Advancing globular cluster constraints on the axion-photon coupling*, *J. Cosmol. Astropart. Phys.* **10** (2022) 096.

[376] **CAST** Collaboration, V. Anastassopoulos et al., *New CAST Limit on the Axion-Photon Interaction*, *Nat. Phys.* **13** (2017) 584–590.

[377] W. Hu and T. Okamoto, *Mass reconstruction with cmb polarization*, *Astrophys. J.* **574** (2002) 566–574, [astro-ph/0111606].

[378] T. K. Kuo and J. Pantaleone, *Neutrino oscillations in matter*, *Rev. Mod. Phys.* **61** (1989) 937–979.

[379] N. Brahma, A. Berlin, and K. Schutz, *Photon-dark photon conversion with multiple level crossings*, *Phys. Rev. D* **108** (2023), no. 9 095045.

[380] M. C. D. Marsh, J. H. Matthews, C. Reynolds, and P. Carenza, *Fourier formalism for relativistic axion-photon conversion with astrophysical applications*, *Phys. Rev. D* **105** (2022), no. 1 016013.

[381] A. Krolewski, S. Ferraro, and M. White, *Cosmological constraints from unWISE and Planck CMB lensing tomography*, *J. Cosmol. Astropart. Phys.* **2021** (Dec., 2021) 028.

[382] S. Amodeo et al., *Atacama Cosmology Telescope: Modeling the gas thermodynamics in BOSS CMASS galaxies from kinematic and thermal Sunyaev-Zel'dovich measurements*, *Phys. Rev. D* **103** (2021), no. 6 063514. [Erratum: Phys.Rev.D 107, 063514 (2023)].

[383] A. Pillepich et al., *First results from the TNG50 simulation: the evolution of stellar and gaseous discs across cosmic time*, *Mon. Not. Roy. Astron. Soc.* **490** (2019), no. 3 3196–3233.

[384] A. N. Kolmogorov, *Dissipation of Energy in Locally Isotropic Turbulence*, *Akademiia Nauk SSSR Doklady* **32** (Apr., 1941) 16.

APPENDICES

Appendix A

Dynamics of Bubble Nucleation

A.1 Real-Time Simulations

In our numerical simulations, we approximate the ensemble-averaged field dynamics by the non-linear classical time evolution of many realizations of some initial conditions. One generates an ensemble of these initial conditions for the field and its conjugate momentum drawn from the ground state defined around the false vacuum minimum. These initial states are evolved classically with a non-linear Hamiltonian. The field configuration in each realization is sampled at late times, and their classical expectation value is recovered from taking ensemble averages over observables.

We interpret a decay event as the emergence of a bubble with a fixed set of characteristics in the field during classical evolution. For example, a common criterion for finding a bubble is to set an amplitude threshold on the field, usually around the turning point in the potential. If the field crosses this threshold at a point and does not return to the false vacuum at any subsequent time, we say that we have identified a nucleation event. The time slice corresponding to this event is defined as the decay time and the collection of all decay times gives the numerical prediction for the decay rate per unit time. This definition matches the usual interpretation of the Euclidean decay rate for a relativistic field.

Thus, real-time simulations give an explicitly time-dependent description of the formation of bubbles, providing a classical time-dependent connection between the initial false vacuum state and the subsequent phase of an expanding bubble. In the simulation of each realization, every nucleation event is different in detail. The formation history and evolution of bubbles can be recorded to obtain an ensemble whose statistical properties can be

investigated in detail. Moreover, no symmetry assumptions about the bubble profile are needed in this approach. Therefore, this treatment allows us to investigate issues related to the dynamics of bubble formation that have previously been inaccessible. Adjusting the total lattice size and resolution gives us access to arbitrarily fine-grained information.

Since our approach relies on running large ensembles of full non-linear simulations, we specialize to 1+1 dimensional systems for computational feasibility. We expect the results to be qualitatively similar in higher spatial dimensions. Time evolution is performed using a 10th-order Gauss-Legendre integrator [175, 176]. Spatial derivatives are computed using pseudo-spectral methods. The spatial dimension is periodic due to the Fourier space sampling. We always ensure that the simulations are well resolved and that the total energy is conserved at machine precision throughout the simulation.

The real-time approach requires an assumption about the statistics of the initial vacuum field fluctuations. Starting with a classical distribution over phase space, this prescription is exact, at least to the extent that a sufficient number of realizations are drawn to sample the possible dynamics properly. In Chapter 3, we employ a classical stochastic description of vacuum decay of a single real scalar field with an initial Bose-Einstein distribution of fluctuations. This procedure referred to as the Classical-Statistical approximation [362, 361, 356], stochastic approach [360, 358, 357, 353, 354, 355], depending on the context and field of study. Early work in this direction was performed for topological solitons and vacuum transitions at finite temperature in [187, 188, 189, 350, 190].

In Chapter 2, we work under the interpretation introduced in [21], used to study vacuum decay at zero temperature starting from a stochastic scalar field in $1 + 1$ dimensions. In this approach, the dynamical phase space evolution of a quantum state initially in the false vacuum is modelled using the truncated Wigner approximation [166, 167]. Under this prescription, the dynamics can be shown to incorporate quantum effects to leading order in $\hbar$. Hence, this procedure yields a semi-classical approximation to the first-order phase transition dynamics. Analogous techniques have been used in other contexts, for example to study preheating at the end of inflation [304, 305, 306, 307], evolution of dilute gas cold atom Bose-Einstein condensates [308, 309], relativistic heavy ion collisions [310, 311]. Other perspectives on this approach were explored in [31, 32, 33, 34, 35, 36, 37].

Heuristically, in the semi-classical interpretation, the uncertainty principle is enforced by carefully choosing the initial conditions. Individual field and momentum Fourier modes are sampled as Gaussian random deviates with an appropriate width that simulates the Minkowski vacuum. However, this approach does not incorporate interference effects between different initial realizations, which in the path integral context is understood as interference between histories.

A.2 Velocity measurement and boosting to the rest frame

In this appendix we describe in detail the procedure for measuring the center-of-mass velocity of bubbles identified in simulations. The first step is to map the trajectories of the expanding bubble walls, denoted $r_{\mathrm{L/R}}(r,t)$. To do that, first we model the field amplitude at every time step by the expression

$$\bar{\varphi}(r, t = \text{const}) = \left(\tanh \frac{r - r_{\mathrm{L}}}{w_{\mathrm{L}}} + \tanh \frac{r_{\mathrm{R}} - r}{w_{\mathrm{R}}} \right) \frac{\bar{\varphi}_{\mathrm{fv}}}{2} + \bar{\varphi}_{\mathrm{fv}}, \tag{A.1}$$

where r is a coordinate that spans the lattice and $w_{\mathrm{L,R}}$ represent the thickness of each wall. In this expression, $r_{\mathrm{R,L}}$ are the best-fit coordinates of the wall centers. The hyperbolic tangent profile provides an excellent fit for the shape of the domain walls. Starting at $t \gg t_{\mathrm{crit}}$, we begin to trace the evolution going backwards in time towards the 'fuzzy' nucleation region, finding the best-fit values for $r_{\mathrm{R,L}}$ at each step. Two examples of such trajectories are illustrated by the dashed curves in Fig. A.1.

To mitigate the effect of fluctuations, we choose several guesses for the start-values of the parameters in (A.1) corresponding to wall amplitudes in the range $\bar{\varphi}_{\mathrm{fv}} + 1.5\sigma_{\bar{\varphi}}$ and $\bar{\varphi}_{\mathrm{fv}} + 3\sigma_{\bar{\varphi}}$. These start-values in general will generate different wall trajectories. At each step t beyond the starting slice, the initial guess on the best-fit parameters will be the values obtained at step $t + \mathrm{d}t_{\mathrm{out}}$.

With the independent trajectories $r_{\mathrm{L,R}}$ obtained this way, we fit each wall to a hyperbola $r_{\mathrm{L,R}}(t) = \pm\sqrt{a_1 + (t - a_2)^2} + a_3$ with free parameters $a_1, a_2, a_3 \in \mathbb{R}$. We obtain a bundle of hyperbolas expanding at roughly similar rates. From here, the instantaneous wall velocity is simply the tangent curve $v_{\mathrm{L,R}}(t) = \partial_t\, r_{\mathrm{L,R}}$. By fitting first to a hyperbolic trajectory we ensure that the $|v_{\mathrm{L,R}}| \leq 1$ at all times, as well as smooth out the effect of fluctuations. This can be seen by comparing the dashed and the solid lines in Fig. A.1.

In the rest frame, the two left- and right-moving wall velocities $v_{\mathrm{wall}}(t)$ are equal. In the boosted frame, $v_{\mathrm{L,R}}(t)$ are related by a gamma factor function of $v_{\mathrm{COM}}(t)$. Since at every time-step we have two equations with two unknowns, the instantaneous center-of-mass velocity is fully determined. Its value *at nucleation* is chosen as the instantaneous $v_{\mathrm{COM}}(t)$ that minimizes the residual $|v_{\mathrm{COM}}(t) - v_{\mathrm{wall}}(t)|$. Once again, this is because at nucleation the expectation is that the walls start off at rest.

For every wall trajectory given by the different choices of initial values of the fit parameters in (A.1), we get a different measurement for the $v_{\mathrm{COM}}(t)$ that minimizes the residual.

Some trajectories will fail, for various reasons, to give a numerical estimate for $v_{\rm COM}(t)$. For example, in most failed cases no hyperbolic fit is found. In general, since the wall amplitude spans a small range in $\bar{\varphi}$ of only $1.5\sigma_{\bar{\varphi}}$, the values of the center-of-mass velocities at nucleation obtained from the different hyperbolas will differ by less than 10%. We use the average of all these values as the final result of the measurement.

We call the center-of-mass velocity measured in this way the *deterministic velocity*. If there were no fluctuations, the procedure could be applied once, and the true center-of-mass velocity would be the deterministic velocity. However, the presence of fluctuations complicates things, and induces uncertainties in the measurement. In the worst case, it can lead the algorithm off a wrong path, and boost the bubble into a *more* relativistic frame. Therefore, we need to iterate over this procedure several times, checking at each step that we are on the right track.

We test the value obtained for the deterministic velocity by applying a Lorentz transformation with the corresponding boost factor $\gamma(v_{\rm COM})$ and measuring the center-of-mass velocity once again. If the new detected velocity is less than the original, the value is accepted. The procedure re-iterates until a residual $\leq 0.03c$ is reached, which becomes a lower bound for the error in the measurement. However, in cases where the deterministic velocity gives a larger residual than measured initially, the deterministic velocity is discarded and random velocities are applied until a frame where the bubble is closer to rest is found. These random values are chosen in the interval $0.05 < |v| < 0.2$. The final, overall $v_{\rm COM}$ is the result of relativistic addition of all boost factors – both stochastic or deterministic – that have been accepted.

To affix a de-boosted bubble onto a transformed grid, we first linearly interpolate the field (in the frame where the velocity was most recently measured), then evaluate it onto the new grid (with coordinates determined via the Lorentz boost). Recall that boosts preserve the spacetime interval, but weight the time and space components differently. The bubble is now distorted. Note, repeated linear interpolation at each intermediate step introduces noise in each realization. To minimize this noise, once the final $v_{\rm COM}$ is measured, we apply a single Lorentz boost with this value onto the original realization and check again that the output bubble is measured at rest. If the residual satisfies $\leq 0.03c$, the procedure has completed successfully.

An illustration of this procedure is shown in Fig. A.1 for two examples of bubbles at $T/m = 0.9$. The left panel shows the spacetime diagram of the bubbles as they appear in a particular simulation. On the right is the final result after applying a Lorentz boost with velocity $v_{\rm COM} = -0.78$ (top) and $v_{\rm COM} = 0.26$ (bottom) centered on the nucleation event. The dashed lines are the measured wall trajectories, while the solid lines are the

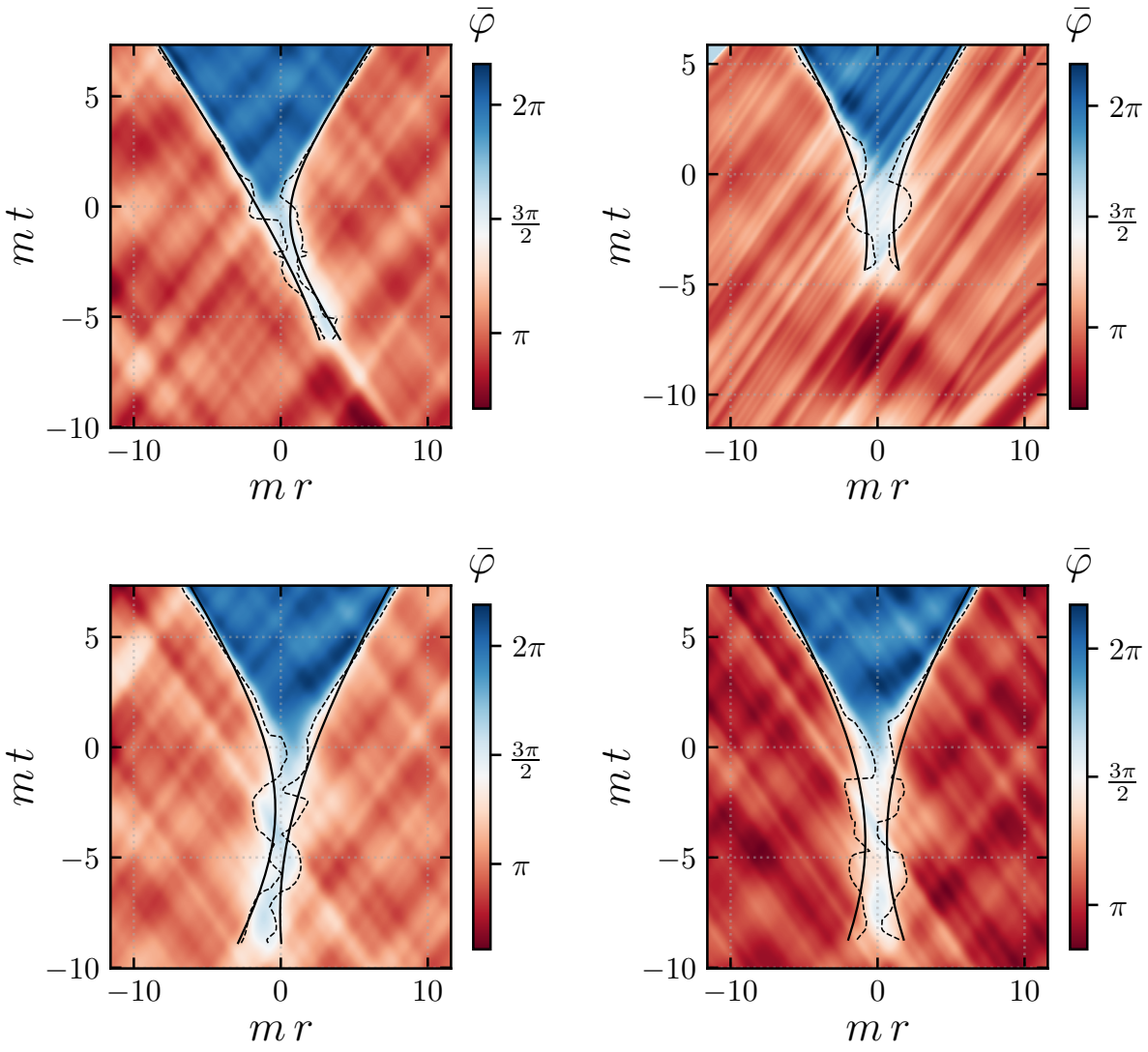

Figure A.1: The image caption is on the next page.

associated hyperbolic fits in each frame. Notice that the de-boosted left and right wall velocities and trajectories are now (almost) symmetric about $r = 0$. Additional examples of bubbles before and after the de-boosting procedure are depicted in Fig. 3.8 in the main text for the case where $T/m = 0.9$.

Figure A.1: The spacetime diagrams on the left hand side depict two bubbles as detected in their original realizations, while on the right we show the same bubbles at rest in the simulation frame, after going through the de-boosting procedure. The top bubble was detected to have the center-of-mass velocity $v_{\rm COM} = -0.78$, while the one in the bottom panels was measured to have $v_{\rm COM} = 0.26$. The greater the center-of-mass velocity is in absolute value, the more Lorentz contracted the bubble appears in the original simulation. The dashed line represents the wall trajectory found by fitting the field at each time-slice to the wall profile in (A.1). The solid black line is the hyperbolic best-fit to the dashed line curve, from which the instantaneous wall velocities are obtained. Stronger boosts lead to stronger field distortion and the introduction of a cutoff for the late-time expansion (e.g. from an original square grid to an area-conserved boosted diamond). This can be seen in the top left corner of the diagram in the top right panel. In the same image a large amplitude coherent fluctuation is seen as the bubble precursor. The bubble precursor as well as the neck of the bubble in the initial stage of expansion are noticeably thinner in the left panel than on the right.

Appendix B

Anisotropic Screening with Hidden-Sector Particles

B.1 Modelling dark screening in a dark matter halo

B.1.1 Dark matter halo models

The halo model of large scale structure assumes that all matter in the Universe is stored in virialized halos whose physical properties are fully described by the mass contained within their boundary (defined e.g. by the virial radius). Galaxies occupy dark matter halos and in doing so they act as tracers for the underlying dark matter distribution. The halo model is a semi-analytical framework used for understanding the non-linear structure of the matter distribution. There are two principal quantities needed to make predictions: the halo mass-function and the halo density profile. The former describes the halo number density as a function of mass and redshift. The latter describes how mass is distributed within each halo. Unlike the mass-function, it is not universal, meaning that it depends on cosmology and astrophysics. To make matters more simple, these expressions are assumed to be a function of a few variables such as mass, redshift and halo radius, and the parameters that enter these expressions are generally obtained from a mix of analytic predictions, simulations and even data. Other quantities that need to be specified in a halo model are the halo bias function, which to first order is fully determined by the mass function, as well as a concentration-mass relation that gives a characteristic scale radius for the halo density profile. Useful reviews on halo models are e.g. [59, 60].

To perform halo model computations throughout Chapter 4 we assume the mass-function of [220] that fixes the bias function [265], and the concentration-mass relation from [371], which fixes the free parameters in the halo density profile. We also work under the assumption that the halo boundary is its virial radius, so that the halo mass is defined in a sphere of radius $r_{\rm vir}$. In this Chapter and throughout Part II of this Thesis, we perform numerical halo-model computations using a modified version of the code *hmvec*[1] [6]. A detailed description of the assumptions that enter this code can be found in the Appendix B of [212].

For our modelling, we use 50 redshift bins of equal comoving radial width in the range $z = [0.01, z^{\rm max}]$, where the reionization redshift $z^{\rm max} \in \{2, 6, 10\}$. The first case was used with the purpose of obtaining a template angular power spectrum for the distribution of galaxies, as measured by a futuristic LSS survey. The latter two provide a conservative range for when reionization was completed. Additionally, the cosmology (to be precise, the linear matter power spectrum) is defined for 10^4 comoving wavenumber bins k logarithmically spaced in the $10^{-4} - 10^3\,{\rm Mpc}^{-1}$ range.

For numerical calculations in this work we considered 100 halo mass bins logarithmically spaced in the $10^{11} - 10^{17}\,{\rm M}_\odot$ interval. The lower bound is a conservative mass limit of halos with feedback processes significant enough to disrupt the gas profile. For the upper bound, the number density of halos in the halo model is exponentially suppressed with mass, and using the halo mass function in [220], one can expect less than one halo with a mass $> 3 \times 10^{16} M_\odot$ in a volume the size of the Hubble sphere. In other words, we consider all halos with mass $\geq 10^{11} M_\odot$.

B.1.2 Charged particle density profiles

In our calculations we considered an idealized scenario where reionization takes place instantaneously: the ionization fraction goes from zero to unity at exactly $z^{\rm reio}$. We compared the case where $z^{\rm reio} = 6$ and $z^{\rm reio} = 10$ and found no significant difference e.g. see Fig. 4.3. However, if we relax the assumption about the lower mass bound of halos where conversion can happen, this no longer holds true. In fact, we found that there is an order $1 - 10\%$ difference in the magnitude of the optical depth monopole $\bar{\tau}$ for masses above $m_{\rm A'} > 10^{-12}$ eV when we consider halos with mass down to $m = 10^9 M_\odot$. This would not affect the contours in Fig. 4.9 significantly, but represents an example of a source of error in the modelling.

A potentially more important assumption has to do with the precise choice of density profile for the charged electrons on small scales. We explore this in more detail in the

[1] `https://github.com/simonsobs/hmvec`

present section. As an example, the density of dark matter is consistently greater towards the core of halos (in fact, it is unbounded at $r \to 0$) than the gas density. Repeating all calculations under the assumption that electrons follow the NFW profile [218] in 4.9 instead of expression (4.7) for gas from [217] that we have been using in the main text, we obtain the results shown in Fig. B.1 for the sky-averaged dark screening optical depth monopole, and in Fig. B.2 for the differential (dimensionful) monopole. Notice that the greatest disagreement between the curves lies in the upper half of the dark photon masses we considered. This is related to the differences in the two density profiles on small scales which we elaborate on further.

Since the NFW profile is unbounded at $r \to 0$, we imposed that no resonant conversion happens below the scale radius r_s of any halo, effectively adding a factor of $\Theta(r_s - r_{\rm res})$ in the expression for the radial probability in (4.13). The NFW profile is monotonically decreasing with radius, hence this approximation excludes halos where the resonance condition is met near their core. As is evident in Fig. B.1, the constraint is most relevant for the production of heavy dark photons, which require the largest overdensities. The same quantitative difference between density profiles shows up in the shape of the angular two-point functions, which is depicted in Fig. B.3. Here, the relevant quantity is the ratio between the 1-halo and 2-halo terms. The distribution of power on small angular scales is influenced by the shape of the density profiles. However, the overall magnitude is given by the corresponding monopole at every mass.

For consistency reasons, we also assume that the NFW model breaks down at the scale radius of the Milky Way, which leads to a hard upper boundary on the range of dark photon masses that can be considered in this case, given by $m_{\rm A'} \propto \sqrt{\rho^{\rm NFW}(r_s^{\rm MW})} \approx 2.86 \times 10^{-12}$ eV. As mentioned in the main text, for the Milky Way we assuming a virial radius and virial mass from [221], and the concentration-mass relation at $z = 0$ from [222] which can be used to compute the scale radius via $r_{\rm vir}^{\rm MW} = c^{\rm MW}(m^{\rm MW}) r_s^{\rm MW}$.

Overall, it appears that the effect of changing the density profile modelling on the overall sensitivity on ε is minimal, as shown in Fig. B.4. This suggests that our projection is relatively insensitive to the exact electron density model for masses below the mass limit set by the Milky Way. This is a indication that the assumptions going into our forecast analysis are reasonable and robust, at least on scales above the scale radii of halos. However, the precise modelling of the gas profile around the core regions of halos will ultimately dictate the sensitivity on ε at larger dark photon masses. On the other hand, for lower dark photon masses, an improved sensitivity can be reached with improving knowledge of the electron density profile in the region right outside the virial radius of a halo [229]. Improving the reach by more than half an order of magnitude in mass towards lower masses is likely with new data from ACT DR6 and DESI.

To conclude, in recent years there has been significant progress in our understanding of the electron density distributions and fluctuations in halos, from new experimental measurements [229] and numerical simulation [370]. Prospective studies with cosmological data and CHIME/FRB [231] will further shrink these uncertainties, and potentially allow us to have more robust projections on the sensitivity at higher dark photon masses.

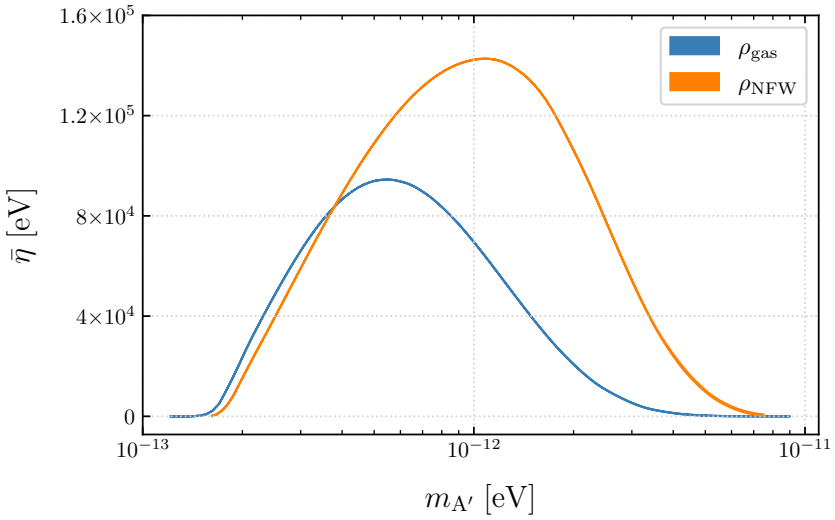

Figure B.1: Comparison between the average dimensionful optical depth for the NFW and gas profiles from [218] and [217], respectively. Here two cases are plotted: the top edge in each line corresponds to taking $z^{\rm reio} = 10$, while the bottom edge is computed for $z^{\rm reio} = 6$. In either case, assumptions about the end of reionization are of little importance. As described in the main text, the shape and magnitude of the monopole $\bar{\eta}$ plays an important role in determining the shape and reach in sensitivity of ε, for any experiment and forecast method. Therefore, the difference in magnitude between the two curves depicted here illustrates the importance of modelling the charged electron density in halos.

B.2 Correlation functions of dark screening

In this appendix, we derive in detail the angular power spectrum of the two-point auto-correlation of optical depth fluctuations. We use the notation conventions from the main text. First, we recall that the optical depth can be written as a sum of a homogeneous and an anisotropic part:

$$\tau(\chi, \hat{n}) = \bar{\tau}(\varepsilon, \omega)\left[1 + \delta\tau(\chi, \hat{n})\right]. \tag{B.1}$$

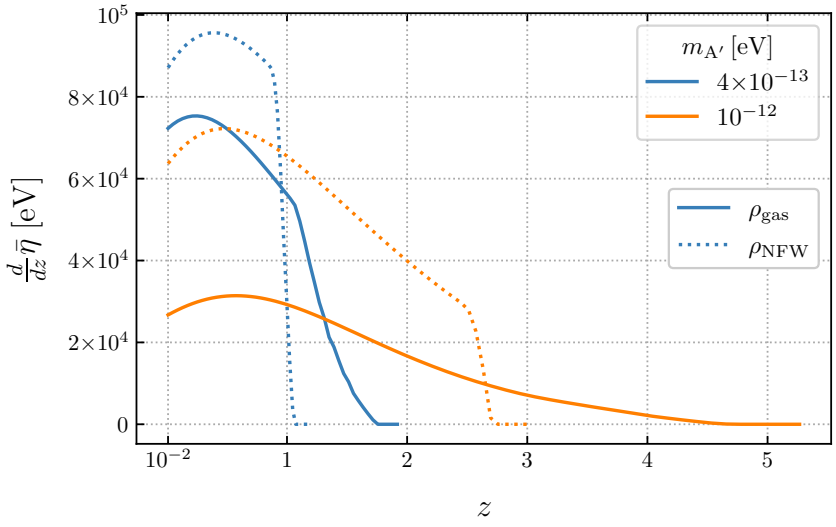

Figure B.2: Comparison between the differential average optical depth per redshift bin for two choices of density profile. Notice that the range of relevant redshift bins is sensitive to this choice, as well as the magnitude of the signal. For example, if we have an LSS template up to $z = 2$ as assumed in the main text, then we expect the cross-correlation with CMB dark screening to be less strong at $m_{A'} \gtrsim 10^{-12}$ eV if gas traces dark matter in the absence of AGN feedback processes.

To fix the notation, we define the volume elements $\mathrm{d}^3\boldsymbol{k} = k^2\,\mathrm{d}k\,\mathrm{d}^2\hat{n}_k$ and $\mathrm{d}^3\boldsymbol{\chi} = \chi^2\mathrm{d}\chi\,\mathrm{d}^2\hat{n}$, where the solid angle $\mathrm{d}^2\hat{n} = \sin\theta\mathrm{d}\theta\mathrm{d}\phi$. The two-point function of the overall optical depth is defined in configuration space as follows:

$$\langle\tau^*(\boldsymbol{\chi_1})\tau(\boldsymbol{\chi_2})\rangle = \bar{\tau}(\varepsilon,\omega)^2\left(1+\xi^{\delta\tau\delta\tau}(\boldsymbol{\chi_1},\boldsymbol{\chi_2})\right), \tag{B.2}$$

where we introduced the notation $\xi^{\delta\tau\delta\tau} = \langle\delta\tau^*(\boldsymbol{\chi_1})\delta\tau(\boldsymbol{\chi_2})\rangle$ to represent the two-point auto-correlation of anisotropies. The physical interpretation is the following: given that a photon following trajectory $\hat{n}_1$ on the observer's sky undergoes resonant conversion in a halo with mass m_1 at redshift z_1, what is the chance that another photon traveling along $\hat{n}_2$ converts as well? In the halo model, this probability is a sum of two terms:

$$\xi^{\delta\tau\delta\tau} = \xi^{1-\mathrm{halo}}(\chi_1,\hat{n}_1,\chi_1,\hat{n}_2) + \xi^{2-\mathrm{halo}}(\chi_1,\hat{n}_1,\chi_2,\hat{n}_2). \tag{B.3}$$

The first describes the case where the two photon conversions happen within the same halo centered at $\chi(z_1)$, and the second term represents the contribution from two different halos at $\chi(z_1)$ and $\chi(z_2)$. To derive the expressions for the sky-averaged power spectra, we will

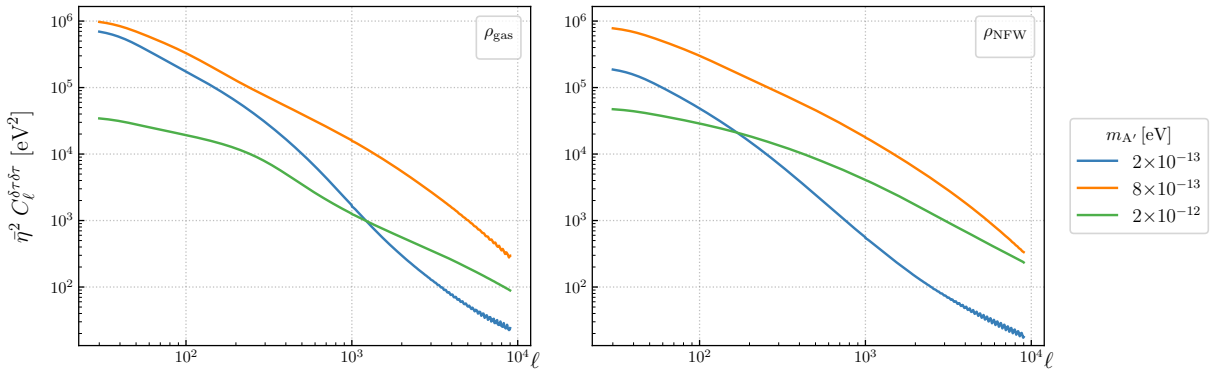

Figure B.3: The left panel shows the dark screening power spectra for three choices of dark photon mass, given a conversion model that assumes electrons in halos follow $\rho_{\rm gas}$, as in the main text. On the right we show the equivalent spectra where $\rho_{\rm NFW}$ is assumed. The $\rho_{\rm gas}$ profile is flat near the core and drops slower with radius than $\rho_{\rm NFW}$, hence at low $m_{\rm A'}$ we expect more power on larger scales on the left side. Meanwhile, $\rho_{\rm NFW}$ favours larger densities near the halo cores, so at large mass $m_{\rm A'}$ we expect more power on smaller scales. All spectra are multiplied by their respective monopole $\bar{\eta}_{\rm gas}$ and $\bar{\eta}_{\rm NFW}$ depicted in Fig. B.1.

need to perform a sum over all halos in the halo model, project onto spherical harmonics, then integrate over the Hubble volume. In the derivations below we sometimes leave the mass and redshift dependence implicit to simplify notation. We also use redshift z and comoving distance $\chi(z)$ interchangeably to denote the parametric dependence on time of various quantities.

B.2.1 One-halo term

We start by computing the 1-halo term. Labeling all halos within each redshift/comoving distance bin by i, we get:

$$\begin{aligned}
\bar{\tau}^2\xi^{\rm 1-halo} &= \left\langle \sum_i P^{i\,*}_{\gamma\to {\rm A}'}(\chi,\hat{n}_1,m_i) P^{i}_{\gamma\to {\rm A}'}(\chi,\hat{n}_2,m_i) \right\rangle \\
&= \left\langle \sum_i \int {\rm d}m\, \delta(m-m_i) \int {\rm d}^2\hat{n}\, \delta^2(\hat{n}-\hat{n}_i)\, |P(\chi,m)|^2\; u^*(\hat{n}_1-\hat{n})\, u(\hat{n}_2-\hat{n}) \right\rangle \\
&= \int {\rm d}m\, n(\chi,m)\, |P(\chi,m)|^2 \int {\rm d}^2\hat{n}\, u^*(\hat{n}_1-\hat{n})\, u(\hat{n}_2-\hat{n}).
\end{aligned} \tag{B.4}$$

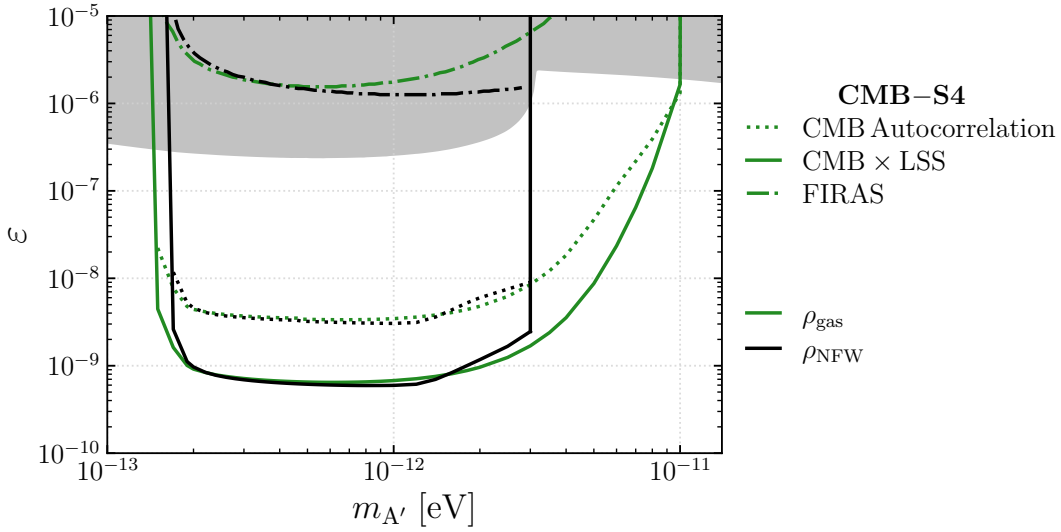

Figure B.4: Comparison between sensitivity given by two different profiles for the distribution of electrons inside halos, assuming CMB-S4-like noise. The green contours are the same as those shown in Fig. 4.9 for the 'AGN feedback' gas profile [217], while the black contours show the equivalent constraints starting from the NFW density profile [218]. As previously, the FIRAS constraint is computed taking into account the total average optical depth, including the Milky Way contribution, which for NFW is monotonically increasing with mass and dominates over the extra-galactic component at the upper mass end. The solid black boundary at $m_{A'} \approx 3 \times 10^{-12}$ eV is imposed by assuming the NFW model breaks down where $m_{A'}^2$ meets the resonance condition on scales less than the Milky Way scale radius $r_s^{\rm MW}$. For the contours that take into account the CMB anisotropies, we point out that the match between the contours shows that our model assumptions are robust on scales between the virial radius and the scale radius. However, the precise modelling of the gas profile around the core regions of halos will ultimately dictate the sensitivity on ε at larger dark photon masses.

In the last line, we used the expression for the average halo number density from (4.16).

Only the second integral is now angle-dependent, so we project it onto spherical harmonics:

$$
\begin{aligned}
&\int \mathrm{d}^2\hat{n}\, u^*(\hat{n}_1-\hat{n}|\chi,m)\, u(\hat{n}_2-\hat{n}|\chi,m) = \\
&\quad = \int \mathrm{d}^2\hat{n} \sum_{\ell' m'} u^*_{\ell' m'}(\chi,m) Y^*_{\ell' m'}(\hat{n}_1-\hat{n}) \sum_{\ell'' m''} u_{\ell'' m''}(\chi,m) Y_{\ell'' m''}(\hat{n}_2-\hat{n}) \\
&\quad = \int \mathrm{d}^2\hat{n} \sum_{\ell' \ell''} u^*_{\ell' 0}\, Y^*_{\ell' 0}(\hat{n}-\hat{n}_1)\, u_{\ell'' 0}\, Y_{\ell'' 0}(\hat{n}-\hat{n}_2) \\
&\quad = \int \mathrm{d}^2\hat{n} \sum_{\ell' \ell''} u^*_{\ell' 0} u_{\ell'' 0} \sum_{m'} \mathcal{D}^{\ell' *}_{0m'}(-\hat{n}_1)\, Y^*_{\ell' m'}(\hat{n}) \sum_{m''} \mathcal{D}^{\ell''}_{0m''}(-\hat{n}_2)\, Y_{\ell'' m''}(\hat{n}) \qquad \text{(B.5)} \\
&\quad = \sum_{\ell' \ell''} u^*_{\ell' 0} u_{\ell'' 0} \sum_{m' m''} \mathcal{D}^{\ell' *}_{0m'}(-\hat{n}_1)\, \mathcal{D}^{\ell''}_{0m''}(-\hat{n}_2)\, \delta_{\ell' \ell''}\, \delta_{m' m''} \\
&\quad = \sum_{\ell' m'} |u_{\ell' 0}|^2\, \mathcal{D}^{\ell' *}_{0m'}(-\hat{n}_1)\, \mathcal{D}^{\ell'}_{0m'}(-\hat{n}_2) \\
&\quad = \sum_{\ell} |u_{\ell 0}|^2 \mathcal{P}_\ell(\cos(\hat{n}_1-\hat{n}_2)).
\end{aligned}
$$

To get to the second equality we assumed that the halo profile $u(\hat{n}) \in \mathbb{R}$ has azimuthal symmetry implying that $\sum_m u_{\ell m} Y_{\ell m} = u_{\ell 0} Y_{\ell 0}$. Next we used the definition of the Wigner D-matrices to rotate the spherical harmonics. Then, we enforced the orthonormality condition $\int \mathrm{d}^2\hat{n}\, Y^*_{\ell m}(\hat{n}) Y_{\ell' m'}(\hat{n}) = \delta_{\ell \ell'} \delta_{m m'}$. In the last step we used the symmetries of the Wigner D-matrices and their relationship to spherical harmonics and Legendre polynomials $\mathcal{P}_\ell$ to simplify the equation.

We perform a multipole expansion on the left hand side of (B.4):

$$
\bar{\tau}^2 \xi^{1-\mathrm{halo}} = \sum_{\ell=0}^{\infty} \sum_{m=-\ell}^{\ell} C_\ell^{1-\mathrm{halo}}(\chi)\, Y^*_{\ell m}(\hat{n}_1)\, Y_{\ell m}(\hat{n}_2). \qquad \text{(B.6)}
$$

We introduced the angular power spectrum of the 1-halo term $C_\ell^{1-\mathrm{halo}}$, here as a function of redshift. To simplify the right-hand side we use the property that $\frac{4\pi}{2l+1} \sum_m Y^*_{\ell m} Y_{\ell m} = \mathcal{P}_\ell$. Next we match the terms in ℓ from both expressions above:

$$
\bar{\tau}^2 C_\ell^{1-\mathrm{halo}}(\chi) = \frac{4\pi}{2l+1} \int \mathrm{d}m\, n(\chi,m) \left[P(\chi,m)\, u_{\ell 0}(\chi,m)\right]^2. \qquad \text{(B.7)}
$$

To obtain the full sky-averaged power spectrum we need to integrate over the comoving radial coordinate χ. Changing also the integration variable to redshift, i.e. $\mathrm{d}\chi = \mathrm{d}z/H(z)$

where $H(z)$ is the Hubble constant, we obtain the final expression for the 1-halo term:

$$\bar{\tau}^2 C_\ell^{1-\text{halo}} = \frac{4\pi}{2l+1} \int \mathrm{d}z \, \frac{\chi(z)^2}{H(z)} \int \mathrm{d}m \, n(z,m) \left[P(z,m) \, u_{\ell 0}(z,m) \right]^2 . \tag{B.8}$$

B.2.2 Two-halo term

For the second term we follow similar reasoning and steps as in the previous case, except now we need to consider the conversion probability inside two different halos. Labeling these by i and j, located at arbitrary comoving distances χ_1 and χ_2 we find the average configuration space two-point function as:

$$\begin{aligned} \bar{\tau}^2 \xi^{2-\text{halo}} &= \left\langle \sum_{ij} P^{i\,*}_{\gamma \to \mathrm{A}'}(\chi_1, \hat{n}_1, m_i) P^{j}_{\gamma \to \mathrm{A}'}(\chi_2, \hat{n}_2, m_j) \right\rangle \\ &= \left(\prod_{x=a,b} \int \mathrm{d}m_x \int \mathrm{d}^2 \hat{n}_x \right) P(\chi_1, m_a) \, u(\hat{n}_1 - \hat{n}_a) P(\chi_2, m_b) \, u(\hat{n}_2 - \hat{n}_b) \\ &\times \left\langle \sum_{ij} \delta(m_a - m_i) \delta(m_b - m_j) \delta^2(\hat{n}_a - \hat{n}_i) \delta^2(\hat{n}_b - \hat{n}_j) \right\rangle . \end{aligned} \tag{B.9}$$

The term in the brackets is related to the number density of each halo's characteristic m and z, as well as to the correlation between positions of halos ξ^{hh} in the following way:

$$\begin{aligned} &\left\langle \sum_{ij} \delta(m_a - m_i) \delta(m_b - m_j) \delta^2(\hat{n}_a - \hat{n}_i) \delta^2(\hat{n}_b - \hat{n}_j) \right\rangle = \\ &\qquad = n(\chi_1, m_1) \, n(\chi_2, m_2) \, \xi^{\text{hh}}(\chi_1, m_1, \chi_2, m_2). \end{aligned} \tag{B.10}$$

Known as the halo-halo auto-correlation function, ξ^{hh} is proportional to the linear matter two-point function. To first order in linear theory, the following is true:

$$\xi^{hh}(\chi_1, m_a, \chi_2, m_b) \simeq b(\chi_1, m_a) b(\chi_2, m_b) \, \xi^{\text{lin}}(\chi_1, \chi_2), \tag{B.11}$$

where the bias function $b(z, m)$ is a deterministic function of the halo mass and redshift. We can further relate this to the linear matter power spectrum by doing a Fourier expansion over comoving wavenumbers:

$$\xi^{\text{lin}}(\chi_1, \chi_2) = \int \frac{\mathrm{d}^3 k}{(2\pi)^3} \, e^{i k \cdot (\chi_1 - \chi_2)} \, P^{\text{lin}}(k, \chi_1, \chi_2). \tag{B.12}$$

On large scales, the linear matter power spectrum is well approximated by

$$P^{\rm lin}(k,\chi_1,\chi_2) = \sqrt{P^{\rm lin}(k,\chi_1)P^{\rm lin}(k,\chi_2)}. \tag{B.13}$$

Consider next the multipole expansion of a plane wave:

$$e^{ik\cdot\chi} = 4\pi\sum_{\ell m} i^\ell j_\ell(k\chi)Y^*_{\ell m}(\hat{n}_k)Y_{\ell m}(\hat{n}), \tag{B.14}$$

where $j_\ell(k\chi)\in\mathbb{R}$ is the spherical Bessel function. Performing the multipole expansion on ξ^{hh} from (B.11) and putting everything together, we obtain the halo-halo angular power spectrum to first order in linear theory:

$$C^{hh}_\ell(\chi_1,\chi_2,m_a,m_b) = \frac{2}{\pi}b(\chi_1,m_a)b(\chi_2,m_b)\int {\rm d}k k^2 j_\ell(k\chi_1)j_\ell(k_2\chi_2)P^{\rm lin}(k,\chi_1,\chi_2). \tag{B.15}$$

We come back to the expression for the 2-halo two-point function in B.9 and project the right hand side onto spherical harmonics. For this, we generalize a result we obtained in the previous section for the angle-dependent integrand:

$$u(\hat{n}_1-\hat{n}_a)\,u(\hat{n}_2-\hat{n}_b) = \sum_{\ell' m'} u^*_{\ell'}(\chi_1)\,\mathcal{D}^{\ell'}_{0m'}(-\hat{n}_1)\,Y^*_{\ell' m'}(\hat{n}_a)\sum_{\ell'' m''} u_{\ell''}(\chi_2)\,\mathcal{D}^{\ell'' *}_{0m''}(-\hat{n}_2)\,Y_{\ell'' m''}(\hat{n}_b). \tag{B.16}$$

Multiplying by the halo-halo auto-correlation and using the properties of $Y_{\ell m}$'s and $\mathcal{D}^\ell_{mm'}$'s to simplify the expression we get

$$\begin{aligned} u(\hat{n}_1-\hat{n}_a)\,u(\hat{n}_2-\hat{n}_b)\,\xi^{hh}(\chi_1,m_a,\chi_2,m_b) &= \\ &= \sum_{\ell m} u^*_\ell(\chi_1)\,\mathcal{D}^\ell_{0m}(-\hat{n}_1)\,u_\ell(\chi_2)\,\mathcal{D}^{\ell *}_{0m}(-\hat{n}_2)\,C^{hh}_\ell \\ &= \sum_\ell u^*_\ell(\chi_1)u_\ell(\chi_2)\,\mathcal{P}_\ell(\hat{n}_1-\hat{n}_2)\,C^{hh}_\ell(\chi_1,\chi_2,m_a,m_b). \end{aligned} \tag{B.17}$$

The multipole expansion for the general 2-halo two-point function is

$$\bar{\tau}^2\xi^{2-{\rm halo}}(\chi_1,\chi_2) = \sum_\ell C^{2-{\rm halo}}_\ell(\chi_1,\chi_2)\,\mathcal{P}_\ell(\hat{n}_1-\hat{n}_2). \tag{B.18}$$

Matching term by term we find

$$\begin{aligned} \bar{\tau}^2 C^{2-{\rm halo}}_\ell(\chi_1,\chi_2) =& \frac{4\pi}{2\ell+1}\int {\rm d}m_a\, n(\chi_1,m_a)P(\chi_1,m_a)u_\ell(\chi_1,m_a)\times \\ & \int {\rm d}m_b\, n(\chi_2,m_b)P(\chi_2,m_b)u_\ell(\chi_2,m_b)\,C^{hh}_\ell(\chi_1,m_a,\chi_2,m_b). \end{aligned} \tag{B.19}$$

Finally, we integrate over redshift to get the final expression for the 2-halo term:

$$\bar{\tau}^2 C_\ell^{2-\mathrm{halo}} = \frac{4\pi}{2\ell+1}\left[\prod_{i=1,2}\int \mathrm{d}z_i \,\frac{\chi(z_i)^2}{H(z_i)}\int \mathrm{d}m_i\, n(z_i,m_i) b(z_i,m_i) P(z_i,m_i) u_\ell(z_i,m_i)\right] C_\ell^{\mathrm{lin}}(z_1,z_2),$$
$$C_\ell^{\mathrm{lin}}(z_1,z_2) = \frac{2}{\pi}\int \mathrm{d}k\, k^2 j_\ell(k\,\chi_1)\, j_\ell(k\,\chi_2)\, P^{\mathrm{lin}}(k,\chi_1,\chi_2). \tag{B.20}$$

B.3 Two-point correlators and quadratic estimators

In this appendix we enumerate the various two-point correlation functions among the temperature and polarization anisotropies. We then list all quadratic estimators for the un-screened CMB temperature and polarization anisotropies as well as the Thomson optical depth and photon to dark photon optical depth.

The temperature correlators are:

$$\begin{aligned}
\left\langle T^{\mathrm{Sc}}_{\ell_1 m_1} T^{\mathrm{Sc}}_{\ell_2 m_2}\right\rangle =& (-1)^{m_1} C_{\ell_1}^{T^{\mathrm{Sc}}T^{\mathrm{Sc}}} \delta_{\ell_1\ell_2}\delta_{m_1 m_2} \\
&- \sum_{\ell m} \tau^{\mathrm{Th}}_{\ell m} (-1)^m \begin{pmatrix} \ell_1 & \ell_2 & \ell \\ m_1 & m_2 & -m \end{pmatrix} \sqrt{2\ell+1} W^{000}_{\ell_1\ell_2\ell}\left[C_{\ell_1}^{TT} + C_{\ell_2}^{TT}\right], \qquad \text{(B.21)} \\
\left\langle T^{\mathrm{dSc}}_{\ell_1 m_1} T^{\mathrm{dSc}}_{\ell_2 m_2}\right\rangle =& (-1)^{m_1} C_{\ell_1}^{T^{\mathrm{dSc}}T^{\mathrm{dSc}}} \delta_{\ell_1\ell_2}\delta_{m_1 m_2} \\
&+ \sum_{\ell m} T_{\ell m} (-1)^m \begin{pmatrix} \ell_1 & \ell_2 & \ell \\ m_1 & m_2 & -m \end{pmatrix} \sqrt{2\ell+1} W^{000}_{\ell_1\ell_2\ell} \bar{T}\left[C_{\ell_1}^{\tau\tau} + C_{\ell_2}^{\tau\tau}\right], \qquad \text{(B.22)} \\
\left\langle T^{\mathrm{dSc}}_{\ell_1 m_1} T^{\mathrm{Sc}}_{\ell_2 m_2}\right\rangle =& (-1)^{m_1} C_{\ell_1}^{T^{\mathrm{dSc}}T^{\mathrm{Sc}}} \delta_{\ell_1\ell_2}\delta_{m_1 m_2} \\
&+ \sum_{\ell m} T_{\ell m} (-1)^m \begin{pmatrix} \ell_1 & \ell_2 & \ell \\ m_1 & m_2 & -m \end{pmatrix} \sqrt{2\ell+1} W^{000}_{\ell_1\ell_2\ell} \bar{T} C_{\ell_1}^{\tau\tau^{\mathrm{Th}}} \\
&- \sum_{\ell m} \tau^*_{\ell m} (-1)^m \begin{pmatrix} \ell_1 & \ell_2 & \ell \\ m_1 & m_2 & -m \end{pmatrix} \sqrt{2\ell+1} W^{000}_{\ell_1\ell_2\ell} C_{\ell_2}^{TT}, \qquad \text{(B.23)}
\end{aligned}$$

where

$$C_L^{T^{\rm Sc}T^{\rm Sc}} = C_L^{TT} + \sum_{\ell\ell'} C_{\ell'}^{\tau^{\rm Th}\tau^{\rm Th}} C_\ell^{TT} \left(W_{L\ell\ell'}^{000}\right)^2, \tag{B.24}$$

$$C_L^{T^{\rm dSc}T^{\rm dSc}} = \bar{T}^2\, C_L^{\tau\tau} + \sum_{\ell\ell'} C_{\ell'}^{\tau\tau} C_\ell^{TT} \left(W_{L\ell\ell'}^{000}\right)^2, \tag{B.25}$$

$$C_L^{T^{\rm dSc}T^{\rm Sc}} = \sum_{\ell\ell'} C_{\ell'}^{\tau\tau^{\rm Th}} C_\ell^{TT} \left(W_{L\ell\ell'}^{000}\right)^2. \tag{B.26}$$

The E-mode correlators are:

$$\begin{aligned}\left\langle E_{\ell_1 m_1}^{\rm Sc} E_{\ell_2 m_2}^{\rm Sc}\right\rangle =& (-1)^{m_1} C_{\ell_1}^{E^{\rm Sc}E^{\rm Sc}} \delta_{\ell_1\ell_2}\delta_{m_1 m_2} \\ & - \sum_{\ell m} \tau_{\ell m}^{\rm Th} (-1)^m \begin{pmatrix} \ell_1 & \ell_2 & \ell \\ m_1 & m_2 & -m \end{pmatrix} \sqrt{2\ell+1} e_{\ell_1\ell_2\ell} W_{\ell_1\ell_2\ell}^{220} \left[C_{\ell_1}^{EE} + C_{\ell_2}^{EE}\right],\end{aligned} \tag{B.27}$$

$$\left\langle E_{\ell_1 m_1}^{\rm dSc} E_{\ell_2 m_2}^{\rm dSc}\right\rangle = (-1)^{m_1} C_{\ell_1}^{E^{\rm dSc}E^{\rm dSc}} \delta_{\ell_1\ell_2}\delta_{m_1 m_2}, \tag{B.28}$$

$$\begin{aligned}\left\langle E_{\ell_1 m_1}^{\rm dSc} E_{\ell_2 m_2}^{\rm Sc}\right\rangle =& (-1)^{m_1} C_{\ell_1}^{E^{\rm dSc}E^{\rm Sc}} \delta_{\ell_1\ell_2}\delta_{m_1 m_2} \\ & - \sum_{\ell m} \tau_{\ell m}^{*} (-1)^m \begin{pmatrix} \ell_1 & \ell_2 & \ell \\ m_1 & m_2 & -m \end{pmatrix} \sqrt{2\ell+1} e_{\ell_1\ell_2\ell} W_{\ell_1\ell_2\ell}^{220} C_{\ell_2}^{EE},\end{aligned} \tag{B.29}$$

where

$$C_L^{E^{\rm Sc}E^{\rm Sc}} = C_L^{EE} + \sum_{\ell\ell'} C_{\ell'}^{\tau^{\rm Th}\tau^{\rm Th}} C_\ell^{EE} e_{L\ell\ell'} \left(W_{L\ell\ell'}^{220}\right)^2, \tag{B.30}$$

$$C_L^{E^{\rm dSc}E^{\rm dSc}} = \sum_{\ell\ell'} C_{\ell'}^{\tau\tau} C_\ell^{EE} e_{L\ell\ell'} \left(W_{L\ell\ell'}^{220}\right)^2, \tag{B.31}$$

$$C_L^{E^{\rm dSc}E^{\rm Sc}} = \sum_{\ell\ell'} C_{\ell'}^{\tau\tau^{\rm Th}} C_\ell^{EE} e_{L\ell\ell'} \left(W_{L\ell\ell'}^{220}\right)^2 \tag{B.32}$$

and

$$e_{\ell\ell'\ell''} \equiv \frac{1}{2}\left[1 + (-1)^{\ell+\ell'+\ell''}\right]. \tag{B.33}$$

The B-mode correlators are:

$$\left\langle iB_{\ell_1 m_1}^{\rm Sc} iB_{\ell_2 m_2}^{\rm Sc}\right\rangle = (-1)^{m_1} C_{\ell_1}^{B^{\rm Sc}B^{\rm Sc}} \delta_{\ell_1\ell_2}\delta_{m_1 m_2}, \tag{B.34}$$

$$\left\langle iB_{\ell_1 m_1}^{\rm dSc} iB_{\ell_2 m_2}^{\rm dSc}\right\rangle = (-1)^{m_1} C_{\ell_1}^{B^{\rm dSc}B^{\rm dSc}} \delta_{\ell_1\ell_2}\delta_{m_1 m_2}, \tag{B.35}$$

$$\left\langle iB_{\ell_1 m_1}^{\rm dSc} iB_{\ell_2 m_2}^{\rm Sc}\right\rangle = (-1)^{m_1} C_{\ell_1}^{B^{\rm dSc}B^{\rm Sc}} \delta_{\ell_1\ell_2}\delta_{m_1 m_2}, \tag{B.36}$$

where

$$C_L^{B^{\rm Sc}B^{\rm Sc}} = \sum_{\ell\ell'} C_{\ell'}^{\tau^{\rm Th}\tau^{\rm Th}} C_\ell^{EE} o_{L\ell\ell'} \left(W_{L\ell\ell'}^{220}\right)^2, \tag{B.37}$$

$$C_L^{B^{\rm dSc}B^{\rm dSc}} = \sum_{\ell\ell'} C_{\ell'}^{\tau\tau} C_\ell^{EE} o_{L\ell\ell'} \left(W_{L\ell\ell'}^{220}\right)^2, \tag{B.38}$$

$$C_L^{B^{\rm dSc}B^{\rm Sc}} = \sum_{\ell\ell'} C_{\ell'}^{\tau\tau^{\rm Th}} C_\ell^{EE} o_{L\ell\ell'} \left(W_{L\ell\ell'}^{220}\right)^2, \tag{B.39}$$

and

$$o_{\ell\ell'\ell''} \equiv \frac{1}{2}\left[1 - (-1)^{\ell+\ell'+\ell''}\right]. \tag{B.40}$$

The E-B correlators are:

$$\left\langle E_{\ell_1 m_1}^{\rm Sc} i B_{\ell_2 m_2}^{\rm Sc} \right\rangle = -\sum_{\ell m} \tau_{\ell m}^{\rm Th} (-1)^m \begin{pmatrix} \ell_1 & \ell_2 & \ell \\ m_1 & m_2 & -m \end{pmatrix} \sqrt{2\ell+1} o_{\ell_1\ell_2\ell} W_{\ell_2\ell_1\ell}^{220} C_{\ell_1}^{EE}, \tag{B.41}$$

$$\left\langle E_{\ell_1 m_1}^{\rm dSc} i B_{\ell_2 m_2}^{\rm dSc} \right\rangle = \left\langle E_{\ell_1 m_1}^{\rm dSc} i B_{\ell_2 m_2}^{\rm Sc} \right\rangle = 0, \tag{B.42}$$

$$\left\langle E_{\ell_1 m_1}^{\rm Sc} i B_{\ell_2 m_2}^{\rm dSc} \right\rangle = -\sum_{\ell m} \tau_{\ell m} (-1)^m \begin{pmatrix} \ell_1 & \ell_2 & \ell \\ m_1 & m_2 & -m \end{pmatrix} \sqrt{2\ell+1} o_{\ell_1\ell_2\ell} W_{\ell_2\ell_1\ell}^{220} C_{\ell_1}^{EE}. \tag{B.43}$$

The T-E correlators are:

$$\begin{aligned}\left\langle T^{\rm Sc}_{\ell_1 m_1} E^{\rm Sc}_{\ell_2 m_2}\right\rangle =&(-1)^{m_1} C_{\ell_1}^{T^{\rm Sc}E^{\rm Sc}} \delta_{\ell_1\ell_2}\delta_{m_1 m_2}\\ &-\sum_{\ell m}\tau^{\rm Th}_{\ell m}(-1)^m \begin{pmatrix}\ell_1 & \ell_2 & \ell\\ m_1 & m_2 & -m\end{pmatrix}\sqrt{2\ell+1}\left[W^{000}_{\ell_1\ell_2\ell}C^{TE}_{\ell_2}+W^{220}_{\ell_2\ell_1\ell}C^{TE}_{\ell_1}\right],\end{aligned} \tag{B.44}$$

$$\begin{aligned}\left\langle T^{\rm dSc}_{\ell_1 m_1} E^{\rm dSc}_{\ell_2 m_2}\right\rangle =&(-1)^{m_1} C_{\ell_1}^{T^{\rm dSc}E^{\rm dSc}} \delta_{\ell_1\ell_2}\delta_{m_1 m_2}\\ &+\sum_{\ell m} E_{\ell m}(-1)^m \begin{pmatrix}\ell_1 & \ell_2 & \ell\\ m_1 & m_2 & -m\end{pmatrix}\sqrt{2\ell+1}e_{\ell_1\ell_2\ell}W^{220}_{\ell_2\ell\ell_1}\bar{T}C^{\tau\tau}_{\ell_1},\end{aligned} \tag{B.45}$$

$$\begin{aligned}\left\langle T^{\rm Sc}_{\ell_1 m_1} E^{\rm dSc}_{\ell_2 m_2}\right\rangle =&(-1)^{m_1} C_{\ell_1}^{T^{\rm Sc}E^{\rm dSc}} \delta_{\ell_1\ell_2}\delta_{m_1 m_2}\\ &-\sum_{\ell m} \tau_{\ell m}(-1)^m \begin{pmatrix}\ell_1 & \ell_2 & \ell\\ m_1 & m_2 & -m\end{pmatrix}\sqrt{2\ell+1}e_{\ell_1\ell_2\ell}W^{220}_{\ell_2\ell_1\ell}C^{TE}_{\ell_1},\end{aligned} \tag{B.46}$$

$$\begin{aligned}\left\langle T^{\rm dSc}_{\ell_1 m_1} E^{\rm Sc}_{\ell_2 m_2}\right\rangle =&(-1)^{m_1} C_{\ell_1}^{T^{\rm dSc}E^{\rm Sc}} \delta_{\ell_1\ell_2}\delta_{m_1 m_2}\\ &+\sum_{\ell m} E_{\ell m}(-1)^m \begin{pmatrix}\ell_1 & \ell_2 & \ell\\ m_1 & m_2 & -m\end{pmatrix}\sqrt{2\ell+1}e_{\ell_1\ell_2\ell}W^{220}_{\ell_2\ell\ell_1}\bar{T}C_{\ell_1}^{\tau\tau^{\rm Th}}\\ &-\sum_{\ell m} \tau^*_{\ell m}(-1)^m \begin{pmatrix}\ell_1 & \ell_2 & \ell\\ m_1 & m_2 & -m\end{pmatrix}\sqrt{2\ell+1}W^{000}_{\ell_1\ell_2\ell}C^{TE}_{\ell_2},\end{aligned} \tag{B.47}$$

where

$$C_L^{T^{\rm Sc}E^{\rm Sc}} = C_L^{TE} + \sum_{\ell\ell'} C_{\ell'}^{\tau^{\rm Th}\tau^{\rm Th}} C_\ell^{TE} W^{000}_{L\ell\ell'} W^{220}_{L\ell\ell'}, \tag{B.48}$$

$$C_L^{T^{\rm dSc}E^{\rm dSc}} = \sum_{\ell\ell'} C_{\ell'}^{\tau\tau} C_\ell^{TE} W^{000}_{L\ell\ell'} W^{220}_{L\ell\ell'}, \tag{B.49}$$

$$C_L^{T^{\rm dSc}E^{\rm Sc}} = \sum_{\ell\ell'} C_{\ell'}^{\tau\tau^{\rm Th}} C_\ell^{TE} W^{000}_{L\ell\ell'} W^{220}_{L\ell\ell'}. \tag{B.50}$$

The T-B correlators are:

$$\left\langle T^{\rm Sc}_{\ell_1 m_1} iB^{\rm Sc}_{\ell_2 m_2}\right\rangle = \left\langle T^{\rm dSc}_{\ell_1 m_1} iB^{\rm dSc}_{\ell_2 m_2}\right\rangle = \left\langle T^{\rm Sc}_{\ell_1 m_1} iB^{\rm dSc}_{\ell_2 m_2}\right\rangle = 0, \tag{B.51}$$

$$\left\langle T^{\rm dSc}_{\ell_1 m_1} iB^{\rm Sc}_{\ell_2 m_2}\right\rangle = \sum_{\ell m} E_{\ell m}(-1)^m \begin{pmatrix}\ell_1 & \ell_2 & \ell\\ m_1 & m_2 & -m\end{pmatrix}\sqrt{2\ell+1}o_{\ell_1\ell_2\ell}W^{220}_{\ell_2\ell\ell_1}\bar{T}C_{\ell_1}^{\tau\tau^{\rm Th}}. \tag{B.52}$$

Moving on to the quadratic estimators, there are two estimators for the un-screened

temperature anisotropies

$$\hat{T}_{LM} = N_L^{T;T^{\rm dSc}T^{\rm dSc}} \sum_{\ell m}\sum_{\ell' m'} (-1)^M \begin{pmatrix} \ell & \ell' & L \\ m & m' & -M \end{pmatrix} \sqrt{2L+1}\, G_{\ell\ell' L}^{T;T^{\rm dSc}T^{\rm dSc}} T_{\ell m}^{\rm dSc} T_{\ell' m'}^{\rm dSc}, \quad \text{(B.53)}$$

$$\hat{T}_{LM} = N_L^{T;T^{\rm dSc}T^{\rm Sc}} \sum_{\ell m}\sum_{\ell' m'} (-1)^M \begin{pmatrix} \ell & \ell' & L \\ m & m' & -M \end{pmatrix} \sqrt{2L+1}\, G_{\ell\ell' L}^{T;T^{\rm dSc}T^{\rm Sc}} T_{\ell m}^{\rm dSc} T_{\ell' m'}^{\rm Sc}. \quad \text{(B.54)}$$

The weights and prefactors are given by

$$G_{\ell\ell' L}^{T;T^{\rm dSc}T^{\rm dSc}} = \frac{W_{\ell\ell' L}^{000}\bar{T}\left[C_\ell^{\tau\tau} + C_{\ell'}^{\tau\tau}\right]}{2C_\ell^{T^{\rm dSc}T^{\rm dSc}} C_{\ell'}^{T^{\rm dSc}T^{\rm dSc}}}, \qquad N_L^{T;T^{\rm dSc}T^{\rm dSc}} = \left[\sum_{\ell\ell'} \frac{\bar{T}^2 \left|W_{\ell\ell' L}^{000}\left[C_\ell^{\tau\tau} + C_{\ell'}^{\tau\tau}\right]\right|^2}{2C_\ell^{T^{\rm dSc}T^{\rm dSc}} C_{\ell'}^{T^{\rm dSc}T^{\rm dSc}}}\right]^{-1}, \quad \text{(B.55)}$$

$$G_{\ell\ell' L}^{T;T^{\rm dSc}T^{\rm Sc}} = \frac{W_{\ell\ell' L}^{000}\bar{T} C_\ell^{\tau\tau^{\rm Th}}}{C_\ell^{T^{\rm dSc}T^{\rm dSc}} C_{\ell'}^{T^{\rm Sc}T^{\rm Sc}}}, \qquad N_L^{T;T^{\rm dSc}T^{\rm Sc}} = \left[\sum_{\ell\ell'} \frac{\bar{T}^2 \left|W_{\ell\ell' L}^{000} C_\ell^{\tau\tau^{\rm Th}}\right|^2}{C_\ell^{T^{\rm dSc}T^{\rm dSc}} C_{\ell'}^{T^{\rm Sc}T^{\rm Sc}}}\right]^{-1}. \quad \text{(B.56)}$$

There are three estimators for the un-screened E-mode polarization anisotropies

$$\hat{E}_{LM} = N_L^{E;T^{\rm dSc}E^{\rm dSc}} \sum_{\ell m}\sum_{\ell' m'} (-1)^M \begin{pmatrix} \ell & \ell' & L \\ m & m' & -M \end{pmatrix} \sqrt{2L+1}\, G_{\ell\ell' L}^{E;T^{\rm dSc}E^{\rm dSc}} T_{\ell m}^{\rm dSc} E_{\ell' m'}^{\rm dSc}, \quad \text{(B.57)}$$

$$\hat{E}_{LM} = N_L^{E;T^{\rm dSc}E^{\rm Sc}} \sum_{\ell m}\sum_{\ell' m'} (-1)^M \begin{pmatrix} \ell & \ell' & L \\ m & m' & -M \end{pmatrix} \sqrt{2L+1}\, G_{\ell\ell' L}^{E;T^{\rm dSc}E^{\rm Sc}} T_{\ell m}^{\rm dSc} E_{\ell' m'}^{\rm Sc}, \quad \text{(B.58)}$$

$$\hat{E}_{LM}^* = N_L^{E;T^{\rm dSc}B^{\rm Sc}} \sum_{\ell m}\sum_{\ell' m'} (-1)^M \begin{pmatrix} \ell & \ell' & L \\ m & m' & -M \end{pmatrix} \sqrt{2L+1}\, G_{\ell\ell' L}^{E;T^{\rm dSc}B^{\rm Sc}} T_{\ell m}^{\rm dSc} B_{\ell' m'}^{\rm Sc}, \quad \text{(B.59)}$$

where

$$G_{\ell\ell' L}^{E;T^{\rm dSc}E^{\rm dSc}} = \frac{e_{\ell\ell' L} W_{\ell' L\ell}^{220}\bar{T} C_\ell^{\tau\tau}}{C_\ell^{T^{\rm dSc}T^{\rm dSc}} C_{\ell'}^{E^{\rm dSc}E^{\rm dSc}}}, \quad N_L^{E;T^{\rm dSc}E^{\rm dSc}} = \left[\sum_{\ell\ell'} \frac{e_{\ell\ell' L}\bar{T}^2 \left|W_{\ell' L\ell}^{220} C_\ell^{\tau\tau}\right|^2}{C_\ell^{T^{\rm dSc}T^{\rm dSc}} C_{\ell'}^{E^{\rm dSc}E^{\rm dSc}}}\right]^{-1}, \quad \text{(B.60)}$$

$$G_{\ell\ell' L}^{E;T^{\rm dSc}E^{\rm Sc}} = \frac{e_{\ell\ell' L} W_{\ell' L\ell}^{220}\bar{T} C_\ell^{\tau\tau^{\rm Th}}}{C_\ell^{T^{\rm dSc}T^{\rm dSc}} C_{\ell'}^{E^{\rm Sc}E^{\rm Sc}}}, \quad N_L^{E;T^{\rm dSc}E^{\rm Sc}} = \left[\sum_{\ell\ell'} \frac{e_{\ell\ell' L}\bar{T}^2 \left|W_{\ell' L\ell}^{220} C_\ell^{\tau\tau^{\rm Th}}\right|^2}{C_\ell^{T^{\rm dSc}T^{\rm dSc}} C_{\ell'}^{E^{\rm Sc}E^{\rm Sc}}}\right]^{-1}, \quad \text{(B.61)}$$

$$iG_{\ell\ell' L}^{E;T^{\rm dSc}B^{\rm Sc}} = \frac{o_{\ell\ell' L} W_{\ell' L\ell}^{220}\bar{T} C_\ell^{\tau\tau^{\rm Th}}}{C_\ell^{T^{\rm dSc}T^{\rm dSc}} C_{\ell'}^{B^{\rm Sc}B^{\rm Sc}}}, \quad N_L^{E;T^{\rm dSc}B^{\rm Sc}} = \left[\sum_{\ell\ell'} \frac{o_{\ell\ell' L}\bar{T}^2 \left|W_{\ell' L\ell}^{220} C_\ell^{\tau\tau^{\rm Th}}\right|^2}{C_\ell^{T^{\rm dSc}T^{\rm dSc}} C_{\ell'}^{B^{\rm Sc}B^{\rm Sc}}}\right]^{-1}. \quad \text{(B.62)}$$

There are four estimators for the Thomson optical depth:

$$\hat{\tau}^{\rm Th}_{LM} = - N^{\tau^{\rm Th};T^{\rm Sc}T^{\rm Sc}}_{L} \sum_{\ell m} \sum_{\ell' m'} (-1)^M \begin{pmatrix} \ell & \ell' & L \\ m & m' & -M \end{pmatrix} \sqrt{2L+1}\, G^{\tau^{\rm Th};T^{\rm Sc}T^{\rm Sc}}_{\ell\ell' L} T^{\rm Sc}_{\ell m} T^{\rm Sc}_{\ell' m'}, \quad \text{(B.63)}$$

$$\hat{\tau}^{\rm Th}_{LM} = - N^{\tau^{\rm Th};E^{\rm Sc}E^{\rm Sc}}_{L} \sum_{\ell m} \sum_{\ell' m'} (-1)^M \begin{pmatrix} \ell & \ell' & L \\ m & m' & -M \end{pmatrix} \sqrt{2L+1}\, G^{\tau^{\rm Th};E^{\rm Sc}E^{\rm Sc}}_{\ell\ell' L} E^{\rm Sc}_{\ell m} E^{\rm Sc}_{\ell' m'}, \quad \text{(B.64)}$$

$$\hat{\tau}^{\rm Th}_{LM} = - N^{\tau^{\rm Th};E^{\rm Sc}B^{\rm Sc}}_{L} \sum_{\ell m} \sum_{\ell' m'} (-1)^M \begin{pmatrix} \ell & \ell' & L \\ m & m' & -M \end{pmatrix} \sqrt{2L+1}\, G^{\tau^{\rm Th};E^{\rm Sc}B^{\rm Sc}}_{\ell\ell' L} E^{\rm Sc}_{\ell m} B^{\rm Sc}_{\ell' m'}, \quad \text{(B.65)}$$

$$\hat{\tau}^{\rm Th}_{LM} = - N^{\tau^{\rm Th};T^{\rm Sc}E^{\rm Sc}}_{L} \sum_{\ell m} \sum_{\ell' m'} (-1)^M \begin{pmatrix} \ell & \ell' & L \\ m & m' & -M \end{pmatrix} \sqrt{2L+1}\, G^{\tau^{\rm Th};T^{\rm Sc}E^{\rm Sc}}_{\ell\ell' L} T^{\rm Sc}_{\ell m} E^{\rm Sc}_{\ell' m'}, \quad \text{(B.66)}$$

where

$$G^{\tau^{\rm Th};T^{\rm Sc}T^{\rm Sc}}_{\ell\ell' L} = \frac{W^{000}_{\ell\ell' L}\left[C^{TT}_{\ell} + C^{TT}_{\ell'}\right]}{2C^{T^{\rm Sc}T^{\rm Sc}}_{\ell} C^{T^{\rm Sc}T^{\rm Sc}}_{\ell'}}, \qquad N^{\tau^{\rm Th};T^{\rm Sc}T^{\rm Sc}}_{L} = \left[\sum_{\ell\ell'} \frac{\left|W^{000}_{\ell\ell' L}\left[C^{TT}_{\ell} + C^{TT}_{\ell'}\right]\right|^2}{2C^{T^{\rm Sc}T^{\rm Sc}}_{\ell} C^{T^{\rm Sc}T^{\rm Sc}}_{\ell'}}\right]^{-1}, \quad \text{(B.67)}$$

$$G^{\tau^{\rm Th};E^{\rm Sc}E^{\rm Sc}}_{\ell\ell' L} = \frac{e_{\ell\ell' L} W^{220}_{\ell\ell' L}\left[C^{\tau\tau}_{\ell} + C^{\tau\tau}_{\ell'}\right]}{2C^{E^{\rm Sc}E^{\rm Sc}}_{\ell} C^{E^{\rm Sc}E^{\rm Sc}}_{\ell'}}, \quad N^{\tau^{\rm Th};E^{\rm Sc}E^{\rm Sc}}_{L} = \left[\sum_{\ell\ell'} \frac{e_{\ell\ell' L}\left|W^{220}_{\ell\ell' L}\left[C^{\tau\tau}_{\ell} + C^{\tau\tau}_{\ell'}\right]\right|^2}{2C^{E^{\rm Sc}E^{\rm Sc}}_{\ell} C^{E^{\rm Sc}E^{\rm Sc}}_{\ell'}}\right]^{-1}, \quad \text{(B.68)}$$

$$iG^{\tau^{\rm Th};E^{\rm Sc}B^{\rm Sc}}_{\ell\ell' L} = \frac{o_{\ell\ell' L} W^{220}_{\ell' \ell L} C^{EE}_{\ell}}{C^{E^{\rm Sc}E^{\rm Sc}}_{\ell} C^{B^{\rm Sc}B^{\rm Sc}}_{\ell'}}, \qquad N^{\tau^{\rm Th};E^{\rm Sc}B^{\rm Sc}}_{L} = \left[\sum_{\ell\ell'} \frac{o_{\ell\ell' L}\left|W^{220}_{\ell' \ell L} C^{EE}_{\ell}\right|^2}{C^{E^{\rm Sc}E^{\rm Sc}}_{\ell} C^{B^{\rm Sc}B^{\rm Sc}}_{\ell'}}\right]^{-1}, \quad \text{(B.69)}$$

$$G^{\tau^{\rm Th};T^{\rm Sc}E^{\rm Sc}}_{\ell\ell' L} = \frac{W^{000}_{\ell\ell' L} C^{TE}_{\ell'} + W^{220}_{\ell' \ell L} C^{TE}_{\ell}}{C^{T^{\rm Sc}T^{\rm Sc}}_{\ell} C^{E^{\rm Sc}E^{\rm Sc}}_{\ell'}}, \quad N^{\tau^{\rm Th};T^{\rm Sc}E^{\rm Sc}}_{L} = \left[\sum_{\ell\ell'} \frac{\left|W^{000}_{\ell\ell' L} C^{TE}_{\ell'} + W^{220}_{\ell' \ell L} C^{TE}_{\ell}\right|^2}{C^{T^{\rm Sc}T^{\rm Sc}}_{\ell} C^{E^{\rm Sc}E^{\rm Sc}}_{\ell'}}\right]^{-1}. \quad \text{(B.70)}$$

There are five estimators for the photon to dark photon optical depth:

$$\hat{\tau}^*_{LM} = -\, N_L^{\tau;T^{\rm dSc}T^{\rm Sc}} \sum_{\ell m}\sum_{\ell' m'} (-1)^M \begin{pmatrix} \ell & \ell' & L \\ m & m' & -M \end{pmatrix} \sqrt{2L+1}\, G^{\tau;T^{\rm dSc}T^{\rm Sc}}_{\ell\ell' L}\, T^{\rm dSc}_{\ell m} T^{\rm Sc}_{\ell' m'}, \quad \text{(B.71)}$$

$$\hat{\tau}^*_{LM} = -\, N_L^{\tau;E^{\rm dSc}E^{\rm Sc}} \sum_{\ell m}\sum_{\ell' m'} (-1)^M \begin{pmatrix} \ell & \ell' & L \\ m & m' & -M \end{pmatrix} \sqrt{2L+1}\, G^{\tau;E^{\rm dSc}E^{\rm Sc}}_{\ell\ell' L}\, E^{\rm dSc}_{\ell m} E^{\rm Sc}_{\ell' m'}, \quad \text{(B.72)}$$

$$\hat{\tau}_{LM} = -\, N_L^{\tau;E^{\rm Sc}B^{\rm dSc}} \sum_{\ell m}\sum_{\ell' m'} (-1)^M \begin{pmatrix} \ell & \ell' & L \\ m & m' & -M \end{pmatrix} \sqrt{2L+1}\, G^{\tau;E^{\rm Sc}B^{\rm dSc}}_{\ell\ell' L}\, E^{\rm Sc}_{\ell m} B^{\rm dSc}_{\ell' m'}, \quad \text{(B.73)}$$

$$\hat{\tau}^*_{LM} = -\, N_L^{\tau;T^{\rm dSc}E^{\rm Sc}} \sum_{\ell m}\sum_{\ell' m'} (-1)^M \begin{pmatrix} \ell & \ell' & L \\ m & m' & -M \end{pmatrix} \sqrt{2L+1}\, G^{\tau;T^{\rm dSc}E^{\rm Sc}}_{\ell\ell' L}\, T^{\rm dSc}_{\ell m} E^{\rm Sc}_{\ell' m'}, \quad \text{(B.74)}$$

$$\hat{\tau}_{LM} = -\, N_L^{\tau;T^{\rm Sc}E^{\rm dSc}} \sum_{\ell m}\sum_{\ell' m'} (-1)^M \begin{pmatrix} \ell & \ell' & L \\ m & m' & -M \end{pmatrix} \sqrt{2L+1}\, G^{\tau;T^{\rm Sc}E^{\rm dSc}}_{\ell\ell' L}\, T^{\rm Sc}_{\ell m} E^{\rm dSc}_{\ell' m'}, \quad \text{(B.75)}$$

where

$$G^{\tau;T^{\rm dSc}T^{\rm Sc}}_{\ell\ell' L} = \frac{W^{000}_{\ell\ell' L} C^{TT}_{\ell'}}{C^{T^{\rm dSc}T^{\rm dSc}}_{\ell} C^{T^{\rm Sc}T^{\rm Sc}}_{\ell'}}, \qquad N_L^{\tau;T^{\rm dSc}T^{\rm Sc}} = \left[\sum_{\ell\ell'} \frac{\left|W^{000}_{\ell\ell' L} C^{TT}_{\ell'}\right|^2}{C^{T^{\rm dSc}T^{\rm dSc}}_{\ell} C^{T^{\rm Sc}T^{\rm Sc}}_{\ell'}}\right]^{-1}, \quad \text{(B.76)}$$

$$G^{\tau;E^{\rm dSc}E^{\rm Sc}}_{\ell\ell' L} = \frac{W^{220}_{\ell\ell' L} C^{EE}_{\ell'}}{C^{E^{\rm dSc}E^{\rm dSc}}_{\ell} C^{E^{\rm Sc}E^{\rm Sc}}_{\ell'}}, \qquad N_L^{\tau;E^{\rm dSc}E^{\rm Sc}} = \left[\sum_{\ell\ell'} \frac{\left|W^{220}_{\ell\ell' L} C^{EE}_{\ell'}\right|^2}{C^{E^{\rm dSc}E^{\rm dSc}}_{\ell} C^{E^{\rm Sc}E^{\rm Sc}}_{\ell'}}\right]^{-1}, \quad \text{(B.77)}$$

$$iG^{\tau;E^{\rm Sc}B^{\rm dSc}}_{\ell\ell' L} = \frac{o_{\ell\ell' L} W^{220}_{\ell'\ell L} C^{EE}_{\ell}}{C^{E^{\rm Sc}E^{\rm Sc}}_{\ell} C^{B^{\rm dSc}B^{\rm dSc}}_{\ell'}}, \qquad N_L^{\tau;E^{\rm Sc}B^{\rm dSc}} = \left[\sum_{\ell\ell'} \frac{o_{\ell\ell' L} \left|W^{220}_{\ell'\ell L} C^{EE}_{\ell}\right|^2}{C^{E^{\rm Sc}E^{\rm Sc}}_{\ell} C^{B^{\rm dSc}B^{\rm dSc}}_{\ell'}}\right]^{-1}, \quad \text{(B.78)}$$

$$G^{\tau;T^{\rm dSc}E^{\rm Sc}}_{\ell\ell' L} = \frac{W^{000}_{\ell\ell' L} C^{TE}_{\ell'}}{C^{T^{\rm dSc}T^{\rm dSc}}_{\ell} C^{E^{\rm Sc}E^{\rm Sc}}_{\ell'}}, \qquad N_L^{\tau;T^{\rm dSc}E^{\rm Sc}} = \left[\sum_{\ell\ell'} \frac{\left|W^{000}_{\ell\ell' L} C^{TE}_{\ell'}\right|^2}{C^{T^{\rm dSc}T^{\rm dSc}}_{\ell} C^{E^{\rm Sc}E^{\rm Sc}}_{\ell'}}\right]^{-1}, \quad \text{(B.79)}$$

$$G^{\tau;T^{\rm Sc}E^{\rm dSc}}_{\ell\ell' L} = \frac{e_{\ell\ell' L} W^{220}_{\ell'\ell L} C^{TE}_{\ell}}{C^{T^{\rm Sc}T^{\rm Sc}}_{\ell} C^{E^{\rm dSc}E^{\rm dSc}}_{\ell'}}, \qquad N_L^{\tau;T^{\rm Sc}E^{\rm dSc}} = \left[\sum_{\ell\ell'} \frac{e_{\ell\ell' L} \left|W^{220}_{\ell'\ell L} C^{TE}_{\ell}\right|^2}{C^{T^{\rm Sc}T^{\rm Sc}}_{\ell} C^{E^{\rm dSc}E^{\rm dSc}}_{\ell'}}\right]^{-1}. \quad \text{(B.80)}$$

B.4 Photon-axion conversion

B.4.1 Homogeneous magnetic field

An axion field a, with mass $m_{\rm a}$, can interact with the SM photon as

$$\mathcal{L}_{\rm a\gamma} = -\frac{1}{4} g_{\rm a\gamma\gamma} F^{\mu\nu} \tilde{F}_{\mu\nu}\, {\rm a} = g_{\rm a\gamma\gamma} \mathbf{E}\cdot\mathbf{B}\, {\rm a}, \tag{B.81}$$

where $F^{\mu\nu}$ is the electromagnetic field-strength tensor, and $\tilde{F}^{\mu\nu} \equiv 1/2\epsilon_{\mu\nu\alpha\beta}F^{\alpha\beta}$ its dual. This term induces photon-axion oscillations in the presence of an external magnetic field transverse to the photon propagation direction. In particular, for a constant transverse magnetic field $\mathbf{B}$, the photon state polarized along the $\mathbf{B}$ field, $A_\parallel$, mixes with an ultra-relativistic axion ($\omega \gg m_{\rm a}$) according to the equation of motion [247, 248, 249]

$$\left[\omega - i\partial_z + \begin{pmatrix} \Delta_{\rm pl} & \Delta_{\rm a\gamma} \\ \Delta_{\rm a\gamma} & \Delta_{\rm a} \end{pmatrix}\right] \begin{pmatrix} A_\parallel \\ {\rm a} \end{pmatrix} = 0, \tag{B.82}$$

where $\Delta_{\rm pl} = -m_\gamma^2/(2\omega)$, $\Delta_{\rm a} = -m_{\rm a}^2/(2\omega)$, $\Delta_{\rm a\gamma} = g_{\rm a\gamma\gamma}|\mathbf{B}|/2$, and $m_\gamma^2 = e^2 n_e/m_e$ denotes the photon plasma mass in an ionized medium with electron density n_e. Notice that we have neglected the Cotton-Mouton birefringence of fluids in the presence of an external magnetic field and Faraday rotation that couples the two photon polarizations, as they do not affect the rest of the discussion. The mixing matrix can be diagonalized by rotating the fields by an angle

$$\theta = \frac{1}{2}\arctan\frac{2\Delta_{\rm a\gamma}}{\Delta_{\rm pl} - \Delta_{\rm a}}, \tag{B.83}$$

and the probability of the $A_\parallel$ state to convert into an axion after traveling a distance r can be obtained, similarly to the case of neutrino oscillations [378], as

$$P(A_\parallel \to {\rm a}) = (\Delta_{\rm a\gamma} r)^2 \frac{\sin^2(\Delta_{\rm osc} r/2)}{(\Delta_{\rm osc} r/2)^2}, \tag{B.84}$$

where $\Delta_{\rm osc}^2 \equiv (\Delta_{\rm pl} - \Delta_{\rm a})^2 + 4\Delta_{\rm a\gamma}^2$ is the oscillation wavenumber, so that one complete oscillation is obtained after a distance $l_{\rm osc} = 2\pi/\Delta_{\rm osc}$. The oscillation length varies significantly between vacuum ($m_{\rm a}^2 \gg m_\gamma^2$) and a resonance region ($m_{\rm a}^2 \simeq m_\gamma^2$):

$$l_{\rm osc} = \begin{cases} \frac{4\pi\omega}{m_{\rm a}^2} \simeq 0.01\,{\rm pc}\,\left(\frac{\omega}{10^{-4}{\rm eV}}\right)\left(\frac{10^{-12}\,{\rm eV}}{m_{\rm a}}\right)^2, & |\delta m^2| \simeq m_{\rm a}^2 \gg 2\omega g_{\rm a\gamma\gamma}|\mathbf{B}|, \\ \frac{2\pi}{g_{\rm a\gamma\gamma}|\mathbf{B}|} \simeq 10\,{\rm Mpc}\,\left(\frac{10^{-12}{\rm GeV}^{-1}}{g_{\rm a\gamma\gamma}}\right)\left(\frac{0.1\,\mu{\rm G}}{|\mathbf{B}|}\right), & |\delta m^2| \ll 2\omega g_{\rm a\gamma\gamma}|\mathbf{B}|, \end{cases} \tag{B.85}$$

where $\delta m^2 \equiv m_{\rm a}^2 - m_\gamma^2$. If the photon path crosses a region where the resonance condition is met, the total conversion probability is dominated by the resonance contribution, while multiple oscillations before and after the resonance average out and can be neglected. Similarly to the well-known case of MSW neutrino resonant conversion in a medium [216, 215], the conversion probability of a photon into an axion is then given by [250]

$$P(A_\parallel \to {\rm a})_{\rm res} = 1 - p, \tag{B.86}$$

where p is the level crossing probability. This expression is valid as long as there are regions before and after the resonance where the mixing angle in (B.83) is small, i.e. where $|\Delta_{\rm pl} - \Delta_{\rm a}| \gg \Delta_{{\rm a}\gamma}$, or

$$|\delta m^2| \gg 2\omega g_{{\rm a}\gamma\gamma}|\mathbf{B}| \simeq (10^{-17}\,{\rm eV})^2 \left(\frac{\omega}{10^{-4}\,{\rm eV}}\right)\left(\frac{{\rm g}_{{\rm a}\gamma\gamma}}{10^{-12}\,{\rm GeV}^{-1}}\right)\left(\frac{|\mathbf{B}|}{0.1\,\mu{\rm G}}\right). \tag{B.87}$$

Assuming that the plasma mass, i.e. the electron number density, varies linearly across the resonance, the level crossing probability can be computed using the Landau-Zener expression [250, 251, 252]

$$P(A_\parallel \to {\rm a})_{\rm res} \simeq \frac{\pi\omega g_{{\rm a}\gamma\gamma}^2|\mathbf{B}|^2}{m_{\rm a}^2}\left|\frac{{\rm d}\ln m_\gamma^2}{{\rm d}t}\right|^{-1}_{t_{\rm res}}, \tag{B.88}$$

where we used the small coupling approximation and the fact that $P(A_\parallel \to {\rm a})_{\rm res} \ll 1$ and $p \simeq 1$. For the low energy CMB photons, axion masses, and small couplings that we are interested in, the above assumptions are always satisfied. The resonance is very narrow and extends over a time scale $\Delta t_{\rm res}$, defined as the time over which $\delta m^2/(2\omega)$ becomes of order $g_{{\rm a}\gamma\gamma}|\mathbf{B}|$,

$$\begin{aligned}\Delta t_{\rm res} &\simeq \frac{2\omega g_{{\rm a}\gamma\gamma}|\mathbf{B}|}{m_{\rm a}^2}\left|\frac{{\rm d}\ln m_\gamma^2}{{\rm d}t}\right|^{-1}_{t_{\rm res}} \sim \frac{\omega g_{{\rm a}\gamma\gamma}|\mathbf{B}|}{m_{\rm a}^2} r_{\rm res} \\ &\simeq 10^{-10} r_{\rm res}\left(\frac{\omega}{10^{-4}{\rm eV}}\right)\left(\frac{10^{-12}\,{\rm eV}}{m_{\rm a}}\right)^2\left(\frac{g_{{\rm a}\gamma\gamma}}{10^{-12}\,{\rm GeV}^{-1}}\right)\left(\frac{|\mathbf{B}|}{0.1\,\mu{\rm G}}\right),\end{aligned} \tag{B.89}$$

where the second expression assumes a power law scaling of m_γ^2 and that the photon trajectory crosses the resonant region in the direction of the number density gradient ($|{\rm d}r/{\rm d}t|_{t_{\rm res}} = 1$). In a realistic scenario, the plasma mass does not change monotonically and the photon trajectory will cross multiple resonances. In particular, we are interested in photons that convert within a halo, that will typically cross a resonance twice. The

contributions from two resonances at r_1 and r_2 can be simply added incoherently, as long as [379]

$$\left| \int_{r_2}^{r_1} \mathrm{d}r' \frac{\delta m^2(r)}{2\omega} \right| \gg 2\pi. \tag{B.90}$$

The above condition is usually easily satisfied, since the integral is typically larger than

$$\frac{m_\mathrm{a}^2}{2\omega} \Delta r \simeq 10^6 \left(\frac{m_\mathrm{a}}{10^{-12}\,\mathrm{eV}} \right)^2 \left(\frac{10^{-4}\,\mathrm{eV}}{\omega} \right) \left(\frac{\Delta r}{\mathrm{kpc}} \right). \tag{B.91}$$

There are two exceptions where interference (or *phase effects*) between the two resonances might be relevant. First, when the photon trajectory crosses the halo close to the edge of the resonance radius, so that Δr is small; however, since the resonance is very narrow, the contribution from these regions to the integrated probability of conversion inside the halo are negligible (see Chapter 4). Second, when the resonance radius is in the innermost part of the halo, where the number density profile is almost flat, so that $\delta m^2(r)$ is small. Also in this case, however, the contribution to the signal is negligible, as it corresponds to small angular scales that are inaccessible to observations.

So far we have considered the unrealistic scenario of a constant magnetic field along the photon trajectory. In the next section we consider a spatially varying magnetic field.

B.4.2 Inhomogeneous magnetic field

Photon-axion mixing for an inhomogeneous plasma and magnetic field can be computed using time-dependent perturbation theory in the limit of small coupling, which is always valid given current constraints on the axion-photon coupling. In this case the conversion probability for a photon traveling over a distance r is given by [247, 380, 379]

$$P(A_\parallel \to \mathrm{a}) = \left| \int_0^r \mathrm{d}r' \Delta_{\mathrm{a}\gamma}(r') e^{i\Phi(r')} \right|^2, \quad \Phi(r) = \int_0^r \mathrm{d}r' \frac{\delta m^2(r')}{2\,\omega}. \tag{B.92}$$

A background magnetic field with coherence length r_dom along the photon propagation direction, can be modeled as a slowly varying component with an oscillatory term $e^{i2\pi r/r_\mathrm{dom}}$, giving a mixing term in the expression above of the form $\Delta_{\mathrm{a}\gamma}(r) = g_{\mathrm{a}\gamma\gamma}|\mathbf{B}(r)|/2\, e^{i2\pi r/r_\mathrm{dom}}$. Therefore, the integrand in the conversion probability has two possible sources of highly oscillatory behavior that can lead to destructive interference. However, as long as the phase of the magnetic field is small compared to $\Phi(r)$, the result is the same as in the case of a constant magnetic field, and (B.92) is dominated by the contributions at the mass

resonances, where the phase varies slowly. (B.92) can be evaluated using the stationary phase approximation and the resonance locations are nearly unchanged if

$$r_{\rm dom} \gg \frac{4\pi\omega}{m_{\rm a}^2} \simeq 10^{-2}\,{\rm pc}\left(\frac{\omega}{10^{-4}{\rm eV}}\right)\left(\frac{10^{-12}{\rm eV}}{m_{\rm a}}\right)^2. \tag{B.93}$$

The result is the same as in (B.88), including the sum over multiple resonances. The short coherence length of the magnetic field compared to the distance between two resonance points, additionally contributes to reduce phase effects between resonances, which are therefore irrelevant. From the equations above it is easy to see that the resonance condition could be met even in the limit of $m_\gamma \ll m_{\rm a}$, if the magnetic field oscillates with a period of $m_{\rm a}^2/(2\omega)$, as pointed out in Ref. [247].

Sub-parsec length scales are too small to be resolved by hydrodynamical cosmological simulations, but given the physics driving the magnetic fields it is reasonable to expect coherent magnetic fields over distances larger than sub-parsec. It is worth emphasizing that although the discussions in this Thesis are mostly in position space, the resonant conversion problem can actually be treated more elegantly in Fourier space [124, 380], where magnetic field consists of Fourier modes with amplitudes described by the power spectrum (see [263, 264] for more details) and uncorrelated phases. In Fourier space, most of the conversion comes from Fourier modes corresponding to the peak of the power spectrum, and small scale fluctuations in the magnetic field do not affect the correlation functions of photon-axion conversion, as long as the superposition principle remains valid and magnetic field power spectrum has a red Kolmogorov scaling [384]. An additional requirement is that the magnetic field must be approximately constant over the length scale of resonance crossing (B.89). However, in the limit of small coupling that we are working in, this requirement is always weaker compared to (B.93).

B.5 Polarization auto-correlations

To derive the polarization auto-power-spectra given in (5.27), we start from the axion signal contribution to the Stokes parameters along the line of sight $\hat{n}$, introduced in (5.15):

$$(Q \pm iU)^{\rm a}(\hat{n}) = -\frac{1-e^{-x}}{x}\bar{T}\int_{z_{\rm min}}^{z_{\rm max}} {\rm d}z\,\frac{{\rm d}\tau^{\rm a}(\hat{n},\chi)}{{\rm d}z}\gamma^{\pm}(\hat{n},\chi), \tag{B.94}$$

where all the quantities appearing here are defined in Sec. 5.3. The left-hand side of the above equation is a spin-2 function and can be expanded in spin-2 spherical harmonics. The

right-hand side contains the product of a scalar $\mathrm{d}\tau^{\mathrm{a}}/\mathrm{d}z(\hat{n},\chi)$ and a spin-2 function $\gamma^{\pm}(\hat{n},\chi)$. Expanding using the appropriate spherical harmonics for each directional-dependent function on both sides of the equation results in

$$\sum_{\ell m} a^{\pm 2}_{\ell m}\ {}_{\pm 2}Y_{\ell m}(\hat{n}) = -\frac{1-e^{-x}}{x}\bar{T}\int_{z_{\min}}^{z_{\max}}\mathrm{d}z\,\frac{\chi^2}{H}\int \mathrm{d}m \sum_i \frac{\delta(\chi-\chi_i)}{\chi^2}\delta^2(\hat{n}'-\hat{n}_i)\delta(m-m_i)\times \\ \sum_{\ell' 0}\sum_{\ell'' m''}\tau^{\mathrm{a}}_{\ell' 0}(\chi,m)\,\gamma^{\pm 2}_{\ell'' m''}(\chi)\,Y_{\ell' m'}(\hat{n})\ {}_{\pm 2}Y_{\ell'' m''}(\hat{n})\int \mathrm{d}^2\hat{n}' Y_{\ell' m'}(\hat{n}'), \tag{B.95}$$

where $\tau^{\mathrm{a}}_{\ell 0}$ was defined in (5.22). The coefficients $a^{\pm 2}_{\ell m}$ on the left-hand side are conventionally replaced by E and B-modes defined in harmonic space

$$a^{\pm 2}_{\ell m} = E^{\mathrm{a}}_{\ell m} \pm i B^{\mathrm{a}}_{\ell m}, \quad E^{\mathrm{a}}_{\ell m} = \frac{a^{+2}_{\ell m}+a^{-2}_{\ell m}}{2}, \quad B^{\mathrm{a}}_{\ell m} = i\frac{a^{+2}_{\ell m}-a^{-2}_{\ell m}}{2}. \tag{B.96}$$

The product of the two spherical harmonics on the right hand side of (B.95) can be rewritten using the relation

$$Y_{\ell' m'}(\hat{n})\ {}_{\pm 2}Y_{\ell'' m''}(\hat{n}) = \\ = \sum_{\ell m}(-1)^m \sqrt{\frac{(2\ell+1)(2\ell'+1)(2\ell''+1)}{4\pi}}\begin{pmatrix}\ell & \ell' & \ell''\\ -m & m' & m''\end{pmatrix}\begin{pmatrix}\ell & \ell' & \ell''\\ \mp 2 & 0 & \pm 2\end{pmatrix}\ {}_{\mp 2}Y_{\ell m}(\hat{n}). \tag{B.97}$$

Therefore, we can read off the expansion coefficients $a^{\pm 2}_{\ell m}$ directly from (B.95) and (B.97),

$$a^{\pm 2}_{\ell m} = -\frac{1-e^{-x}}{x}\bar{T}\int_{z_{\min}}^{z_{\max}}\mathrm{d}z\,\frac{\chi^2}{H}\int \mathrm{d}m \sum_i \frac{\delta(\chi-\chi_i)}{\chi^2}\delta^2(\hat{n}'-\hat{n}_i)\delta(m-m_i)\times \\ \sum_{\ell' m'}\sum_{\ell'' m''}(-1)^m\sqrt{2\ell+1}W^{202}_{\ell\ell'\ell''}\begin{pmatrix}\ell & \ell' & \ell''\\ -m & m' & m''\end{pmatrix}\tau^{\mathrm{a}}_{\ell' 0}(\chi,m)\,\gamma^{\pm 2}_{\ell'' m''}(\chi)\int \mathrm{d}^2\hat{n}' Y_{\ell' m'}(\hat{n}'). \tag{B.98}$$

where we introduced

$$W^{mm'm''}_{\ell\ell'\ell''} = \sqrt{\frac{(2\ell'+1)(2\ell''+1)}{4\pi}}\begin{pmatrix}\ell & \ell' & \ell''\\ -m & m' & m''\end{pmatrix}. \tag{B.99}$$

To compute the correlators, note that, from the definition of the functions $\gamma^{\pm}(\hat{n},\chi)$ in (5.16), the only non-vanishing correlators (see (5.19)) are, in harmonic space,

$$\begin{aligned}\left\langle \gamma^{\pm 2*}_{\ell'' m''}(\chi)\gamma^{\pm 2}_{L'' M''}(\chi)\right\rangle &= \frac{9}{N_{\mathrm{res}}(\chi)}\frac{2}{15}2\pi\theta_{\mathrm{dom}}(\chi)^2\,e^{-\ell''(\ell''+1)\theta^2_{\mathrm{dom}}/2}\delta_{\ell'' L''}\delta_{m'' M''} \\ &\equiv \mathcal{C}^{\pm}_{\ell''}(\chi)\delta_{\ell'' L''}\delta_{m'' M''},\end{aligned} \tag{B.100}$$

while $\left\langle \gamma^{\pm 2*}_{\ell'' m''}(\chi)\gamma^{\mp 2}_{L'' M''}(\chi)\right\rangle = 0$, and correlations between different halos also vanish. The $\mathcal{C}_\ell^\pm$ above have been obtained using the flat-sky approximation, since the magnetic field domains extend over a small angular scale. Therefore, the only contribution to the polarization power spectra comes from the 1-halo term and reads

$$\begin{aligned}&\left\langle a^{\pm 2*}_{\ell m} a^{\pm 2}_{LM}\right\rangle = \\ &= \left(\frac{1-e^{-x}}{x}\bar{T}\right)^2 \int_{z_{\rm min}}^{z_{\rm max}} \mathrm{d}z\, \frac{\chi^2}{H} \int \mathrm{d}m\, n(\chi, m) \left\{ \sum_{\ell' \ell''} (W^{220}_{\ell \ell' \ell''})^2 [\tau^{\rm a}_{\ell''}(\chi, m)]^2 \mathcal{C}^{\mp}_{\ell'}(\chi) \right\} \delta_{\ell L} \delta_{m M},\end{aligned} \tag{B.101}$$

where the orthonormality of the spherical harmonics $\int \mathrm{d}^2\hat{n}' Y_{\ell' m'}(\hat{n}') Y_{L' M'}(\hat{n}') = \delta_{\ell' L'} \delta_{m' M'}$ has been used, together with the following properties of the 3j-symbols

$$\sum_{m' m''} \begin{pmatrix} \ell & \ell' & \ell'' \\ -m & m' & m'' \end{pmatrix} \begin{pmatrix} L & \ell' & \ell'' \\ -M & m' & m'' \end{pmatrix} = \frac{1}{2\ell+1} \delta_{\ell L} \delta_{m M}, \qquad (W^{m m' m''}_{\ell \ell' \ell''})^2 = (W^{m m'' m'}_{\ell \ell'' \ell'})^2. \tag{B.102}$$

The E and B mode correlations can be written in terms of the correlations of the $a^{\pm 2}_{\ell m}$ coefficients from their definition,

$$\langle E^{\rm a *}_{\ell m} E^{\rm a}_{\ell' m'} \rangle = \langle B^{\rm a *}_{\ell m} B^{\rm a}_{\ell' m'} \rangle = \frac{1}{4} \left[\left\langle a^{+2*}_{\ell m} a^{+2}_{\ell' m'} \right\rangle + \left\langle a^{-2*}_{\ell m} a^{-2}_{\ell' m'} \right\rangle \right], \tag{B.103}$$

noting that $\left\langle a^{\pm 2*}_{\ell m} a^{\mp 2}_{\ell' m'} \right\rangle = 0$. The resulting $\mathcal{C}_\ell^{E^{\rm a} E^{\rm a}}$ and $\mathcal{C}_\ell^{B^{\rm a} B^{\rm a}}$ correspond to the expressions given in (5.27). The cross-correlation $\langle E^{\rm a *}_{\ell m} B^{\rm a}_{\ell m} \rangle$ vanishes because it is proportional to $C_\ell^+ - C_\ell^- = 0$.

B.6 Halo occupation distribution and galaxy power spectra

In this appendix we summarize the HOD and the associated power spectra of Ref. [277] which we use to model the unWISE blue sample in our forecasts. The galaxy-galaxy power spectrum is

$$\begin{aligned} C_\ell^{gg} &= C_\ell^{gg,\,1-\rm halo} + C_\ell^{gg,\,2-\rm halo} + A_{\rm SN}, \\ C_\ell^{gg,\,1-\rm halo} &= \int \mathrm{d}z \frac{\chi(z)^2}{H(z)} \int \mathrm{d}m\, n(z,m) \left\langle \left| u^g_\ell(z,m) \right|^2 \right\rangle, \\ C_\ell^{gg,\,2-\rm halo} &= \int \mathrm{d}z \frac{\chi(z)^2}{H(z)} \left[\int \mathrm{d}m\, n(z,m) b(z,m) u^g_\ell(z,m) \right]^2 P^{\rm lin}\left(\frac{\ell + \frac{1}{2}}{\chi(z)}, z \right), \end{aligned} \tag{B.104}$$

The galaxy multipole space kernel $u_\ell^g(z,m)$ is defined as:

$$\begin{aligned} u_\ell^g(z,m) &= W(z)\bar{n}_g^{-1}\left[N_c(m) + N_s(m)u_\ell^{\rm NFW}(z,m)\right], \\ \bar{n}_g(z) &= \int \mathrm{d}m\, n(z,m)\left[N_c(m) + N_s(m)\right], \\ W(z) &= \frac{H(z)}{\chi(z)^2}\frac{\mathrm{d}N_g}{\mathrm{d}z}, \end{aligned} \tag{B.105}$$

and its second moment is

$$\left\langle |u_\ell^g(z,m)|^2 \right\rangle = W_g(z)^2\bar{n}_g^{-2}\left[N_s(m)^2 u_\ell^{\rm NFW}(z,m)^2 + 2N_s(m)u_\ell^{\rm NFW}(z,m)\right]. \tag{B.106}$$

$\mathrm{d}N_g/\mathrm{d}z$ is the redshift distribution of the unWISE blue galaxies normalized to 1. This distribution has a median redshift of $z = 0.6$, and is relatively flat in the redshift range between $0.2 \lesssim z \lesssim 0.8$. The functions $N_c(m)$ and $N_s(m)$ represent the expectation values for the number of central and satellite galaxies respectively in a halo of mass m. These are parametrized as:

$$N_c(m) = \frac{1}{2} + \frac{1}{2}\,\mathrm{erf}\left(\frac{\log m - \log m_{\rm min}}{\sigma_{\log m}}\right), \quad N_s(m) = N_c(m)\left(\frac{m}{m_*}\right)^{\alpha_s}. \tag{B.107}$$

Central galaxies lie exactly at the center of the halo profile and their number is modelled as a smoothed step function. Meanwhile, satellites are distributed inside halos according to an NFW profile. The function $u_\ell^{\rm NFW}(z,m)$ is the normalized harmonic transform of the truncated NFW density profile [373]. Given a truncation radius $r = \lambda r_\Delta$, the Fourier transform has an exact analytical form given by [273, 374]:

$$\begin{aligned} u^{\rm NFW}(k|z,m) = &\left[\ln\left(1+\lambda c_\Delta\right) - \frac{\lambda c_\Delta}{(1+\lambda c_\Delta)}\right]^{-1} \times \\ &\left[\cos(q)\left[\mathrm{Ci}\left(\tilde{q}\right) - \mathrm{Ci}(q)\right] + \sin(q)\left[\mathrm{Si}\left(\tilde{q}\right) - \mathrm{Si}(q)\right] - \frac{\sin\left(\tilde{q}-1\right)}{\tilde{q}}\right], \end{aligned} \tag{B.108}$$

where Si, Ci are the cosine and sine integrals with arguments $q \equiv kr_\Delta/c_\Delta$ and $\tilde{q} \equiv 1+\lambda c_\Delta q$. The scales are chosen with respect to a halo boundary defined at $\Delta = 200$ times the critical density. Under this convention, r_Δ is the halo radius that encloses mass m_Δ and c_Δ is the corresponding concentration. Making the substitution $k \to (\ell+1/2)/\chi$ gives the multipole projection function $u_\ell^{\rm NFW}(z,m)$. This HOD model is defined by 6 free parameters. The

values we use are taken from Table VI of [276]:

$$\begin{aligned}\text{HOD}:\{\ \alpha_{\rm s} &= 1.06,\\ \sigma_{\log m} &= 0.02,\\ \lambda &= 1.80,\\ \log m_* &= 12.78 M_\odot,\\ \log m_{\rm min} &= 11.86 M_\odot,\\ 10^7 A_{\rm SN} &= 0.87\ \}\,,\end{aligned} \tag{B.109}$$

where $A_{\rm SN}$ is the shot noise. It only appears in the definition for the galaxy auto-correlation function and for our purposes, it acts as a noise term.

To simplify the computation of the polarization-polarization-galaxy bispectrum, we assume that only central galaxies contribute to the signal. This is equivalent to setting $N_s(m) = 0$ everywhere in the auto- and cross-power spectra defined above. The centrals-only power spectrum is given by

$$\begin{aligned}C_\ell^{gg,\rm cen} &= C_\ell^{gg,\rm cen,\,2-halo} + A_{\rm SN}^{\rm cen},\\ C_\ell^{gg,\rm cen,\,2-halo} &= \int {\rm d}z \frac{\chi(z)^2}{H(z)} \left[\int {\rm d}m\, n(z,m) b(z,m) u_\ell^{g,\rm cen}(z,m)\right]^2 P^{\rm lin}\left(\frac{\ell+\frac{1}{2}}{\chi(z)}, z\right),\end{aligned} \tag{B.110}$$

where

$$\begin{aligned}u^{g,\rm cen}(z,m) &= W(z)\bar{n}_{g,\rm cen}^{-1} N_c(m),\\ \bar{n}_{g,\rm cen}(z) &= \int {\rm d}m\, n(z,m) N_c(m),\end{aligned} \tag{B.111}$$

and we define the shot noise from the total number of expected centrals in the unWISE blue sample:

$$A_{\rm SN}^{\rm cen} = 4\pi \left(\int {\rm d}z \frac{\chi(z)^2}{H(z)} \frac{{\rm d}N_g}{{\rm d}z} \bar{n}_{g,\rm cen}(z)\right)^{-1} \approx 2.87 \times 10^{-7}. \tag{B.112}$$

B.7 Bispectrum derivation

The axion-induced polarization signal is correlated with the location of LSS. The leading-order non-vanishing cross-correlation between CMB and LSS is the three-point function:

$$\langle (Q \pm iU)^{\rm a*}(\hat{n}_1)(Q \pm iU)(\hat{n}_2) g(\hat{n}_3)\rangle\,, \tag{B.113}$$

where $(Q \pm iU)^{\rm a}$ is defined in (5.15) and $g(\hat{n})$ represents the galaxy density field. We include only central galaxies, and model this map as

$$g(\hat{n}, \chi) = \sum_i u^{g,\rm cen}(\chi, m_i)\delta^2(\hat{n} - \hat{n}_i) \tag{B.114}$$

at each redshift, where $u^{g,\rm cen}$ was defined in (B.111). Two terms contribute to the bispectrum in (B.113): a 1-halo term for points $\{\hat{n}_1, \hat{n}_2, \hat{n}_3\}$ crossing the same halo, and a 2-halo term for $\{\hat{n}_1, \hat{n}_2\}$ crossing one halo and $\{\hat{n}_3\}$ crossing a different halo. The first term contributes at small scales, while the second term includes the large-scale clustering of structure. Due to the hierarchy of scales between the magnetic field coherence length, the characteristic radius of photon-axion resonance conversion, and the distance between halos, both terms are dominated by squeezed triangle configurations. Note that there is no three-halo term, because the polarization signal from different halos is uncorrelated.

B.7.1 One-halo term

We write explicitly the three-point function by summing the contributions from all halos i, such that the 1-halo contribution to (B.113) becomes

$$\begin{aligned}
&\left(\frac{1-e^{-x}}{x}\bar{T}\right)^2 \int \mathrm{d}\chi\chi^2\,\mathrm{d}m\,\mathrm{d}^2\hat{n}\,\frac{1}{9}P^2(\chi,m)N^2_{\rm res}(\chi,m)u(\hat{n}_1-\hat{n})u(\hat{n}_2-\hat{n})u^{g,\rm cen}(\chi,m)\times \\
&\delta^2(\hat{n}_3-\hat{n})\left\langle\sum_i \delta(m-m_i)\frac{\delta(\chi-\chi_i)}{\chi^2}\delta^2(\hat{n}-\hat{n}_i)\right\rangle\left\langle\gamma^{\pm}(\hat{n}_1,\chi)\gamma^{\pm}(\hat{n}_2,\chi)\right\rangle = \\
&\left(\frac{1-e^{-x}}{x}\bar{T}\right)^2 \int \mathrm{d}\chi\chi^2\,\mathrm{d}m\,n(\chi,m)\frac{1}{9}P^2(\chi,m)N^2_{\rm res}(\chi,m)u^{g,\rm cen}(\chi,m)\times \\
&u(\hat{n}_1-\hat{n}_3)u(\hat{n}_2-\hat{n}_3)\left\langle\gamma^{\pm}(\hat{n}_1,\chi)\gamma^{\pm}(\hat{n}_2,\chi)\right\rangle .
\end{aligned} \tag{B.115}$$

The last line of the equation above contains all the angular dependent functions. We can simplify the calculation by noting that the magnetic field domains are much smaller than the typical size of a halo, therefore, expect for the a small area around the center of the halo, most triangles will be such that $|\hat{n}_1-\hat{n}_2| \ll |\hat{n}_1-\hat{n}_3| \simeq |\hat{n}_2-\hat{n}_3|$. We therefore approximate $u(\hat{n}_1-\hat{n}_3)u(\hat{n}_2-\hat{n}_3) \simeq [u(\hat{n}_1-\hat{n}_3)^2 + u(\hat{n}_2-\hat{n}_3)^2]/2$. We show the calculation for the first term with $\hat{n}_1$ below, since the one with $\hat{n}_2$ can be obtained in the same way. Expanding in

spherical harmonics,

$$\begin{aligned} u(\hat{n}_1-\hat{n}_3)^2 =& \sum_{LM}\sum_{L'M'}\frac{4\pi}{\sqrt{(2L+1)(2L'+1)}}u_{L0}(m,z)u_{L'0}(m,z)\times \\ & Y_{LM}(\hat{n}_1)Y_{LM}(\hat{n}_3)Y_{L'M'}(\hat{n}_1)Y_{L'M'}(\hat{n}_3) \\ =& \sum_{LL'}\frac{4\pi}{\sqrt{(2L+1)(2L'+1)}}u_{L0}(m,z)u_{L'0}(m,z)\times \\ & \sum_{\ell''m''}\left(W^{000}_{\ell''LL'}\right)^2 Y_{\ell''m''}(\hat{n}_1)Y_{\ell''m''}(\hat{n}_3), \end{aligned} \tag{B.116}$$

where $u_{\ell 0}$ was defined in (5.22) and we used the result from (B.97), adapted to the case of spin-0 spherical harmonics, to contract their product. Now we expand also the correlator $\langle\gamma^{\pm}(\hat{n}_1,\chi)\gamma^{\pm}(\hat{n}_2,\chi)\rangle = \mathcal{C}^{\pm}_{\ell'}(\chi)\,{}_{\pm2}Y_{\ell'm'}(\hat{n}_1)\,{}_{\pm2}Y_{\ell'm'}(\hat{n}_2)$, where $\mathcal{C}^{\pm}_{\ell'}$ was introduced in (B.100). Using again (B.97), we further combine the two remaining spin-0 and spin-2 spherical harmonics evaluated at $\hat{n}_1$, to get the bispectrum

$$\begin{aligned} & \left(\frac{1-e^{-x}}{x}\bar{T}\right)^2\int \mathrm{d}\chi\chi^2\,\mathrm{d}m\,n(\chi,m)u^{g,\mathrm{cen}}(\chi,m)\times \\ & \sum_{\ell m}\sum_{\ell'm'}\sum_{\ell''m''}\sum_{LL'}(-1)^m\sqrt{\frac{(2\ell+1)(2\ell'+1)(2\ell''+1)}{4\pi}}\begin{pmatrix}\ell & \ell' & \ell''\\ -m & m' & m''\end{pmatrix}\begin{pmatrix}\ell & \ell' & \ell''\\ \mp2 & \pm2 & 0\end{pmatrix}\times \\ & \frac{1}{2}\left(W^{000}_{\ell''LL'}\right)^2\tau^{\mathrm{a}}_{L0}(m,z)\tau^{\mathrm{a}}_{L'0}(m,z)\mathcal{C}^{\pm}_{\ell'}(\chi)\,{}_{\mp2}Y_{\ell m}(\hat{n}_1)\,{}_{\pm2}Y_{\ell'm'}(\hat{n}_2)Y_{\ell''m''}(\hat{n}_3), \end{aligned} \tag{B.117}$$

where $\tau^{\mathrm{a}}_{\ell 0}$ was defined in (5.22). Now, adding the second piece coming from doing the same calculation but replacing $\hat{n}_1\to\hat{n}_2$ in the u screening function, we can read off the bispectra

$$\begin{aligned} \left\langle a^{\pm2}_{\ell m}a^{\pm2}_{\ell'm'}g_{\ell''m''}\right\rangle =& (-1)^m\sqrt{\frac{(2\ell+1)(2\ell'+1)(2\ell''+1)}{4\pi}}\begin{pmatrix}\ell & \ell' & \ell''\\ -m & m' & m''\end{pmatrix}\begin{pmatrix}\ell & \ell' & \ell''\\ \mp2 & \pm2 & 0\end{pmatrix}\times \\ & \left(\frac{1-e^{-x}}{x}\bar{T}\right)^2\int \mathrm{d}\chi\,\mathrm{d}m\,n(\chi,m)u^{g,\mathrm{cen}}(\chi,m)\times \\ & \sum_{LL'}\left(W^{000}_{\ell''LL'}\right)^2\tau^{\mathrm{a}}_{L0}(\chi,m)\tau^{\mathrm{a}}_{L'0}(\chi,m)\frac{\mathcal{C}^{\pm}_{\ell'}(\chi)+(-1)^{\ell+\ell'+\ell''}\mathcal{C}^{\pm}_{\ell}(\chi)}{2}. \end{aligned} \tag{B.118}$$

To write the three-point function in terms of the E and B-modes, we note that $\left\langle a^{\pm2*}_{\ell m}a^{\mp2}_{\ell'm'}g_{\ell''m''}\right\rangle = 0$, which from the definition of E and B means that $\langle E^*_{\ell m}E^*_{\ell'm'}g_{\ell''m''}\rangle = \langle B^*_{\ell m}B^*_{\ell'm'}g_{\ell''m''}\rangle$.

Similarly to what obtained in App. B.5 for the power spectrum, it can then be shown that

$$\begin{aligned}
&\langle E^{\mathrm{a}*}_{\ell m} E^{\mathrm{a}}_{\ell' m'} g_{\ell'' m''}\rangle = \langle B^{\mathrm{a}*}_{\ell m} B^{\mathrm{a}}_{\ell' m'} g_{\ell'' m''}\rangle = \frac{1}{4}\left(\left\langle a^{+2*}_{\ell m} a^{+2}_{\ell' m'} g_{\ell'' m''}\right\rangle + \left\langle a^{-2*}_{\ell m} a^{-2}_{\ell' m'} g_{\ell'' m''}\right\rangle\right) = \\
&= (-1)^m \sqrt{\frac{(2\ell+1)(2\ell'+1)(2\ell''+1)}{4\pi}} \begin{pmatrix} \ell & \ell' & \ell'' \\ -m & m' & m'' \end{pmatrix} \begin{pmatrix} \ell & \ell' & \ell'' \\ +2 & -2 & 0 \end{pmatrix} e_{\ell\ell'\ell''} \times \\
&\left(\frac{1-e^{-x}}{x}\bar{T}\right)^2 \int \mathrm{d}\chi\, \mathrm{d}m\, n(\chi, m) u^{g,\mathrm{cen}}(\chi, m) \times \\
&\sum_{LL'} \left(W^{000}_{\ell'' L L'}\right)^2 \tau^{\mathrm{a}}_{L0}(\chi, m) \tau^{\mathrm{a}}_{L'0}(\chi, m) \frac{\mathcal{C}^{\mathrm{pol}}_{\ell}(\chi) + \mathcal{C}^{\mathrm{pol}}_{\ell'}(\chi)}{2},
\end{aligned} \tag{B.119}$$

where where C^{pol}_{ℓ} is defined in (5.28) and

$$e_{\ell\ell'\ell''} \equiv \frac{1}{2}\left[1 + (-1)^{\ell+\ell'+\ell''}\right]. \tag{B.120}$$

From the equation above we can read off the angle-averaged bispectrum $\mathcal{B}$ as

$$\langle X^{\mathrm{a}}_{\ell m} X^{\mathrm{a}}_{\ell' m'} g_{\ell'' m''}\rangle = (-1)^m \begin{pmatrix} \ell & \ell' & \ell'' \\ -m & m' & m'' \end{pmatrix} \mathcal{B}^{X^{\mathrm{a}} X^{\mathrm{a}} g}_{\ell\ell'\ell''}, \tag{B.121}$$

which results in the expression given in Sec. 5.3.3, in (5.35). $\mathcal{B}^{X^{\mathrm{a}} X^{\mathrm{a}} g}_{\ell\ell'\ell''}$ is symmetric under the exchange of $\ell \leftrightarrow \ell'$, as expected from the approximations made in the calculation above when taking the limit of squeezed triangles. In the signal-to-noise ratio only the angle-averaged bispectrum enters, since the sum over m simplifies as

$$\sum_{mm'm''} \left[(-1)^m \begin{pmatrix} \ell & \ell' & \ell'' \\ -m & m' & m'' \end{pmatrix}\right]^2 = 1. \tag{B.122}$$

B.7.2 Two-halo term

We write explicitly the three-point function by summing the contributions from two different halos i and j, such that the 2-halo contribution to (B.113) becomes

$$\begin{aligned}
&\left(\frac{1-e^{-x}}{x}\bar{T}\right)^2 \int \mathrm{d}\chi_a \chi_a^2\, \mathrm{d}\chi_b \chi_b^2\, \mathrm{d}m_a\, \mathrm{d}m_b\, \mathrm{d}^2\hat{n}_a\, \mathrm{d}^2\hat{n}_b\, \delta^2(\hat{n}_3 - \hat{n}_b)\, u^{g,\mathrm{cen}}(\chi_b, m_b) \times \\
&\frac{1}{9} P^2(\chi_a, m_a) N^2_{\mathrm{res}}(\chi_a, m_a) u(\hat{n}_1 - \hat{n}_a) u(\hat{n}_2 - \hat{n}_a) \left\langle \gamma^{\pm}(\hat{n}_1, \chi_a) \gamma^{\pm}(\hat{n}_2, \chi_a)\right\rangle \times \\
&\left\langle \sum_{i \neq j} \delta(m_a - m_i) \delta(m_b - m_j) \frac{\delta(\chi_a - \chi_i)}{\chi_a^2} \frac{\delta(\chi_b - \chi_j)}{\chi_b^2} \delta^2(\hat{n}_a - \hat{n}_i) \delta^2(\hat{n}_b - \hat{n}_j) \right\rangle.
\end{aligned} \tag{B.123}$$

The average in the last line of the equation above is related to the halo-halo auto-correlation function ξ^{hh},

$$\left\langle \sum_{i\neq j} \delta(m_a - m_i)\delta(m_b - m_j)\frac{\delta(\chi_a - \chi_i)}{\chi_a^2}\frac{\delta(\chi_b - \chi_j)}{\chi_b^2}\delta^2(\hat{n}_a - \hat{n}_i)\delta^2(\hat{n}_b - \hat{n}_j)\right\rangle = \\ = n(m_a,\chi_a)n(m_b,\chi_b)\xi^{hh}(\hat{n}_a - \hat{n}_b|m_a,\chi_a,m_b,\chi_b). \tag{B.124}$$

Eq. (B.123) then becomes

$$\left(\frac{1-e^{-x}}{x}\bar{T}\right)^2 \int \mathrm{d}\chi_a\chi_a^2\,\mathrm{d}\chi_b\chi_b^2\,\mathrm{d}m_a\,\mathrm{d}m_b\,n(\chi_a,m_a)n(\chi_b,m_b)u^{g,\mathrm{cen}}(\chi_b,m_b)\times \\ \frac{1}{9}P^2(\chi_a,m_a)N_{\mathrm{res}}^2(\chi_a,m_a)\left\langle\gamma^{\pm}(\hat{n}_1,\chi_a)\gamma^{\pm}(\hat{n}_2,\chi_a)\right\rangle\times \\ \int \mathrm{d}^2\hat{n}_a\,u(\hat{n}_1-\hat{n}_a)u(\hat{n}_2-\hat{n}_a)\xi^{hh}(\hat{n}_a-\hat{n}_3). \tag{B.125}$$

The integral over $\hat{n}_a$ can be simplified by noting that the magnetic field domains are much smaller than the typical size of a halo, such that $|\hat{n}_1 - \hat{n}_2| \ll |\hat{n}_a - \hat{n}_1| \simeq |\hat{n}_a - \hat{n}_2|$. On the other hand, the halo-halo auto-correlation is dominated by larger scales, which means $|\hat{n}_a - \hat{n}_1| \simeq |\hat{n}_a - \hat{n}_2| \ll |\hat{n}_a - \hat{n}_3|$. Therefore, the bispectrum is dominated by the squeezed triangles, with $|\hat{n}_1 - \hat{n}_2| \ll |\hat{n}_3 - \hat{n}_1| \simeq |\hat{n}_3 - \hat{n}_2|$. In the equation above we can then replace $\hat{n}_a \to \hat{n}_{1,2}$ inside the halo-halo auto-correlation ξ^{hh} and simply perform the integral over $\hat{n}_a$. We therefore approximate $\xi^{hh}(\hat{n}_a - \hat{n}_3) \simeq \left[\xi^{hh}(\hat{n}_1 - \hat{n}_3) + \xi^{hh}(\hat{n}_2 - \hat{n}_3)\right]/2$. We show the calculation with $\hat{n}_1$ below, since the one with $\hat{n}_2$ can be obtained in the same way. Using the result from Appendix B.2.1,

$$\int \mathrm{d}^2\hat{n}_a\,u(\hat{n}_1-\hat{n}_a)u(\hat{n}_2-\hat{n}_a) = \sum_{\ell m}\frac{4\pi}{2\ell+1}u_{\ell 0}^2(\chi_a,m_a)Y_{\ell m}(\hat{n}_1)Y_{\ell m}(\hat{n}_2), \tag{B.126}$$

where $u_{\ell 0}$ was defined in (5.22). Expanding all the angular-dependent functions into spherical harmonics, the three-point function simplifies to

$$\left(\frac{1-e^{-x}}{x}\bar{T}\right)^2 \int \mathrm{d}\chi_a\chi_a^2\,\mathrm{d}\chi_b\chi_b^2\,\mathrm{d}m_a\,\mathrm{d}m_b\,n(\chi_a,m_a)n(\chi_b,m_b)u^{g,\mathrm{cen}}(\chi_b,m_b)\times \\ \sum_{\ell m}\sum_{\ell' m'}\sum_{\ell'' m''}\frac{1}{2}[\tau_{\ell 0}^{\mathrm{a}}(\chi_a,m_a)]^2\mathcal{C}_{\ell'}^{\pm}(\chi_a)C_{\ell''}^{hh}(m_a,\chi_a,m_b,\chi_b)\times \\ Y_{\ell m}(\hat{n}_1)Y_{\ell m}(\hat{n}_2)\,{}_{\pm2}Y_{\ell' m'}(\hat{n}_1)\,{}_{\pm2}Y_{\ell' m'}(\hat{n}_2)Y_{\ell'' m''}(\hat{n}_1)Y_{\ell'' m''}(\hat{n}_3), \tag{B.127}$$

where $\tau^{\rm a}_{\ell 0}$ was defined in (5.22), $\mathcal{C}^{\pm}_{\ell'}$ was introduced in (B.100), and C^{hh}_{ℓ} is the power spectrum of the real-space halo-halo auto-correlation ξ^{hh}. This takes the following form:

$$\begin{aligned} &C^{hh}_{\ell}\left(m_a,\chi_a,m_b,\chi_b\right) = \\ &\quad = \frac{2}{\pi} b(m_a,\chi_a) b(m_b,\chi_b) \int \mathrm{d}k k^2 j_\ell\left(k\chi_a\right) j_\ell\left(k\chi_b\right) \sqrt{P^{\rm lin}(k,\chi_a) P^{\rm lin}(k,\chi_b)}, \end{aligned} \tag{B.128}$$

where $P^{\rm lin}(k,\chi)$ is the linear matter power spectrum, and $b(m,\chi)$ is the linear halo bias. In the limit of small angle, $\ell \to \infty$, we can approximate the spherical Bessel function by $j_\ell(x) \to \sqrt{\pi/\left(2\ell+1\right)}\delta(\ell+1/2-x)$, where $x = \chi k$. Thanks to the delta function, the integral over comoving wavenumber k simplifies to

$$C^{hh}_{\ell}\left(m_a,\chi_a,m_b,\chi_b\right) \approx b(m_a,\chi_a) b(m_b,\chi_b) \frac{\delta(\chi_a-\chi_b)}{\chi_a^2} P^{\rm lin}\left(\frac{\ell+\frac{1}{2}}{\chi_a},\chi_a\right). \tag{B.129}$$

This simplification is equivalent to the Limber approximation [269, 270]. The delta function in the expression above further simplifies the integral over χ_b in the bispectrum.

Now we want to reduce the product of spherical harmonics in (B.127) down to three, to read off the coefficients of the bispectrum. From the derivation of the polarization power spectra in App. B.5, we already know that

$$\sum_{mm'} Y_{\ell m}(\hat{n}_1) Y_{\ell m}(\hat{n}_2)\, {}_{\pm2}Y_{\ell' m'}(\hat{n}_1)\, {}_{\pm2}Y_{\ell' m'}(\hat{n}_2) = \sum_{LM} \left(W^{220}_{L\ell'\ell}\right)^2 {}_{\mp2}Y_{LM}(\hat{n}_1)\, {}_{\mp2}Y_{LM}(\hat{n}_2). \tag{B.130}$$

Therefore, after relabeling, the bispectrum from (B.127) becomes

$$\begin{aligned} &\left(\frac{1-e^{-x}}{x}\bar{T}\right)^2 \int \mathrm{d}\chi_a \chi_a^2\, \mathrm{d}m_a\, \mathrm{d}m_b\, n(\chi_a,m_a) n(\chi_a,m_b) u^{g,\rm cen}(\chi_a,m_b) b(m_a,\chi_a) b(m_b,\chi_a) \times \\ &\sum_{\ell' m'} \sum_{\ell'' m''} \sum_{LL'} \frac{1}{2} \left(W^{220}_{\ell' L' L}\right)^2 \left[\tau^{\rm a}_{L0}(\chi_a,m_a)\right]^2 \mathcal{C}^{\pm}_{L'}(\chi_a) P^{\rm lin}\left(\frac{\ell''+\frac{1}{2}}{\chi_a},\chi_a\right) \times \\ &{}_{\mp2}Y_{\ell' m'}(\hat{n}_1)\; Y_{\ell'' m''}(\hat{n}_1)\, {}_{\mp2}Y_{\ell' m'}(\hat{n}_2) Y_{\ell'' m''}(\hat{n}_3). \end{aligned} \tag{B.131}$$

Finally, replacing the product ${}_{\mp2}Y_{\ell'm'}(\hat{n}_1)Y_{\ell''m''}(\hat{n}_1)$ with one spherical harmonics, we get

$$\left(\frac{1-e^{-x}}{x}\bar{T}\right)^2\int \mathrm{d}\chi_a\chi_a^2\,\mathrm{d}m_a\,\mathrm{d}m_b\,n(\chi_a,m_a)n(\chi_a,m_b)u^{g,\mathrm{cen}}(\chi_a,m_b)b(m_a,\chi_a)b(m_b,\chi_a)\times$$
$$\sum_{\ell m}\sum_{\ell' m'}\sum_{\ell'' m''}\sum_{LL'}(-1)^m\sqrt{\frac{(2\ell+1)(2\ell'+1)(2\ell''+1)}{4\pi}}\begin{pmatrix}\ell & \ell' & \ell''\\ -m & m' & m''\end{pmatrix}\begin{pmatrix}\ell & \ell' & \ell''\\ \pm2 & \mp2 & 0\end{pmatrix}\times$$
$$\frac{1}{2}\left(W^{220}_{\ell'L'L}\right)^2[\tau^{\mathrm{a}}_{L0}(\chi_a,m_a)]^2\mathcal{C}^{\pm}_{L'}(\chi_a)P^{\mathrm{lin}}\left(\frac{\ell''+\frac{1}{2}}{\chi_a},\chi_a\right){}_{\pm2}Y_{\ell m}(\hat{n}_1)\,{}_{\mp2}Y_{\ell'm'}(\hat{n}_2)Y_{\ell''m''}(\hat{n}_3). \tag{B.132}$$

Now, adding the second piece coming from doing the same calculation but replacing $\hat{n}_a\to\hat{n}_2$ in the halo-halo auto-correlation function, we can read off the bispectra

$$\left\langle a^{\pm2}_{\ell m}a^{\pm2}_{\ell'm'}g_{\ell''m''}\right\rangle =$$
$$=(-1)^m\sqrt{\frac{(2\ell+1)(2\ell'+1)(2\ell''+1)}{4\pi}}\begin{pmatrix}\ell & \ell' & \ell''\\ -m & m' & m''\end{pmatrix}\begin{pmatrix}\ell & \ell' & \ell''\\ \pm2 & \mp2 & 0\end{pmatrix}$$
$$\left(\frac{1-e^{-x}}{x}\bar{T}\right)^2\int \mathrm{d}\chi_a\chi_a^2\,\mathrm{d}m_a\,\mathrm{d}m_b\,n(\chi_a,m_a)n(\chi_a,m_b)u^{g,\mathrm{cen}}(\chi_a,m_b)b(m_a,\chi_a)b(m_b,\chi_a)\times$$
$$\sum_{LL'}\frac{\left(W^{220}_{\ell L'L}\right)^2+\left(W^{220}_{\ell' L'L}\right)^2}{2}[\tau^{\mathrm{a}}_{L0}(\chi_a,m_a)]^2\mathcal{C}^{\pm}_{L'}(\chi_a)P^{\mathrm{lin}}\left(\frac{\ell''+\frac{1}{2}}{\chi_a},\chi_a\right). \tag{B.133}$$

To write the three-point function in terms of the E and B-modes, we note that the correlator $\left\langle a^{\pm2*}_{\ell m}a^{\mp2}_{\ell'm'}g_{\ell''m''}\right\rangle=0$, which from the definition of E and B means that $\langle E^*_{\ell m}E^*_{\ell'm'}g_{\ell''m''}\rangle=\langle B^*_{\ell m}B^*_{\ell'm'}g_{\ell''m''}\rangle$. Similarly to what was obtained in App. B.5 for the power spectrum, it can be shown that

$$\langle E^{\mathrm{a}*}_{\ell m}E^{\mathrm{a}}_{\ell'm'}g_{\ell''m''}\rangle=\langle B^{\mathrm{a}*}_{\ell m}B^{\mathrm{a}}_{\ell'm'}g_{\ell''m''}\rangle=\frac{1}{4}\left(\left\langle a^{+2*}_{\ell m}a^{+2}_{\ell'm'}g_{\ell''m''}\right\rangle+\left\langle a^{-2*}_{\ell m}a^{-2}_{\ell'm'}g_{\ell''m''}\right\rangle\right)=$$
$$=(-1)^m\sqrt{\frac{(2\ell+1)(2\ell'+1)(2\ell''+1)}{4\pi}}\begin{pmatrix}\ell & \ell' & \ell''\\ -m & m' & m''\end{pmatrix}\begin{pmatrix}\ell & \ell' & \ell''\\ +2 & -2 & 0\end{pmatrix}e_{\ell\ell'\ell''}\times$$
$$\left(\frac{1-e^{-x}}{x}\bar{T}\right)^2\int \mathrm{d}\chi_a\chi_a^2\,\mathrm{d}m_a\,\mathrm{d}m_b\,n(\chi_a,m_a)n(\chi_a,m_b)u^{g,\mathrm{cen}}(\chi_a,m_b)b(m_a,\chi_a)b(m_b,\chi_a)\times$$
$$\sum_{LL'}\frac{\left(W^{220}_{\ell L'L}\right)^2+\left(W^{220}_{\ell' L'L}\right)^2}{2}[\tau^{\mathrm{a}}_{L0}(\chi_a,m_a)]^2\mathcal{C}^{\mathrm{pol}}_{L'}(\chi_a)P^{\mathrm{lin}}\left(\frac{\ell''+\frac{1}{2}}{\chi_a},\chi_a\right), \tag{B.134}$$

where C^{pol}_ℓ is defined in (5.28) and $e_{\ell\ell'\ell''}$ in (B.120). From the equation above we can read off the angle-averaged bispectrum which results in the expression given in Sec. 5.3.3,

in (5.36). As for the 1-halo term, also in this case $\mathcal{B}^{X^{\rm a}X^{\rm a}g}_{\ell\ell'\ell''}$ is symmetric under the exchange of $\ell \leftrightarrow \ell'$.

B.8 Foregrounds and noise

In this appendix, we outline our prescription for estimating the noise covariance matrix $\mathbf{N}_\ell$ used in the ILC described in Sec. 5.4.1 for temperature and polarization. We consider temperature and polarization data from two CMB experiments: the combination of the Low Frequency Instrument (LFI) [233] and High Frequency Instrument (HFI) [234] on the Planck satellite and CMB Stage-4 [206]. For each experiment, we specify the observed frequency channels and angular resolution as defined by a Gaussian beam

$$G_\ell(\omega) = \exp\left[-\ell(\ell+1)\,\frac{\theta^2_{\rm FWHM}}{8\ln 2}\right], \tag{B.135}$$

where the full width at half maximum $\theta_{\rm FWHM}\,[\rm rad]$ varies with frequency. The assumed values are recorded in the top two panels of Table 4.2, where $\theta_{\rm FWHM}$ represents the full width at half maximum of the Gaussian beams, which characterizes the resolution of the instrument in each frequency channel, and Δ_T represents the amplitude of the white uncorrelated noise in CMB temperature units.

For Planck, since data is readily available, we take an empirical approach. Our analysis is based on publicly available individual frequency and component-separated CMB maps from the Planck Public Data Release 3 (PR3) [14]. We first subtract the SMICA CMB from individual frequency maps at 30-353 GHz in intensity as well as Q and U Stokes parameters. We mask the resulting maps with a galactic cut retaining 40% of the sky, apodized to 2 degrees. We compute the auto- and cross-spectra between all masked maps. We do not correct for mode-coupling from the mask, approximating full-sky power spectra by the cut-sky pseudo-C_ℓ spectra divided by the effective unmasked sky-fraction ~ 0.4. Additionally, for polarization we use the full-sky expressions to produce E and B-mode spectra from the Stokes parameter. We populate the matrices $\mathbf{N}_\ell$ used in the ILC using these auto- and cross-spectra. Our treatment provides an estimate of the level of foregrounds and instrumental noise on the cleanest region of the sky. A more careful treatment accounting for mode-coupling would improve the accuracy of our estimate primarily on large angular scales, and particularly for polarization spectra where the E-B decomposition is particularly sensitive to masking.

For CMB-S4, we take a hybrid approach to estimating the noise covariance, considering three contributions: galactic foregrounds empirically measured from Planck, instrumental

noise, and simulated extragalactic foregrounds. To estimate the contribution from galactic foregrounds, we first fit the low-ℓ (defined as $\ell < 100$) entries in $\mathbf{N}_\ell$ for Planck temperature and Stokes parameters to a power law $[\mathbf{N}_\ell]_{ij} = A_{ij}\ell^{-n_{ij}}$. We then use linear interpolation/extrapolation to obtain entries at the S4 frequencies, listed in the top row of the bottom panel in Table 4.2. The instrumental noise contribution is modeled as

$$I_\ell^{TT} = I_\ell^{E^{\rm a}E^{\rm a}}/\sqrt{2} = I_\ell^{BB}/\sqrt{2} = \Delta_T^2\left[1 + (\ell/\ell_{\rm knee})^{\alpha_{\rm knee}}\right], \tag{B.136}$$

where $\Delta_T\,[\mu{\rm K\,rad}]$ is the level of white noise representing the sensitivity in each frequency channel (values recorded in Table 4.2), and the parameters $\alpha_{\rm knee} = -3$ and $\ell_{\rm knee} = 100$ parameterize atmospheric systematics on large angular scales. The dominant extragalactic foreground at high frequencies (where the axion-induced screening signal is most important) is the cosmic infrared background (CIB). We model this by computing the auto- and cross-power spectra of CIB maps from the Websky suite of simulations at $93, 145, 225, 278$ GHz respectively [279]. For polarization, we assume that the CIB is 1% polarized, and use the temperature maps to estimate the polarization signal from extragalactic sources. The full noise covariance is obtained by summing the three components described above for all auto- and cross-power spectra of the CMB-S4 frequency channels in temperature and polarization.

B.9 Effectively massless axions

When the axion is effectively massless ($m_{\rm a} \ll 10^{-14}\,{\rm eV}$), we no longer expect to find plasma densities that yield resonant conversion. In this scenario, we can apply the treatment in App. B.4 for a small magnetic field with domain size $r_{\rm dom}$ to obtain a conversion probability given by

$$P(A_\parallel \to {\rm a}) = (\Delta_{{\rm a}\gamma} r_{\rm dom})^2 \frac{\sin^2(\Delta_{\rm osc} r_{\rm dom}/2)}{(\Delta_{\rm osc} r_{\rm dom}/2)^2} \approx 4\left(\frac{\Delta_{{\rm a}\gamma}}{\Delta_{\rm pl}}\right)^2 \sin^2(\Delta_{\rm pl} r_{\rm dom}/2). \tag{B.137}$$

We expect photon-axion conversion to happen in different astrophysical and cosmological environments, including

$$\begin{aligned}
&\text{ISM:} && |\mathbf{B}| \simeq \mu G, \quad m_\gamma \simeq 10^{-11}\,{\rm eV}, \quad {\rm r_{dom}} \simeq 1\,{\rm kpc} \\
&\text{CGM:} && |\mathbf{B}| \simeq 0.1\mu G, \quad m_\gamma \simeq 10^{-12.5}\,{\rm eV}, \quad {\rm r_{dom}} \simeq 10\,{\rm kpc} \\
&\text{IGM:} && |\mathbf{B}| \simeq nG, \quad m_\gamma \simeq 10^{-14}\,{\rm eV}, \quad {\rm r_{dom}} \simeq 1\,{\rm Mpc},
\end{aligned} \tag{B.138}$$

where ISM refers to the interstellar medium around the location of the Solar system, CGM refers to the circumgalactic medium in the vicinity of the Milky Way and other galaxies,

and IGM refers to the intergalactic medium between galaxies. In all three cases, $\Delta_{\rm pl} \gg \Delta_{\rm a\gamma}$ and $\Delta_{\rm pl} r_{\rm dom} \gg 1$. In this limit, the conversion probability per domain is

$$P(A_\parallel \to {\rm a}) = 2\left(\frac{\Delta_{\rm a\gamma}}{\Delta_{\rm pl}}\right)^2 \approx \frac{2g_{\rm a\gamma\gamma}^2 |\mathbf{B}|^2 \omega^2}{m_\gamma^4}. \tag{B.139}$$

and the conversion rate per unit length in the three different environments is approximately

$$\frac{{\rm d}P}{{\rm d}r} = \frac{2g_{\rm a\gamma\gamma}^2 |\mathbf{B}|^2 \omega^2}{m_\gamma^4\, r_{\rm dom}} \approx \begin{cases} 4\times 10^{-15}/{\rm Mpc} & ({\rm ISM}), \\ 4\times 10^{-12}/{\rm Mpc} & ({\rm CGM}), \\ 4\times 10^{-12}/{\rm Mpc} & ({\rm IGM}), \end{cases} \tag{B.140}$$

for $\omega = 10^{-4}\,{\rm eV}$ and $g_{\rm a\gamma\gamma} = 10^{-10}\,{\rm GeV}^{-1}$. This suggests that if the axion is effectively massless, the conversion rate is small towards the center of the galaxy and peaks somewhere in between the circumgalactic medium and the intergalactic medium. The exact dependence of this conversion probability on the distance from the halo center depends on how the plasma density, the magnetic field strength and the magnetic field domain sizes change, in particular in the region several virial radii away from the galaxy center. This region is notoriously hard to model as a result of baryonic feedback. Recent and upcoming observations and simulations [264, 231, 382, 383] that target the missing baryon problem might also shed more light on this question, and we leave a more detailed study to future work when more information is available.

However, to motivate further studies, we estimate the sensitivity of axion-induced screening of the CMB to this signal with a simple heuristic model, first studied in [249]. We add to the toy model in [249] galaxies with sharp boundaries at fixed $r_{\rm b}$ from the halo center. Inside the sharp boundary, we assume the properties of the medium is similar to the ISM around the location of the Sun, while outside the sharp boundary, the medium is similar to the environment of the IGM. In this toy model, axion-photon conversion only happens outside the sharp boundary, and as a result, is anti-correlated with the location of halos. Similar to [249], we treat $m_{\gamma,{\rm eff}} = \sqrt{m_\gamma^2 - m_{\rm a}^2}$ as well as $g_{\rm a\gamma\gamma}|\mathbf{B}|$ in the intergalactic medium as free parameters.

In this toy model, we can compute the 1-halo and 2-halo contribution to the correlations of the conversion probability. In the limit where the 2-halo term completely dominates, the toy model qualitatively captures the anisotropies of this non-resonant conversion. The conversion probability along a line of sight direction $\hat{n}$ with a halo centered along the direction $\hat{n}_i$ can be computed to be

$$P(\chi_i, m_i) = \bar{P} - \frac{4}{3}\frac{g_{\rm a\gamma\gamma}^2 |\mathbf{B}|^2 \omega^2}{m_{\gamma,{\rm eff}}^4\, r_{\rm dom}} r_{\rm b} \sqrt{1 - \left(\frac{\chi_i \theta}{(1+z_i) r_{\rm b}}\right)^2}, \tag{B.141}$$

where θ is again the angular separation between $\hat{n}$ and $\hat{n}_i$, and $\bar{P}$ is the conversion probability along a line of sight with no halos. We neglect the latter contribution since it contributes only to the monopole. Note the additional *minus* sign, which suggests that this signal appears as an emission (lack of absorption) that is correlated with the location of halos. We generally expect a cross correlation between the halo location and the conversion probability, though the sign can depend on the exact shape of the density and magnetic field profile. The result of our estimate is presented in Fig. B.5, where we forecast the sensitivity of Planck and CMB-S4 to the axion photon coupling in the massless axion limit. The result is presented in the units used in [249] to highlight the prospect of improvement with the methodologies presented in Chapter 5. With CMB-S4, we expect an improvement of up to two orders of magnitude over the constraints presented in [249].

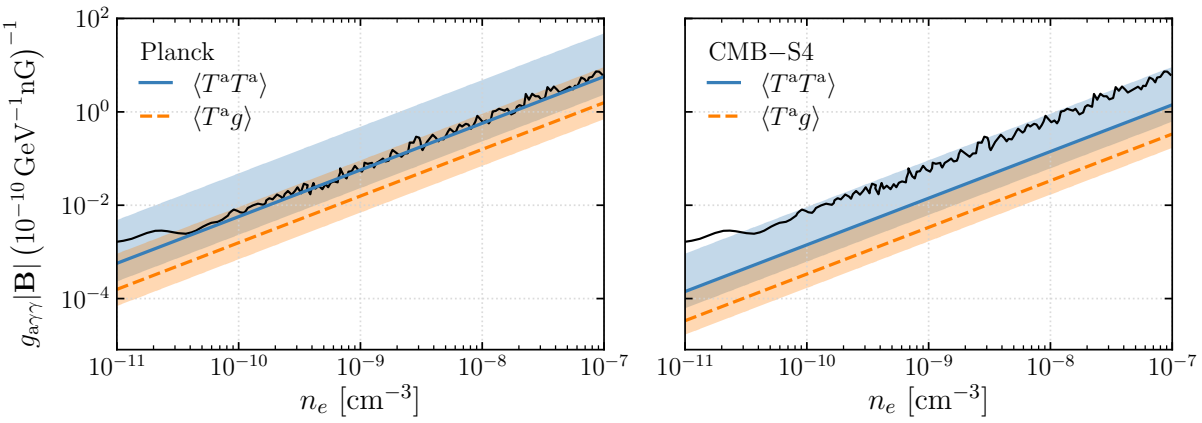

Figure B.5: Projected sensitivity of axion-induced screening to the combination of axion-photon coupling $g_{{\rm a}\gamma\gamma}/10^{-10}{\rm GeV}^{-1}$ and the extra-galactic magnetic field $|\mathbf{B}|/{\rm nG}$ in the simple sharp boundary model (see equation (B.141)), assuming Planck (left) and CMB-S4 (right) sensitivity and the unWISE blue galaxy sample. The blue solid (orange-dashed) line is the projected sensitivity with temperature auto-correlation (cross-correlation with unWISE galaxies) assuming $r_b = 5R_{\rm vir}$, while the shaded band is obtained for r_b in the range $(R_{\rm vir}, 10R_{\rm vir})$. The magnetic domain size is fixed at $r_{\rm dom} = 1\,{\rm Mpc}$ in the IGM and the effective electron density in the IGM $n_e = m_e m_{\gamma,{\rm eff}}^2/e^2$ is a free parameter, as in Ref. [249]. The region above the black solid line is excluded from the analysis of COBE/FIRAS data in [249].

B.10 Rough sensitivity estimate

In this appendix, we provide quick but clearly imprecise methods to estimate the sensitivity of dark screening to various beyond standard model scenarios of interest. These estimates apply to cases where we inject or remove photons (in the CMB frequency band) in a frequency and position dependent manner. The estimates will be in a language that is familiar to researchers thinking about precision experiments to search for dark matter/dark sector, and will be increasing in rigor.

The information carried by CMB photons is enormous, partly due to the fact the total number of observable CMB photons is very large. The total number of CMB photons we can collect with CMB-S4 will be $\mathcal{N}_\gamma \sim 10^{28}$. With zero noise and perfect distinguishability, we can in principle measure an optical depth, the probability of injecting or removing of CMB photons, as small as $1/\sqrt{\mathcal{N}_\gamma} \sim 10^{-14}$. This estimate is certainly very crude, since photon removal generally happens only in a small fraction of the universe, and more importantly, there are other contributions to the noise level that should be taken into account.

Generally, the temperature perturbation generated from axion-induced screening (similar for dark photon) is $\delta T^{\rm a} \simeq \bar{T}\delta\tau^{\rm a}$, which should be compared to the noise $\delta T^{\rm noise}$, consisting of the primary CMB perturbations, foregrounds, and instrumental noise. For signals that cannot be distinguished from background (including the primary CMB anisotropies), one can constrain an optical depth of $\delta\tau^{\rm a} \sim 10^{-5}$.

The dark screening signal can be distinguished from background in two major aspects. Firstly, the optical depth, from both photon to dark photon, or photon to axion conversion, is frequency dependent. This allows for significant reduction of contamination by using the ILC technique, which can reduce $\delta T^{\rm noise}$ by more than three orders of magnitude, for example, in the case of searches for dark photon screening with CMB-S4 (see Fig. 5.6 and Fig. 4.8 in Chapter 4; note that this factor depends on the reference frequency used and can vary by about an order of magnitude across the whole frequency range). This reduction of noise depends on the instrument, as well as the frequency scaling of $\tau^{\rm a}$, and has to be worked out explicitly. Secondly, the signal and noise generally have different spatial profile, or ℓ-dependence. Qualitatively, this can be thought of as doing ℓ^2-measurements at the same time, and the sensitivity increases when more ℓ-modes get included in the experiment. For example, the sensitivity in $\delta\tau^{\rm a}$ scales approximately as $1/\sqrt{\ell}$ for the auto-correlation observable (which contains two factors of $\delta\tau^{\rm a}$), and as $1/\ell$ for cross-correlation with large-scale structure observable (which has only one factor of $\delta\tau^{\rm a}$). Combining the two improvements from the characteristic frequency and spatial dependence of the signal, we can estimate the sensitivity to $\delta\tau^{\rm a} \sim 3\times10^{-10}$ with auto-correlation, and $\delta\tau^{\rm a} \sim 10^{-11}$ with

cross-correlation. Keep in mind that optimizing the correlation functions only changes the scaling of the sensitivity with ℓ, but the other parameters (such as $\bar{T}$, conversion radius, or magnetic field strength) appear in the same combination.

Depending on the BSM model, the optical depth can have different parametric dependence on the physical quantities of distant galaxies and halos, as well as BSM parameters. For example, the photon to axion conversion optical depth $\tau^{\rm a}$ scales as

$$\tau^{\rm a} \sim \frac{g_{\rm a\gamma\gamma}^2 \, |\mathbf{B}|^2 \, \omega \, r_{\rm res}}{m_{\rm a}^2}, \tag{B.142}$$

and a rough sensitivity of $g_{\rm a\gamma\gamma}$ can be estimated to be $g_{\rm a\gamma\gamma} \sim 10^{-13}{\rm GeV}^{-1}$ with cross correlation function $\langle T^{\rm a} g \rangle$ and CMB-S4 sensitivity. Note that the parameters $r_{\rm res}$ and $|\mathbf{B}|$ both depend on the halo mass and the axion mass, which in turn gives a scaling of the sensitivity to $g_{\rm a\gamma\gamma}$ with $m_{\rm a}$ that is more complicated than the one appearing in the equation above. Similar estimates can be obtained for searches of polarization signals once the residual noise-level post-ILC is estimated.

B.11 Likelihood and sensitivity forecast

For a fixed axion mass, all observables in this Chapter have a simple scaling with the axion-photon coupling as $\propto g_{\rm a\gamma\gamma}^n$, with $n = 2$ or 4. Given some angular correlation function d_ℓ from the ILC subtracted maps and an expected axion-induced signal $g_{\rm a\gamma\gamma}^n s_\ell^{\rm a}$, the likelihood can be written as

$$-2 \ln \mathcal{L}(g_{\rm a\gamma\gamma}) = \sum_\ell \frac{\left(d_\ell - g_{\rm a\gamma\gamma}^n s_\ell^{\rm a}\right)^2}{\sigma_\ell^2} + \text{const.}, \tag{B.143}$$

where σ_ℓ represents the noise covariance at each ℓ whose form depends on the specific observable considered; note that in this notation σ_ℓ also includes the appropriate factor to account for the number of samples available at each scale, including the effect of fractional sky coverage. Assuming that the data has no signal, we have $\langle d_\ell s_\ell^{\rm a} \rangle = 0$ and $\langle d_\ell^2 \rangle = \sigma_\ell^2$, and the likelihood is maximized at $g_{\rm a\gamma\gamma} = 0$. The expectation value of the likelihood is therefore

$$\langle -2 \ln \mathcal{L}(g_{\rm a\gamma\gamma}) \rangle = g_{\rm a\gamma\gamma}^{2n} \sum_\ell \frac{\left(s_\ell^{\rm a}\right)^2}{\sigma_\ell^2} + \text{const.} \tag{B.144}$$

Following a Bayesian approach, the posterior distribution of the parameter $g_{a\gamma\gamma}$ is then

$$f(g_{a\gamma\gamma}) = \frac{e^{-\frac{g_{a\gamma\gamma}^{2n}}{2\sigma_n^2}}}{(2\sigma_n^2)^{\frac{1}{2n}}\Gamma\left(1+\frac{1}{2n}\right)}, \tag{B.145}$$

where we have defined $\sigma_n^2 \equiv \sum_\ell \left[\left(s_\ell^a\right)^2/\sigma_\ell^2\right]$ and obtained the denominator from normalizing the distribution to 1 for $g_{a\gamma\gamma} \geq 0$, i.e. assuming a flat prior over positive couplings. To estimate the $1-\sigma$ sensitivity on the parameter, $\sigma_{g_{a\gamma\gamma}}$, we compute the largest value of the parameter that is compatible with the observation at 68% CL. In general this is given by $\sigma_{g_{a\gamma\gamma}} = x(\sigma_n)^{1/n}$, where the numerical coefficient x can be obtained by solving the equation

$$\int_0^{x(\sigma_n)^{1/n}} f(g_{a\gamma\gamma}) = 0.68. \tag{B.146}$$

For the case of $n = 1$, one simply recovers a Gaussian posterior distribution and $x = 1$; in that case the parameter σ_1^2 is just the inverse of the Fisher matrix, where now the likelihood is simply quadratic in the parameter and therefore the usual second order Taylor expansion defining the Fisher matrix is exact. For our purposes, we are interested in the cases of $n = 2, 4$ that give

$$x \simeq 0.76 \quad \text{for} \quad n = 2, \qquad\qquad x \simeq 0.7 \quad \text{for} \quad n = 4. \tag{B.147}$$

As expected if the leading order term in likelihood is $g_{a\gamma\gamma}^4$ or $g_{a\gamma\gamma}^8$, it will change more rapidly away from the maximum when $g_{a\gamma\gamma}$ deviates from 0, leading to a smaller uncertainty on the parameter. The numerical factors obtained here are used to estimate the sensitivity on the photon-axion coupling from the two- and three-point functions in Sec. 5.4.2 – see Eqs. (5.40), (5.41) and (5.42). A similar procedure can be followed if one wants to combine all the observables that have different scaling with $g_{a\gamma\gamma}$, by adding up their contributions in (B.143) (neglecting cross-correlations).